Dublin City University

Ollscoil Chathair Bhaile Átha Cliath

Development of Hierarchical Magnetic Nanocomposite Materials for Biomedical Applications

Sarah P. Clarke, B.Sc.

Thesis submitted for the Degree of
Doctor of Philosophy

Supervisor: Dr. Dermot Brougham

School of Chemical Sciences January 2013

I hereby certify that this material, which I now submit for assessment on the programme of study leading to the award of doctor of philosophy is entirely my own work, that I have exercised reasonable care to ensure that the work is original, and does not to the best of my knowledge breach any law of copyright, and has not been taken from the work of others save and to the extent that such work has been cited and acknowledged within the text of my work.

Signed:_____(Candidate) Student No.:_____

Date :_____

List of abbreviations

Abbreviation (units)

AC	Alternating Current
AML	Aqueous Magnetoliposome
AuNP	Gold Nanoparticle
Au-IONP	Gold-Iron oxide Nanoparticle
Au-IONPC	Gold-Iron oxide Nanocluster
BPC	Bilayer Particle Cluster
Cit-IONP	Citrate-stabilised Iron Oxide Nanoparticle
Cit-IONP/PACA	Citrate-stabilised Iron Oxide/PACA Nanocomposite
CPMG	Carr-Purcell Meiboom Gill
D	Diffusion coefficient (s)
D_{H2O}	Diffusion coefficient of water (s)
DDT	Dodecanethiol
DDV	Drug Delivery Vehicle
d_{hyd}	Hydrodynamic diameter (nm)
d_{PCS}	Diameter obtained by Photon Correlation Spectroscopy (nm)
d_{SPM}	Diameter obtained by SPM simulations (nm)
d_{TEM}	Diameter obtained by Transmission Electron Microscopy (nm)
DOPG	1,2-Dioleoyl-*sn*-glycero-3-[phospho-rac-(1-glycerol)] (sodium salt)
DTAB	Dodecyltrimethyl ammonium Bromide
DTAB-IONP	Dodecyltrimethyl ammonium Bromide-stabilised iron oxide
DTAB-IONP/PACA	DTAB-stabilised iron oxide Nanocomposite
FFC-NMR	Fast-field Cycling NMR
$G(\tau)$	Exponential time correlation function
HPPS	High-performance Particle Sizer

ICP-AES	Inductively coupled plasma atomic emission spectroscopy
IONP	Iron oxide Nanoparticle
IONPC	Iron oxide Nanoparticle Cluster
LDV	Laser Doppler Velocimetry
M_S	Saturation Magnetisation
M_0	Bulk (net) Magnetisation
MCL	Magnetic Cationic Liposome
MDT	Magnetic Drug Targeting
MFH	Magnetic Fluid Hyperthermia
MRI	Magnetic Resonance Imaging
MTC	Magnetic Targeted Carrier
μ	Magnetic moment of a particle
mV	millivolts ($1x10^{-3}$ V)
MHz	megahertz ($1x10^{6}$ Hertz)
nm	nanometer
NMR	Nuclear Magnetic Resonance
NMRD	Nuclear Magnetic Resonance Dispersion
NNLS	Non-negative Least Squares
NP	Nanoparticle
NP^*	Activated nanoparticle
OAc	Oleic Acid
OAm	Oleylamine
OAc/Oam IONP	Oleic acid/oleylamine-stabilised iron oxide nanoparticles
Oam IONP	Oleylamine-stabilised iron oxide nanoparticles
PACA	Poly (alkyl-cyanoacrylate)
PALS	Phase-analysis Light Scattering

PCS	Photon Correlation Spectroscopy
PDI	Polydispersity Index
PEG	Polyethylene Glycol
PNIPAM	poly(N-isopropylacrylamide)
R_1 ($1/T_1$)	Longitudinal (spin-lattice) relaxation rate (s)
r_1	Relaxivity (s^{-1})
RF	Radiofrequency
SAR	Specific Absorption Rate
SML	Solid Magnetoliposome
SPM	Superparamagnetism
T_1	Spin-lattice relaxation
T_2	Spin-spin relaxation
TEM	Transmission Electron Microscopy
TGA	Thermogravimetric Analysis
ν_L	Larmor Frequency (MHz)
ΔE_{anis}	Anisotropy Energy (GHz)

Abstract

Magnetic Nanocomposite Materials for Image-Guided Drug Release in Cancer

Magnetic nanocomposites and nanoparticle assemblies have gained significant interest for biomedical applications including MRI, hyperthermia and targeted drug delivery. Their efficacy depends on colloidal stability, optimal magnetic properties and appropriate size and surface chemistry for good biodistribution.

The first part of this thesis focuses on the preparation of sub 20 nm magnetic nanoparticles (IONP) and the modification of their surface charge for subsequent encapsulation or adsorption to the polymer poly n-butyl cyanoacrylate (PACA) to produce IONP dilute assemblies. In addition to this, IONP-dense assemblies were prepared using established methods, and the effect of IONP density on the magnetic resonance properties of the assemblies was assessed. It was found that the NMR response was very sensitive to the IONP density and also to the structure of the assembly. This suggests potential routes to novel materials with tunable MRI properties.

The second part of the thesis focuses on the assembly of IONP into dense assemblies (or clusters) in organic media using a novel *in situ* assembly technique based on reducing surfactant coverage. Particular attention was paid to the kinetics of the assembly process and the effect of adding surfactants and/or gold nanoparticles to the metastable IONP assemblies was also studied.

CHAPTER 1

Introduction

1.1 Thesis overview

Magnetic Nanocomposite Materials for Image-Guided Drug Release in Cancer

Magnetic iron oxide nanoparticles (IONP) and their composite materials have received considerable interest due to their many potential bio-applications. IONP prepared via non-hydrolytic thermal decomposition syntheses of iron precursors followed by phase transfer into aqueous media are usually preferable as the process provides nanoparticles with good particle size control and superior crystallinity. This approach also allows functionalisation of the IONP and engineering of the surface charge. These advantages could be used in the design of therapeutics for Magnetic Drug Targeting (MDT), which could be tracked in the body by MRI. For MDT, drugs could also be incorporated into the core of the nanocomposite, or adsorbed via ionic or covalent linkage onto its surface. Once transported to the site of interest, drug release can be facilitated by many methods such as bond degradation, pH cleavage, or RF irradiation producing a local temperature increase (hyperthermia).

The first part of this thesis focuses on the preparation of sub 20 nm IONP and their functionalisation using both anionic and cationic surface ligands, followed by their combination by encapsulation or adsorption with Poly n-butyl cyanoacrylate (PACA) in an effort to synthesise nanocomposites for targeted drug delivery and heat-mediated drug release. The second part of this thesis focuses on the assembly of iron oxide nanoparticles into larger nanoparticle assemblies (or clusters) in organic media. The kinetics of the assembly process was observed over time by Photon Correlation Spectroscopy. The effect of adding additional surfactant on the assembly/disassembly of the clusters was studied. The effect of gold nanoparticles on the assembly kinetics and stability were also assessed. Nanoparticles of this type offer additional diagnostic potential due to their plasmonic properties.

1.2 Applications of magnetic Iron oxide nanoparticles in biomedicine

The application of iron oxide nanoparticles in the biomedical sciences has been ongoing since the 1970s, in the areas of drug delivery, magnetic resonance imaging, cell recognition and thermogenic treatments. More specifically, iron oxide nanoparticles of magnetite (Fe_3O_4) and maghemite (γ-Fe_2O_3) have shown to be very promising candidates for use in the above mentioned applications, due to the many favorable physical and chemical properties associated with them [1, 2]. Iron oxide nanoparticles can be prepared via straight-forward synthetic routes, typically yielding small nanoparticles of < 20 nm, they exhibit low toxicity in-vivo and are easily excreted from the body [3]. Their excellent magnetic properties are key to their potential as therapeutic and diagnostic agents. Iron oxide nanoparticles possess a large magnetic moment and are typically superparamagnetic in nature, that is they do not retain any bulk magnetisation on removal of an external field [4].

In vivo applications of IONP can be divided into their therapeutic and diagnostic uses. Therapeutic applications of magnetic particles include their use in magnetic fluid hyperthermia [5, 6] and the development of a variety of drug delivery vehicles for a wide range of purposes, including the development of magnetic targeted carriers, or MTCs for the treatment of solid tumours [7] . Diagnostically, IONP and their composite materials have been used in the development of a class of compounds known as 'Magneto-pharmaceuticals', particularly for the enhancement of MRI imaging and are components in a wide range of contrast agents e.g. Endorem or Resovist [8, 9].

1.2.1 Magnetic drug targeting and the use of magnetic carriers as potential drug delivery vehicles in biomedicine

One of the major obstacles in drug delivery, in particular of chemotherapeutics, is the delivery of the drugs to a specific site in the body while minimising potential undesired cytotoxic effects on surrounding healthy tissue caused by administration

of the drug itself or by any processes that may follow e.g. heating of the tumour region using an applied magnetic field.

Magnetic drug targeting (MDT) processes have been developed for this reason, and involve the delivery of the drug of interest, under the influence of a static magnetic field, to a particular site of interest in the body using a drug delivery vehicle (DDV). Iron oxide nanoparticles have shown excellent (although size dependent), capability to be transported through the vasculature system of the body, thus allowing them to be potentially concentrated at a chosen site [10].

MDT therapies offer many benefits over more conventional non-specific methods such as chemo- and radiotherapies, as they allow for maximum drug efficacy while using the lowest possible dose and, in turn, reducing the potential toxicity and side effects usually associated with increased drug concentration in vivo [11], although they are limited by the accessibility of the target area to the externally applied static field. Targeting can also be achieved by two other routes; passive targeting, where carriers are allowed to circulate freely through the vasculature system and biodistribution is determined by size, and active targeting, which involves direct control of DDV circulation by specific recognition of ligands on the delivery vehicle [10, 12].

With magnetic drug targeting, drugs can be encapsulated into the core of a delivery vehicle [13, 14], or adsorbed (via ionic or covalent linkage) onto its surface [15, 16]. The latter is more favourable as it allows for a much lower required drug dose while maintaining efficacy of that drug. Once transported to the site of interest, drug release can be facilitated via many methods such as bond degradation [17], pH dependent cleavage [18], irradiation [19], or the use of an elevated temperature (Hyperthermia) [20].

Multiple systems and strategies have been investigated to meet the goals of selective delivery of chemotherapeutic agents, with some successfully reaching clinical trials in humans. The use of Magnetic Cationic Liposomes (MCLs), for example, has proven successful in the delivery of magnetic iron oxide nanoparticles to target cells by electrostatic interaction of their positive surface charge with an oppositely charged cell surface (particularly in the Kupfer cells of

the liver), making them potential mediators for successful passive drug targeting. In addition to this MCLs were observed to provide extended accumulation times of chemotherapeutic drugs at the tumour site, make them extremely promising candidates for intelligent drug delivery and active targeting strategies [7]. In one particular study by Ito et. al. [21], a ten-fold increase was observed for MCLs towards targeted tumour cells relative to their neutral equivalents, resulting in a much improved transfection efficiency and successful nucleic acid delivery to the site of interest in vivo. MCLs generate heat by hysteresis under the influence of an applied magnetic field, with temperatures of ~42°C being achieved in the affected tumour site. Furthermore, the temperature of the surrounding healthy tissue has been observed to remain in the region of 37-39°C upon heating of the cancerous mass, which further outlines the benefits of the use of MCL delivery vehicles in hyperthermia.

Another widely reported type of delivery vehicle in the literature are those based on polymer-associated magnetic nanoparticles where the polymer is used to encapsulate both the magnetic colloid and any drug substances to be delivered. Three main methods of entrapment of drugs and other 'model compounds' have been widely reported within the literature; encapsulation, where the drug of choice is combined with the monomeric material [22] or pre-polymerisation/sorption which involves the addition of the drug after the polymerisation process is complete [23]. Selection of the method used usually depends on the type of drug to be entrapped, in addition to the polymer synthesis chosen and the structural properties of the polymer itself (chain length, degree of polymerisation etc).

The entrapment efficiencies of loaded bioactives depend strongly on the method of entrapment used and also on the solubility of the drug in the polymerisation medium. For example, entrapment in nanospheres is favoured more for hydrophilic drugs [24], whereas drugs more lipophilic in nature are more successfully incorporated into nanocapsule structures [25]. A wide variety of bioactives including insulin, ovalbumin and oligonucleotides have been efficiently entrapped within polymer nanoparticles possessing an aqueous core for oral peptide and protein delivery [26].

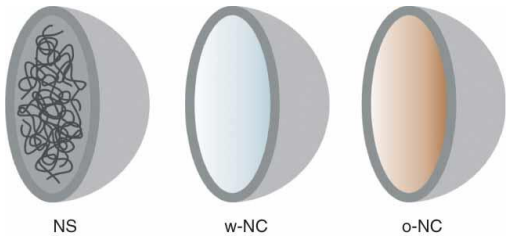

Figure 1.1: General structure of polymer nanospheres (NS), water-containing nanocapsules (w-NC) and oil-containing nanocapsules (o-NC) (Ref Couvreur)

The use of these so called 'thermosensitive' polymer materials allow for successful inductive heating using an applied magnetic field to temperatures above the critical phase transition temperature, or the LCST, of the polymer, which can fall within the range of approximately 30-45°C. Above this temperature, phase separation occurs due to the positive value of the free energy of mixing, and the result is an observed shrinkage or compaction of the polymer particles. A transformation in the structure of the polymer chains from an expanded hydrophilic structure to a more compact hydrophobic one is also observed at this characteristic temperature. This process, in turn, results in an initial rapid release of any encapsulated substances i.e. the drug to be delivered, followed by a more controlled release phase, making these stimuli-responsive polymer drug carriers attractive candidates for intelligent temperature-responsive drug delivery due to their attractive responses to changes in their environmental conditions e.g. pH, temperature or magnetic field strength [27]. The most commonly used polymers reported in the literature are polyethylene glycol (PEG) [28] and derivatives of poly(N-isopropylacrylamide) (PNIPAM) [29].

Another attractive potential candidate for polymer-based magnetic carriers may also be a more biocompatible and biodegradeable polymer, poly(alkylcyanoacrylate) (PACA), with previous studies already demonstrating its capacity for successful loading of doxorubicin into the particle core [30]. The alkyl-cyanoacrylates are a family of strong, fast acting adhesives that have been previously exploited as effective surface and tissue adhesives in both medical and non-medical applications. Cyanoacrylate monomers such as methyl-2-cyanoacrylate, ethyl-2-cyanoacryalte and n-butyl-cyanoacrylate are amongst the members of the cyanoacrylate family that have been used since the 1960s for the formulation of many commercially sold adhesive glues (e.g. Superglue) and

veterinary and skin-adhesive glues for use in suture-free surgeries (e.g. Vetbond and Indermil).

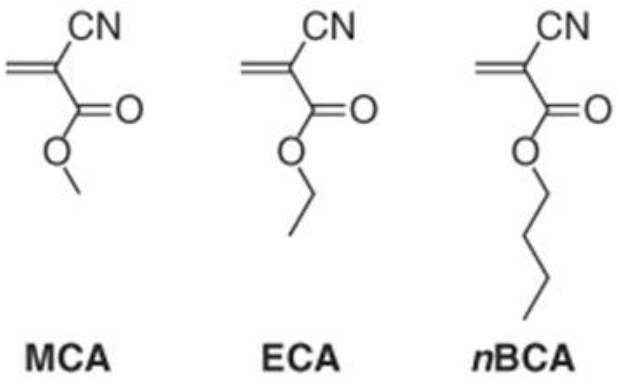

Figure 1.2: Structures of methyl-cyanaocrylate (MCA), ethyl-cyanoacrylate (ECA) and n-butylcyanoacrylate (nBCA) monomers.

Most recently, interest in these materials has increased due to applications for the delivery of a wide range of therapeutics, particularly for the treatment of many cancers as they minimise the threat of high drug toxicity in healthy regions of surrounding tissue to the tumour site by confining the nanoparticles and/or drug to an aqueous or oily matrix within a biodegradeable polymeric carrier shell.

Polymers were first introduced into the area of drug delivery by Patrick Couvreur in the 1970s with his research into lysosomotropic therapeutics for cancer chemotherapy [14]. Their many favourable properties such as biocompatibility, biodegradability, simple and highly reproducible syntheses, compatibility and entrapment efficiency with a vast range of therapeutics suggest their excellent potential as effective drug delivery agents. Research into their method of delivery has focused primarily on the oral route of administration, but recent studies are expanding into potential methods of ocular and transdermal administration, in addition to penetration of the blood-brain barrier [31]. Furthermore, polymer nanoparticles possess the advantage of high stability in biological media, protecting therapeutics in vivo against enzymatic degradation and also provide a feasible method for controlled drug release. Despite the extent of research conducted on PACA nanoparticles, no product has entered the market to date, although many formulations have been investigated as far as clinical phase II/III trials [32].

1.2.2 Thermogenic use of magnetic nanoparticles and their composites in biomedicine (Magnetic Fluid Hyperthermia)

Magnetic nanoparticles and their composite drug delivery formulations possess an excellent potential for uniform heating and non-invasive delivery of therapeutics and are widely studied as potential hyperthermic treatment agents in biomedicine. Magnetic Fluid Hyperthermia (MFH) has received much attention as a method for the treatment and control of a variety of malignant tumour types due to its provision of significant heating effects in the presence of an AC magnetic field without any significant interference from any anatomical obstructions e.g. bones. MFH is a technique whereby magnetic fluids (or ferrofluids as they are otherwise known) are coupled to an AC magnetic field and heat the tissue of interest to temperatures in the region of 43-55°C. The temperature to which the tumour region is heated depends on the hyperthermic method employed. Traditional magnetic hyperthermia involves heating within the 45-47ºC temperature range, whereas magnetic thermoablation utilises temperatures up to 55ºC. Temperatures in the higher range result in rapid immediate cell death.

Although hyperthermic methods are frequently successful in the treatment of malignancies, limitations to the treatment also exist. For example, deep rooted tumours can sometimes be difficult to access by heat induction, and often recur in many patients as a result. Other alternatives for more difficult to treat malignancies, or cancers where secondaries are already present, include whole body hyperthermia (WBH), local hyperthermia and interstitial hyperthermia [6]. More often the entire tumour is not destroyed and secondaries can subsequently occur. These secondaries are most commonly observed in the vicinity of the bone of the pelvis or skull, where shielding of the tissue from the applied RF occurs. This problem often results in thermal underdosage in the target of interest and, in turn, regrowth of the malignant tumour. These problems are often counteracted by direct injection of the magnetic nanoparticles into the tumour, which can be effective in treating large accessible solid tumours of this type.

In a typical MFH treatment, colloidal dispersions of magnetic nanoparticles are injected into the vasculature system of the body and are localised at the site of interest using a static external magnetic field. Alternating magnetic fields are then

utilised to generate heat energy from the nanoparticles present, via two relaxation mechanisms, Néel relaxation and rotational Brownian relaxation [33].

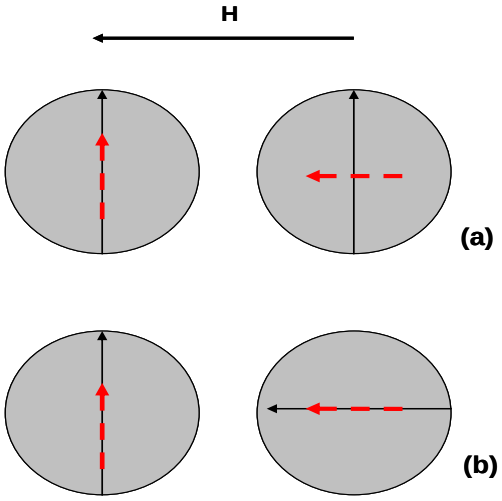

Figure 1.3: Relaxational losses leading to heating in an alternating field (H). (a) ´Neel relaxation. The magnetic moment (dotted arrow) originally locked along the crystal easy axis (solid arrow) rotates away from the crystal axis towards the external field H.(b)Brownian mode. The whole particle oscillates towards the field, with the moment locked along the crystal axis, under the effect of a thermal force [34].

Heat generation via Néel relaxation is due to rotation of the magnetic moments contained within the nanoparticle core relative to the crystal lattice (internal dynamics), where the magnetic moments, originally locked along the easy axis of the crystal, rotate away in the direction of the external field. Heat energy is generated as a result of these oscillations of the magnetic moments in the presence of the alternating magnetic field applied [35]. The time taken for these oscillations to occur is known as the Néel relaxation time and is represented by the following equation:

$$\tau_n = \tau_0 \exp\left[\frac{KV}{k_B T}\right] \qquad \text{Equation 1.1}$$

where τ_0 is the time constant (~10^{-9} s), K is the anisotropy constant ,V is the volume of the particle core, k_B is the Boltzmann constant and T is the absolute temperature [36]. It follows that, the frequency ν_N for maximal heating via Néel relaxation is given by Equation 1.2:

$$\nu_N = \frac{1}{2\pi\tau_N} \qquad \text{Equation 1.2}$$

Brownian motion contributions to the heating process arise due to rotation of the particle as a whole due to the torque exerted on the magnetic moment by the external AC magnetic field. The time taken for this process to occur, the correlation time for Brownian motion, is given by:

$$\tau_B = \frac{3\eta V_H}{k_B T} \qquad \text{Equation 1.3}$$

where η is the viscosity of the carrier liquid and V_H represents the hydrodynamic volume of the particle responsible for the process [37]. The frequency required for maximal heating via this process is given by:

$$\nu_B = \frac{1}{2\pi\tau_B} \qquad \text{Equation 1.4}$$

The quantity of heat delivered by a magnetic nanoparticle material can be represented by the specific absorption rate, or SAR, of that material. This is essentially a measure of the heating potential of the material and may be defined by the following equation:

$$SAR = C\frac{\Delta T}{\Delta t}\frac{1}{m_{Fe}} \qquad \text{Equation 1.5}$$

with C representing the specific heat capacity of the sample and $\Delta T/\Delta t$ being the initial slope of the time dependent temperature curve where the maximum value for SAR is observed and m_{Fe} is the iron content per gram of the iron oxide nanoparticle suspension. SAR values are given in Watts per kilogram ($W.kg^{-1}$), with typical values for the ferrites of 50-500 $W.kg^{-1}$ [38]. Higher SAR values are favourable as they are associated with lower particle concentrations to produce a temperature jump.

The SAR of magnetic nanoparticle suspensions has been demonstrated in the literature to exhibit strong dependence on a number of physiochemical properties of the nanoparticles present such as particle size, size distribution, and particle shape in addition to electromagnetic field parameters such as the frequency and the amplitude of the magnetic field applied.

Ma et al. [39] demonstrated how the SAR for magnetite nanoparticles in the size range of 7-13 nm was attributed to the presence of Néel and Brownian rotation losses, and to hysteresis loss for particles in excess of ~46 nm. As these losses are subsequently dependent on the size of the particles present, a dependency exists between the core size of the particles and their SAR. It has been previously reported in the literature that, on decreasing the core particle size, a transition from ferromagnetic to superparamagnetic behaviour occurs [38], thus changing the loss mechanism and, in turn, the heating effect observed. Nanoparticles used for hyperthermia primarily exploit Néel relaxation processes over all other types, as even at smaller field amplitudes, superparamagnetic nanoparticles exhibit higher SAR than their multi-domain counterparts. In addition to this, narrow particle size distributions have been linked with higher SAR values as they are commonly associated with heat generation through Neél relaxation processes.

One other physical property that has been reported to have a significant effect on the SAR is the surface coverage of the particles used in hyperthermic treatments. In one particular study for example, it was observed that γ-Fe_2O_3 nanoparticles coated with dextran of higher molecular weight values exhibited higher SAR values in vitro than those coated with lower molecular weight varieties [38, 40]. In a different study on the use of gold-coated magnetite nanoparticles (Au-IONP), it was observed that the temperature rise and the time required to reach the therapeutic temperature of 42°C was faster for Au-IONP than those without Au coverage. Furthermore, the SAR of Au-coated IONP have been shown to exhibit a 4-5 fold increase in the SAR value relative to those in the absence of Au coverage [41]. The reported results in both of the above cases suggest that the observed increases in the SAR was as a result of the presence of the ligands/surface coatings as opposed to increases due to nanoparticle aggregation. These observations are very promising for advances in hyperthermia, as it provides the potential for tuning the surface coverage of the magnetic materials used for specific cancers. It is

therefore vital that control of nanoparticle properties is considered, as it has been observed that factors such as those mentioned above have a significant influence on the efficacy of the treatment.

The value of the SAR of a given magnetic material is also strongly dependent on the frequency and amplitude of the magnetic field applied during the heating process. Hergt et al. [36] highlight that at low frequencies, for superparamagnetic nanoparticles, hysteresis losses increase with the square of the frequency and amplitude of the applied field. Non-specific heating of surrounding tissue during hyperthermia, however, places a limit on the RF frequency and field amplitude range that can be used to generate these losses and maximise the effects of heat-mediated treatment of pathological cells. Non-specific heating effects associated with eddy currents not only in the tumour site but also in the surrounding healthy tissue reduce the selectivity of the treatment. In addition to this, magnetic resonance induced heating is greatest at the surface of the targeted tissue mass than in the center, resulting in what are known as thermal 'hot spots' in the tumour region, particularly in the region of the resonance frequency of maximum heat absorption. The FDA have outlined a number of limitations for acceptable SAR ranges in particular regions of the human body and are as follows:

- 0.4 $W.kg^{-1}$ for whole body exposure
- 3.2 $W.kg^{-1}$ average in the head/brain region
- 8.0 $W.kg^{-1}$ peak in any 1 gram of exposed tissue

The literature reports a wide range of studies on the determination of the optimum field frequency and amplitude required to optimise the hyperthermic potential, i.e. the SAR for a number of nanoparticle types including iron oxide nanoparticles, cobalt ferrites, manganese ferrites and a series of Fe doped AuNP to mention a few. Each nanoparticle type possesses its own characteristic field frequency and field amplitude at which they produce a maximum heating potential (SAR). Iron oxide nanoparticles, however, continue to attract more attention over other nanoparticle types due to their lack of toxicity and excellent biocompatibility in vivo. With nanoparticles of this nature, it has been reported in the literature that field frequencies of approximately 400 kHz with an amplitude of 10 $kA.m^{-1}$ are the

most optimum in producing the highest possible SAR value of 960 $W.kg^{-1}$ for 15 nm single domain IONP [42].

One effect that has not gained enough interest, however, is the effect of aggregation or clustering of nanoparticles on SAR. In one particular study conducted by Jordan et. al. [6] it was deduced that, despite the dependence of SAR on core nanoparticle size, an increase in the particle hydrodynamic diameter due to aggregation in particular had no impact on the SAR of the material.

1.2.3 Iron oxide nanoparticles in the development of contrast agents for MRI (Magnetic Resonance Imaging)

The use of contrast agents in MRI applications has been extensively demonstrated over the last 15 years to further enhance and increase the sensitivity of generating image contrast between healthy and pathological tissues in vivo. MRI agents operate on the basis of effectively decreasing T_1 and/or T_2 relaxation times of the object or tissue under analysis. For this reason, they may be deemed "T_1 agents" or "T_2 agents", depending on the relaxation process on which they have an effect. The measure of how a given agent can reduce relaxation times of the H_2O proton signal within a given suspension is known as its relaxivity. Relaxivity can be defined as the "proton relaxation enhancement per unit concentration" of the material used and can be denoted as r_1 and r_2 for the T_1 and T_2 relaxation processes, respectively. Relaxivities (given the units $s^{-1}mM^{-1}$) are parameters used to quantify relaxation enhancements by the following relations:

$$R_{1\,obs} = R_{1H2O} + r_1\,[Fe]$$

or

$$R_{2\,obs} = R_{1H2O} + r_2\,[Fe]$$

Equation 1.6

where R_{1obs} and R_{2obs} represent the measured relaxation rates, and R_{1H2O} and R_{2H2O} the rate in the absence of any agent. Concentration independent relaxivities r_1 and r_2 are, in turn, defined as the change in longitudinal or transverse relaxation as a

function of iron content in the contrast medium, can then be derived by Equation 1.7

$$r_1 = \frac{(R_{1obs} - R_{1tissue})}{[Fe]} \quad \text{or} \quad r_2 = \frac{(R_{2obs} - R_{2tissue})}{[Fe]}$$

Equation 1.7

Contrast agents that possess higher r_1 values and, as a result, lower r_2/r_1 ratios, are typically composed of individually-dispersed nanoparticles in suspension and generate positive (bright) contrast in the MRI image under T_1 weighting conditions due to enhancement of the MRI signal due to reduction of T_1 proton relaxation times. Agents exhibiting higher r_2 values, and therefore higher r_2/r_1 ratios will generate a negative (dark) contrast in the MRI image under T_2 weighting conditions due to signal suppression as a result of shortened T_2 relaxation processes, and are typically composed of larger clustered materials as illustrated in Figure 1.4 below:

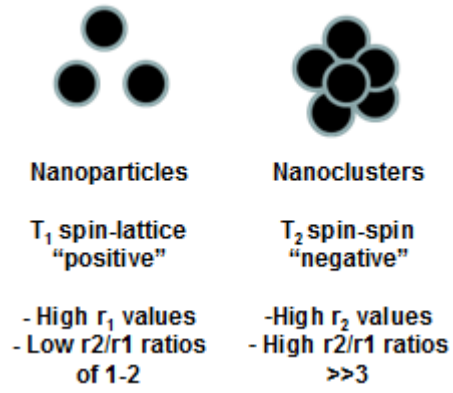

Figure 1.4: Properties of T_1- and T_2-weighted contrast agents and their characteristic properties

Iron oxide nanoparticle (IONP) dispersions in particular have exhibited excellent potential for use in MRI contrast agent development, as they are metabolised by the body and are easily excreted following treatment, thus avoiding the problem of toxicity. Current IONP formulations in use include Endorem® (T_2 agent, AMAG-Pharma), Lumirem®(T_2^* agent, AMAG), Resovist®(predominantly T_2 agent, Bayer) and most recently VSOP-C184 (T_1 agent, Ferrofarm GmbH) . Such formulations provide promising potential for the replacement of their Gadolinium-

based alternatives, which have been shown to present occasional toxicity problems, specifically nephrogenic systemic fibrosis (NSF) of skin, joints, eyes, and internal organs in cancer patients with liver disease.

1.3 Synthesis of iron-oxide nanoparticles

The synthesis of superparamagnetic iron-oxide nanoparticles has become of increasing interest as their potential in many industrial, medical and biosensing applications continues to increase. For this reason, it is vital that the resulting physical, chemical, optical and magnetic properties of the nanoparticles be strongly considered in their preparation, as these properties determine the efficacy and application of the IONP. It follows that good size control is therefore crucial, as it provides the opportunity to engineer the resulting properties of the nanoparticles produced. Many methods are available for the preparation of iron-oxide nanoparticles including alkaline coprecipitation [43], microemulsion [44], pyrolysis [45] and high-temperature thermal decomposition in organic media [46]. For the purpose of this thesis, the coprecipitation and high temperature thermal decomposition methods will be further discussed.

1.3.1 Alkaline coprecipitation of iron salts in aqueous medium

The use of aqueous coprecipitation of iron salts has been widely employed and extensively reported in the literature as a simple and effective route in the preparation of relatively small, water dispersible iron-oxide nanoparticles. The procedure involves a stoichiometric mix of ferric and ferrous iron salts in aqueous medium as demonstrated by the following equation:

$$Fe^{2+} + 2Fe^{3+} + 8OH^- \rightarrow Fe_3O_4 + 4H_2O$$

Equation 1.8

Complete nanoparticle precipitation occurs within the range of pH 8 to 14 and is facilitated by the addition of ammonia into the reaction mixture. A ratio of 2:1 of iron salts (Fe^{3+}: Fe^{2+}) is required to avoid the formation of oxide mixtures (i.e. both maghemite and magnetite nanoparticles in the same suspension). In addition to this, control over the Fe^{3+}: Fe^{2+} ratio has shown to have a significant effect on the

crystallisation and the magnetic properties of the nanoparticles produced [47]. Typically, magnetite, or Fe_3O_4, nanoparticles are produced via this process, but oxidative processes that may occur can often result in the formation of maghemite, or γ-Fe_2O_3 via Equation 1.9 [48].

$$2Fe_3O_4 + \tfrac{1}{2}O_2 + 2H^+ \rightarrow 3\gamma\text{-}Fe_2O_3 + H_2O$$

Equation 1.9

Nanoparticles prepared by this method are also very susceptible to agglomeration, to reduce their surface energy. For this reason, the use of stabilisers or surfactants is vital to create steric repulsion between individual nanoparticles, thus inhibiting cluster formation. A vast range of surfactants and stabilisers have been reported in the literature and include fatty acids (oleic, acid, lauric acid, dodecanoic acid) [49], carboxylates (citric acid) [50] , phosphates [51], polymeric stabilisers(e.g. Polyethylene Glycol, PEG) [28] and phospholipids [52].

The coprecipitation method offers a straightforward and convenient method of producing iron oxide nanoparticles of a relatively small size in the presence of a stabilising surfactant or ligand. Despite average nanoparticle size being fairly reproducible between syntheses, control over nanoparticle size is very limited with resulting particle distributions being quite broad. For this reason, thermal decomposition methods in organic media have gained increasing interest as an option for nanoparticle production. These nanoparticles can then be transferred to aqueous media in order to generate water-dispersible nanoparticles for biomedical application. Nanoparticles of this type and their potential applications will be discussed in Chapters 3 and 4.

1.3.2 Thermal decomposition of iron precursors in organic media

The thermal decomposition process of IONP synthesis, although not fully understood, is proposed to proceed via a two-stage mechanism involving an initial nucleation stage and a subsequent growth period. Separation of these stages is vital for obtaining size monodispersity and a narrow size distribution, and can be achieved using two strategies; heterogenous nucleation and homogenous nucleation [53].

The most commonly used form of heterogenous nucleation in the literature is the seed-mediated process, whereby preformed nanocrystals are used as seed nuclei for the further growth of larger nanoparticles in the presence of a low concentration of additional monomers. This ensures that the nucleation stage is physically separated from the subsequent growth stage that follows. It is vital that the concentration of the monomers introduced is kept low in order to prevent further heterogenous nucleation processes. The growth phase of heterogenous nucleation is marked by the deposition of metal atoms on the surface of the preformed seed nanocrystals, resulting in the growth and formation of larger nanoparticles. Monodisperse single-nanoparticle and core-shell structures have been reported to be produced by seed-mediated processes [54], providing that the seed particles are uniform in size.

Homogenous nucleation can be achieved by one of two primary methods, the ‘hot-injection’ technique (introduction of precursor into a hot solvent) or by ‘heating up’ processes. The latter technique was employed in the synthesis of iron oxide nanoparticles for the purpose of this thesis. Hot injection techniques are those in which a state of high supersaturation is induced by the rapid injection of highly reactive reactants into a hot surfactant solution, resulting in a rapid homogenous nucleation, followed by a slower diffusion-controlled process of 'focussing' of a monodisperse nanoparticle size distribution . The common objective of this method is to generate a condition of ‘burst nucleation’, whereby the concentration of the precursor in the medium rapidly decreases, thus slowing down the rate of nucleation. This stage, in combination with the slower, more controlled growth phase, is critical in the formation of monodisperse nanoparticles in suspension.

In the "heating up" approach the combination of the solvent, precursor and any additional surfactants or stabilizing ligands occurs at room temperature before heating up to the reflux temperature of the carrier solvent used. The precursor decomposes during the heating stage, and thus generates ions in solution. After the concentration of these ions reaches super-saturation, a short period of ‘burst nucleation’ occurs in which the concentration of the precursor rapidly decreases and subsequently inhibits the formation of further secondary nucleations. Otswald ripening is then believed to occur following this in a slower, more controlled

growth stage which is responsible for the formation of a monodisperse suspension of nanoparticles of uniform size.

There have been very limited studies reported in the literature on the proposed mechanism of nanoparticle formation by heating up processes, mainly due to the lack of characterisation methods that could facilitate following both the nucleation and growth processes in real time. The one main difference of this method to the hot injection variety is that there is no process that induces instantaneous supersaturation for formation of monodisperse nanoparticle dispersions. However, the underlying mechanism for size control via this method is not yet fully understood, and cannot be simply explained using the proposed mechanism presented for hot injection processes.

In one particular study by Kwon et. al. [54], a series of aliquots of the reaction solution were extracted during a thermal decomposition synthesis of iron oxide nanoparticles in an attempt to identify the actual mechanism of particle formation and to separate the synthesis into its nucleation and growth phases. The conclusion of the above study was that the mechanism underlying the formation of the nanocrystals in the heating-up process was very similar to that of the “hot injection” method, in that there was a sudden increase in the concentration of the nanocrystals, rapid narrowing of the size distribution and a high growth rate. On analysis of aged nanoparticle dispersions following synthesis, it was observed that termination of growth occurred approximately 2-3 min after the reflux temperature of the reaction was reached. Noticeable changes in the particle morphology was evident from TEM analyses in this instance, with the particles adopting a smoother, more 'rounded' shape when maintained at these high temperatures for a number of minutes following synthesis. At aging times in excess of 20 minutes, however, the once-spherical particles began to transform into cubed-shaped structures with a broader size distribution.

The main advantages of nanoparticle preparation by both 'hot injection' and 'heating up' processes is their remarkable ease and simplicity in producing particles of a small crystallite size with a high degree of monodispersity, in addition to providing the potential to engineer the size, and thus the characteristic physical, chemical and magnetic properties of the nanoparticles produced. Despite these

advantages, a number of drawbacks can be associated with conventional decomposition syntheses such as the use of large quantities of surfactants e.g. oleylamine, oleic acid used in the Sun et. al synthesis [46], which firstly, is of environmental concern, and, furthermore, involves coating of the IONP by large quantities of strongly bound surfactants. This seriously limits biomedical applications of the synthesised IONP. These drawbacks can be overcome by syntheses of the type reported by Pinna et. al [55], where the solvent, benzyl alcohol, simultaneously acts as both the reaction medium and the ligand during nanoparticle formation, instead of using a more complex mixtures of solvents and ligands. Critically the benzyl alcohol moieties are weakly bound and so are easily replaced. In addition to this, benzyl alcohol is known to be an environmentally friendly solvent and is commonly used in the food industry.

Thermal decomposition syntheses as reported by Pinna et. al and Sun et. al were utilised for IONP syntheses as described in Chapters 3 and 5 respectively, with the use of those prepared by Pinna et. al. also described in Chapter 4 in the formation of IONP/polymer nanocomposites.

1.4 Surface functionalisation and control of nanoparticle/nanocomposite properties

Successful preparation of stable, well-dispersed iron oxide nanoparticle suspensions requires that the nanoparticles are coated with appropriate surfactants that allow the dispersion of the nanoparticles in the chosen medium. For example, for dispersion of nanoparticles in non-aqueous ferrofluids, long chain surfactants such as oleic acid can be used to stabilise IONP in organic media via chemisorption of the carboxylic acid head group to the nanoparticle surface, leaving the hydrophobic tail exposed to the solvent. Steric interactions then provide effective dispersion in organic media [56]. For successful dispersion in aqueous media, a wide variety of short/long chain surfactants [44], lipid bilayers [49] and copolymer moieties [57] have been reported in the literature to have been successfully attached to the surface of iron oxide nanoparticles.

Apart from providing stability of nanoparticles in their dispersing solvent, surfactants are also the key element in the functionalisation of the nanoparticles

formed as they allow for specific engineering of surface charge of the nanoparticles toward a particular biomedical application. This can be useful, for example, in the design of therapeutics for specific targeted drug delivery, particularly if the site of interest possesses a specific surface charge, thus increasing the efficacy of the delivery vehicle used.

1.5 Zeta Potential of particles and the Electrical Double Layer

Colloidal particles dispersed in aqueous suspension are generally electrically charged, arising from their own natural surface charge or any surface coatings that may be attached to them. Each individual particle dispersed in solution is surrounded by a ‘fixed layer’, or ‘Stern Layer’ as it is otherwise known, that consists of oppositely charged ions strongly bound to the surface. Surrounding this layer exists a more fluid-like layer, known as the diffuse double layer, where a collection of ions of opposite polarities exist. Combined, these two layers comprise what is known as the ‘Electrical Double Layer’. In addition to this, the bulk liquid surrounding the particle also possesses its own characteristic electrical charge. When a voltage is applied to dispersion, particles are attracted to the electrode of the opposite polarity, along with the fixed layer and part of the diffuse double layer, or internal side of the "sliding surface". The difference in electrical charge between the dense layer of ions surrounding the particle and the bulk of the suspended fluid is known as the Zeta Potential.

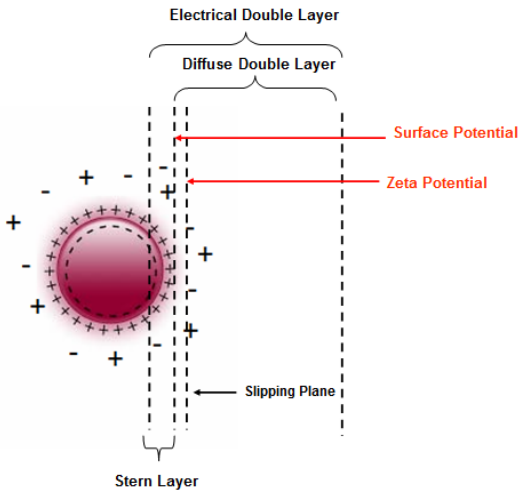

Figure 1.5: Schematic of the Electrical Double Layer of a particle [58]

The magnitude of the Zeta Potential gives an indication of the stability of the particles in the medium in which it is dispersed. For example, if the majority (or indeed all) of the particles in suspension possess a very positive or indeed very negative surface charge, then the probability of aggregation will decrease as the particles will repel each other. It follows that if a low overall charge is present, there will be no electrostatic repulsion forces to keep particles apart, allowing aggregation to occur in the absence of other repulsive interparticle interactions. Typically, a Zeta Potential in excess of 30 mV (positive or negative) indicates a stable dispersion.

Four main effects, or electrokinetic effects as they are otherwise known, may occur during this application of an external electrical field; **Electroosmosis**, **Electrophoresis**, **Streaming Potential** (generated when a liquid is forced to flow past a stationary charged surface) and **Sedimentation Potential** (field generated due to sedimentation of particles from suspension).

Electroosmosis involves the movement of a liquid through a capillary, membrane or porous material due to the application of an external electrical field. On application of this field, an electrical double layer of mobile ions form at the interface of the static surface and the liquid. The net charge in this layer is induced to move by the resulting Coulomb force and the resulting flow is termed electroosmotic flow.

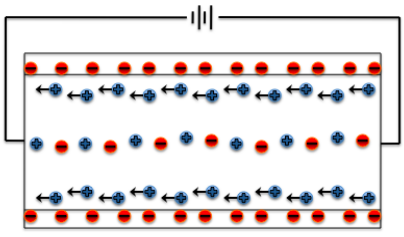

Figure 1.6: Schematic representation of electroosmotic flow.

Electrophoresis (Electrophoretic mobility) can be defined as the movement of charged particles relative to the medium in which they are suspended while under the influence of a magnetic field. When a field is applied, charged particles move towards the electrode of opposite charge. Forces due to the viscosity of the solvent oppose such motion, and the particles move with a constant velocity once

equilibrium is reached. A particles velocity is dependent on a number of factors; the Zeta potential, the applied field, the dielectric constant of the particle and the viscosity of the solvent.

Zeta Potential is related to electrophoretic mobility via the Henry Equation:

$$U_E = \frac{2\varepsilon z F(ka)}{3\eta} \qquad \text{Equation 1.10}$$

where U_E is the electrophoretic mobility, z is the Zeta Potential, ε is the dielectric constant (ratio of the permittivity of a substance to the permittivity of free space), η is the viscosity and F (ka) is Henry's function. Henry's function can be further explained by its individual parameters where **k** is the Debye length (used to describe the 'thickness' of the electrical double layer and **a** represents the radius of the particle. Combined, the term can be said to represent the ratio of particle radius to the thickness of the double layer.

Measurement of the electrophoretic mobility of a particle was initially achieved by visual methods, but is now addressed using the Laser Doppler Effect. This is the M3-PALS technique in the Malvern Zeta Sizer software. In the experiment, a laser beam is passed through the sample in the cell in the presence of an electrical field at an angle of 17º relative to the incident beam. The scattered light from the moving particles is shifted in frequency, ΔF, given by the following equation:

$$\Delta F = \frac{2\nu(Sin\theta/2)}{\lambda} \qquad \text{Equation 1.11}$$

where ν is the particle's velocity, λ is the laser wavelength and θ is the scattering angle.

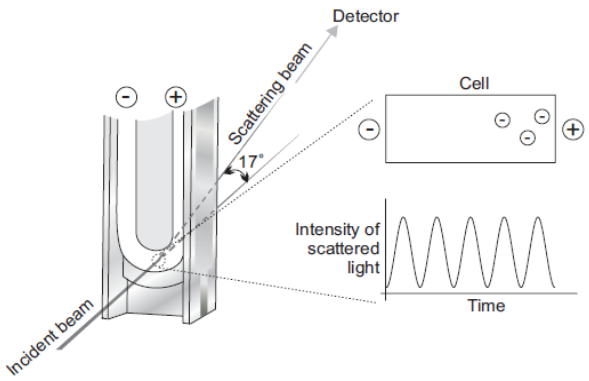

Figure 1.7: Process of light scattering in the Zeta cell, outlining the angles of the incidence and scattering beam, in addition to the behaviour of the ions and intensity of the scattered light on application of an electrical charge [58].

The scattered light is combined with a reference beam and a digital signal processor produces a fluctuating signal or phase plot, which is essentially a representation of the difference in phase between the measured beat frequency and the reference frequency as a function of time. The rate of fluctuation is proportional to the velocity of the particles, with particles of a higher level of mobility resulting in more frequent fluctuations than their slower counterparts. These fluctuations are what are responsible for the initial artefact in the resulting phase plot of the plot as outlined in Figure 1.8, whereas the latter part is determined by the surface charge of the particle and the magnitude by which the measured beat frequency differs from the reference frequency of 320 Hz.

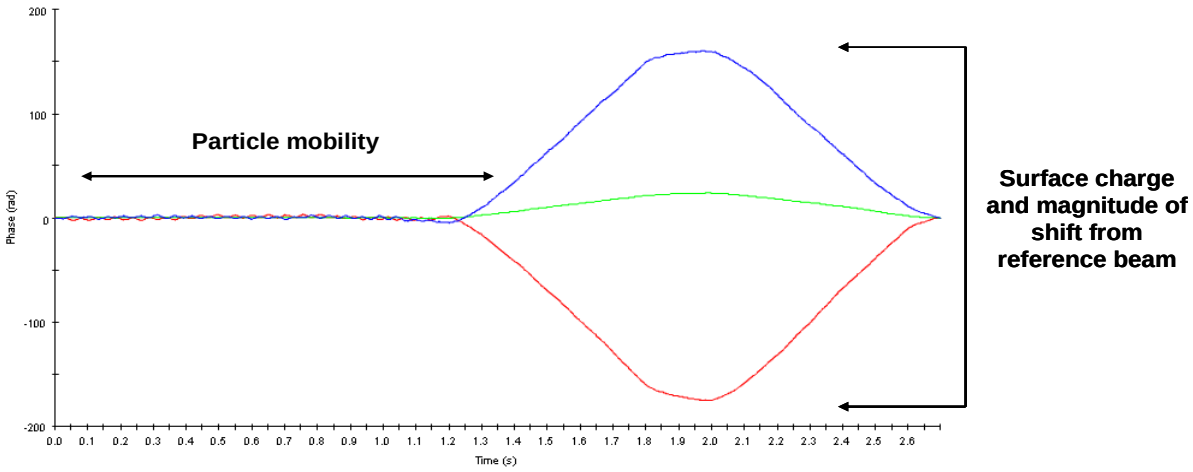

Figure 1.8: Sample phase plot for a particle with a negative (-), neutral (-) and positive (-) zeta potential

1.6 Principles of NMR

Nuclear spin and the effect of an applied magnetic field

Hydrogen nuclei (protons) possess magnetic properties known as nuclear spins that have magnetic characteristics. The concept of spin was first postulated by Pauli in the 1920's, with the aid of Ralph Kronig, George Uhlenbeck and Samuel Goudsmit whom, following Pauli's mathematical predictions, provided further information into its interpretation as the activity of a particle spinning on its own axis. Spin is a property that can be defined as a form of angular momentum that is a fundamental characteristic of primary particles. This angular momentum, the spin angular momentum, is quantised and can be represented by the following equation

$$S = h\sqrt{S(S+1)}$$

Equation 1.12

where h represents Planck's constant and S is the Spin angular momentum (a non-negative integer or half integer). It follows from this equation, that the nuclear angular momentum can be derived (Equation 1.13)

$$P = \hbar\sqrt{I(I+1)}$$

Equation 1.13

where I is defined as the nuclear spin quantum number and is expressed as 0 or ½ numerical values. Associated with this angular momentum is a particles' magnetic moment, μ, which can also be related to the gyromagnetic ratio by the following equation:

$$\mu = \gamma I$$

Equation 1.14

where γ is the proportionality constant otherwise known as the gyromagnetic ratio and is unique for a given nucleus and determines the sensitivity of that nucleus in NMR ,with higher γ values resulting in a greater sensitivity). It follows that, for nuclei of zero spin *I*, there is no associated magnetic moment (Equation 1.14),

whereas ^{1}H nuclei of I =½ will possess a magnetic moment according to the same equation.

Quantum mechanics describes that a nucleus of spin I will have $2I + 1$ possible orientations in the presence of a magnetic field. For nuclei (e.g. ^{1}H, ^{13}C) that possess a spin of +1/2, two possible orientations (2(1/2) +1)) will exist. This is known as the Zeeman Effect and can be represented (in this instance for nuclei of spin ½) with the following diagram:

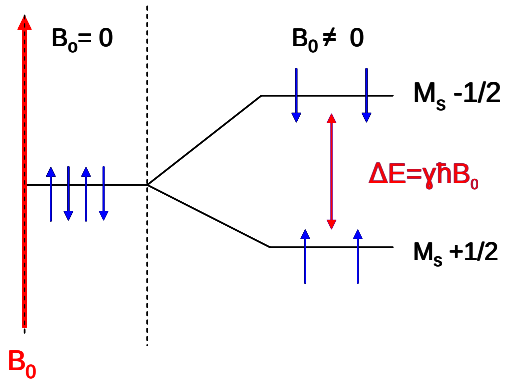

Figure 1.9: Schematic representation of Zeeman equilibrium distribution of nuclear spins with I = ½ in the presence of a magnetic field, B_0.

In the absence of a strong applied magnetic field, all spins are randomly distributed, resulting in zero net magnetisation in the sample. When a magnetic field B_0 is applied, however, spins adopt an alignment with (parallel) or against (anti-parallel) the applied field i.e. spins can exist in one of two states; the α-state or the β-state. The α-state is lower in energy and tends to possess a higher population of spins. The ratio of nuclear spin population in the α-state to the β-state is represented by the Boltzmann equation (Equation 1.15).

$$\frac{N_\alpha}{N_\beta} = e^{\frac{\Delta E}{k_B T}} \qquad \text{Equation 1.15}$$

where ΔE is the difference in energy of the two states and T is the absolute temperature (Kelvin). The energy difference is proportional to the strength of the field applied and can be defined by:

$$\Delta E = h\nu = \frac{\mu B_0}{I}$$ Equation 1.16

This energy difference is low in energy due to a small population bias towards the lower energy α-state, and results in a small net magnetisation (M_0), that aligns with the applied field, B_0. The bulk sample magnetisation, M_0 can be visually represented with the use of the vector model diagram for angular momentum. A typical diagram is constructed as shown:

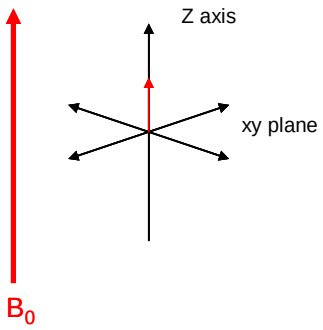

Figure 1.10: Vector model diagram for an assemble of ^{1}H nuclei in the presence of a magnetic field applied along the z-axis.

When a 90º pulse is applied, M_0 will be rotated into the xy plane and will precess there for a period of time. The frequency at which the magnetisation precesses is called the Larmor frequency, ν_L, and is represented by:

$$\nu_L = \frac{\gamma B_0}{2\pi}$$ Equation 1.17

There are two processes that exist by which M_0 can evolve as it returns to a state of thermal equilibrium following perturbation via an RF pulse. The first process, T_1, or the spin-lattice relaxation time is associated with the recovery of longitudinal magnetisation towards equilibrium and the second is the spin-spin relaxation time, which represents the dephasing of the transverse component magnetisation, in the xy plane.

Spin-Lattice Relaxation time (T_1)

A typical T_1 measurement is initiated by perturbing the magnetisation of a system out of equilibrium using a 180º pulse so that the magnetisation orientates itself in the opposite direction on the z-axis. The magnetisation is then allowed to precess for a time τ, after which the bulk magnetisation vector returns to complete thermal equilibrium. This process is exponential in duration and can be defined by:

$$\frac{dM_z}{dt} = M_0(1 - e^{\frac{-t}{T_1}})$$ Equation 1.18

The longitudinal relaxation (T_1) process may be diagrammatically illustrated as follows:

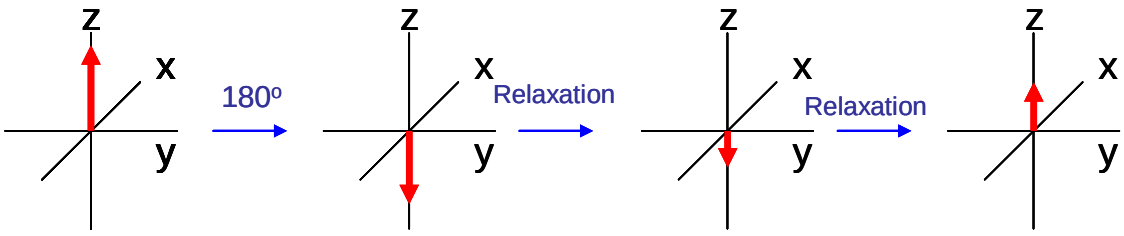

Figure 1.11:Vector model diagram illustrating the longitudinal relaxation (T_1) of the bulk sample magnetisation, M_0, following application of a 180° RF pulse.

The subsequent application a 90º pulse generates measurable (transverse) magnetisation. This experiment is known as inversion recovery, it can be used to measure T_1 by systematic variation of the inter-pulse separation. Full recovery of M_0 back to equilibrium is only achieved when a time of 5 times T_1 is allowed. Similarly, in all NMR (and MRI) a recycle delay, of 5 times T_1 between each measurement is usually applied. Alternatively, by reducing the recycle delay, the experiment can be T_1-weighted, i.e. any spins with faster relaxation will contribute more to the measured signal (or they recover faster).

Spin-spin relaxation time (T_2)

If instead we use a 90º pulse to perturb the system, M_0 will be rotated into the xy plane and all spins precess in-phase with each other. As time progresses, the individual nuclei undergo spontaneous relaxation by exchanging RF energy with the spin system, resulting in an increase in thermal energy (entropy). A loss in the organisation of the spins is observed as they begin to 'fan out', losing phase coherence as they do so. This leads to the eventual loss of magnetisation in the xy plane. T_2 relaxation processes are represented by the equation below:

$$\frac{dM_{xy}}{dt} = M_0(e^{\frac{-t}{T_2}}) \qquad \text{Equation 1.19}$$

The typical dephasing of the transverse magnetisation, prior to recovery, is shown in the following series of vector diagrams:

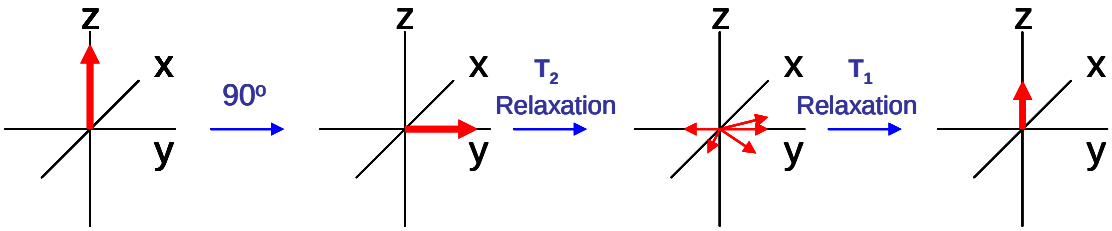

Figure 1.12: Vector diagram series for a typical spin-spin T_2 relaxation process of the bulk magnetisation, M_0 where $T_2<T_1$

In addition to T_2 relaxation, inhomogeneity in the applied field also gives rise to a T_2^* process, which is defined as the characteristic time taken for the transverse magnetisation to decay to approximately 1/3 (37%) of its original magnetisation. T_2^* process arise due to field inhomogeneities causing variations in the magnetic field experienced by individual nuclei which, in turn, cause them to move at different frequencies. This typically results in a more rapid decay of the bulk magnetisation than that observed in T_2 processes. The manner in which the transverse magnetisation actually decays is by a combination of both T_2 and T_2^* processes, and can be summarised by Equation 1.18 below:

$$\frac{1}{T_2^*} = \frac{1}{T_2} + \frac{1}{T_{2B_0 in\,\mathrm{homog}}} \qquad \text{Equation 1.20}$$

In an attempt to eliminate field inhomogeneity, a spin-echo pulse sequence (Hahn sequence) can be used to refocus the magnetisation back to equilibrium [59]. This process involves the application of a 90º pulse to initially dephase the magnetisation vector into the xy plane as a result of both T_2 and T_2^* processes, followed by a 180º pulse after a time τ to refocus or rephase the spins, due to field inhomogeneities (i.e. due to T_2^*) allowing them to gain phase coherence. The transverse magnetisation is thus recovered, and an echo is produced at a time 2τ. As true T_2 processes occur spontaneously in nature, dephasing of nuclear spins in this case cannot be reversed, and phase differences between the first and second fractions of the echo exist. This results in attenuation of the echo intensity according to T_2, with a noticeable decay in the intensity of subsequent echoes evident at a rate of $1/T_2$.

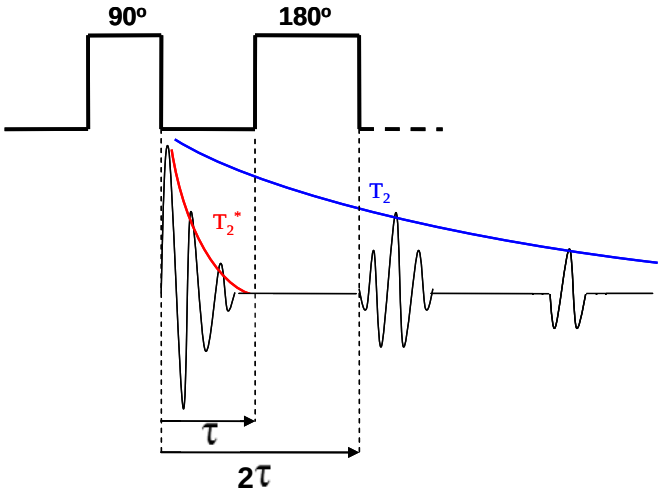

Figure 1.13: Spin echo pulse sequence and the attenuation of echo intensity after a single 180° pulse

Meiboom and Gill [60] developed a modification of Carr and Purcell's multi-echo pulse sequence, more commonly referred to as the Carr-Purcell-Meiboom-Gill (CPMG) model, to compensate for diffusion effects and thus improve T_2 determination. The CPMG sequence involves the application of multiple coherent 180º pulses and can be demonstrated by the following sequence diagram:

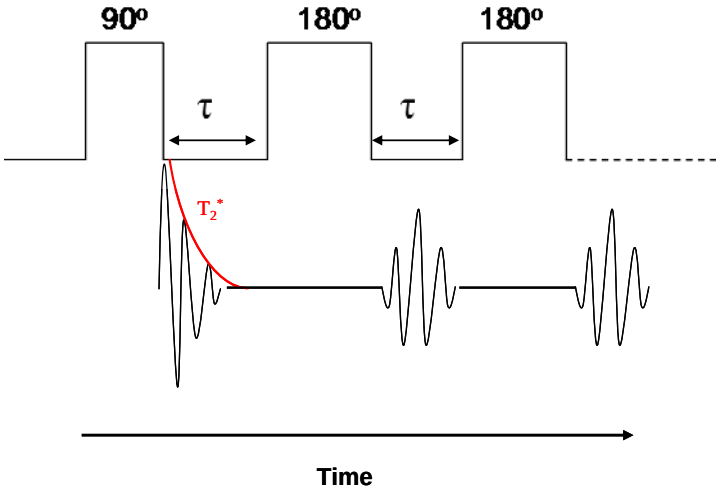

Figure 1.14: CPMG pulse sequence with application of multiple 180° pulses

In the model shown above, it can be seen that successive echoes are formed halfway between any two consecutive 180º pulses, with the amplitude of subsequent echoes decreasing with characteristic time T_2 [61]. The application of multiple 180° pulses ensures that any errors that arise due to deviations of the exact angle of the applied pulse are rectified, thus improving measurement reproducibility. The CPMG pulse sequence was used throughout this thesis for measurement of T_2.

1.7 Fast-Field Cycling NMR (FFC-NMR)

Fast-field cycling NMR (FFC-NMR) is a technique used to obtain the frequency (or magnetic field) dependence of longitudinal relaxation times, T_1, or alternatively relaxation rates R_1 ($1/T_1$) for a given colloidal suspension over a particular magnetic field strength range (typically 10kHz to 10MHz). Through this method, plots of R_1 as a function of frequency are generated. These plots are more commonly referred to as nuclear magnetic dispersion profiles, or NMRD profiles, and are useful in the investigation of the molecular dynamics within a colloidal system and the properties of particles contained within it.

The technique involves the polarisation of the sample magnetisation in a magnetic field with a high flux density. Relaxation of the magnetisation is permitted to take place by switching to the relaxation field for a time τ and, following this, to an acquisition field (9.25 MHz) where the signal is acquired. This process is repeated a number of times for a range of τ values, to measure T_1, and then for a range of

B_{rlx} values forming an NMRD profile. Longitudinal relaxation processes require a time-dependent magnetic field that fluctuates at a particular frequency, known as the Larmor frequency. The fluctuations that initiate the transitions driving relaxation arise due to modulation of the proton-proton (or proton-electron) dipolar interactions driven by dynamic processes over a time scale ω. NMRD profiles provide information in relation to the molecular motions of a system in the form of the spectral density function, J(ω). For a system where relaxation is driven by a single motion, the spin-lattice relaxation rate, R_1, is given by:

$$R_1 = \frac{9}{8}\left(\frac{\mu_0}{4\pi}\right)^2 \gamma^4 \left(\frac{h}{2\pi}\right)^2 \frac{1}{r^6}\left[\frac{4}{15}J(\omega)+\frac{16}{15}J(2\omega)\right] \qquad \text{Equation 1.21}$$

where μ_0 is the vacuum permeability, h is Planck's constant, r is the distance between neighbouring ^{1}H nuclei and J(ω) and J(2ω) are the spectral density functions evaluated at the Larmor frequency and twice the Larmor frequency respectively. These functions represent the only allowed frequencies for induced single- and double-spin flip transitions between the energy levels of the spin system. The efficiency of the local fluctuating fields to induce transitions is given by the spectral density function, which is defined by Equation 1.22.

$$J(\omega) = \int_{-\infty}^{\infty} G(\tau)\, e^{-i\omega\tau}\, dt \qquad \text{Equation 1.22}$$

Fluctuations of these local magnetic fields originating from random rotational, vibrational and diffusional motions of the particles present give rise to exponential functions of the form:

$$G(\tau) = G(0)e^{\frac{-\tau}{\tau_c}} \qquad \text{Equation 1.23}$$

where τ_c is the correlation time which characterises the dynamic processes in suspension and is a decay constant of G (τ). Longer τ_c times indicate the presence of larger particles whereas shorter times represent those smaller in size. Fourier transforms of exponential functions give rise to Lorentzian spectral density functions where:

$$G(\tau) \xrightarrow{FT} C(0)\frac{\tau_c}{1+(\omega\tau_c)^2} = J(\omega)$$ Equation 1.24

The rate of the random vibrational, rotational and diffusional motions mentioned above, represented by τ_c^{-1}, can be derived from the half-width of the Lorentzian spectral function. Cosine Fourier transforms of the correlation function (spectral density function) are directly connected with relaxation (Equation 1.21). Thus the NMRD profile allows mapping of the spectral density.

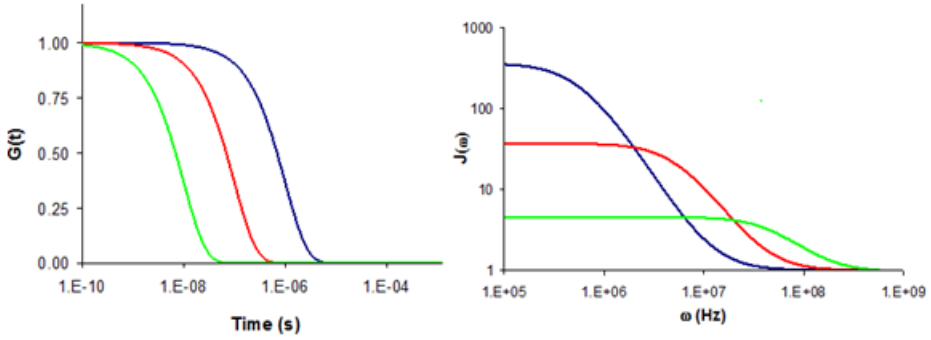

Figure 1.15: Correlation functions G(t) for three different values of τ_c of 10 ns (-), 100 ns (-) and 1000 ns (-) and their corresponding simulated spectral density functions J(ω)

The spin-lattice relaxation time, T_1 (and also the spin-spin relaxation time, T_2) can also be expressed as a function of the correlation time at a particular Larmor frequency with the relationship outlined in Figure 1.16 below. Interaction with the small random fluctuating magnetic fields leads to spin-lattice relaxation with the most efficient relaxation effected by motions with $\tau_c = 1/(2\pi\nu_o)$. Equally, these same random local magnetic fields are also necessary for spin-spin relaxation, with the difference being that the relaxation becomes more efficient as τ_c becomes longer, i.e. as the motions become slower and the local magnetic fields become more static. It follows that, as τ_c becomes larger, i.e., the molecular motion becomes slower, the value of T_2 becomes smaller than T_1. The literature outlines the typical correlation times for molecular motion, either rotational or translational, is 10^{-12} to 10^{-11} s for small molecules (e.g. water), 10^{-9} to 10^{-6} s for macromolecules of increasing size (or small molecules bound to macromolecules), and 10^{-6} to 10^{-3} s for some motions in membranes.

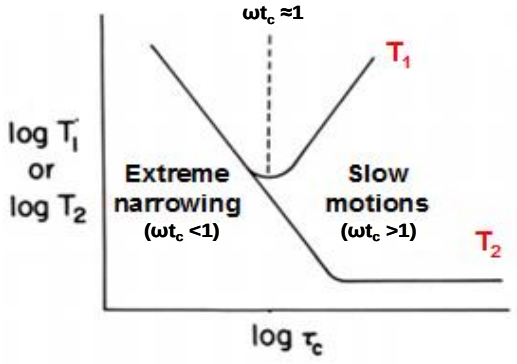

Figure 1.16: A typical plot of log T_1 and log T_2 as a function of log τ_c mapping out the extreme narrowing and slow motion limit phases.

It is evident from the plots presented in Figure 1.16 above, that three distinct ranges for $\omega\tau_c$ exist. These can be categorised as follows:

(i) Extreme narrowing phase ($\omega\tau_c < 1$): In this range, the rate of fluctuations is much higher than the resonance frequency and is generally observed for small molecules in non-viscous solvents. The fast motions of the molecules averages out the interactions between them and $T_1 = T_2 \approx \sim 1/5K\tau_c$, where K is a constant equal to $3\mu_0^2\hbar^2\gamma^4/160\pi^2r^6$, and the relaxation times are independent of frequency [62].

(ii) Point of T_1 minimum ($\omega\tau_c \approx 1$): This is where the relaxation is observed to be most efficient and is typical of medium sized molecules or viscous solvents.

(iii) Slow-motion limit phase ($\omega\tau_c > 1$): The rate of fluctuations in this region is slow, and is generally characteristic of slowly tumbling molecules or macromolecules in viscous media. There is no strong spectral density contribution to the relaxation near the Larmor frequency, corresponding to the high frequency limit in Figure 1.16. Thus, the value for T_1 is high.

In conventional NMR, T_1 is measured as a function of τ_c, e.g. by changing the temperature. Analysis of such data (Figure 1.16) requires a model for the dynamics. The most prominent advantage of field cycling methods over conventional NMR analyses is in the ability to study the dynamics of a system over a wide field frequency range, while keeping the temperature of the measurement

constant. This provides the scaled spectral densities, removing the need for a dynamic model. In addition to this, if a Lorentzian spectral density function is not inappropriate, e.g. for non-random motions, this will instantly be obvious from the shape of the profile. The use of NMRD in studying the dynamics of magnetic moments, e.g. of IONP in suspension, is a good example of these advantages, as will be discussed below.

1.8 Magnetism and classes of magnetic materials

All materials, regardless of whether they are magnetic or non-magnetic in nature, can be classified based on their response to the application of an external magnetic field. Five main types of behaviour exist and are as follows; diamagnetism, paramagnetism, ferromagnetism, antiferromagnetism and ferrimagnetism.

The extent to which a given material becomes magnetized when in the presence of such a field is known as the magnetic susceptibility, as expressed by the following equation:

$$\chi = \frac{M}{H} \qquad \text{Equation 1.25}$$

where M represents the magnetisation and H is the applied magnetic field. As both M and H are measured in amperes per meter, χ is a dimensionless quantity.

When a material is placed under the influence of a magnetic field, electromagnetic interactions take place which concentrate or disperse the lines of the magnetic field, resulting from the actions of orbital and delocalized electrons within the species. These interactions are then responsible for the induction of an internal magnetisation that either opposes or amplifies the applied magnetic field. When the direction of this field is opposite to that of the internal magnetisation of the material, it is said to be diamagnetic in nature [63]. In the opposite scenario, the material is categorized as paramagnetic [64].

Diamagnetic materials typically include organic molecules and some metals e.g. gold, copper, lead, water and biological tissue. They possess no net magnetic

moment in the absence of a magnetic field. This can be attributed to the absence of unpaired electrons within the orbital shells of such materials. Upon application of an external magnetic field, the magnetic dipoles within these materials align in a manner so as to oppose the direction of the applied field. The result is a small and negative bulk magnetic susceptibility as shown in Figure 1.17 below:

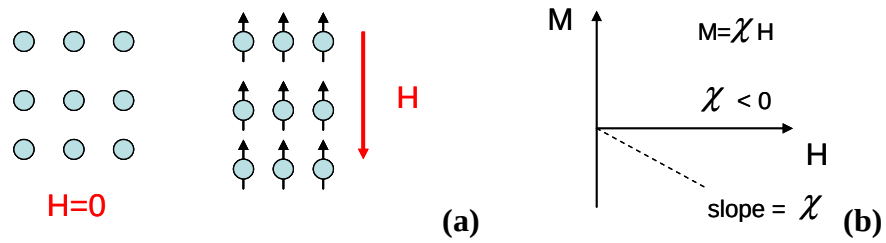

Figure 1.17: (a) Behaviour of dipole moments in the presence and absence of a magnetic field for a diamagnetic material and (b) direction and magnitude of magnetic susceptibility

Paramagnetic materials exhibit behaviours that contrast those of their diamagnetic counterparts in terms of their alignment on application of a magnetic field. They also possess no net magnetisation in the absence of an external field but for a different reason. Paramagnetic materials are composed of small magnetic dipoles that are randomly oriented, resulting from the presence of unpaired electrons. In the presence of an applied field, these dipoles line up in parallel with the field and produce a net magnetisation. Magnetic susceptibilities in this instance are small and positive as shown in Figure 1.18.

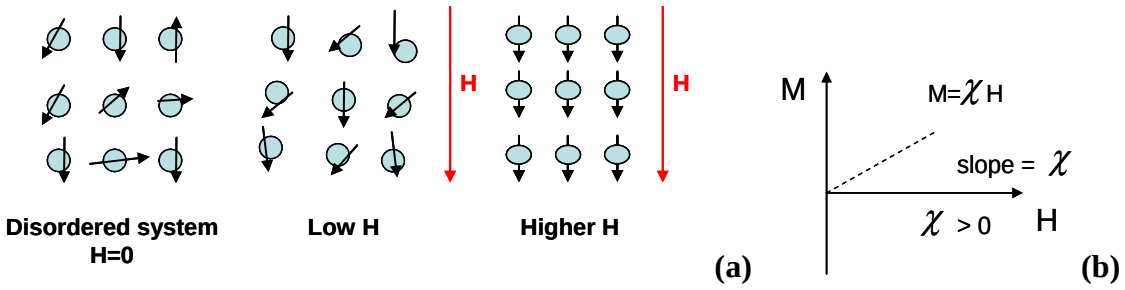

Figure 1.18: (a) Behaviour of a paramagnetic material with increasing external field and (b) characteristic direction and magnitude of magnetic susceptibility

On increasing the temperature of a paramagnetic material, however, the alignment of the moments in the applied magnetic field is compromised by thermal agitation of the atoms present, which causes them to lose alignment and results in an overall

decrease in the magnetisation of the material. This results in a temperature dependent susceptibility.

The inverse relationship between the magnetic susceptibility and temperature can be described by the Curie Law, that states that the magnetisation in a paramagnetic material is inversely proportional to its temperature and can be described by Equation 1.26.

$$\chi = \frac{C}{T} \quad \text{or} \quad M = C\left(\frac{H}{T}\right) \qquad \text{Equation 1.26}$$

where C represents the Curie constant, H the applied magnetic field and T is the temperature of the material. The Curie Law only holds true for conditions of high temperature or low magnetic field strength, as at low temperatures and high field strengths, saturation of magnetisation occurs and dipoles align with the field to a point where further increase in field strength has a minimal effect.

Ferromagnetic materials possess the property of acting as ‘permanent magnets’, in that they demonstrate bulk magnetisation in the presence and the absence of a magnetic field [63]. Ferromagnetic materials are composed of many small magnetic domains aligned in the same direction, usually due to quantum mechanical exchange coupling. This coupling results in either parallel or anti-parallel alignment of moments of the material under the influence of the field. Ferromagnetic materials possess multiple magnetic domains in which all spins in a given domain will align with one another and become locked in one single orientation, as shown by Figure 1.19:

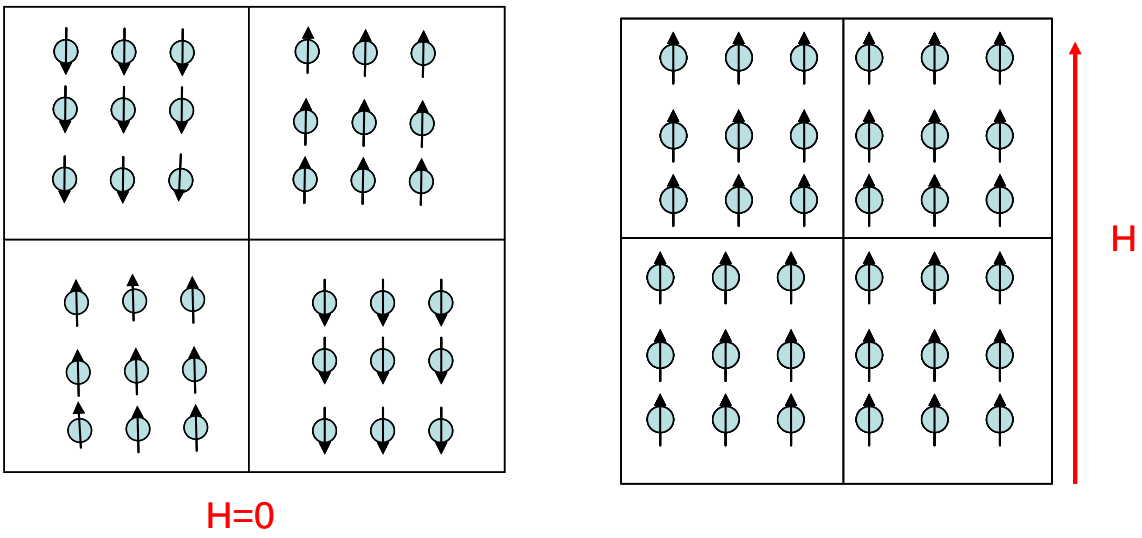

Figure 1.19: Behaviour of a ferromagnetic material in the absence and presence of a magnetic field

Two principal phenomena exist that are characteristic of ferromagnetic materials; spontaneous magnetisation and a magnetic ordering temperature. In the absence of a magnetic field, the net magnetisation present will depend on the spin magnetic moments of the electrons present. On removal of an applied magnetic field, ferromagnetic materials retain a small fraction of the applied magnetisation. This phenomenon is more commonly referred to as magnetic hysteresis. A plot of the change in magnetisation with respect to the applied field is known as a hysteresis loop and is representative of the magnetic parameters of a given ferromagnetic material. When an alternating magnetic field is used, the resulting hysteresis loop adopts the shape shown in Figure 1.20.

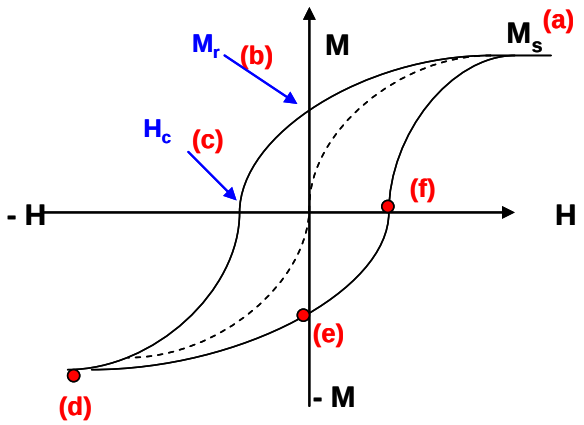

Figure 1.20: Typical shape of a hysteresis loop outlining the relationship between the magnetisation of the sample (M) and the strength of the external magnetic field (H).

The first stage of hysteresis loop formation involves driving the material using an applied magnetic field to a state of magnetic saturation, M_s (Figure 1.20(a)), where all moments are locked and aligned along the same axis so as to oppose or align with the field. On removal of this field, the magnetisation does not return directly to zero, as some moments remain aligned with the field and so must be driven back by an applied field in the opposite direction. The remnance (M_r) (Figure 1.20(b)), of a material originates from the small population of magnetic domains that remain aligned with the field for some time upon the gradual reduction of the field back to zero and is essentially the residual magnetisation that remains in the sample following removal of that field. On reversal of the direction of the applied field, a fraction of the magnetic domains will change their direction of orientation or 'flip', resulting in an overall net magnetisation of zero (Figure 1.20(c)),. This is what is known as the coercive field (H_c), or coercivity, and the force required to overcome the remnance is known as the coercive force. The magnetisation is once again driven to saturation in the negative direction (Figure 1.20(d)), before driving it again in the positive direction by reversing the direction of H (Figure 1.20(e)). A final increase in the magnetic field in the positive direction then brings the sample magnetisation to zero (Figure 1.20(f)). The curve then adopts a path from this point back to the saturation magnetisation in the positive direction, thus completing the loop.

Manipulation of the magnetisation of ferromagnetic systems can also be achieved through variations in temperature, where disorder can be generated within the material, creating a randomising effect on the exchange forces of the electrons present. The temperature at which this disorder is observed is known as the Curie temperature (T_c) and is an intrinsic property that provides an indication of the thermal energy required to perturb the ordering within the ferromagnet. Below, T_c the ferromagnet will appear ordered, whereas temperatures above T_c will result in disorder of the system where the material will exhibit normal paramagnetic behaviour once again.

Antiferromagnetism arises from the coupling of adjacent moments which align themselves in an opposite or antiparallel manner with each other (opposite situation to ferromagnetism hence the term anti-ferromagnetic) [64]. In contrast to ferromagnetic materials, these exhibit a net overall magnetisation of zero in the

absence of an applied field. This alignment may be disturbed by thermal energy, and disorder can be generated within the material above a particular temperature, known as the Néel temperature (T_N). Above this temperature, thermal agitation perturbs the alignment of the moments and the material exhibits paramagnetic behaviour.

Ferrimagnetic materials are quite similar in nature to those which are antiferromagnetic, in that individual moments align themselves in an anti-parallel manner with the applied magnetic field but differ in the fact that the magnitude of the opposing magnetic sub-lattices are unequal in magnitude. This results in a small net magnetisation when such a material is placed in a magnetic field. Ferrimagnetic behaviour is commonly observed in ferrite materials, which include the iron oxides magnetite (Fe_3O_4) and maghemite (γ-Fe_2O_3).

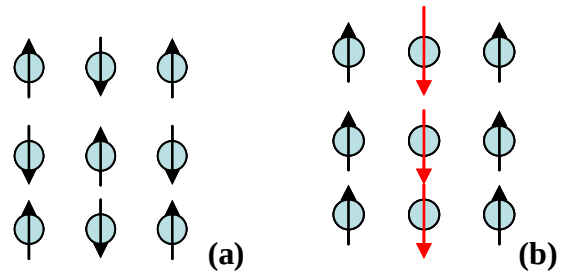

Figure 1.21: Illustration of dipole alignment in an (a) antiferromagnetic and (b) ferrimagnetic material

In the case of magnetite, an inverse-spinel structure exists within the crystal, which can be separated into two distinct ferromagnetic sublattices; tetrahedral sites, occupied by trivalent iron ions (Fe^{3+}), and octahedral site that contains both di- and trivalent iron ions (Fe^{2+} and Fe^{3+}) [65]. The structural formula for arrangements of this type can be written as $[Fe^{3+}]_A\,[Fe^{2+}, Fe^{3+}]_B\,O_4^{2-}$. In terms of the oxygen atoms present, Fe has 6 Oxygens as nearest neighbour at the octahedral site and 4 at the tetrahedral site. This arrangement is illustrated by Figure 1.22 below. Below the Curie temperature, the true magnetic sublattices are strongly exchange coupled, and oppose each other.

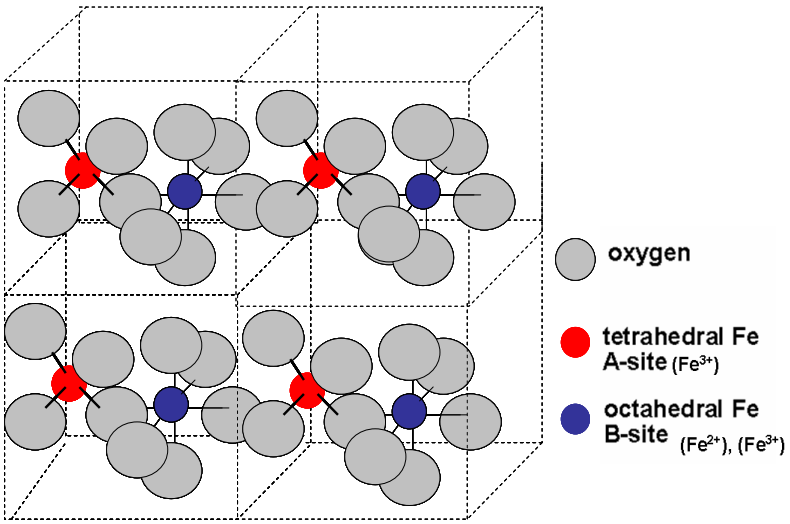

Figure 1.22: Crystal structure of Magnetite

In the case of maghemite, or γ-Fe_2O_3, a similar crystal structure is observed. However, both the tetrahedral and octahedral sites are occupied by Fe^{3+} ions only, in addition to cation vacancies in some octahedral sites [65]. Similar exchange coupling is observed to Fe_3O_4 but the total magnetisation is much smaller.

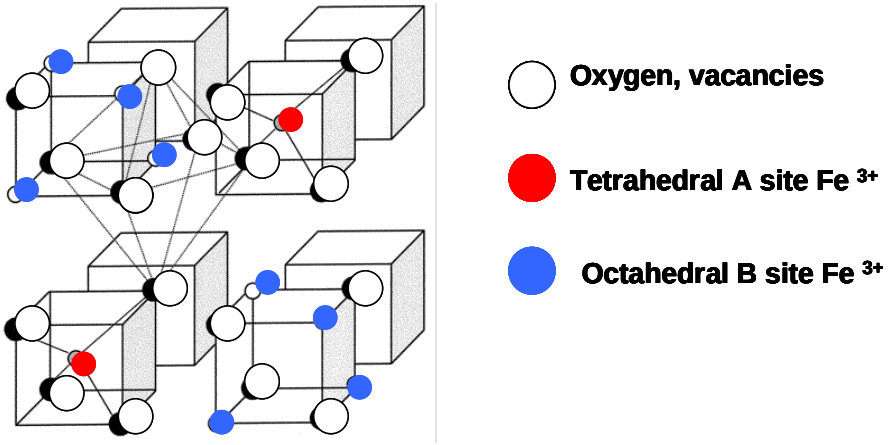

Figure 1.23: Crystal structure of Maghemite

One further type of magnetism can be observed for very small, single-domain crystalline particles, and it is known as 'superparamagnetism'. In this case the magnetisation of the individual domains (particles) exhibit magnetisation due to the exchange coupling of electrons (ferrimagnetic for Fe_3O_4 and or γ-Fe_2O_3). When the diameter of ferro- or ferrimagnetic particles are decreased below their characteristic critical diameter, the formation of these individual domains becomes unfavourable due to an increased relative domain wall energy, and particles adopt a

single-domain arrangement as a result. This critical diameter, D_c, can be defined by the following equation:

$$D_c \approx 18\frac{(AK_{eff})^{1/2}}{\mu_0 M_S^2} \qquad \text{Equation 1.27}$$

where A is the exchange constant, K_{eff} is the uniaxial anisotropy constant, μ_0 is the constant of permeability and M_S is the saturation magnetisation. For Fe_3O_4 and γ-Fe_2O_3, D_c values have been determined at 128 nm and 166 nm respectively [66].

On decreasing the size of the single domain particles further, a transition in the magnetisation of the particles from a ferromagnetic to a superparamagnetic state is observed to occur. Below the superparamagnetic size limit, D_{SPM}, the thermal energy k_BT is greater than that required to reverse the direction of the magnetic moments. The magnetisation can then spontaneously flip between two equivalent magnetic orientations about a particular axis, known as the 'easy axis', in either a parallel or anti-parallel fashion with the applied field. The energy required for this process is commonly referred to as the anisotropy energy and can be represented by the following equation:

$$\Delta E_{anis}(\theta) = K_{eff} V Sin^2\theta \qquad \text{Equation 1.28}$$

where k_{eff} is the anisotropy constant, V is the particle volume and θ denotes the angle between the magnetisation and the easy axis.

A plot of the change in energy as a function of the magnetisation direction for a single domain particle is as shown in Figure 1.24. The resulting plot exhibits two energy minima at $\theta = 0$ and $\theta = \pi$, which correspond to magnetisation directions parallel and anti-parallel to the easy axis respectively.

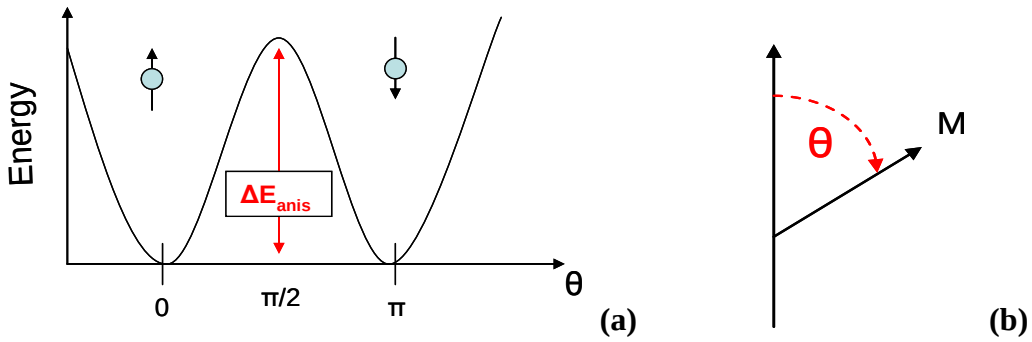

Figure 1.24: (a) Illustration of anisotropy energy for a single-domain particle with uniaxial anisotropy. ΔE_{anis} is the energy barrier for the rotation of the magnetisation, and θ is the angle between the magnetisation, M, and the easy axis as illustrated by 1.27 (b).

For an assembly of isotropic single-domain particles where no inter-particle interactions exist, values for k_BT are much greater than those for the uniaxial anisotropy constant, K_{eff} and the system behaves more like a paramagnet, with the exception that its magnetic moment is not just that of a single atom. Instead, the sum of the moments of all atoms present in the particle are accountable for the total magnetisation of each single domain particle, otherwise known as a 'super-spin' which fluctuates in an orderly fashion [67].

In the absence of an applied field, the moments will readopt their random distribution in the domain and alignment in one particular direction is no longer observed, i.e. the material retains no net magnetisation.

The time taken for this ‘flipping’ process or fluctuation to occur is represented by the Néel correlation time (τ_N) and is calculated using the following equation:

$$\tau_N = \tau_0 \exp\left(\frac{k_{eff}V}{k_BT}\right) \qquad \text{Equation 1.29}$$

where k_B is the Boltzmann constant, T is the temperature and τ_0 is ~10^{-9} s.

The rate at which this process occurs is, in turn, dependent on temperature, with the rate of fluctuation decreasing with decreasing temperature until the moments are static, where their motions and are said to be ‘blocked’. The temperature at

which this process occurs is known as the blocking temperature given by Equation 1.30:

$$T_B = \frac{kV}{25k_B} \qquad \text{Equation 1.30}$$

1.9 SPM theory for estimation of nanoparticle physical parameters

An increasing interest has emerged in the use of SPM theory in fitting experimentally derived NMRD profiles using a model system that allows for estimation of several physical parameters of nanoparticles and nanoparticulate materials. These are the IONP size, saturation magnetisation (M_s), Néel correlation time (τ_n) and anisotropy energy (ΔE_{anis}). Several studies into the superparamagnetic relaxation mechanism have been reported in the literature [68] validating its use in the determination of these parameters by SPM theory. The first theoretical approach, and the most generally accepted theory to date, was developed by Müller et. al [69], in an attempt to describe the magnetic interactions between superparamagnetic colloids and solvent molecules in aqueous suspension. It has since extended from the classical outer sphere theory of relaxation to include a high Curie component, associated with the high field fragment of the NMRD profile (>0.02 T), and the internal anisotropy energy of the crystal, responsible for the lower one. The theory is based on the interpretation of NMRD profiles that represent the dependence of ^{1}H longitudinal relaxivity, r_1, on the strength of the external magnetic field.

The shape of the NMRD profiles for superparamagnetic nanoparticles possess common features, namely the occurrence of a low field plateau, followed by an observed increase in R_1 at higher field to produce the high field dispersion before finally decreasing to zero at much higher fields [70].

Both Néel and Brownian relaxation processes contribute to the overall resulting shape of the NMRD profile, with smaller particles exhibiting low field dispersion due to Néel relaxation processes. As the anisotropy, or indeed the particle size increases, fewer contributions are made from Néel process and Brownian

contributions dominate. This results in the attenuation of the low field dispersion until it vanishes. These effects are illustrated in Figure 1.25 overleaf.

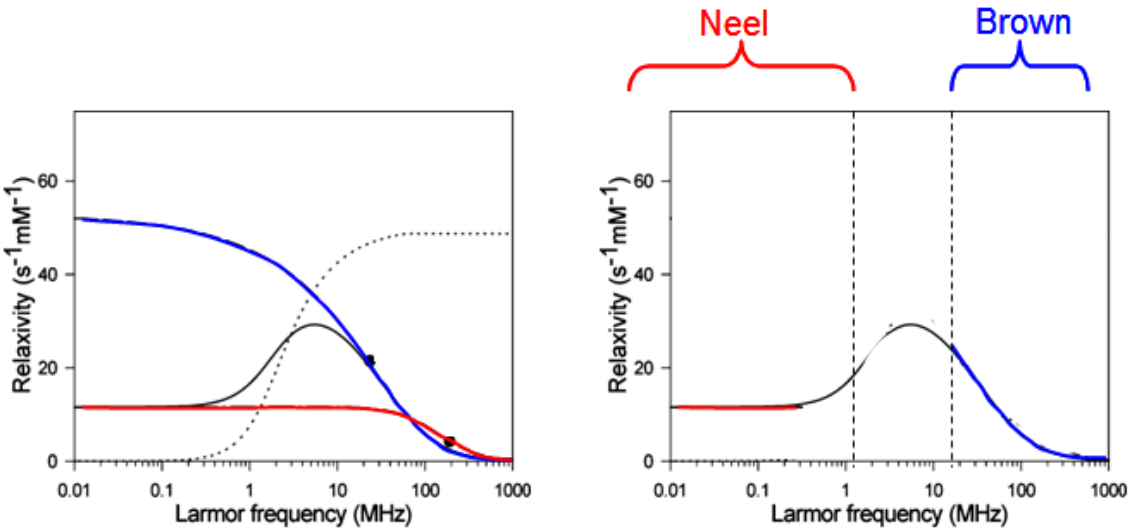

Figure 1.25: Néel and Brownian relaxation contributions to the shape of the NMRD profile for a superparamagnetic material [71].

The key parameters that determine the shape and relaxivity of the NMRD profile include the primary particle core size, which defines the frequency of the r_1 maximum in the NMRD profile (as the high frequency relaxation is driven by the diffusion of the solvent). Nanoparticles of larger core sizes will exhibit r_1 maxima at lower frequencies. The relevant timescale is the characteristic diffusion time τ_D, defined by:

$$\tau_D = \frac{d^2}{4D} \qquad \text{Equation 1.31}$$

where d is the core diameter of the colloid and D is the diffusion coefficient. The dependence of the r_1 maximum on particle size is shown in Figure 1.26.

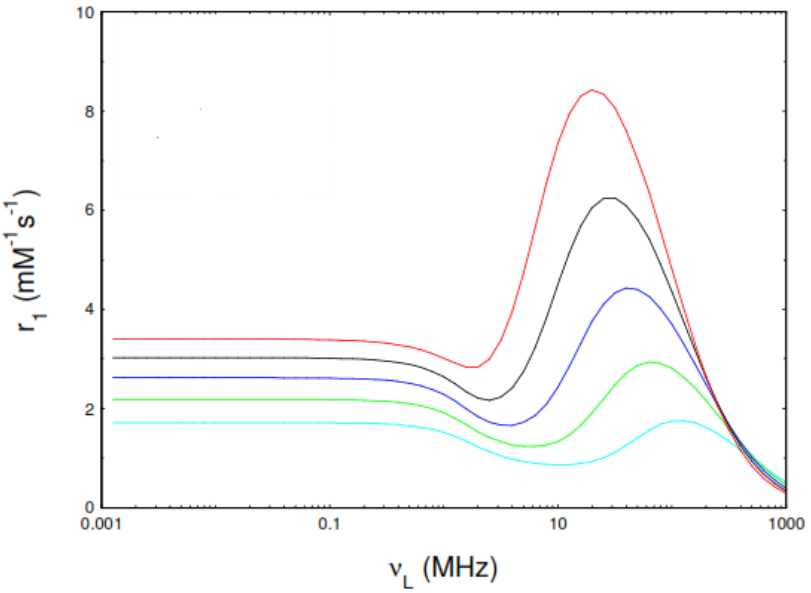

Figure 1.26: Simulated relaxivity plots demonstrating the effect of increasing the particle diameter from 4 nm (-) to 5 nm (-) , 6 nm (-), 7 nm (-) and 8nm (-) All other parameters were kept constant at values of M_s = 40 emu.g^{-1}, τ_N = 2 ns, ΔE_{anis} = 2 GHz and D=3.5x10^{-5} ns

The relaxivity is also largely governed by the saturation magnetisation (M_s), and is defined as the maximum magnetisation achieved by a material in a magnetic field. Colloids possessing higher saturation magnetisation will exhibit profiles of higher amplitude than those of lower M_s values as demonstrated by Figure 1.27 .

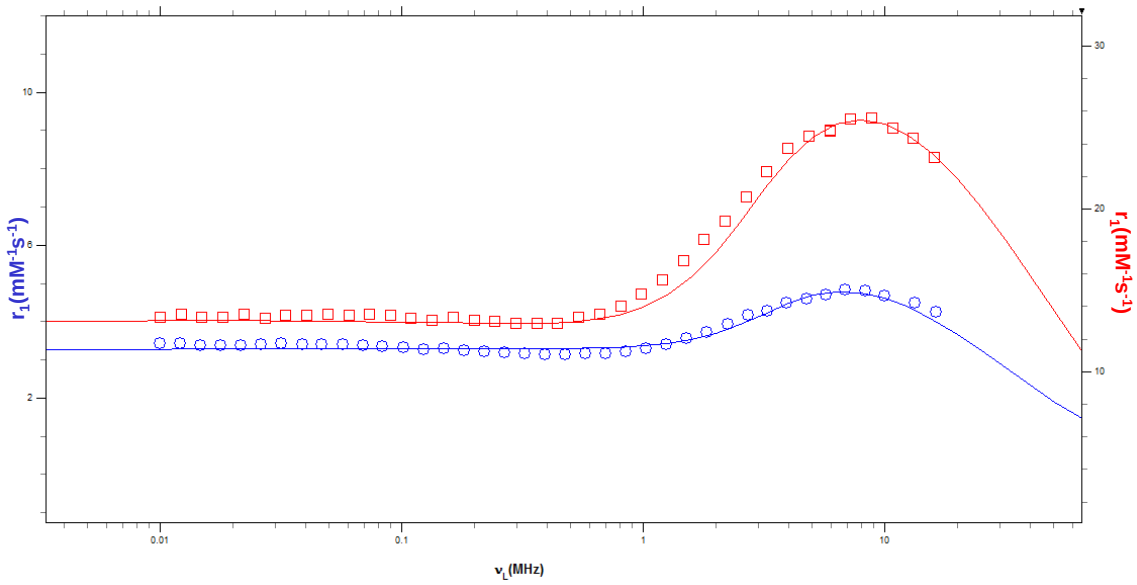

Figure 1.27: Simulated relaxivity plots demonstrating the effect of changing the saturation magnetisation where Ms=17 emu.g^{-1}(-), and 56emu.g^{-1}(-). All other parameters were kept constant with , τ_N = 2 ns, d_{SPM}= 12 nm, ΔE_{anis} = 2 GHz and D_{H2O}= 3.5E-5 cm^{2}s^{-1}

The relaxation at low fields is dependent on the fluctuations of the magnetic moments present and, hence on the Néel correlation time, τ_n. Simulations of the effect on changing τ_n are shown in Figure 1.28 below.

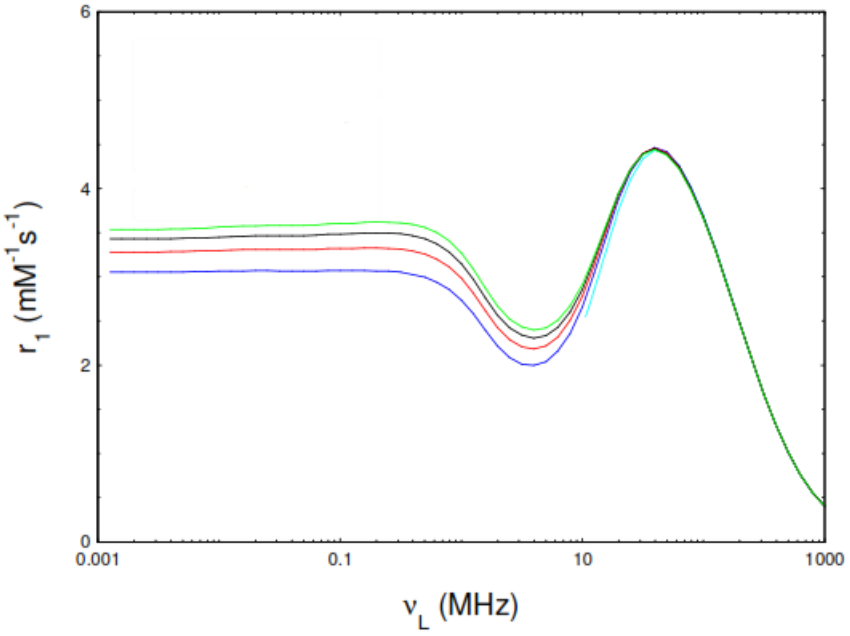

Figure 1.28: Simulated relaxivity curves showing the effect of increasing the Neel correlation time where values for τ_N were set at 4 ns (-), 6 ns (-), 8 ns (-) and 10 ns (-) with all other parameters kept constant at M_s = 40 emu/g, d_{SPM}= 12 nm, ΔE = 2 GHz, and D_{H2O} = 4.02e-5cm^{2}s^{-1}

Furthermore, modification of the diffusion coefficient can influence both the amplitude of r_1 and also the position of the r_1 maxima/minima. Upon reduction of the diffusion coefficient, D, from a value of 2.5x10^{-5} cm^2/s to 1.5x10^{-5} cm^2/s and further to 1.25x10^{-5} cm^2/s for example, we observe an increase in the overall relaxivity of the NMRD profile, in addition to an increase in the amplitude of the peak at higher frequency. This increase in r_1 may be attributed in the simulation to increasing the local viscosity of the water in the immediate vicinity of the magnetic nanoparticles, thus increasing τ_D and driving the maximum r_1 back to lower frequency. Increasing D is equivalent to increasing τ_c, which, in some sense, is equivalent to increasing particle size (Equation 1.31). This demonstrates that altering the water dynamics in the vicinity of the nanoparticles can have a significant effect on the relaxivity properties of the nanoparticles.

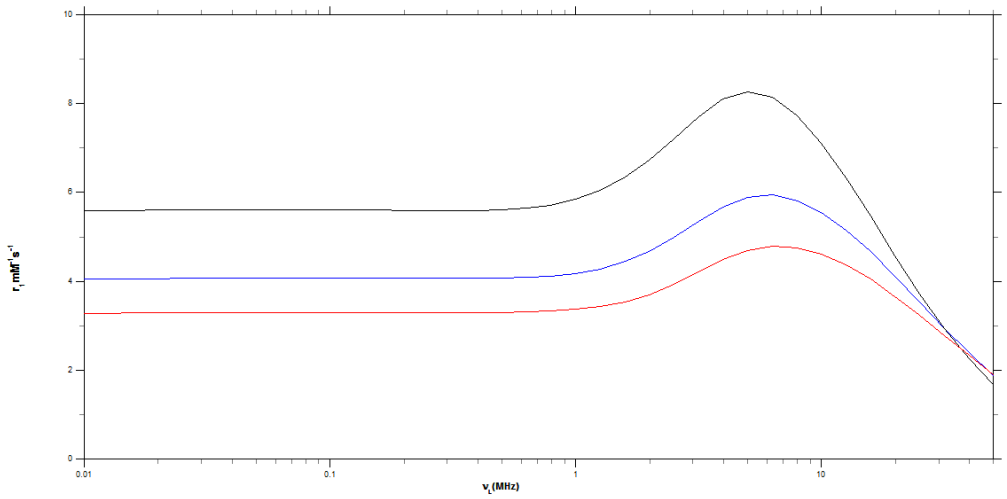

Figure 1.29: Simulated relaxivity curves showing the effect changing the diffusion coefficient, where D=3.5E-5 (-), 1.5E-5 (-) and 1.25E-5 (-). The remaining parameters were M_s = 40 emu/g, d_{SPM}= 12 nm, τ_N = 2 ns

The final parameter that can be estimated by SPM plot simulations is the anisotropy energy, or ΔE_{anis}, and is the effective activation energy required to invert the orientation of the particle spin. The depth of the dip at the mid-frequency region of the profile is dependent on this value which, in turn, is dependent on the diameter of the particles present. The anisotropy energy for single-domain particles is proportional to their volume, and will be observed to increase with increasing diameter.

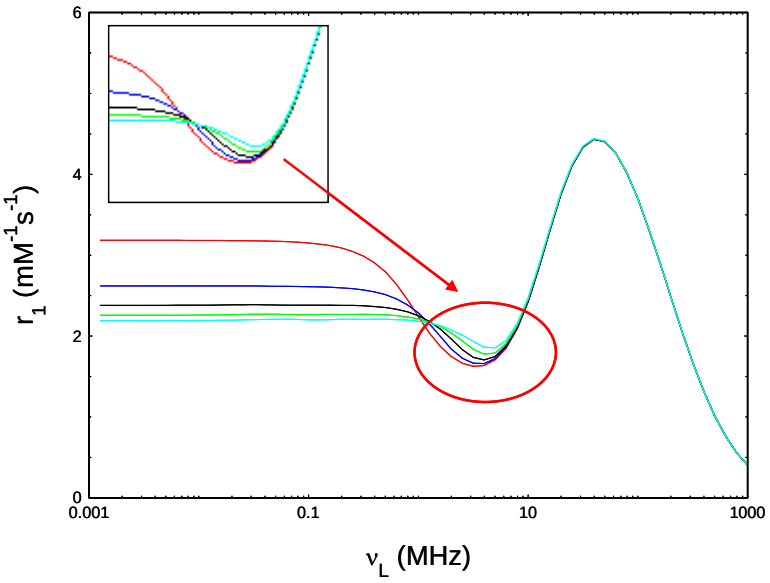

Figure 1.30: Simulated relaxivity curves showing the effect of increasing the anisotropy energy ΔE. The values of ΔE in these simulations were 1 GHz(-), 2 GHz(-), 3 GHz(-) , 4 GHz (-) and 5 GHz (-) the remaining parameters were M_s = 40 emu/g, d_{SPM}= 12 nm, τ_N = 2 ns, D_{H2O} = 4.02e-5 cm^{2}s^{-1}

The SPM model approach has received much interest in the literature as it provides information on the magnetic properties of the colloid in situ, as sensed by the diffusing solvent molecules. Taboada et al, for example [68], report the efficacy of the model in studying the relaxometric behaviour of ultra-small nanoparticles of maghemite and estimating the potential of prepared dispersions for use as contrast agents for MR imaging [72].

CHAPTER 2

Experimental

2.1 Objective

The purpose of this chapter is to outline all experimental techniques that were used throughout the course of the work presented in this thesis. Each technique is described in terms of its general background and theory, including discussion of any relevant physical relationships involved, in addition to experimental conditions used and practical considerations to be considered during analysis.

2.2 Photon Correlation Spectroscopy (PCS)

2.2.1 Theory of PCS

Photon Correlation Spectroscopy (PCS), or Dynamic Light Scattering (DLS) as it is otherwise known, is a light scattering technique used to determine the hydrodynamic size of dispersed, sub-micron sized particles by measuring the time-dependent fluctuations in scattering intensity and subsequently determining the translational diffusion coefficient (D) and hydrodynamic diameter (d_{hyd}) of the suspended nanoparticles giving rise to the scattering [73]. The fluctuation arises due to the random motion of sub-micron dispersed nanoparticles observed within a given solvent medium. This constant random motion, Brownian motion, occurs due to collisions of individual nanoparticles with the surrounding solvent [74].

A typical PCS measurement is conducted as follows; a laser light (typically 3 mW He-Ne laser), operating at a wavelength of 633 nm is passed through a cuvette containing the sample of interest. A fraction of this light is then scattered by the particles dispersed within the solvent the backscattered fraction of which is measured by a detector at an angle of 173˚. The signal intensity of the light is governed by the constant motion of the particles, and fluctuates as a function of time. A digital auto-correlator is used to process the resulting signal intensities at specific time intervals in order to determine the time scale of the fluctuations and thus the size of the particles present. Larger particles cause signal intensities to change more slowly due to their slower diffusion rates, whereas smaller particles move faster through the solvent leading to more rapid signal fluctuations. Smaller particles will therefore result in a more rapid reduction of the signal correlation, while larger particles will demonstrate a much more gradual decay. Particles that

are monodisperse and are in random Brownian motion will thus give rise to an exponential correlation function (G), represented by Equation 2.1:

$$G(\tau) = G(0)^{\frac{-|\tau|}{\tau_c}} \qquad \text{Equation 2.1}$$

where τ is the sample time of the correlator and τ_c is the correlation time of the decay of G (τ). The correlation time is defined as the mean time between diffusional steps and the inverse of this correlation time gives the diffusional rate τ_c^{-1}.

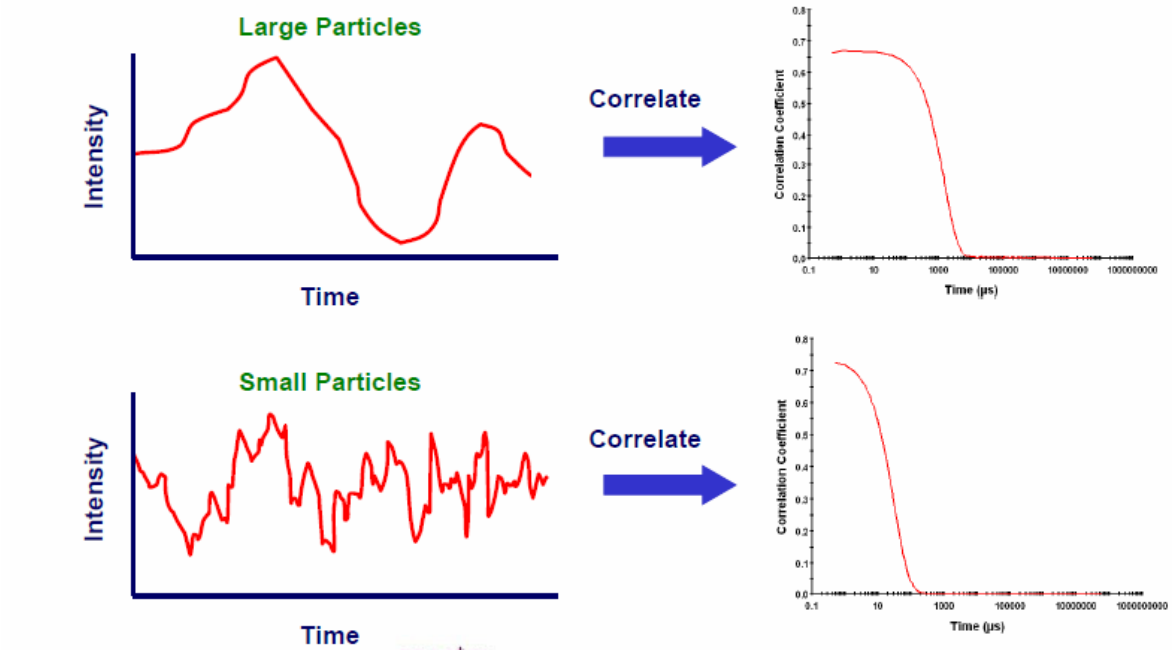

Figure 2.1: Correlation functions and differences in the intensity fluctuations of large and small particles [74]

This time dependence of scattered light intensity can then be related to the particles diffusion coefficient, D, using Equation 2.2 below where k, representing the magnitude of the scattering vector, can in turn be represented by Equation 2.3:

$$D = \frac{1}{2\tau_c k^2} \qquad \text{Equation 2.2}$$

$$k = \frac{2\pi\eta}{\lambda}\sin\frac{\theta}{2}$$ Equation 2.3

The calculated diffusion coefficient can then be related to hydrodynamic size of the particles present using the Stokes Einstein equation (Equation 2.4):

$$D = \frac{kT}{3\pi\eta d_{hyd}}$$ Equation 2.4

where k_B is Boltzmann's constant, T is the absolute temperature, η is the viscosity of the solvent medium and d_{hyd} is the hydrodynamic diameter of the particle .

The hydrodynamic diameter (d_{hyd}) of an individual particle is defined as the diameter of the core of the nanoparticle plus any associated ligands or bound solvent molecules attached and is not the true size of the nanoparticle itself [73]. It can be observed from the Stokes-Einstein equation outlined above (Equation 2.4) that a number of factors exist that can have an impact on the measured d_{hyd} of a given particle. It is evident, for example, that the hydrodynamic size of the particle is dependent on measurements carried out at a constant temperature (and therefore viscosity) as this governs the diffusion coefficient, D. The shape and surface characteristics of the particle also have an effect on the overall observed hydrodynamic size.

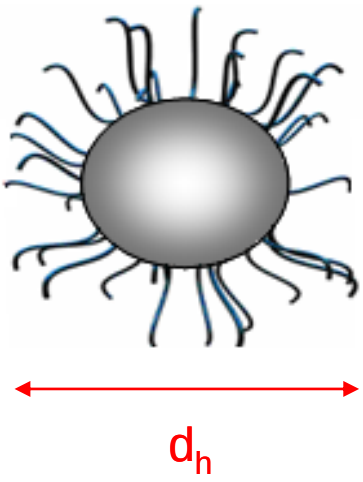

Figure 2.2: Schematic of the hydrodynamic diameter of a particle

The correlation function contains the diffusion coefficient information required by the Stokes-Einstein equation for determination of the hydrodynamic size of a given particle in solution and the subsequent polydispersity index (PDI) of the dispersion in which it exists [75]. These coefficients are obtained by fitting the correlation function with one of two suitable algorithms; the cumulants analysis, which fits a modified exponential to the correlation function in order to determine a mean size and PDI, or the distribution analysis, which utilises Mie scattering simulations of trial particle distributions to model the exponential response.

The cumulants analysis is defined in the International Standard on Dynamic Light Scattering ISO13321 (1996) [76] which states that a third order polynomial should be used in the determination of mean hydrodynamic size and PDI of the form shown in Equation 2.5 below:

$$\ln[G_1] = a + b\tau + c\tau^2 \qquad \text{Equation 2.5}$$

where τ represents the delay time of the correlator. A plot of ln [G_1] as a function of time can then be used to derive the z-average diffusion coefficient and the polydispersity index of the dispersion as the terms b and $2c/b^2$, respectively, as shown in Figure 2.3 below:

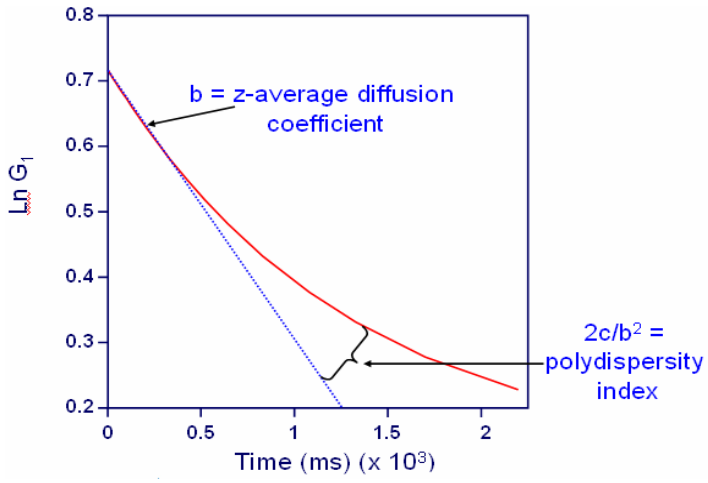

Figure 2.3: Derivation of Z-Average and Polydispersity index from cumulants analysis [74]

The polydispersity index (PDI) is essentially a representation of the distribution of size populations within a given dispersion. It typically ranges from values of 0.0 to

1.0, the latter suggesting a highly polydisperse dispersion with multiple particle sizes present. Values of 0.2 and below are most commonly deemed acceptable in practice, with some dispersions exhibiting PDI values of as low as 0.02 for polymer-based nanoparticle materials.

The correlation function can also be fitted to a multiple exponential model to obtain intensity size distributions using the Multiple Narrow Modes algorithm based upon a non-negative least squares (NNLS) analysis [77] using commercially available software (Dispersion Technology Software, Malvern Instruments; Worcestershire, UK). Size distributions are displayed as a plot of the relative intensity of light scattered as a function of particle size. A typical intensity distribution is presented in Figure 2.4 below:

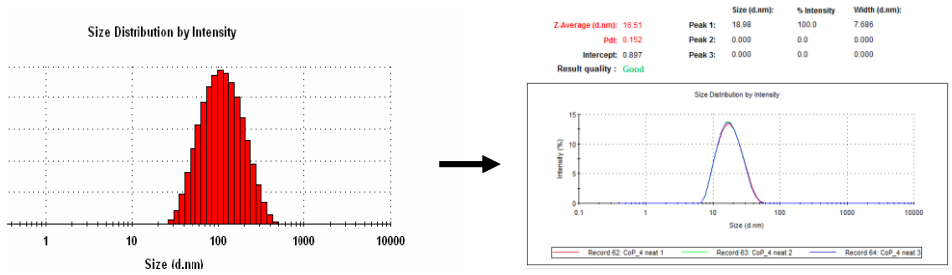

Figure 2.4: Typical intensity histogram and distribution.

2.2.2 Analysis Procedure

PCS measurements were carried out on a High Performance Particle Sizer (HPPS) or a Zetasizer Nano ZS supplied by Malvern Instruments, UK. A 3 mW He-Ne laser operating at 633 nm was passed through the sample volume (typically 1 mL) within a suitably chosen cuvette (plastic for aqueous samples and quartz for non-aqueous samples) at a constant temperature of 25ºC. A thermal equilibration time was first observed at the onset of all measurements to ensure this. The intensity of the scattered light was then detected at an angle of 173º to the incident beam (backscatter detection). This configuration results in an 8-fold increase in the detected scattering volume when compared to the classical 90º scattering detection method and, in turn, a similar increase in the count rate observed at the detector. This provides an opportunity to measure smaller nanoparticle sizes at lower concentrations, as the count rate is directly related to the sensitivity of the

instrument. The Z-Average (hydrodynamic diameter) and the PDI are then calculated from the cumulants analysis as defined in the International Standards ISO13321 (1996) [76] and ISO22412 (1998) [75]. A typical setup of a PCS instrument may be illustrated by Figure 2.5 below:

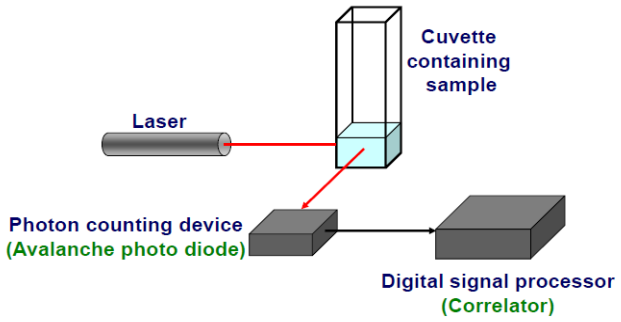

Figure 2.5: General setup of a typical PCS instrument

2.2.3 Practical Considerations

Typically speaking, PCS is a widely used analytical technique in the determination of particle diameters within the nano to micron size range, the lower end of which is highly dependent on overcoming experimental obstacles such as thermal fluctuations, background noise contributions, any particle contaminants and environmental disturbances. It is therefore vital that a number of practical considerations are observed when performing dynamic light scattering measurements.

In terms of sample preparation, an optimum nanoparticle concentration within the sample must be selected. This concentration should be low enough to avoid multiple scattering, which can often lead to overestimation of hydrodynamic size, but high enough to provide a sufficiently high number of particles for successful measurement. The particles must also be fully stable in the solvent medium in which they are dispersed so that the number of scatterers (particles) within the medium remains constant (i.e. no sedimentation can be seen to occur). Additionally, samples should be free from foreign particles (such as dust), as their presence will dominate the smaller, more weakly scattering particles of interest.

PCS, despite its limitations is, in comparison to other size-determination techniques, a fast, user-friendly method of determining particle size within the sub-micron range which requires little sample preparation and is usually non-destructive to the sample under analysis. It allows particles to be analysed in suspension without the need for drying or precipitation into their solid form (as is required with Transmission Electron Microscopy). Measurements are obtained within a number of minutes and slight changes in size and polydispersity can be observed in real time. This is a critical advantage for some of the work to be presented.

2.3 Zeta Potential

2.3.1 Principle of Zeta Potential

As described in greater detail in Chapter 1 (Section 1.5), particles existing in a colloidal dispersion in polar solvents can carry their own characteristic surface charge or potential, otherwise known as the Zeta Potential, arising from the physics of the particles in the dispersion and any associated ligands that may be present. Zeta Potential can be defined as the electric potential in the interfacial double layer (DL) at the location of the slipping plane (i.e. the point at which the bulk fluid meets the particle surface) [58]. In other words, zeta potential is the potential difference between the dispersion medium and the stationary layer of fluid attached to the dispersed particle. Knowledge of the Zeta Potential of a given dispersion is useful in estimating the overall stability of a given colloidal dispersion against aggregation as particles with similar surface charges will easily repel each other and remain fully dispersed throughout the medium in which they exist. It is most favourable that all particles present possess highly positive or negative surface charges (usually in excess of ± 30 mV) in order to achieve complete dispersion stability.

2.3.2 Analysis procedure

Zeta Potential measurements were carried out on a Zetasizer Nano ZS instrument supplied by Malvern instruments (Worcestershire, UK) as illustrated by Figure 2.6 (below). This system uses a technology known as M3-PALS, a second generation

form of the well-established phase analysis light scattering (PALS) technique combined with the patented mixed mode measurement (M3) technique [78]. PALS is essentially a variation of Laser Doppler Velocimetry (LDV), which involves the application of a potential to a dispersion and the measurement of the mobility of the particles present using the observed shift in frequency of the light moving throughout the cell. This shift is then related to the electrophoretic mobility which, in turn, can then be converted to zeta potential using established physical relationships.

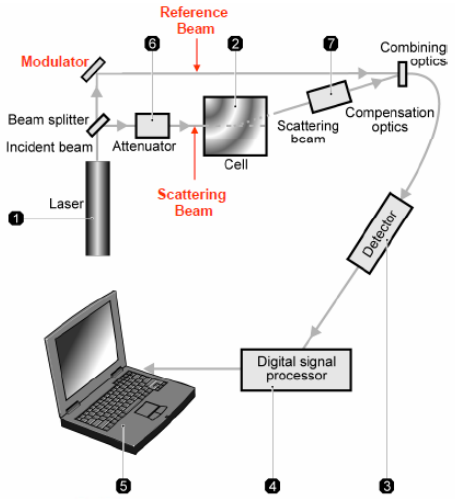

Figure 2.6: Zetasizer instrument setup [58]

The M3 method is a relatively new technique in the measurement of zeta potential and involves the use of a technique known as fast field reversal (FFR) which greatly enhances the accuracy and resolution of the measurement process. Colloidal particles will respond much faster to the applied field as opposed to the surrounding liquid inside the capillary cell when this field reversal is rapid, thus suppressing any electroosmotic effects that may occur. This means that the mobility measured during this period is due to the electrophoresis of the particles only. More specifically, an M3 measurement involves the following steps; firstly, an FFR measurement is performed at the centre of the capillary cell to determine the mean distribution of the potential, followed by a slower field reversal (SFR) process which further enhances the resolution of the measurement [58]. The mean values for both processes are calculated and subtracted from one another to determine the electroosmotic flow of the particles dispersed within the medium. This value, in turn, is used to calculate the zeta potential. A representation of the FFR and SFR contributions to the resulting phase plot is as shown in Figure 2.7.

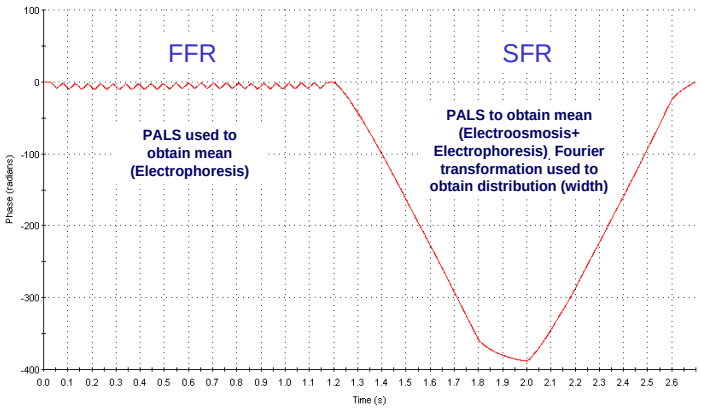

Figure 2.7: FFR and SFR contributions to Zeta Potential Phase Plot

Combining PALS with the M3 technique ensures a much more accurate measurement of the Zeta Potential of the particles present within a given dispersion, particularly if the said particles exhibit tendencies of low mobility and/or high conductivity. Particle mobility measurements using PALS are made by comparing the phase of the detected signal of the scattered light with that of a reference beam or signal with a set frequency of 320 Hz. A plot of the phase difference as a function of time demonstrates a gradient dependent on the magnitude of this difference, which then is used to determine the value for the Zeta Potential. The sign of the potential (positive or negative) results from whether the observed frequency of the scattered light is in excess or falls below the frequency of the reference beam.

2.3.3 Practical considerations

As with PCS particle sizing experiments, the measurement of Zeta Potential is also dependent on a number of preparative and practical considerations involving both sample preparation and measurement. For example, nanoparticle stability and concentration within the dispersing medium are equally as important for the measurement of Zeta Potential as measurements are extremely sensitive to factors such as attractive and repulsive particle-particle interactions that are ultimately damaging to particle stability within their dispersed media. In addition to this, the nanoparticle concentration must fall within an acceptable range so as to allow for the laser beam to pass through the chamber and thus achieve a successful measurement.

The most important factor, however, for accurate Zeta Potential estimation is the pH of the dispersion under analysis. A Zeta Potential reported without its characteristic pH value is rendered as meaningless. Take, for example a positively charged particle in suspension. As a more alkaline solution is added to the dispersion, the particles present will acquire a more negative surface charge. If further alkali are added, the particles will eventually reach a point of neutrality (charge will be zero), before exhibiting a fully negative surface charge. This point of zero charge is known as the isoelectric point (IEP) and can be determined via titration and a plot of Zeta Potential versus pH. However, it is often found that rapid aggregation occurs close to the IEP.

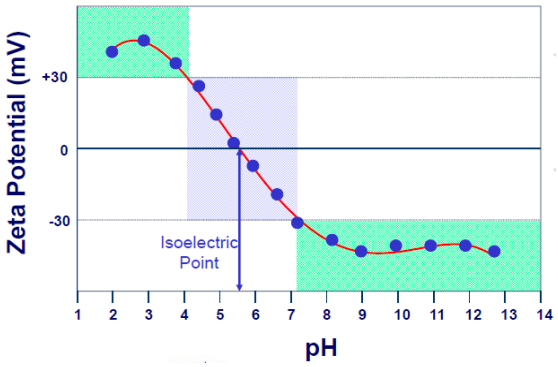

Figure 2.8: Schematic plot of Zeta Potential versus pH and IEP determination of a typical aqueous nanoparticle suspension [58]

2.4 Fast Field-Cycling Nuclear Magnetic Relaxometry (FFC-NMR)

2.4.1 Principles of FFC-NMR

FFC-NMR involves the rapid switching of magnetic fields throughout the course of an experiment in order to measure the spin-lattice relaxation time, T_1, over a range of magnetic fields, and hence Larmor frequencies, as $\nu_L = \gamma B_0/2\pi$. Where γ is the gyromagnetic ratio for ^1H and B_0 is the magnetic flux density of the applied field. The spin-lattice relaxation time is the time taken for the longitudinal component, M_z, of the nuclear spin magnetisation vector of an ensemble of ^1H nuclei to recover fully to thermodynamic equilibrium. The field dependence of the spin-lattice relaxation rate R_1 ($1/T_1$) is represented by what is known as an NMRD

or Nuclear Magnetic Resonance Dispersion profile. NMRD profiles can provide a detailed insight into the molecular dynamics of a particulate system using spectral density functions; functions that describe the statistical distribution of motional frequencies in a given dynamic system. In the case of magnetic nanoparticle suspensions these profiles contain a wealth of information about the properties of the particles present, including their size, magnetisation and interaction with the solvent.

In order to measure T_1, one of two field-cycling sequences is performed; the pre-polarised sequence (PP/S) and the non-polarised sequence (NP/S). The pre-polarised sequence is used to measure T_1 values below ~6 MHz and involves the polarisation of the ^1H magnetisation of the sample at a high polarisation field, or B_{Pol} (usually in the range of 10-14 MHz). The field is then rapidly switched to one of a much lower value (known as $B_{rlx,}$ or the relaxation field) where the relaxation process is allowed to proceed for a time τ. A signal is then detected at a third field, known as the acquisition field, of 9.25 MHz (B_{acq}) following a 90º RF pulse which generates a free induction decay (or FID) [79, 80]. Equilibrium is then achieved following a time delay, or recycle delay (RD) which is typically of the order of $5xT_1$. This process is repeated a number of times as a function of τ and generates values for T_1 at the relaxation field observed. A typical pre-polarised sequence can be illustrated by the schematic shown in Figure 2.9.

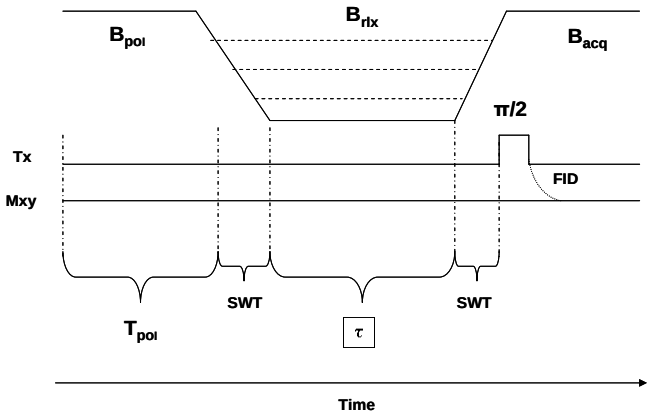

Figure 2.9: Schematic representation of a typical pre-polarised sequence. T_{POL} is the polarisation time, and B_{POL} is the polarisation magnetic field. The switching time (SWT) is the time required by the field to switch between the different levels. Tx represents the transmitter output and Mxy is the magnetisation in the xy plane. B_{acq} is the detection/acquisition field. The multiple dotted lines drawn for B_{RLX} represent various relaxation fields.

At field frequencies in excess of 6 MHz, the non-polarised sequence is then applied, where the magnetisation is permitted to grow from zero as a fraction of τ. A polarisation field of zero is used in this instance, to allow for maximum difference between the polarisation and relaxation fields [80]. Sample magnetisation differences for short and long τ are therefore maximized, providing a more accurate estimation of T_1. The basic non-polarised sequence can be illustrated as follows:

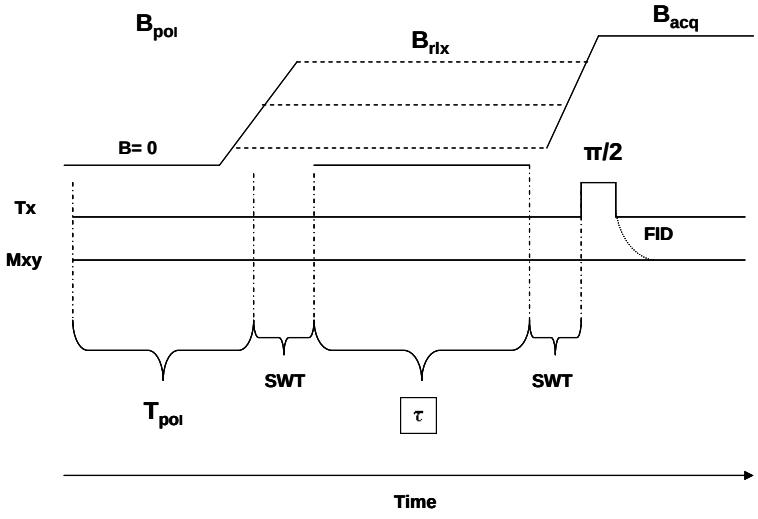

Figure 2.10: The basic non-polarised sequence (NP/S). All parameters are as described in Figure 2.9 legend (above).

2.4.2 Analysis Procedure

FFC-NMR measurements were performed on a Spinmaster FFC-2000 Fast Field-Cycling NMR Relaxometer provided by Stellar (Italy) and Variable Temperature Controller (VTC, also Stellar). Samples (typically 0.3-1mL) were analysed at a constant temperature of 25ºC in addition to the following parameters:

B_{POL}	= 12 - 14 MHz
T_{POL}	= 0.3 - 0.5 s
B_{ACQ}	= 9.25 MHz
Slew rate	= 12 - 18 MHz/ms
Switching time	= 0.0015 - 0.003 s
TAU delay	= 0.001 s
Block size	= 256 – 512
Sweep width	= 1000000 Hz
FLTR	= 270000 – 930000 Hz
90° pulse duration	= 6 - 7 ms

Table 2.1: Typical parameters used for NMRD profile acquisition

The field strength range could be further extended in the region of 30 - 80 MHz using a stronger electromagnet external to the Stellar Relaxometer (Bruker WP80 variable field electromagnet). This provided further information on the behaviour of a given dispersion's magnetisation with increased field strength.

2.4.3 Practical Considerations

In addition to the boundaries set by the available measurable frequency range, NMRD analyses also have many associated practical considerations that one must observe prior to analysis. Firstly, sample concentration must be within a range that results in a measurable T_1, so that does not fall short of nor exceed the experimental switching time of the measurement between changing field frequencies More dilute dispersions will result in a much longer T_1 values (magnitudes of seconds) at any given field, while the opposite is observed for much more concentrated samples (orders of milliseconds). Particle dispersions must also be stable at all measured field strengths, and no sedimentation or precipitation should occur.

2.5 Inductively coupled plasma atomic emission spectroscopy (ICP-AES)

2.5.1 General theory

Inductively coupled plasma atomic emission spectroscopy (ICP-AES) is a well-established analytical technique used in the detection and quantification of individual and/or multiple elements and their relative concentrations in a wide range of liquid media. This method exploits the fact that excited electrons emit energy at a particular wavelength characteristic of the element under analysis as they return to ground state [81]. The intensity of the light emitted is then related to concentration of ions present via the Beer-Lambert law and the use of a set of calibration standards of known concentration and their resulting standard curve.

ICP-AES utilises a plasma source as the origin of ionisation and excitation during the analysis. The associated high temperatures of the plasma source (typically 7,000-10,000 K) ensure that the analyte becomes fully nebulised into its aerosol form that, in turn, is composed of droplets of a variety of sizes. Larger droplets are disposed of to waste, and the smaller droplets are directed toward the Argon plasma source. It is in the plasma source that the transfer of energy occurs to promote the ions to a more excited state, shortly followed by the emission of electromagnetic radiation (light energy) as atoms return to their natural ground state.

2.5.2 Analysis Procedure and Standard Calibration curve Preparation

The role of ICP-AES in the work presented in this thesis was to determine the iron concentration of all nanoparticle dispersions and composite materials. This information was useful, for example, in the correction of NMRD profiles for iron content and in the determination of the amount of iron oxide nanoparticles being introduced prior to nanoparticle-polymer composite formation.

Iron determination analyses for the purpose of the work presented in this thesis were carried out on a Varian Liberty 220 Inductively Coupled Plasma Atomic Emission Spectrometer, of which the typical instrument setup may be demonstrated as in Figure 2.11:

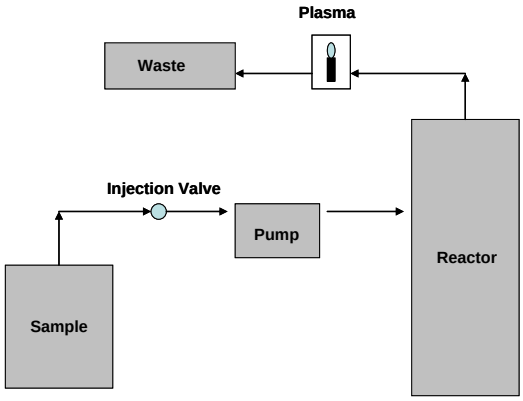

Figure 2.11: Typical setup of an ICP-AES instrument

Prior to analysis, samples required subjection to an acid digestion process, in order to transfer all iron present in the sample into solution. To obtain the samples in this manner, approximately 0.5 mL of 6 N analar grade HCl and 1 mL of deionised water were added to a conical flask, followed by a known volume of the analyte. The solution was heated until 1-2 drops remained at the bottom of the flask. A small volume of water was then added and the resulting solution was brought to the boil. Following cooling, the solution was transferred to a volumetric flask and made to the mark with 1 M HNO_3. It should also be noted that all glassware used in the digestion and analysis process was pre-rinsed with deionised water and HNO_3 to ensure no ions were already present, thus affecting the detection of the iron in the solution of interest.

For successful conversion of the resulting light intensities of all samples to their respective concentrations, it was necessary for a calibration curve to be constructed using a series of standards of known concentration. An iron standard solution (0.5 M $Fe(NO_3)$ in HNO_3 ; Merck, Germany) was diluted accordingly to prepare a series of standard solutions ranging from 0.05 mg/mL to 5 mg/mL Fe, with the range used depending on the estimated resulting intensities of the samples involved. From these standards, a calibration curve was generated and a linear fit to the data was used to extrapolate sample concentrations from the resulting equation of the fitted line using the obtained intensity values. A typical calibration curve is demonstrated below in Figure 2.12. An R^2 value of 0.9995 indicates that the standards can successfully be used in the analysis and allow for an estimation of random error better than 1%.

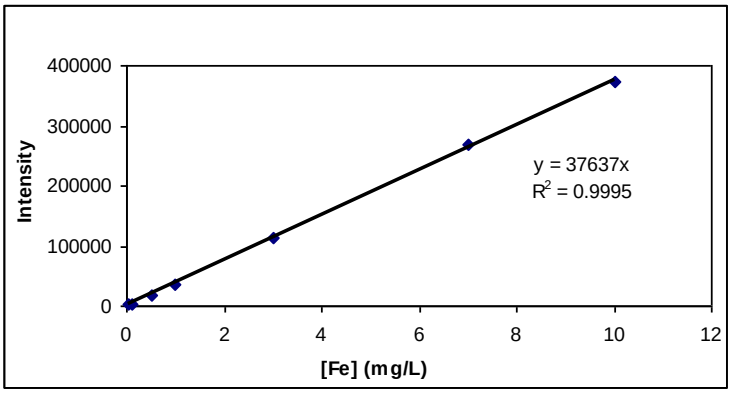

Figure 2.12: A typical ICP-AES standard curve for Fe standards of the range 0.5-10 mg/mL

2.5.3 Practical Considerations

For successful ICP-AES measurement and accurate elemental analysis, it is vital that a number of considerations be met prior to any sample analysis. Firstly, the range of calibration standards used must be sufficient to cover the estimated concentration range of all analytes included in the measurement. It is suggested that all samples fall within 10 times the detection limit of the linear working range for Fe(0.006 μg/mL - 5 mg/mL [81].

In terms of sample preparation, it is vital that all samples for the purpose of use on this instrument were dispersed in 1 M HNO_3 and exhibited no sedimentation or presence of any precipitate. This often requires the use of Triton X-100 for digestion of polymer-based samples, ensuring that the polymer did not generate a precipitate in solution that may result in blocking of the internal tubing of the instrument.

2.6 Transmission Electron Microscopy (TEM)

2.6.1 Principles of TEM

Transmission Electron Microscopy (TEM) is a unique analytical microscopy technique used to characterise the structure of micro- and nano-materials using a combination of diffraction and imaging techniques. In a conventional Transmission Electron Microscope, an ultra-thin specimen is irradiated with an energised beam of electrons of a uniform current via an electron gun. This gun is connected to a

high voltage source (usually a tungsten filament) of ~100-300 kV and provides a beam source of high energy electrons via thermionic or field emission which illuminate the specimen through a two or three stage condenser lens system. Electrons are emitted from the gun source and are accelerated through the specimen towards an anode. The incident electrons interact with the specimen and are deflected from their path by direct collisions or electrostatic interactions with the surrounding electrons of the specimen. This results in a non-uniform distribution of electrons which provides structural information of the particles under analysis. The electron intensity distribution is then refocused and magnified via a three or a four objective lens system, which results in the formation of an image that can then be projected onto a fluorescent screen and processed by a computer/recording system. A typical setup of a Transmission Electron Microscope is as illustrated in Figure 2.13.

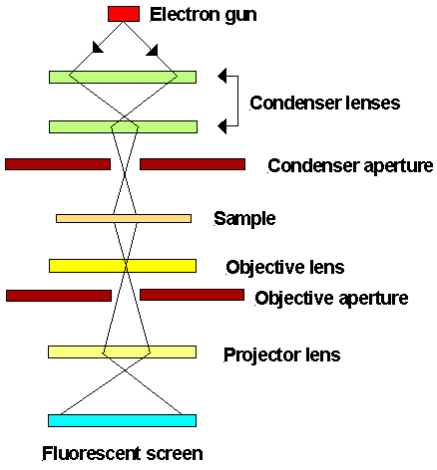

Figure 2.13: Setup of a Transmission Electron Microscope

As the incident electrons first pass through the specimen sample before reaching the imaging screen, they contain all structural information of that specimen. Image formation is therefore based on the principle of electron scattering. When the electrons come into contact with the sample, they can either 'bounce off' elastically (where the electrons change direction but not kinetic energy) or inelastically (incident electrons will change direction but also donate kinetic energy to the analyte). Scattered electrons are usually scattered in the forward direction, i.e. in parallel with the incident beam. These forward scattered electrons are responsible for image generation in TEM [82]. Scattering can be single, plural or

multiple (>20 times) in nature. The greater the amount of scattering, the more complicated the interpretation of the images and diffraction patterns become. It is therefore important that thin specimens are used for TEM analysis, as the number of backscattered electrons increases with increased sample thickness [82].

Image contrast arises when there is interference between electrons coming from a range of diffraction angles. Electrons that interact with the sample are bent away from their original path, and interfere either constructively or destructively with the main electron beam. When a narrow objective aperture is used, electrons that get deflected at a greater angle are blocked, and the contrast of the image is enhanced. This however, is at the expense of electrons with a high deflection containing high resolution information being lost. It is therefore vital that a balance between good resolution and image contrast is met. This loss of electrons (and therefore amplitude) from the main electron beam is known as amplitude contrast, and is the main source of contrast in a TEM image. Amplitude contrast is dependent on two main factors; the sample thickness and the atomic number of the specimen under analysis. Elements with higher atomic numbers (and thus high electron densities) will exhibit a larger amount of scattering, leading to images of higher contrast (e.g. Au). It follows that elements with lower atomic numbers (e.g. Fe) will generate images of much lower contrast due to their decreased degree of scattering intensity.

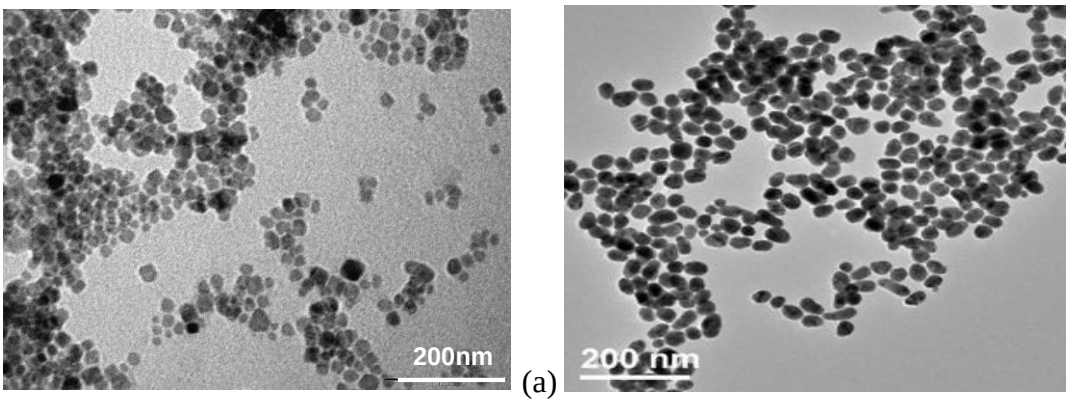

(a) (b)

Figure 2.14: Contrast differences in TEM images of (a) Iron and (b) Gold nanoparticles

2.6.2 Practical Considerations

A number of practical considerations exist with TEM in order to obtain images of good resolution and contrast. Firstly, the specimen thickness, as mentioned

previously, must be very thin in order for the transmission of high energy electrons through the sample. It therefore follows that the concentration of particles in the dispersion introduced onto the TEM grid must be at an optimal level to avoid sample buildup over the surface of the grid. The drying process of the sample upon the grid is also important, as unwanted artefacts can often be introduced during this process. Other technical considerations include careful selection of the correct magnification and field of view during the analysis process.

2.6.3 Experimental conditions

TEM images were obtained using a JEOL 2000 FX TEM scan (at an accelerating voltage of 80 kV) for samples deposited on carbon-coated (400 mesh) copper grids. Access was courtesy of the Electron Microscopy Laboratory at University College Dublin. The preparation of samples involved depositing a drop (15 μL) of the diluted relevant dispersion in heptane onto the grids and allowing the solvent to evaporate, prior to imaging.

2.7 Thermogravimetric analysis (TGA)

2.7.1 Basics of TGA

Thermogravimetric Analysis (TGA) is a useful analytical tool in the determination of many physical properties of a material such as purity, thermal stability, decomposition kinetics, composition (particularly for mixtures) and in the identification of many chemical processes such as desolvation, decomposition, chemisorption and oxidation.

TGA is an analytical technique whereby the mass loss of a material is investigated as a function of temperature and/or time when subjected to a controlled temperature ramp [83]. When a substance is heated at a uniform, controlled rate, a continuous graph of mass change versus temperature is obtained and is known as a Thermogravimetric (TG) curve. TG curves can exhibit many stages of decomposition, each of which is composed of an initial (T_i) and a final (T_f) temperature value. T_i may be defined as the point at which decomposition begins to occur, and T_f as the point at which decomposition appears to be complete for

that particular stage. The difference between these times ($T_f - T_i$) is known as the reaction interval [84]. An example of this is shown in Figure 2.15.

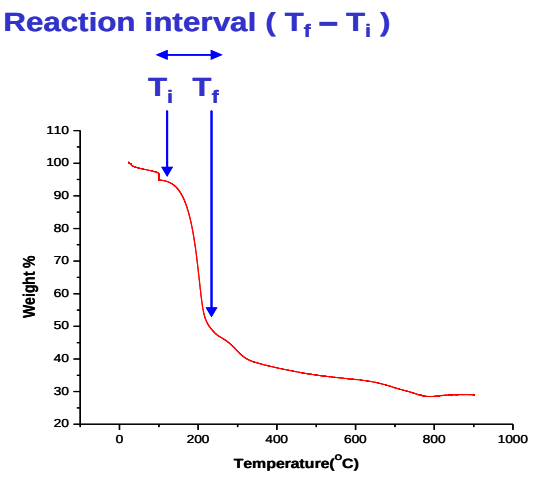

Figure 2.15: Demonstration of a reaction interval in a TGA curve

2.7.2 Instrumentation and Experimental setup

The basic components of the TGA instrument are as follows; the sample balance, the heating furnace, a temperature control/measurement source and a recorder. The sample balance is composed of a sample pan that houses the analyte and resides in the furnace and is heated or cooled during the course of the experiment. The temperature gradient is controlled via use of a thermocouple and can range from approximately -150˚C to 1000˚C depending on the requirements of the experiment. A purge gas is also present in the chamber of the instrument and controls the environment for the analysis and is most commonly an inert gas such as Nitrogen. The mass change of the sample is then monitored on changing of the reaction temperature by a recording device (graphic recorder or X-Y recorder) and a plot of change in weight versus temperature is obtained. A typical setup of a TGA instrument is as shown in Figure 2.16

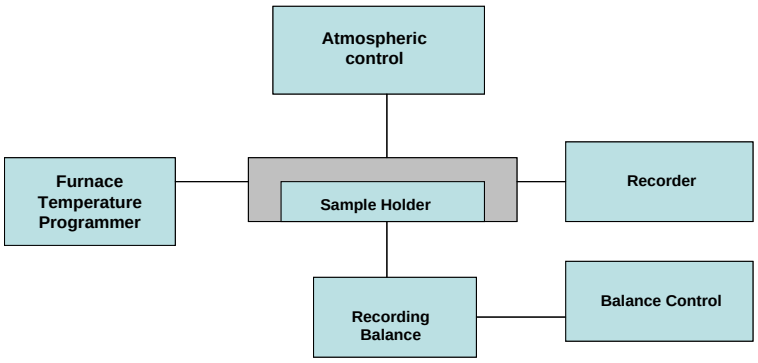

Figure 2.16: Setup of a typical TGA instrument

TGA analyses were carries out on a Q Series Q-50 Thermogravimetric Analyser (TA Instruments, Delaware, USA) with Nitrogen gas pumped through the system at a rate of 50 mL/min to ensure an inert atmosphere for sample analysis. Samples were dried prior to analysis either by solvent evaporation or freeze drying, depending on the sample being analysed to ensure all moisture was removed from the material prior to measurement.

2.7.3 Practical considerations and Sources of Error

Factors such as the furnace heating rate, recording speed, furnace atmosphere and sensitivity of the recorder can greatly influence the accuracy of the results obtained [84]. Although no optimum heating rate can be suggested to give the best graphical resolution, a rate of approximately 3-10˚C/min is typically used, depending on the nature and number of decomposition stages present [85, 86]. In addition to this, it is suggested that for slower-decomposing samples, slower recording rates should be observed, as higher speeds may result in curve flattening and loss of resolution of the reaction interval(s). Sample quantity, packing, particle size and the nature of the material are among the many sample dependent factors that need to be considered prior to analysis. It is suggested that for most applications, 2-50 mg of sample is sufficient, where 50-100 mg may be necessary for more volatile materials. The sample must exhibit good coverage and packing upon the sample balance to ensure that controlled diffusion of evolved gases occurs throughout the course of the experiment. Samples of smaller particle sizes may be observed to exhibit a greater extent of decomposition, so it can also be important to check for ramp rate dependence of the particles under analysis prior to more accurate measurement. Finally, purity of the material will have an affect on the outcome of

the experiment and should also be taken into account during the experimental design. Purity should be confirmed by alternative means, where possible.

CHAPTER 3

Synthesis of Charged Iron Oxide Nanoparticles and their Characterisation in Aqueous Media

3.1 Introduction

The dispersion of iron oxide nanoparticles within a wide range of both aqueous and non-aqueous media has been successfully achieved and extensively reported in the literature [21, 44, 46, 49, 50, 87-92]. Their stabilisation in carrier liquids is of great importance, particularly as they are increasingly being considered for biomedical application. Nanoparticles developed for in vivo applications, for example, require the attachment of surfactants, or ligands, that will permit their dispersion and stability in aqueous biological media. The interpenetration of the ligands causes steric repulsion when two particles approach each other, reducing the probability of agglomeration. An additional benefit of coating with surfactants is that it inhibits air oxidation, to which the particles are susceptible [93].

Ligand attachment also provides electrostatic stabilisation to the dispersed nanoparticles which, in addition to generating colloidal stability, plays a significant role in the biokinetics and biodistribution of the nanoparticles and their associated drug delivery vehicles in vivo [44]. Coating nanoparticles with a wide range of materials such as gold [94], silica [95], polymers [96], antibodies [97] and proteins [98] can often assist in the binding of a variety of biological ligands at the nanoparticle surface, allowing for their attachment onto the cell membrane in addition to providing more extended blood circulation times and thus a greater probability of nanoparticle interaction with the tumour/cancer site of interest. This alternative targeting strategy has resulted in the formulation of a vast library of natural product-like molecules for use in many biomedical advances.

Blood circulation times are determined by the process of opsonisation, which involves the removal of unrecognized foreign bodies from the body by the mononuclear phagocytic system (MPS) [99]. Macrophages present in the MPS, for example the macrophages of the Kupfer cells of the liver, possess the ability to remove unprotected nanoparticles and their carriers from the body within seconds of intravenous administration, rendering them ineffective in delivering therapeutics to their chosen targeted site [100].

During opsonisation, foreign objects become covered by blood serum components known as opsonins, which aid in phagocytic recognition and eventual elimination

from the body. The rate at which this occurs is dependent on the surface properties of the nanoparticles which, if engineered correctly, can sometimes even avoid elimination for long periods of time. These nanoparticles, known as 'stealth' nanoparticles, have coatings composed of polymeric ligands such as polyethylene glycol (PEG) [99] .

Studies into the dependence of surface coatings on the rate of opsonisation suggest that nanoparticles coated with hydrophilic ligands are less likely to be eliminated quickly as compared to their hydrophobic counterparts. A correlation between surface charge and opsonisation also exists [101], with research demonstrating that neutrally charged nanoparticles possessed much slower opsonisation rates than charged species, suggesting a mode of action for shielding groups such as the PEG moieties mentioned above.

Nanoparticles intended for bioapplication must also be seen to exhibit a high degree of stability under a wide range of physiological and environmental conditions (e.g. changes in temperature, pH, magnetic environment etc.). It is therefore vital that nanoparticles are coated with appropriate ligands, while maintaining a reasonably small size (<100 nm) for transport within the body's vasculature system.

While aqueous coprecipitation syntheses would be more favourable for use in biomedical application (due to their ease of scalability and non-toxic reaction conditions), the moderate size control and poor crystallinity restricts their applicability for biomedical application (MRI, hyperthermia, MDT etc.) [102]. For this reason, high temperature thermal decomposition methods for nanoparticle formation have been widely employed in a range of organic mediaThermal methods involve the decomposition of a metal precursor at high temperature in the presence of a stabilising surfactant and have been demonstrated to produce highly crystalline nanoparticles of sizes less than 20 nm (d_{PCS}) [46, 103]. In addition to this, syntheses of this type demonstrated potential for excellent size control, yielding highly monodisperse, crystalline nanoparticle dispersions of sizes tuneable from 5-12 nm which, in turn, contributes to their greater saturation magnetisation than IONP prepared by coprecipitation. One disadvantage to this method, however, is that nanoparticles formed are not dispersible in aqueous media and require subsequent phase transfer and/or ligand exchange to achieve solubility.

The literature reports a wide range of transfer agents used to facilitate this process, extending from lipid bilayers to copolymers. The work of Yu et al. [104] demonstrates the successful transfer of iron oxide nanoparticles, coated initially with oleic acid and octadecene, to aqueous solution with full stability and successful dispersion using a PEG-ylated copolymer moiety, Poly(maleic anhydride-*alt*-1-octadecene) (PMAO-PEG). The use of Pluronic F127 (PF127) has also been extensively utilised by many groups for functionalisation of oleic acid-stabilised nanoparticles that could be ultimately dispersed in water [89]. Quite often, however, addition of these ligands onto the IONP surface involve the use of bulky substituents, generating nanoparticles or nanoclusters in excess of 20-30 nm in diameter. For this reason, the use of short chain surfactants such as citric acid, as demonstrated by Sahoo [50] and DTAB, as used by Cao et al. [105] have proven to be beneficial as they can provide water dispersibility while maintaining a small ($\leq$20 nm) hydrodynamic size, providing a source of highly biocompatible functionalized nanoparticles that can be used in the delivery of many potential drugs which can also be used as effective heating sources for the hyperthermia treatment of cancer. Another important application of magnetic IONPs of this nature is as contrast agents for MRI, as the presence of nanoparticles in the contrast medium can be used for enhancement (T_1 agents) of the ^{1}H NMR signal intensity, resulting in a positive (or bright) contrast in the MRI image. This signal enhancement relies on the nanoparticles being fully dispersed in the medium, hence the need for hydrophilic ligand attachment to the IONP surface [106]. Alternatively, suspensions of clustered IONP are used as T_2 agents for signal suppression of the NMR signal.

In the work presented here, we have utilised the methods, or modifications thereof, reported by both Sahoo et. al. and Cao et. al to produce citrate-stabilised IONP (Cit-IONP) and DTAB-stabilised IONP (DTAB-IONP) respectively. Nanoparticles were synthesised with a view to their combination with n-(butyl cyanoacrylate) and poly-n-(butyl cyanoacrylate) respectively as described in Chapter 4 to follow to produce nanocomposite materials for potential MRI and/or drug delivery applications. In the case of Cit-IONP, nanoparticles were prepared as per reported in the literature. For DTAB-IONP, the ligand exchange process was followed as outlined in the literature, with nanoparticles ultimately being dispersed in aqueous medium as opposed to the reported PVP/ethylene glycol mixture.

3.2 Experimental

3.2.1 Synthesis of Citrate-stabilised Iron Oxide nanoparticles

Materials

Iron (II) chloride tetrahydrate (≥99.0%) was purchased from Fluka, Iron (III) chloride hexahydrate (puriss) was obtained from Riedel-de Haën and Citric acid (99+%) and Ammonium Hydroxide (28% NH_3 in water, ≥99.99%) were purchased from Sigma Aldrich.

Synthesis

Citrate stabilised nanoparticles were prepared by coprecipitation of iron salts using a previously published method by Sahoo et al. [50]. In a typical synthesis a mixture of $FeCl_3$**.**$6H_2O$ and $FeCl_2$**.**$4H_2O$ in a 2:1 molar ratio was added to 40 mL deoxygenated water, in a three-necked round bottomed flask. The solution was purged with nitrogen for 15 minutes before heating to 80 ˚C with stirring under a constant flow of N_2 in an oil bath. Once the solution had reached the required temperature, 5 mL of NH_4OH was introduced dropwise into the reaction vessel, resulting in the formation of a black precipitate. A further 30 minutes heating at this temperature was applied, before the addition of 2 mL of citric acid solution (2.6 M) into the nanoparticle suspension. The temperature was then raised to 95 ˚C and the suspension was maintained at this temperature with magnetic agitation for 10 min. The nanoparticle suspension was then allowed to cool and it was dialysed against deionised water in an approximate 4:1 volume ratio (H_2O: IONP suspension) for 72 hours to remove any excess unbound citric acid. Following dialysis, nanoparticle suspensions were centrifuged for 30 min at 13,200 RPM (16,100 RCF) to remove any large aggregates.

3.2.2 Phase transfer of iron oxide nanoparticles from organic to aqueous medium using Dodecyltrimethyl ammonium bromide (DTAB) as a transfer agent (Synthesis of DTAB-stabilised Iron oxide)

Materials:

Dodecyltrimethyl ammonium bromide (DTAB) (≥98 %), Iron (III) acetylacetonate (≥99.9 % trace metals basis) and Benzyl alcohol (anhydrous, 99.8 %) were purchased from Sigma Aldrich. All other reagents were used as required.

Synthesis:

Nanoparticles were synthesised using the non-hydrolytic surfactant assisted method as proposed by Pinna et. al. [55]. In a typical preparation 1.00 g of iron precursor, iron (III) acetylacetonate was placed in a three neck round-bottomed flask, followed by the addition of 20 mL benzyl alcohol. The solution was degassed using nitrogen for a period of 15 minutes, before bringing the reaction solution to reflux (195 ˚C) for a period of 7 hours. The dark brown/black suspension was then allowed to cool and stored at room temperature until further use was required.

The solids were collected by centrifugation, washed twice with acetone and redispersed in chloroform using a small amount of oleic acid (50 μL/mL IONP suspension) as a stabilising agent. Chloroform suspensions of nanoparticles were then introduced in varying ratios to aqueous solutions containing the transfer agent, DTAB using vortex mixing. Suspensions were then allowed to stir for a number of hours under a nitrogen atmosphere to evaporate the chloroform present, resulting in stable aqueous suspensions of water-dispersible nanoparticles.

3.2.3 Characterisation

Nanoparticle dispersions were primarily characterised using PCS and NMRD, as described in Chapter 2. In addition to T_1 measurements, the transverse relaxation time, T_2 was recorded for a selection of nanoparticle dispersions at a field of 9.25 MHz using the Spinmaster FFC-2000 Field Cycling NMR Relaxometer (Stelar, Italy) and at fields between 40-60 MHz using a Bruker WP80 variable field electromagnet. The

Carr-Purcell-Meiboom-Gill (CPMG) pulse sequence was used in this instance with values for number of echoes and echo delay periods varied so as to reduce the % error of all measurements. For correction of all results obtained for iron content, ICP-AES was used, as described in Chapter 2.

Visual imaging of nanoparticle dispersions was carried out using Transmission Electron Microscopy (TEM) imaging on a JEOL 2000 FX TEM scan (at an accelerating voltage of 80 kV) for samples deposited on carbon-coated (400 mesh) copper grids (courtesy of the Electron Microscopy Laboratory at University College Dublin).

3.3 Results and Discussion

3.3.1 PCS Characterisation

Illustrated below is a typical particle size distribution plot for iron oxide nanoparticles stabilised by citric acid. Typical nanoparticle hydrodynamic diameters were in the range of 13-18 nm and all dispersions were relatively monodisperse (PDI 0.15-0.2) following centrifugation and dialysis steps. Citrate stabilised nanoparticles were stable for many months following synthesis.

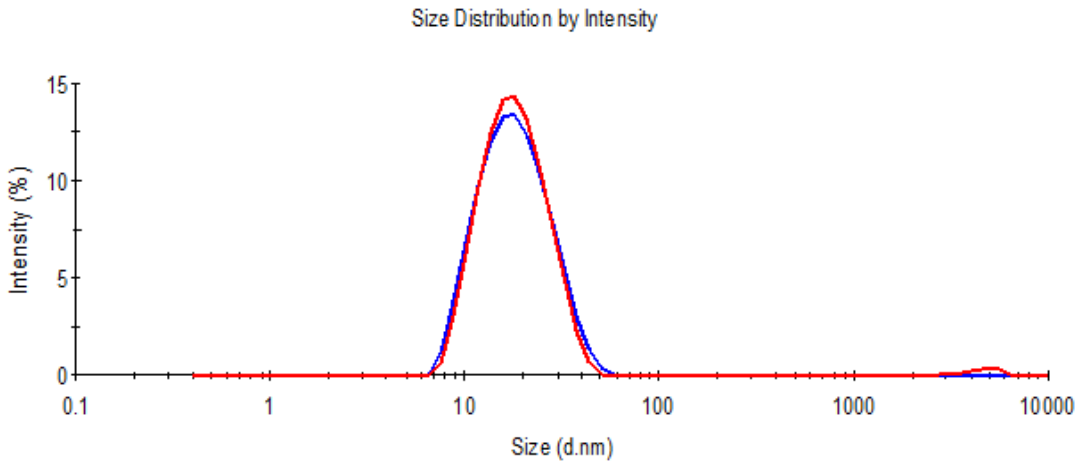

Figure 3.1: Size distribution of citrate-stabilised IONP (where citrate concentration=0.2M) (d_{hyd} 16.5 nm, PDI 0.15) (-) and a retest for stability (d_{hyd} 16.7 nm, PDI 0.14) (-)

Sample	Z-average(nm)	PDI
Cit 2	15.8	0.18
Cit 3	13.6	0.20
Cit 4	16.5	0.15
Cit 4 (+2weeks)	16.7	0.15

Table 3.1: Z-Average data (and PDI) for repeat Cit-IONP syntheses

Stability of the citrate stabilised nanoparticles was also investigated within an observed pH and dilution range (See section 3.3.7 below).

The size distribution plots shown below in Figure 3.2 are of iron oxide nanoparticles pre- and post-transfer using Dodecyltrimethyl ammonium bromide (DTAB) as a transfer agent (DTAB-IONP). It is interesting to observe that the hydrodynamic size distributions are almost unchanged following transfer from organic to aqueous medium. An increase in polydispersity was observed in some cases, however, with a small peak often presenting itself at the higher end of the distribution plot (omitted in Figure 3.2 below), which was difficult to remove by washing and/or centrifugation. This may be explained by the presence of excess transfer agent in the resulting dispersion, or slight aggregation of particles that were insufficiently coated (most likely the former). Nanoparticle sizes were generally reproducible across a range of syntheses, once the DTAB: Fe mole ratio was kept at 1:1 and suspensions were seen to remain stable over a period of weeks.

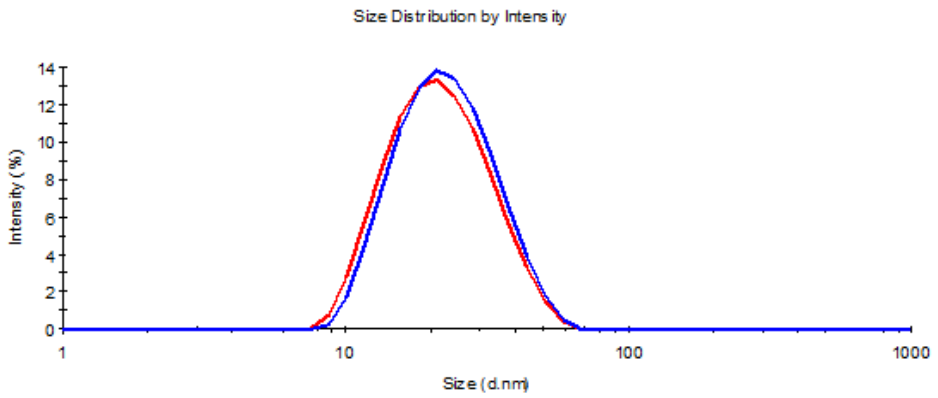

Figure 3.2: Size distributions of Pinna IONP pre-transfer (d_{hyd}, 20.4 nm PDI 0.18) (-) and post-transfer (d_{hyd}, 22.1 nm, PDI 0.11) (-)

3.3.2 Effect of reaction conditions on primary nanoparticle size

It was observed for both the synthesis of citrate- and DTAB-stabilised iron oxide nanoparticles that moderate size control could be achieved on varying specific parameters throughout their synthesis. For citrate-stabilised IONP, nanoparticles of d_{hyd} 13-18 nm (d_{TEM} 10-13 nm) were prepared by ensuring that a sufficient concentration of surfactant (citric acid) was present throughout the synthesis and that dialysis and centrifugation was used following synthesis to remove any excess starting materials and large aggregates. For DTAB-stabilised IONP, good size control was facilitated by the use of a 1:1 ratio for the concentration of both the IONP and the transfer agent (DTAB) in the phase transfer medium, with typical sizes in the range of 18-22 nm (d_{PCS}) and 10-12 nm (d_{TEM}).

In the absence of surfactant molecules, nanoparticles are generally unstable and naturally form large aggregates or 'clusters' to reduce their surface free energy [107]. Inclusion of surfactant molecules during the synthesis of individual nanoparticles is therefore crucial if stable monodisperse suspensions of fully dispersed nanoparticles are to be achieved. The literature demonstrates a wide variety of uses of surfactant molecules, the choice of which depends on the envisaged properties of the nanoparticles and the medium in which they are to be dispersed. Oleic acid, for example is a commonly used surfactant for dispersion of iron oxide nanoparticles in non-aqueous media [46], whereas surfactants such as citric acid and Dodecyltrimethyl ammonium Bromide (DTAB) are often attached to the surface of nanoparticles to promote water dispersibility [50, 105].

The method of synthesis employed can also have a large impact on the size of the particles produced and the degree to which these sizes can be controlled. It has been extensively reported in the literature that moderate size control can be achieved for iron oxide nanoparticles prepared by the coprecipitation of iron salts in aqueous medium. Size control is typically dependent on factors such as the nature of the Fe salts used (chlorides, sulphates etc), the mole ratio (e.g. for Fe_3O_4 a ratio of 2:1 Fe^{3+} to Fe^{2+} is used), the pH and ionic strength of the medium, the presence of surfactants on the nanoparticle surface and the reaction temperature, with typical nanoparticle core sizes ranging from 3 to 20 nm (d_{TEM}) depending on the reactions conditions used during the synthesis [102].

For preparation of Fe_3O_4 nanoparticles coated with citrate, it appears that the citrate concentration used in the IONP synthesis plays an important role in determining the resulting hydrodynamic size of the nanoparticles produced. For citrate-stabilised nanoparticles synthesised for the purpose of this thesis, for example, it was found that at citrate concentrations of less than 0.2 M or in excess of 0.35 M produced nanoparticle dispersions of large hydrodynamic sizes, with efforts to centrifuge, precipitate or sonicate to recover nanoparticles of smaller sizes proving unsuccessful. At concentrations of approximately 0.2 M, however, success was demonstrated in preparing dispersed nanoparticles of approximately 20 nm (d_{PCS}), with reproducibility.

In a similar study, the work of Bee et al. [108] reports a relationship between concentration and core size control through XRD and TEM, where a noted decrease in crystallite size from 8.2 nm to 2.3 nm was observed with increased concentration of citric acid added during nanoparticle synthesis. It should be noted that, although the nanoparticles were claimed to be dispersed in aqueous medium, particle size analyses were only obtained with the particles in a dried state (i.e. no PCS analyses in their 'dispersed' state). This size dependence may be attributed to either the enhancement of the nucleation rate and/or suppression of the growth during nanoparticle synthesis.

Studies into the use of NaCl for similar size control of IONP have been also reported in the literature, in addition to those previously carried out in our group. Qiu et. al., for example, reported a reduction in size of ~1.5 nm (calculated by TEM) for IONP prepared in the presence of NaCl than those prepared at lower ionic strength (i.e. in the absence of NaCl) [109]. It can also be noted that a decrease in saturation magnetisation on increasing the ionic strength of the IONP medium was observed.

As mentioned previously in this chapter, nanoparticles synthesised via thermal decomposition methods are typically more favoured over those prepared by aqueous coprecipitation due to their much improved physical and chemical properties [110]. Nanoparticles prepared via these methods, however, require subsequent phase transfer for their dispersion into aqueous media. It is therefore vital that further steps are taken to ensure size and monodispersity are maintained on transfer, i.e. that no aggregation occurs during the transfer process. In addition to this the ligands, usually oleate/oleylamine, are chemisorbed onto the surface of the IONP and are difficult to

replace. Hence it is difficult to generate stable aqueous suspensions following phase transfer using ligand exchange.

Phase transfer of Pinna-IONP to aqueous medium was achieved using dodecyltrimethylammonium bromide (DTAB). Prior to this, the temporary ligand (benzyl alcohol) of the prepared Pinna-IONP was replaced by a subsequent surfactant, oleic acid, ahead of the phase transfer process. DTAB-IONP formation was then driven by hydrophobic van der Waals interactions between the hydrocarbon chain of the IONP ligand (i.e. oleic acid) and the hydrocarbon chain of the surfactant (i.e. DTAB), encapsulating the IONP and allowing for dispersion in aqueous media. This can essentially be summarised as a ligand exchange process between the benzyl alcohol and oleic acid followed by encapsulation by the DTAB moiety. This method of DTAB-IONP formation was similar to that reported by Cao et. al., where a similar phase transfer process was carried out in order to disperse what they described as 'colloidal super-particles' of approximately 190 nm ± 28 nm (d_{TEM}) in a PVP/ethylene glycol medium [111] .

The advantage of the simultaneous phase transfer/encapsulation method mentioned above is that the solvent acts as a **temporary ligand only** during nanoparticle synthesis, and provides a single-step ligand exchange process for IONP dispersion in aqueous media. The result is a relatively stable aqueous suspension of IONP with high relaxivity and a surface charge that allows for their electrostatic assembly with oppositely charged surfaces/particles for potential application in drug delivery.

The mole ratio of transfer agent (DTAB) to iron oxide was found to have a drastic effect on the outcome of the transfer process, and much time was taken to achieve an optimum concentration of both species during the process. The initial concentration of the IONP pre-transfer was also important in achieving successful phase transfer, with concentrations of approximately 15-20 mg/mL necessary for the reaction to produce good dispersions, i.e. suspensions of individual nanoparticles of small hydrodynamic size with good PDI.

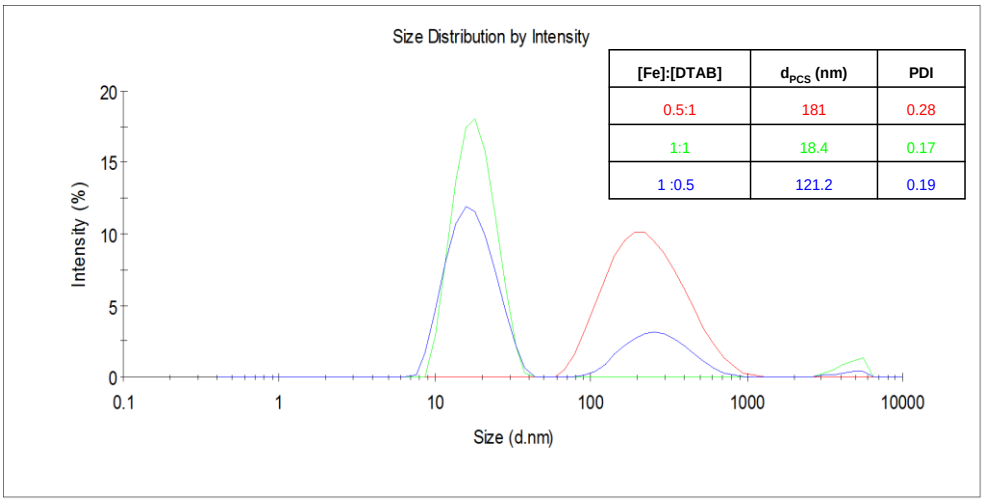

Figure 3.3: PCS size distribution data for different ratios of [Fe]: [DTAB] investigated for phase transfer. The colour-coding in the table to right of graph is representative to that in the size distribution plot.

Figure 3.3 above illustrates the PCS hydrodynamic size distributions for three subsequent experiments with varied ratios of [Fe]: [DTAB] used during the phase-transfer process. It is clear from this result that a 1:1 ratio was the most optimum for the reaction, as d_{hyd} remained small in size and nanoparticles were most monodisperse. This ratio corresponded to approximately 1500 DTAB ligands per IONP present in the suspension, which meant that the DTAB was in great excess and ensured that all IONP were thoroughly coated following phase transfer. Given that the surface area of a typical DTAB-IONP is 6.2×10^{-16} m^2, and assuming that each DTAB goes onto the second layer, this is equivalent to a DTAB a footprint of 4.1×10^{-19} m^2, which is approximately 1.1 times that of oleic acid (with a footprint of 3.8×10^{-19} m^2) [112]. This strongly suggests that a full DTAB monolayer, but no more, is required for IONP stabilisation.

On observing the hydrodynamic diameters of both nanoparticle types over a period of weeks and, in some cases, months, it was noted that nanoparticles stabilised by citrate ligands were significantly more stable than those stabilised by DTAB (Figure 3.4). Citrate-IONP maintained hydrodynamic diameters identical to, or in close agreement with, the primary particle sizes measured initially following synthesis whilst maintaining good PDI values after periods of up to 9 to 12 months, where the DTAB-IONP were seen to increase in both size and polydispersity within a number of days or weeks. This may be due to the fact that the DTAB encapsulates the particle by

physisorption as opposed to the citrate ligands that were more strongly chemisorbed onto the nanoparticle surface.

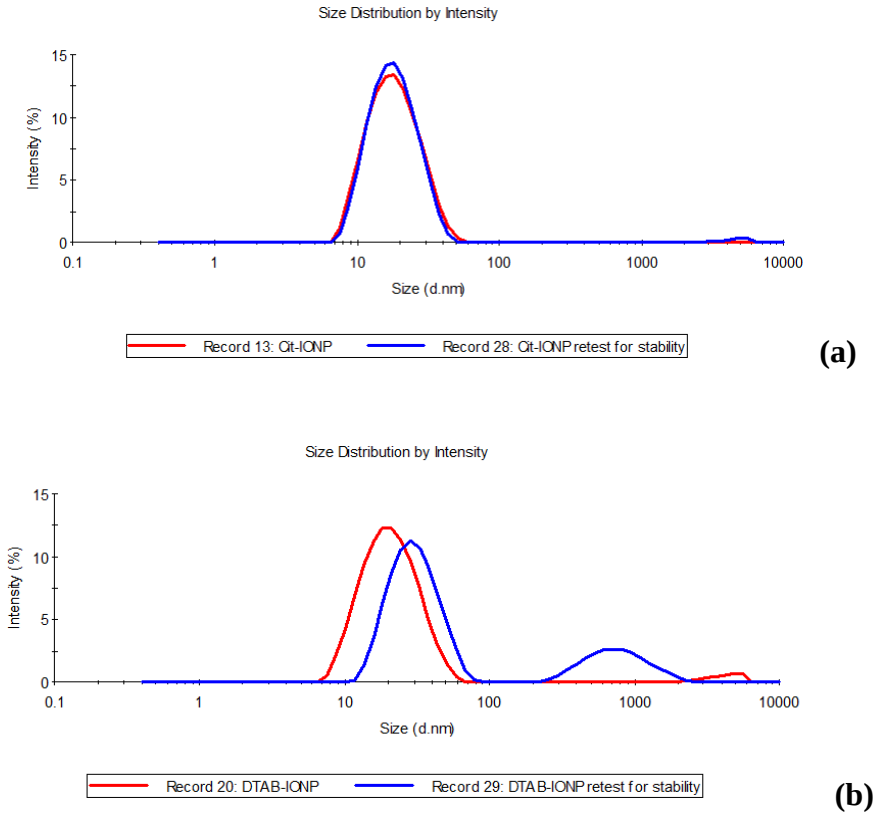

Figure 3.4: PCS analyses of stability of (a) Cit-IONP over a period of 1 month and (b) DTAB-IONP over a period of 3 days

On subjecting both nanoparticle types to magnetic filtration at fields of 1.0-1.5 T, it was observed that the resulting retentate of any given Cit-IONP suspension demonstrated very similar hydrodynamic sizes to the same suspension prior to filtration. This was not the case for DTAB-IONP suspensions, which demonstrated signs of aggregation on exposure to the magnet. This observation may be due to partial loss of the physisorbed DTAB layer on the surface of the IONP.

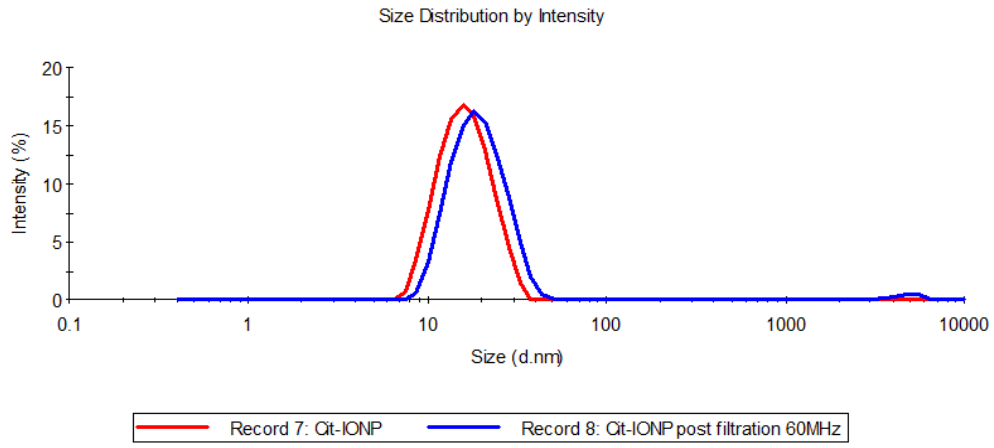

(a)

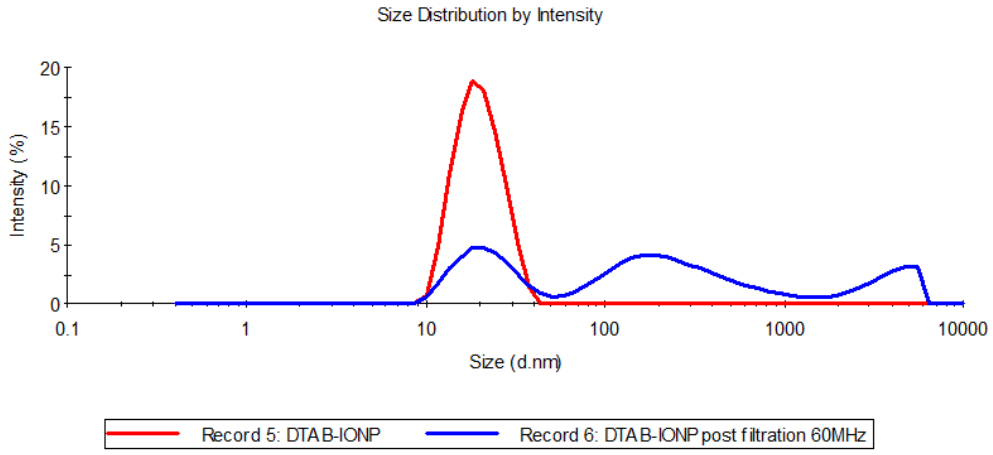

(b)

Figure 3.5: PCS analyses of (a) Cit-IONP and (b) DTAB-IONP pre- and post magnetic filtration at 1.5 T

3.3.3 Zeta Potential

Iron oxide nanoparticles stabilised by citrate ligands exhibited a negative surface charge, typically in the range of -25 to -56 mV. Their negative charge is consistent with the long-term stability of the nanoparticles in solution, as it is generally found that particles that possess a surface charge in excess of ±30 mV will exhibit relatively good (if not excellent) stability in aqueous solution. It was found that zeta phase plots were of good quality for nanoparticle dispersions as presented in Figure 3.6 (inset).

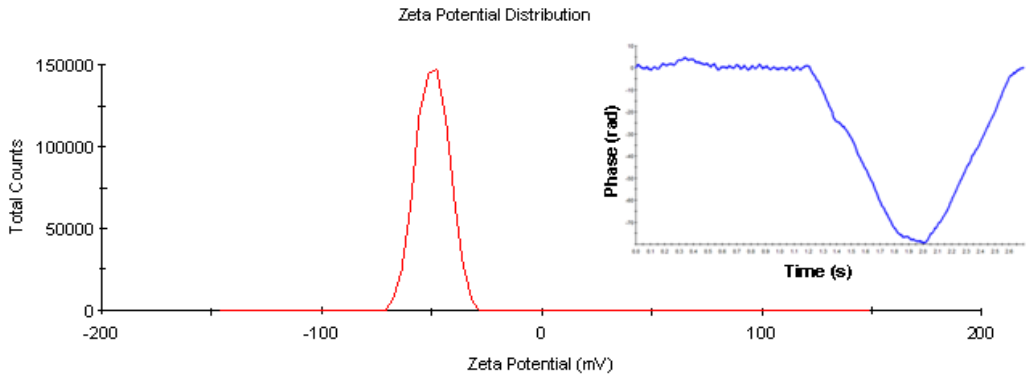

Figure 3.6: Zeta potential distribution and phase plot (inset) of citrate IONP (Zeta Potential -46mV for above sample) at pH 6.7

In contrast to the citrate-stabilised iron oxide nanoparticles presented previously, nanoparticles stabilised using DTAB as a stabilising ligand exhibit a positive Zeta Potential, and values measured were typically in the range of +30 to +40 mV. Phase plots obtained were characteristic of positively charged nanoparticles (inverted phase as compared to the negatively charged citrate IONP) and were observed to demonstrate good shape (see phase plot (inset),Figure 3.7).

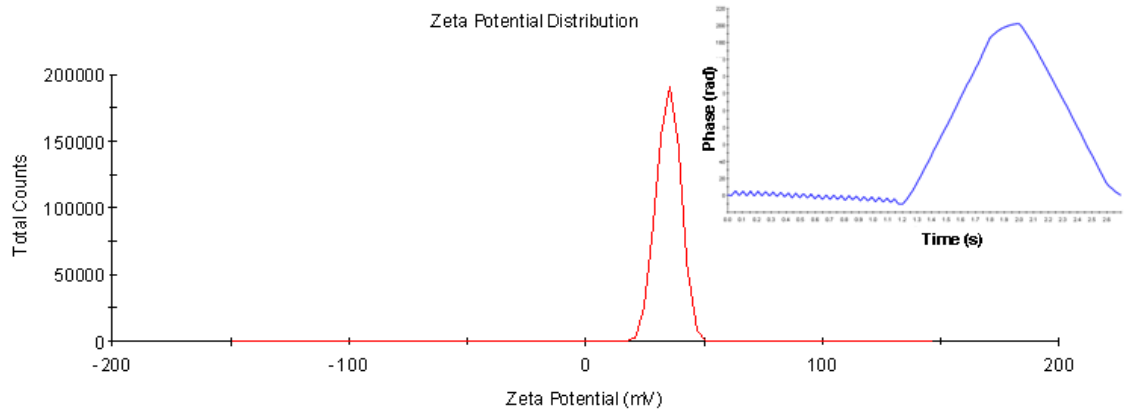

Figure 3.7: Zeta Potential distribution and Phase Plot (inset) of DTAB-stabilised IONP (for a Zeta Potential of ~ +35mV at pH 7

3.3.4 Effect of surfactant choice on the surface properties of nanoparticles (Zeta Potential)

Cit-IONP were found to exhibit a negative surface charge due to the presence of non-ligating carboxylate functionalities on the surface bound ligands. As stated previously,

Zeta Potential measurements for citrate-IONP varied between -25 mV at pH 3 to -56 mV at pH 9 and were highly stable for long periods due to the strong negative charge. Note that the pK_a values for citric acid are approximately 3.1, 4.8 and 6.4 [113]. In contrast to this, DTAB-IONP were found to be of opposite charge, with values in the region of +10 mV at pH 3 to +35mV at pH 7. This arises due to the positive charge on the quaternary nitrogen of the surfactant species arising from the pendant ammonium groups at neutral pH (pH7).

On analysis of the phase plots for both nanoparticle species synthesised (Figure 3.8 below), it is evident that nanoparticles of opposite charge produce phase diagrams of opposite frequency (or Doppler) shift, depending on their surface charge. This shift originates when the mobility of the nanoparticles in solution produce a characteristic shift away from that of a modulated, or reference, frequency (of the incident and reference beams) of 320 Hz. Positively charged nanoparticles possess beat frequencies in excess of this value, and thus generate an upward shift from the reference frequency. Alternatively, negatively charged nanoparticles will cause a shift in the opposite direction, causing a downward 'dip' in the phase plot diagram.

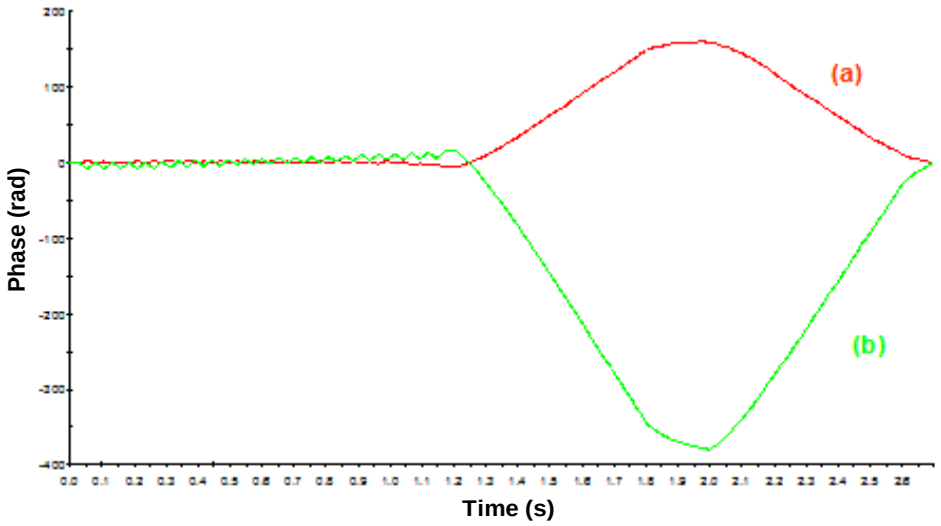

Figure 3.8: Typical Phase plots of (a) positively-charged IONP (in this case DTAB-IONP) and (b) negatively charged nanoparticles (citrate-IONP) measured at pH~7

Apart from providing stability of nanoparticles in their dispersing solvent, surfactants are also a key aspect for functionalisation of the nanoparticles. For instance they can provide a location for ionic or covalent bonding of other functionalities [114]. They may also prove disadvantageous, however, as they may block the nanoparticle surface and/or reduce the interaction of the water with the moment of the particle.

3.3.5 Effect of pH on nanoparticle size and surface charge

The pH of small aliquots of Cit-IONP was adjusted in the range of 3-9 using 1M NaCl or 1M NaOH, and individual samples were analysed for their changes in d_{hyd}, PDI and their relative surface charge (Zeta Potential). The natural pH of Cit-IONP suspensions in the mM Fe range was found to be ~pH 6.7. Hydrodynamic sizes remained relatively stable (16-19 nm in diameter) over the pH range 3-7, beyond which the size and polydispersity were seen to increase as illustrated by Figure 3.9 below, due to particle aggregation at pH values of ~8 and above. Zeta Potential values were seen to increase in negativity on increasing pH as expected, and varied between -20 and -60 mV, illustrating good to excellent nanoparticle stability within the medium. It was not possible to identify the isoelectric point in the accessible pH range.

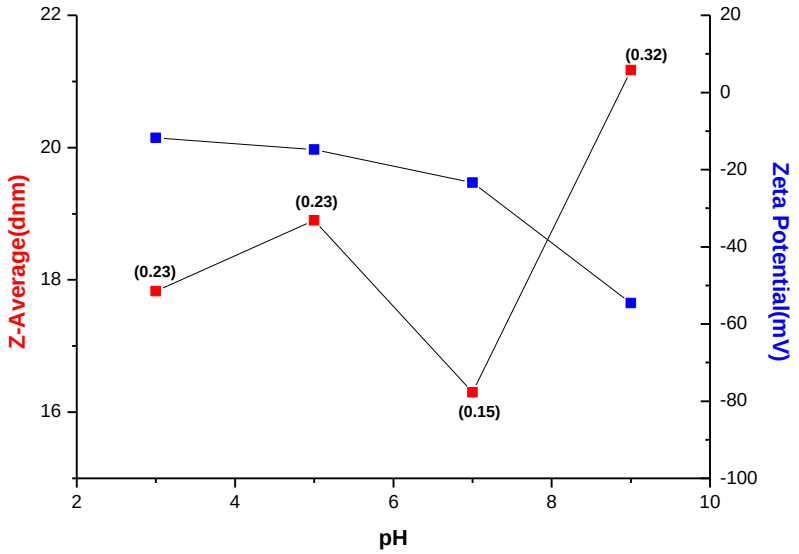

Figure 3.9: Size and Zeta Potential data as a function of pH for citrate-IONP

A similar series of experiments was carried out for a suspension of DTAB-stabilised IONP within the pH range of 3-11. In this instance, hydrodynamic sizes were seen to be very unstable above pH 7, where noticeable aggregation was observed from both the Z-Average and PDI values. Due to this, Zeta Potential values at higher pH values could not be taken to be accurate and, in contrast with citrated-IONP suspensions, those at lower pH values were not seen to demonstrate a proportional change in surface charge.

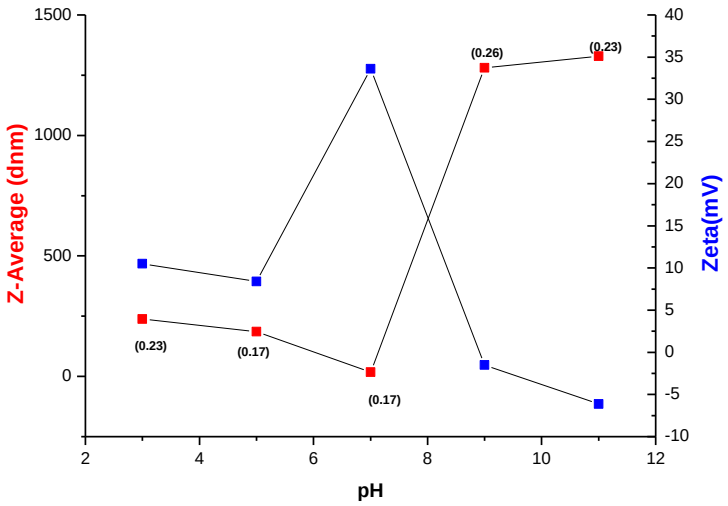

Figure 3.10: Size and Zeta Potential data as a function of pH for DTAB-IONP

This observed instability of the DTAB-IONP may be explained by the fact that the encapsulating ligand in this instance is not chemisorbed to the surface of the IONP as is the case for Cit-IONP but is more weakly physisorbed and therefore is more prone to desorption or displacement from the IONP surface on changing pH.

3.3.6 NMRD analysis

The NMRD profiles below are representative of two subsequent syntheses of citrate-stabilised iron oxide nanoparticles. Both profiles appear similar in shape, thus implying that they are reasonably reproducible in their measurement (within ~20% in the case of Figure 3.11 below), and that the properties of the nanoparticles produced by both syntheses were similar.

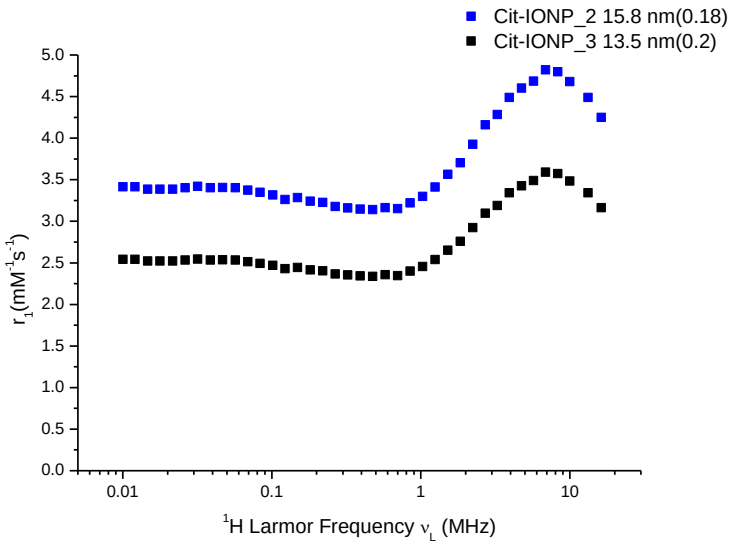

Figure 3.11: NMRD profiles of two separate citrate IONP syntheses

The shape of the profiles shown is typical of superparamagnetic nanoparticle behaviour, in particular the maximum at a high frequency confirms the presence of small nanoparticles in the dispersion. The magnetisation of the nanoparticles was also apparently quite low, with an r_1 plateau located at approximately 2.2-3.5 $mM^{-1}s^{-1}$. This observation is quite common in nanoparticles prepared by coprecipitation methods and suggests moderate crystallinity. This may be attributed to the rapidity and reduced control over nucleation and growth during IONP formation by coprecipitation methods as compared to those involving thermal decomposition.

As in the case of the citrate nanoparticle NMRD profiles presented previously (Figure 3.11), the shape of the profile for DTAB-IONP is typical of superparamagnetic nanoparticles in suspension (Figure 3.12). The maximum at a high frequency confirms the presence of small nanoparticles in the dispersion. However, the relaxivity of the DTAB-stabilised nanoparticles was found to be far greater, most probably due to their increased magnetisation.

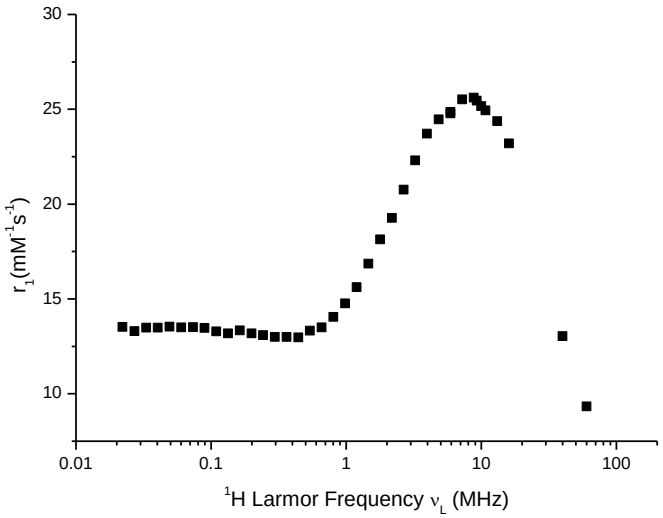

Figure 3.12: NMRD profile of DTAB-stabilised IONP (d_{hyd} 22.1nm, PDI 0.11)

T_2 measurements were made for both nanoparticle types at a field of 9.25 MHz and their relative r_2/r_1 ratios were calculated (Table 3.2). According to SPM theory, this ratio is predicted to increase with both an increase in the magnetisation of the entire particle and the particle size [70], which would account for the higher relaxivity ratio observed for the DTAB-IONP in comparison to that for Cit-IONP.

Sample	r_1	r_2	ratio
	$mM^{-1}s^{-1}$		
Cit-IONP	4.55E+01	7.32E+01	1.61
DTAB-IONP	4.61E+01	7.61E+01	1.83

Table 3.2: Relaxivity data and r_2/r_1 ratios for Cit-IONP and DTAB-IONP at 9.25 MHz

3.3.7 Effect of preparation method on the physical properties of the suspensions

The results presented here show that the synthetic method chosen for nanoparticle formation can have a significant effect on other properties of the nanoparticles. In our case we monitor the nanoparticles' magnetic properties through their effect on the ^1H spin-lattice relaxation times of the solvating H_2O molecules, which in effect act as a local reporter of the magnetic properties of the particles. The NMRD profiles presented previously are a clear demonstration of the difference in magnetic properties

between the nanoparticle types (see Figures 3.11 and 3.12). For example, the suspensions prepared by thermal decomposition (Pinna method) exhibit a much higher relaxivity than those prepared by aqueous co-precipitation (citrate stabilisation). This underlying cause can be studied using SPM theory [70], to simulate relaxivity profiles for comparison with experiment.

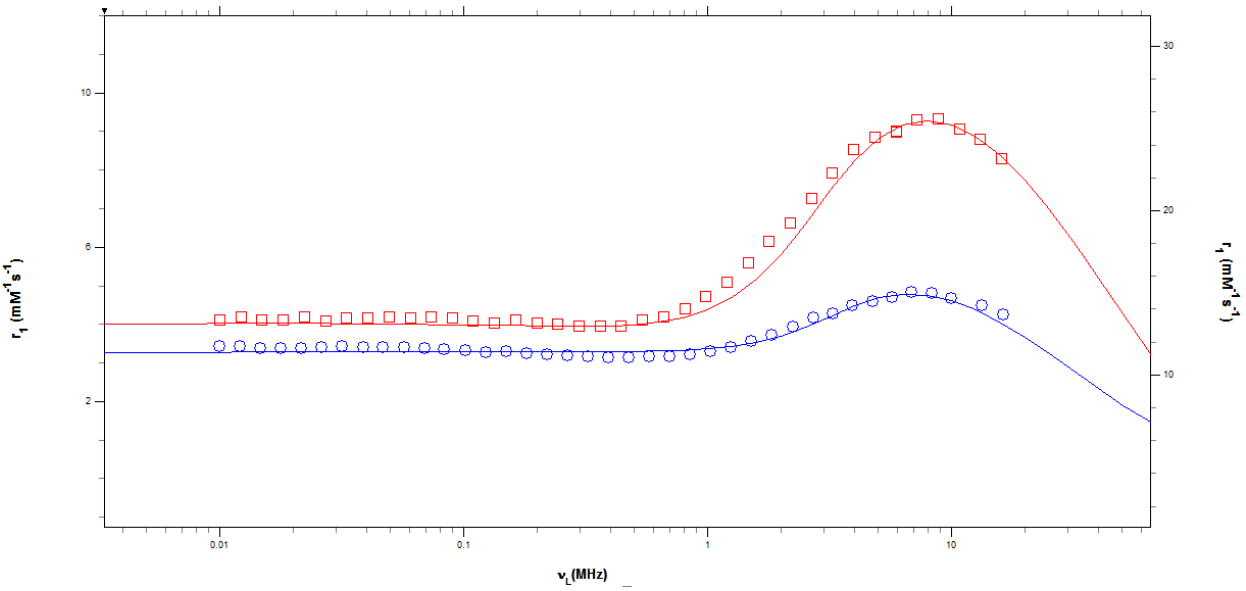

Figure 3.13: NMRD profiles of Cit-IONP (○) and DTAB-IONP(□) and their SPM simulations included as solid lines. Calculated SPM parameters are listed in Table 3.3 below

SPM simulations of the NMRD profiles for both citrate-IONP and DTAB-IONP were generated and are as outlined in Figure 3.13 (above). From these simulations, values for the estimated core size, saturation magnetisation, anisotropy energy and Néel Correlation time were extracted. These parameters, in addition to values for the estimated nanoparticle core diameters by PCS and TEM and the frequency of the r_1 maximum from NMRD, are given in Table 3.3.

	NP Type	
	Citrate-IONP	DTAB-IONP
d_{PCS} (nm)	13-18	18-22
d_{TEM} (nm)	10-13	10-12
d_{SPM} (nm)	11.6	10.4
ν_{max} (MHz)	7.8	8.2
Ms (emu/g)	17	48
ΔE (GHz)	3	2.5
τ_N (ns)	28	10

Table 3.3: Values of all estimated SPM parameters, in addition to further parameters determined by PCS, TEM and NMRD analyses.

Analysis of Table 3.3 shows that the core size estimated by SPM theory is in close agreement with that measured by TEM analyses, suggesting that for both nanoparticle types, the water diffuses all the way to the core through the surface ligands, which is somewhat surprising. It has been found in the literature that SPM theory can overestimate particle size by 20 %. [68, 72], which is contrary to our findings.

For both nanoparticle types, the primary particle size is very similar. For DTAB-IONP, d_{PCS} is slightly higher which could be consistent with some minor aggregation, possibly during the ligand exchange process. The ν_{max} values are very similar and as a result the extracted d_{SPM} values are also almost the same. This confirms that the NMR response is dictated in this case by the primary particle size. The relaxivity ratios are also very similar (as shown in Table 3.2). Taken together, these results strongly suggest that there is no appreciable aggregation for DTAB-IONP and the increased d_{PCS} is due to the thicker ligand shell.

SPM theory also provides an estimation of saturation magnetisation (Ms) values for fully dispersed nanoparticles [72]. It is clear from the fits and the table outlined above that the saturation magnetisation of the DTAB-IONP prepared by the Pinna decomposition method is much higher than that obtained for citrate-IONP prepared by coprecipitation. This may be explained by the fact that nanoparticles prepared by the Pinna method are of higher crystallinity due to extended particle annealing at elevated temp [55]. Confirmation of these findings, however, would require SQUID magnetometry analyses which were unfortunately unavailable to us. Finally, the anisotropy energies are low, as expected for superparamagnetic suspensions, values

for ΔE_{anis} of 2.5-3 GHz are as expected for individual particles of this size. Note that an energy barrier of 1 GHz is equivalent to ~6 k_BT, at 298 K [103].

Further work could include the possible attachment of citrate ligands to nanoparticles prepared by the Pinna decomposition method, as the high magnetic properties combined with the long-term stability provided by the citrate ligand would produce a very interesting nanoparticulate system for potential biomedical applications. It will also provide a direct comparison to assess the effect of preparation method on the NMR properties.

3.3.8 Effect of change in viscosity on Cit-IONP suspensions

Table 3.4 (below) illustrates a series of additions of 1M sucrose solution to an aqueous dispersion of Cit-IONP. Small aliquots were introduced into the nanoparticle dispersion in 0.5-1 mL increments, and the corresponding viscosities were measured at on a A&D SV-10 Vibro Viscometer (Japan) supplied by Particular Sciences (Dublin, Ireland). Temperature control was achieved using a water bath maintained at 25°C using a Yellow Line MSC ceramic top hotplate stirrer (Lennox Laboratories, Dublin).

Total vol sucrose soln(1M) added (mL)	Total moles sucrose (moles)	[sucrose] [M]	Viscosity (mPa.s@25oC)
0 (neat citrate IONP)	0	0	0.95
0.5	0.005	0.016	0.97
1.5	0.0015	0.016	1.05
2	0.002	0.017	1.06
3	0.003	0.018	1.26
4.5	0.0045	0.019	1.2
6.5	0.0065	0.02	1.75
8	0.008	0.023	2.04

Table 3.4: Sucrose addition data for citrate-IONP viscosity studies

Experimental viscosities were found to increase with sugar concentration, as expected. PCS measurements were taken for a small selection of the samples obtained in an attempt to determine the effect of sucrose addition on the hydrodynamic diameter and the PDI of the nanoparticles in suspension on changing the viscosity of the medium under the assumption that there is no aggregation.

When the value for the viscosity of water was used for the PCS analysis, nanoparticle diameters appeared to increase on increasing the sucrose concentration within the

nanoparticle medium from 18 nm (primary NP size), to 22 nm and 25 nm for suspensions η=1.5 and η=1.8 respectively as expected. In addition to this, the PDI appeared to increase from 0.15 to 0.25 over the course of the sucrose addition, suggesting that aggregation may have occurred in the latter samples. On scaling the correlograms for each of the three samples seen in Figure 3.14 below, it is evident that the slope of the distribution becomes more gradual, indicating a slight increase in the hydrodynamic diameter of the particles present.

On using the actual measured viscosities for both modified suspensions, a decrease in nanoparticle diameter was observed on increasing the viscosity, with calculated diameters of 15 nm and 12 nm for suspensions of η=1.5 and η=1.8 respectively (with primary nanoparticle sizes equal to 18 nm in diameter prior to sucrose addition).

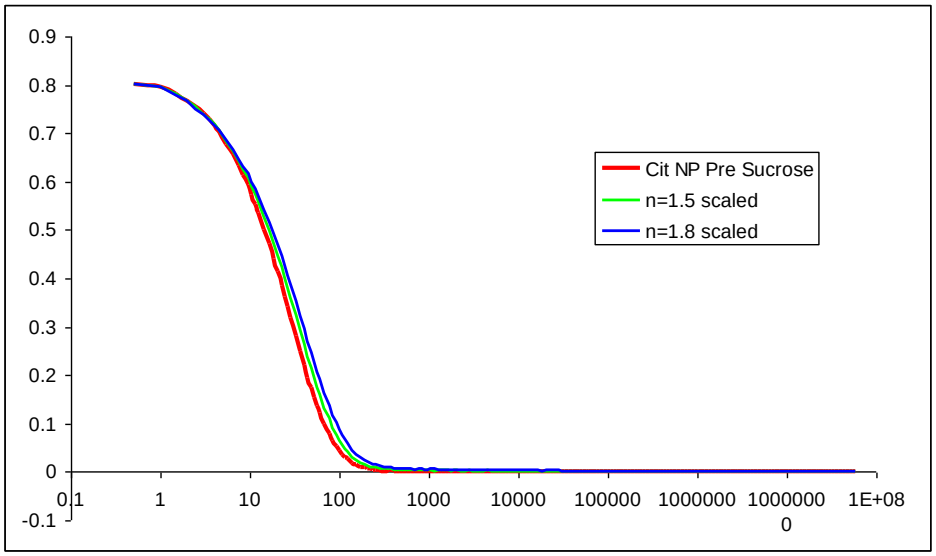

Figure 3.14: Overplot and scaling of PCS correlograms for samples pre-sucrose addition and for samples of η=1.5 mPa.s^{-1} and η=1.8 mPa.s^{-1}

In a second experiment, two citrate nanoparticle dispersions were modified by addition of sucrose to yield solutions of different viscosity and their NMRD profiles were recorded (Figure 3.15). The observed result was a significant increase in the relaxivity (r_1) on increasing the overall viscosity of the nanoparticle medium.

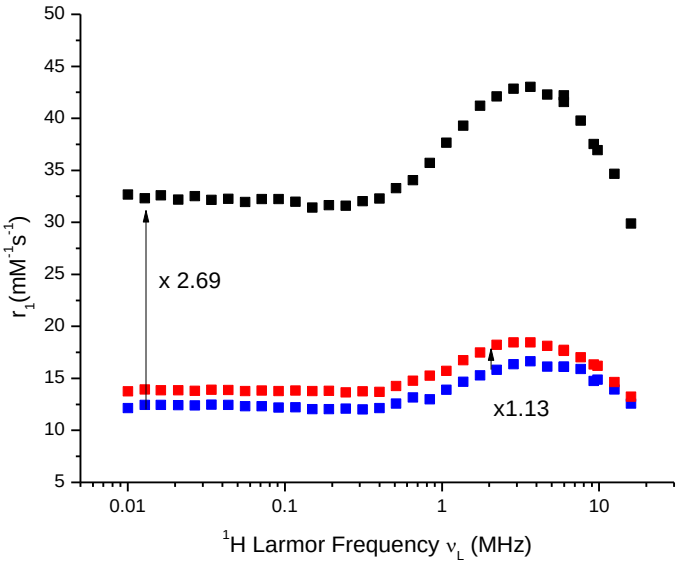

Figure 3.15: NMRD profiles of sucrose addition experiments to Cit-IONP where η = 0.99 mPa.s^{-1} (i.e pre addition) (■),η = 1.5 mPa.s^{-1} (■) and η = 1.8 mPa.s^{-1} (■)

Sample	r1(mM-1s-1)	r2	r2/r1ratio
Pre sucrose	14.74416	2.90E+01	1.97E+00
Viscosity=1.5	16.32547	3.46E+01	2.12E+00
Viscosity=1.8	37.52319	82.17247	2.19E+00

Table 3.5: NMRD data at 9.25 MHz for Cit-IONP and η=1.5 and η=1.8 suspensions

A slight shift of the r_1 maximum to lower frequency on increasing the viscosity was also observed. This is more apparent on scaling the r_1 values (Figure 3.16). That shift is consistent with a slight increase in nanoparticle size. The strong increase in r_1 is difficult to explain. However, PDI values were also seen to increase, suggesting some possible particle aggregation. In addition to this, the r_2/r_1 ratios demonstrated a slight increase (Table 3.5).

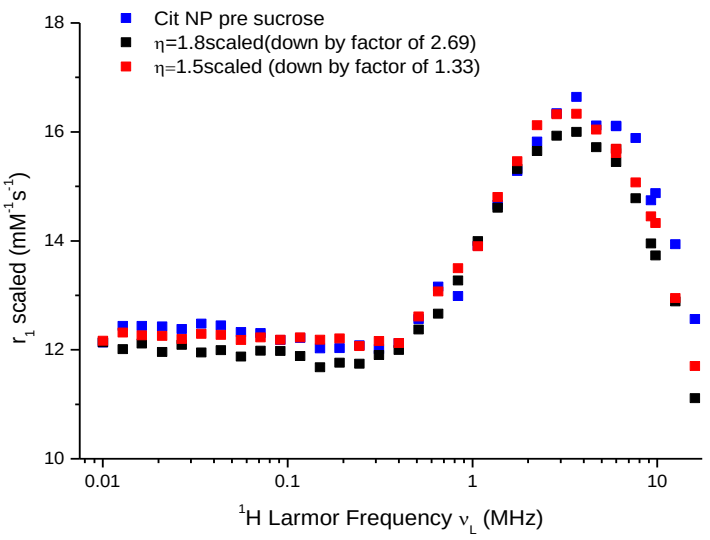

Figure 3.16: Overplot and scaling of cit-IONP/sucrose sample NMRD profiles

The literature presents a number of studies on the effect of sucrose addition on water mobility in aqueous suspensions. In one particular paper by Padua and Schmidt [115], an increase in the relaxation rate of the protons in pure H_2O was observed on increasing the concentration of sucrose within an aqueous medium and was attributed to the increase in viscosity effects as a result. The rotational mobility of the water molecules in the medium was seen to decrease on introduction of the sugar molecules. The conclusions drawn were that the concentration of free water had become depleted and became associated with the added sucrose and that small clusters of sugar molecules had formed which moved at a much slower rotational rate than their individual counterparts. Note that this observation was made for aqueous sugar, solutions containing no nanoparticles, in the range of 0.5-2.0 g sucrose/g of water. For nanoparticle suspensions presented in this work, the concentration range was much lower at 0.1-0.2 g sucrose/g of water. Despite this fact, the experiments demonstrate that the effect of adding sucrose does not change the bulk water relaxation, but rather the relaxivity of the IONP. This may be explained by one of two possibilities; either the sucrose alters the viscosity of the bulk sample, or the rate of exchange with the citrated IONP surface.

SPM theory was then used to investigate whether the change in the profile on adding sugar to the suspension could be due to changes in the diffusion coefficient of water. The fractional changes in the viscosity required to reproduce the primary nanoparticle size in PCS measurements were used to scale the diffusion coefficients in the SPM

simulations. For the 0.016 M sucrose sample (η = 1.5) for example, a 7% increase in η was required so that the D_{SPM} value was scaled by 1/1.07. Similarly, for the 0.02 M sucrose sample (η = 1.8), a 18% increase in η was required to scale the D_{SPM} value by 1/1.18.

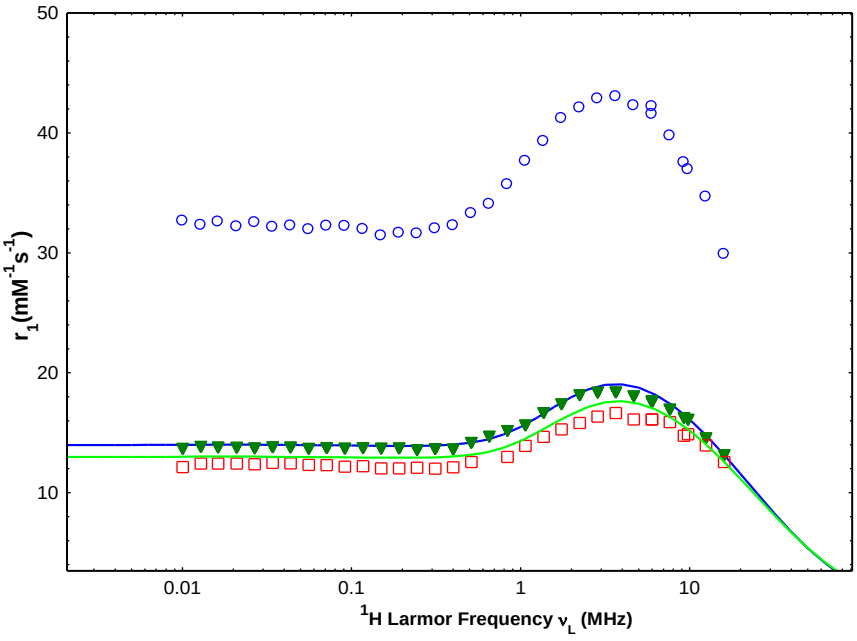

Figure 3.17: NMRD profiles for Cit-IONP (□) and Cit-IONP of modified viscosities of η=1.5 (▼) and η=1.8 (○) and SPM simulations as indicated by the solid lines for a decrease of 7 %(-) and 18 % (-) in D_{SPM} in an effort to match the observed change in the NMRD response (r_1 profiles) for the modified suspensions.

It is apparent from the plot illustrated in Figure 3.17, that the appropriate modification of the diffusion coefficients in the SPM simulations (D_{SPM}) in line with the expectations of Figure 3.15 was insufficient to reproduce the observed changes. This suggests that bulk viscosity changes are not the cause of the increase in r_1 for this experiment.

Cit-IONP suspension were then modified with respect to their pH over the range in which the nanoparticles were seen to be stable (i.e. pH 3-8) and the results are as presented in Figure 3.18.

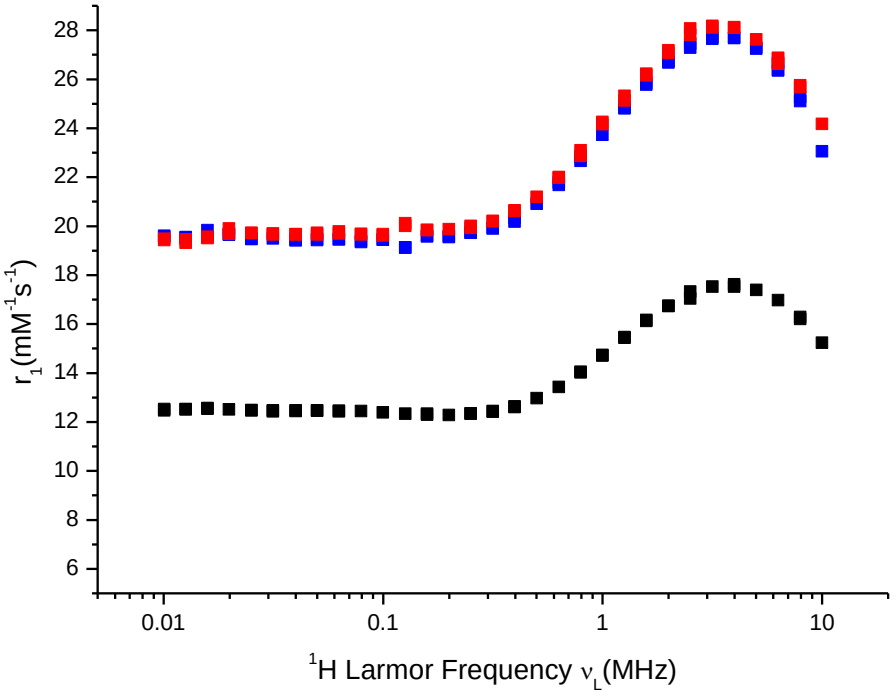

Figure 3.18: NMRD data for Cit-IONP suspensions at pH 3(■), pH7(■) and pH 8/9 (■)

It can be observed that, on modifying the pH of the suspension in either direction from its natural value, we see a noticeable increase in the r_1 of the nanoparticles. It therefore seems that, on altering the pH of the suspension or adding sucrose, the contact times in the vicinity of the nanoparticles are altered and a change in the environment about the IONP is sensed by the protons of the diffusing water.

3.3.9 TEM imaging

TEM analysis was also used to provide visual and structural information of nanoparticles in suspension. From measurement of particle size by TEM, we can observe that d_{TEM} values are systematically lower than those obtained by PCS. This is due to the fact that PCS provides the total hydrodynamic diameter of the particles (i.e. the core particle plus any added surfactant), whereas TEM estimates the size of the core nanoparticle only. The discrepancy in both cases between d_{PCS} and d_{TEM} can be explained by the presence of surfactants on the surface of the nanoparticle.

For Cit-IONP, the ~3 nm discrepancy between the TEM diameter (11.66 ± 1.5 nm) and the PCS diameter (13-18 nm) can be explained by the presence of the citrate

ligand attached to the surface (in agreement with citrate-stabilised VSOP-C184 nanoparticles that have been reported to possess a d_{TEM} of 4 nm and a d_{hyd} of 7.0 ± 0.15 nm) [102, 116].

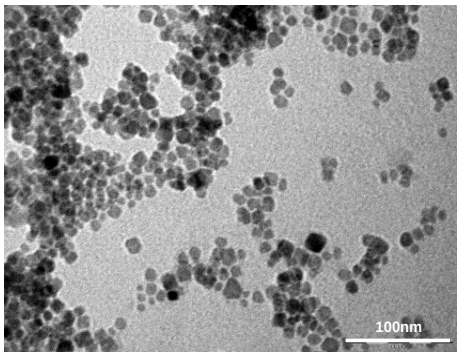

Figure 3.19: TEM image of citrate IONP of d_{TEM} ~10-13 nm.

TEM imaging was also carried out on Pinna IONP pre- and post transfer with DTAB. It is evident from both images that size and monodispersity were generally maintained following the transfer process, with TEM diameters of 11.25 ± 1.3 nm pre- and post phase transfer. This suggests that all particles were successfully phase transferred.

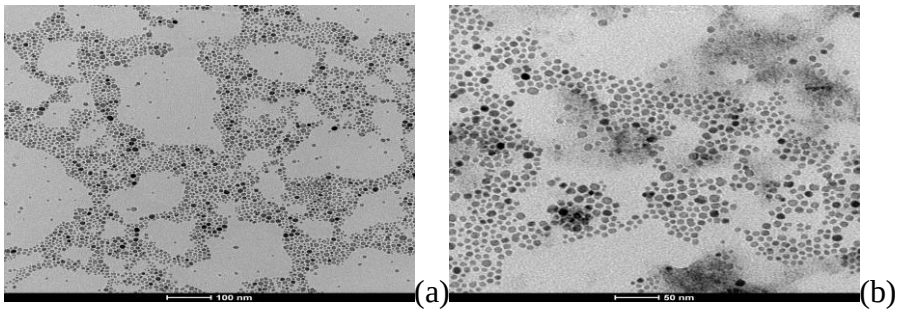

(a) (b)

Figure 3.20: TEM images of Pinna IONP (a) pre-transfer in $CHCl_3$ and (b) post-phase transfer in H_2O

For the DTAB-IONP, however, this increase between the observed diameters for TEM and PCS is much larger (~10nm). This, as mentioned earlier, is probably due to the thicker DTAB ligand shell, or that the DTAB is actually interacting with the oleic acid ligands already bound to the IONP surface as a result of hydrophobic Van der Waals interactions [117] (see Figure 3.21). Very strong evidence for this is provided by the measured r_2/r_1 for both nanoparticle types, which are very similar and typical for dispersed IONP in suspension (Table 3.2)

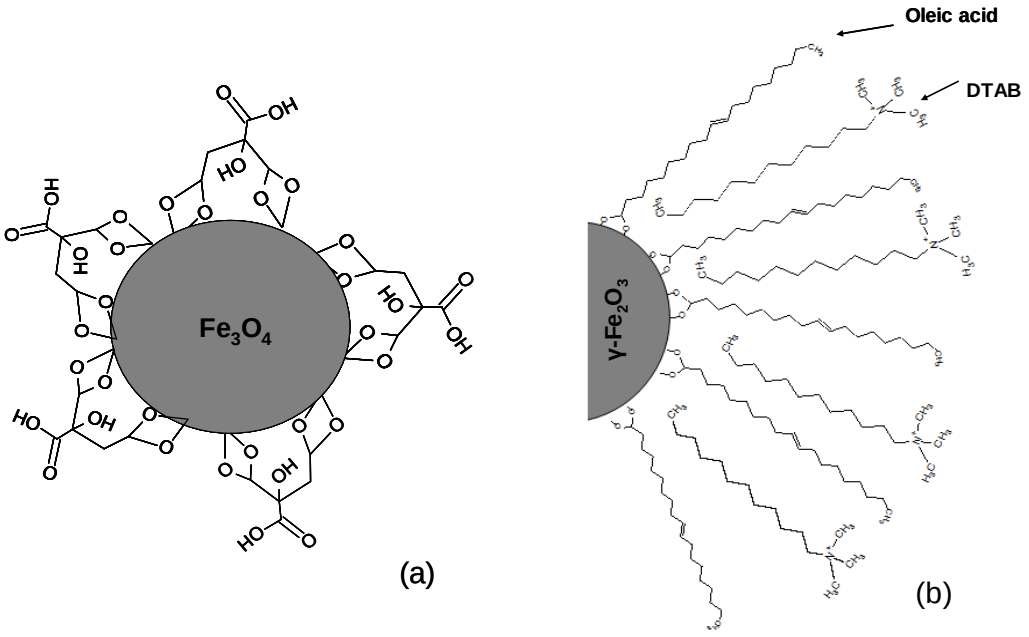

Figure 3.21: Chemical structures of (a) Cit-IONP and (b) DTAB-IONP

3.4 Conclusions

The syntheses of iron oxide nanoparticles using both hydrolytic and non-hydrolytic methods and their successful stabilisation in aqueous medium by both ligand displacement and encapsulation methods are presented. Particle size information was indicative of well-dispersed individual nanoparticles of reproducibly small hydrodynamic diameters. The Zeta Potential measurements confirmed the expected characteristic surface charges associated with the ligands. NMRD analyses demonstrated that suspensions prepared using thermal decomposition methods exhibited higher relaxivity than those prepared by coprecipitation methods possibly due to improved crystallinity. It was also encouraging to observe that these observed higher r_1 values were maintained in the case of nanoparticles prepared by decomposition methods on their transfer into aqueous medium.

CHAPTER 4

Synthesis and Characterisation of Polymer-Nanoparticle Composite Materials for Potential Biomedical Application

4.1 Introduction

The therapeutic application of composite materials including magnetic nanoparticles in the development of drug delivery vehicles (DDVs) for a wide range of purposes has gained a significant amount of interest. The development of magnetic targeted carriers (MTCs) for use in magnetic drug targeting (MDT), for example, is particularly attractive for the treatment of solid tumours where surgical eradication or radiation is not possible. MDT therapies offer many benefits over more conventional non-specific methods such as chemo- and radiotherapies, as they allow for maximum drug efficacy while using the lowest possible dose and, in turn, reducing the potential toxicity and side effects usually associated with increased drug concentration in vivo. With magnetic drug targeting, drugs can be incorporated into the core of a delivery vehicle, or adsorbed via ionic or covalent linkage onto its surface. The latter is more favourable as it allows for a much lower required drug dose while maintaining efficacy of that drug. Once transported to the site of interest, drug release can be facilitated via many methods such as pH dependent cleavage [118], irradiation [44] or the use of elevated temperature (hyperthermia) [42].

In addition to this, the magnetic properties of these delivery vehicles may be used to provide a platform for monitoring the efficacy of drug delivery through MRI [119]. Conjugation of a chemotherapeutic drug to magnetic DDVs enables simultaneous monitoring of drug delivery with MRI imaging, allowing physicians to quantify the amount of drugs taken up at the tumour site and monitor response to treatment in real time [120].

This chapter focuses on the use of poly (alkyl-cyanoacrylate) nanoparticles (PACA) as potential drug delivery vehicles which, when combined with magnetic iron oxide nanoparticles, form ‘composite materials’. These materials possess one of two types of iron oxide nanoparticles; either positively charged dodecyltrimethyl ammonium bromide (DTAB) stabilised IONP (forming DTAB-IONP/PACA), or negatively charged citrate stabilised IONP (Cit-IONP/PACA), depending on the formulation of the composite material in question. Composite materials formulated using DTAB IONP were proposed to form a ‘surface-decorated’ structure, where the IONP were attached to the surface of the polymer

nanoparticles (Figure 4.1). Those prepared using citrate-stabilised IONP were expected to form a 'core-shell' structure, where the nanoparticles were incorporated into the internal matrix of the PACA spheres (Figure 4.1). Strong evidence of the former appeared to present itself, with all PCS, Zeta and NMRD data accounting for the formation of the proposed decorated structure. Difficulties arose when attempting to prove successful formation of the Cit-IONP/PACA composite, nonetheless a series of interesting observations were made such as the overall increase in r_1 across the NMRD profile and the increase in d_{hyd} while maintaining a low PDI, suggesting a high degree of size monodispersity within the suspension.

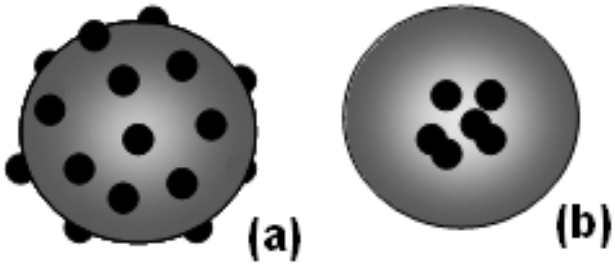

Figure 4.1: Proposed structure for both (a) decorated and (b) core-shell composite materials

4.2 Experimental

4.2.1 Synthesis of Poly-n-butyl cyanoacrylate (PACA) nanoparticles

Materials

Monomer, n-butyl cyanoacrylate (medical grade), was obtained from Henkel Loctite Corporation, Ireland. Citric acid (99+%) and Dextran 40 (Fluka, mol. Wt. 40 kDa) were purchased from Sigma.

Synthesis

Poly(n-butyl-cyanoacrylate) nanoparticles were prepared via an open anionic polymerisation of n-butylcyanoacrylate monomer (20 mg/mL) in aqueous medium, acidified using citric acid (0.2% w/v) and in the presence of a steric colloidal stabiliser, Dextran 40 (0.8% w/v). Polymerisation was carried out for a

period of 3hr at ambient temperature with magnetic agitation, after which the resulting suspension was adjusted to pH 7 using 1M NaOH.

4.2.2 Synthesis of Citrate-stabilised IONP/PACA nanocomposites

Citrate-stabilised IONP for use in Cit-IONP/PACA nanocomposite syntheses (as described below) were prepared as described previously in Chapter 3.

Nanocomposite materials of citrate-stabilised IONP and Poly-(n-butyl-cyanoacrylate) nanoparticles were prepared via the following method; an aqueous suspension of citrate-stabilised IONP was used as the polymerisation medium for PACA nanoparticle formation, where all necessary reagents for the synthesis were added to the IONP dispersion (as opposed to an equal volume of water). The polymerisation was carried out as described previously. The aim of this experiment was to attempt encapsulation of the IONP in a polymer matrix, forming a core-shell nanostructure containing a magnetic core.

4.2.3 Synthesis of DTAB-stabilised IONP/PACA nanocomposites

The formation of DTAB-IONP/PACA composite materials relied on electrostatic interaction of two particles of opposite charge; the DTAB-stabilised IONP exhibiting a highly positive charge and the PACA nanoparticles possessing an opposite negative one. Dispersions of DTAB-stabilised IONP and PACA nanoparticles were combined using overnight agitation at room temperature. Composite materials were then centrifuged or filtered accordingly depending on the results of initial PCS measurements.

4.2.4 Characterisation

As with the nanoparticle dispersions discussed in Chapter 3, composite materials were primarily characterised by PCS and NMRD analysis. ICP-AES was used as described in Chapter 2 of this thesis to determine the iron content contained within the composites formed. Zeta Potential measurements were also carried out on a Zetasizer Nano ZS (Malvern Instruments, UK) following composite preparation. Finally, Transmission Electron Microscopy was used in an attempt to confirm the outcome of IONP-PACA combination.

4.3 Results and Discussion

4.3.1 PCS Characteristation

The synthesis of PACA nanoparticles is known to be one of great success and extremely high reproducibility, with nanoparticles in the range of 110 to 140 nm (d_{hyd}) being formed with ease and a high level of monodispersity, with PDI values of 0.04 to 0.1 obtained in syntheses in this work [30]. Nanoparticles formed are stable for a number of months particularly when refrigerated, and at pH 3-7.

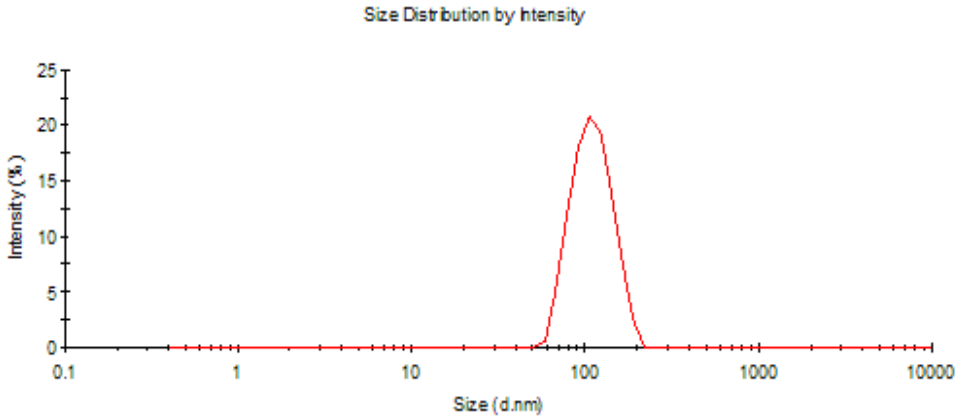

Figure 4.2: Size distribution of PACA NP (d_{hyd} 114nm, PDI 0.08)

It is evident from the size distribution plot below that the hydrodynamic size of the Cit-IONP/PACA composite material had increased significantly compared to that of the pure PACA (d_{PCS} (PACA) 114 nm, PDI 0.08) and indeed the value is far greater than that of the citrate-stabilised IONP (d_{PCS} (citrate) 16.5 nm, PDI 0.15). One interesting observation, however, is that the PDI (0.09) had not increased significantly from those characteristic of PACA nanoparticle dispersions. This suggests that a very different monodisperse structure had been formed.

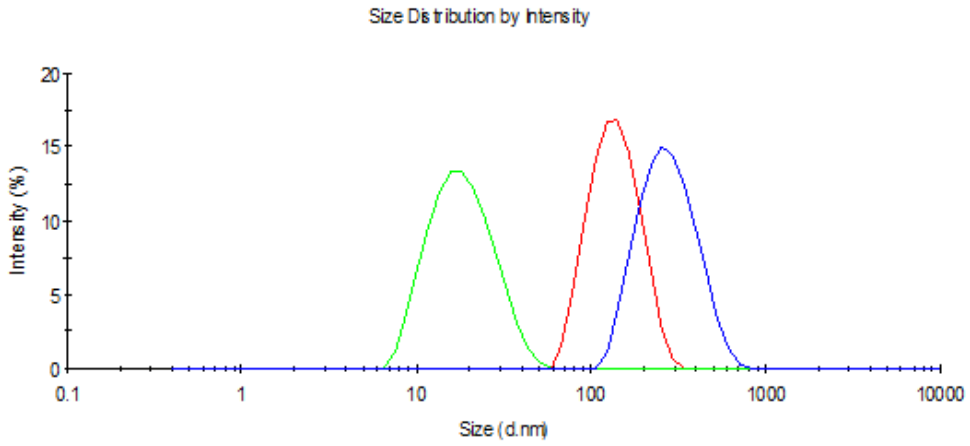

Figure 4.3: Comparison of hydrodynamic diameters of all species involved in citrate-IONP/PACA composite formation; citrate-IONP (----) d_{PCS} 16.5nm (0.15), PACA (----) d_{PCS} 114nm (0.08) and IONP-PACA composite (----) d_{PCS} 300nm (0.09)

Figure 4.4 (below) demonstrates PCS size distribution data for a dispersion of DTAB- IONP/PACA nanoparticles. The hydrodynamic diameters of the DTAB-IONP, PACA, and nanocomposite material were ~20 nm, 100-110 nm and 115-120 nm respectively, suggesting the formation of a composite material. The presence of a faint peak in the higher end of the size distribution for both the DTAB-IONP and the composite indicates that some larger aggregates were present in both suspensions, which, in turn, would have contributed to the larger PDI values obtained as opposed to that of the PACA.

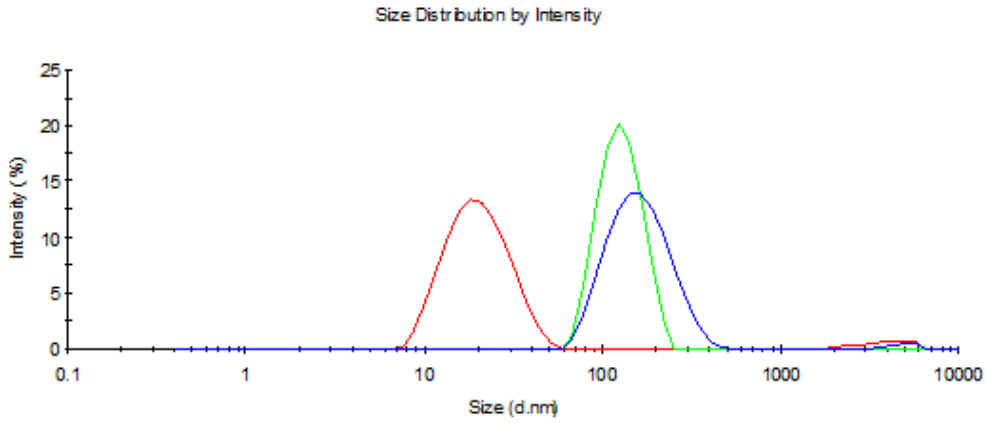

Figure 4.4: Comparison of hydrodynamic size distribution of all nanoparticles involved in DTAB-IONP-PACA composite formation; DTAB-IONP (----) d_{PCS} 19.2 nm (0.20), PACA (----) d_{PCS} 119 nm (0.07) and IONP-PACA composite (----) d_{PCS} 151 nm (0.18)

4.3.2 Zeta potential

Zeta potential measurements were also performed to confirm the characteristic negative charge of the polymer nanoparticles. Within a suitable concentration range (approx 0.2-1.0 mg/mL PACA), phase plots and zeta distributions met all the quality criteria of the Zetasizer software.

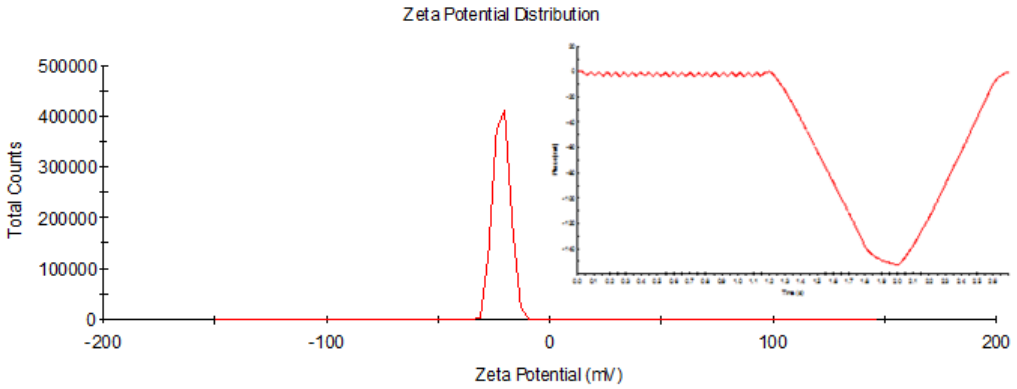

Figure 4.5: Zeta Potential distribution and Phase Plot (inset) for PACA NP (for Zeta Potential of -21mV)

In the case of the Cit-IONP/PACA composite, however, it is difficult to determine from the Zeta Potential data whether a composite material was formed, as both species involved are individually negatively charged, with values typically of the same order of magnitude as those observed for the composite material. We can, however, deduce that the species is still highly negatively charged, with zeta potential values typically in the region of -5 to -30 mV, depending on dilution.

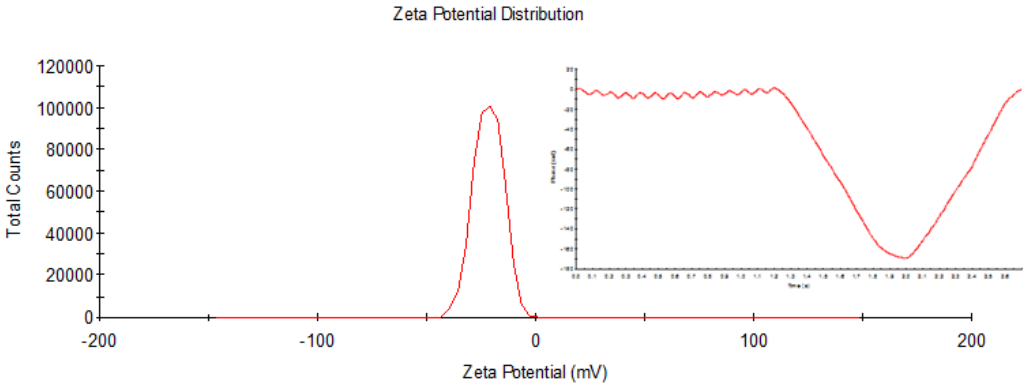

Figure 4.6: Zeta Potential distribution and phase plot (inset) for citrate-IONP/PACA composite (-21 mV)

The Zeta Potential data obtained for the DTAB-IONP/PACA suspension (Figure 4.7) also supported the hypothesis of a composite material being formed, as opposed to a co-suspension. Distributions were typically monodisperse and had values ranging from +2 to +11 mV, suggesting reasonable short term stability of the composite materials produced. These values were between those obtained for very positively charged DTAB-stabilised IONP (~+35 mV) and the negatively charged PACA nanoparticles (~ -30 mV) (see Figure 4.8).

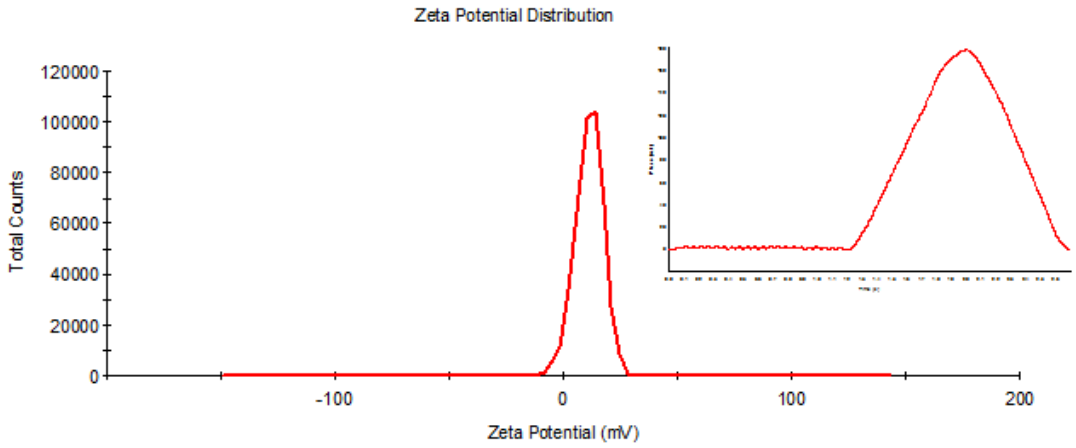

Figure 4.7: Zeta Potential distribution of composite (Zeta Potential 11.2mV)

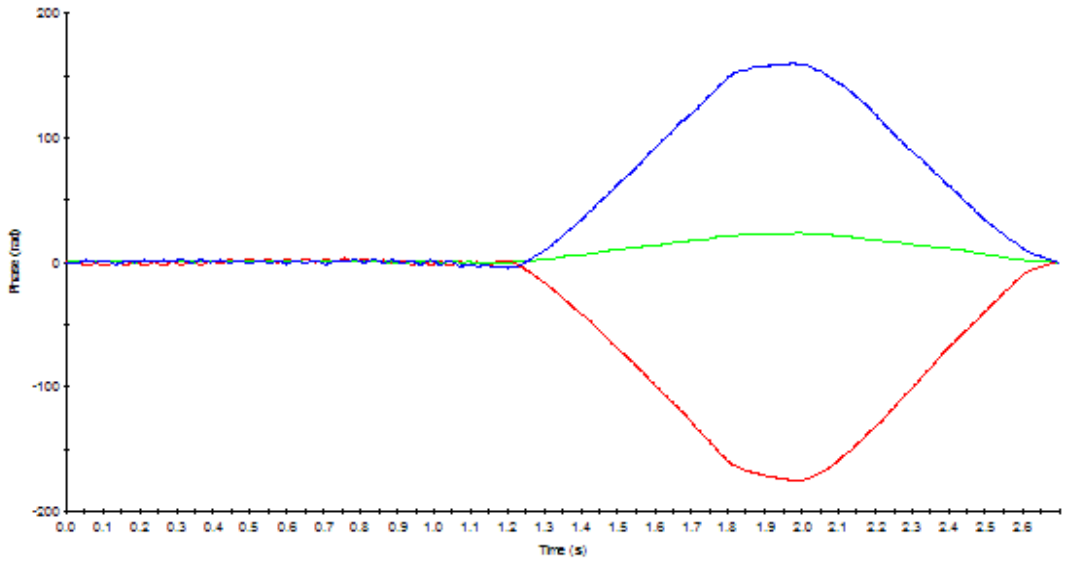

Figure 4.8: Phase plots of all nanoparticles involved in DTAB-IONP/PACA composite formation; DTAB-IONP(-) (+35mV), PACA (-) (-21mV) and DTAB-IONP-PACA(-) (+11mV).

4.3.3 Effect change in pH on nanoparticle/nanocomposite properties

Figure 4.9 below illustrates the data obtained following pH titration of small aliquots of water-dispersed PACA nanoparticles over the pH range of 3-10 using 1M NaOH and 1M NaCl. The natural pH of the suspensions were typically pH 7-7.5. Hydrodynamic diameters varied from 105 nm to 125 nm over the observed pH range for the chosen sample and PDI values remained within an acceptable range for monodisperse suspensions. Zeta Potential values remained negative throughout the course of the experiment, with values ranging between -8.5 and -25 mV and phase plots maintaining good shape the pH range demonstrating the acceptable quality of the data obtained. PACA NP dispersions were observed to remain stable at neutral pH for a period of months when refrigerated.

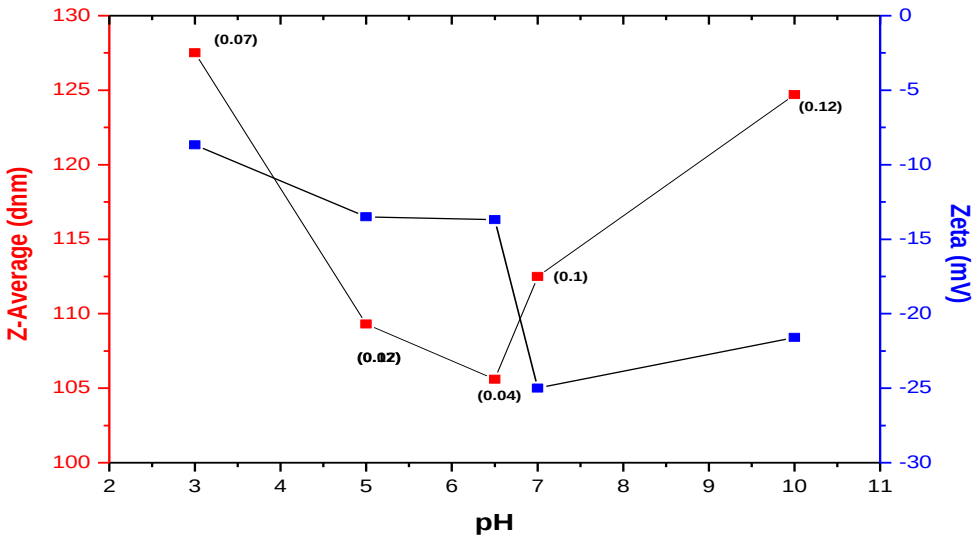

Figure 4.9: Size/Zeta versus pH for PACA nanoparticles

The pH dependence of hydrodynamic size and zeta potential was also investigated for a representative citrate-IONP/PACA composite material, (Figure 4.10 below). In this instance, hydrodynamic sizes remained relatively unchanged within the pH range of 3-9, beyond which the suspended material appeared to disassemble, and a sharp decrease in the particle size was observed.

Zeta potential values fell between -19 mV and -35 mV and corresponding phase plots were good for the majority of the measurements. This was with the

exception of the measurement at pH 11 where the phase plot was very noisy. This value can therefore not be taken as an accurate estimation of the surface charge at that pH. This problem may have arisen due to accumulation of ions about the electrode due to an increased base concentration, causing degradation of the electrodes and/or sample within the cell. The latter explanation may be supported by the sharp decrease in the hydrodynamic size of the particles present in the medium from approx 200 nm to 150 nm, suggesting degradation of the structure of the composite at this pH.

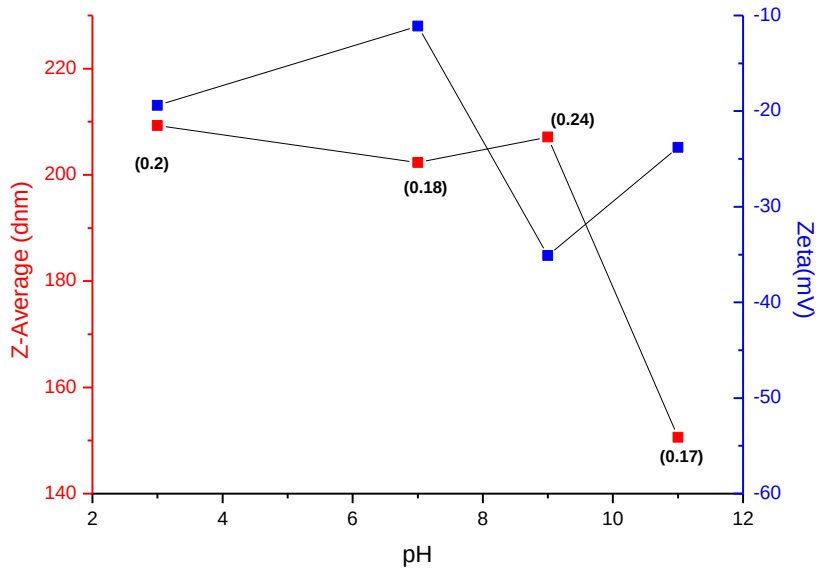

Figure 4.10: Size/Zeta versus pH for citrate-IONP/PACA composite

When compared to the pH titration plot of the unloaded PACA NP (Figure 4.9), Cit-IONP/PACA suspensions appeared to have similar stability; both d_{hyd} and Zeta Potential values were stable over a reasonably broad pH range, with the exception of pH 11 for the composite.

Finally, the pH dependence of the DTAB-IONP/PACA was investigated (Figure 4.11 below). Hydrodynamic size was again maintained over the majority of the pH range with good PDI associated with these measurements, with the exception of a particle size of ~750 nm observed at pH 11 with a PDI value of 0.6. Zeta potential measurements were made on all samples demonstrating good particle sizes, and were observed to become more negative on increasing the

concentration of the base in the nanoparticle medium, as expected. This was the first instance over the course of the three titration experiments outlined in this chapter that an isoelectric point was observed, and was present for the DTAB-IONP composite material at pH~3.5.

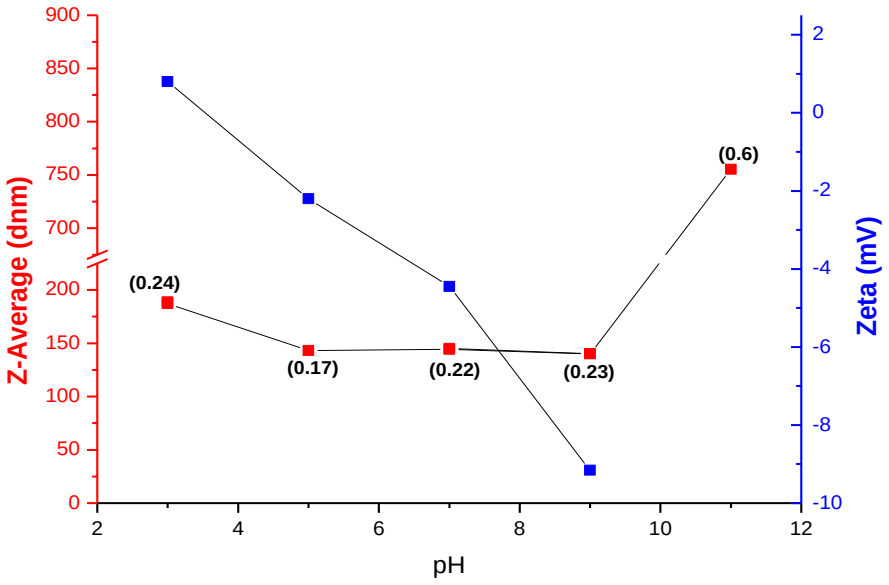

Figure 4.11: Size/Zeta versus pH for DTAB-IONP/PACA composite

The pH range over which the composite was seen to remain stable was much narrower in this instance, compared to PACA and Cit-IONP/PACA, with a gradual increase in d_{hyd} for DTAB-IONP/PACA dispersions below pH 4-5 and also above pH 9.

4.3.4 TEM imaging

PACA nanoparticles were also viewed under a Transmission Electron Microscope. The images obtained demonstrated good nanoparticle monodispersity as was also observed by PCS analysis. Particles appeared to be highly spherical and measured particle diameters by both techniques were similar (d_{pcs} 110 nm (PDI 0.08), d_{TEM} 102 ± 8.1 nm) confirming the highly monodisperse nature of the material.

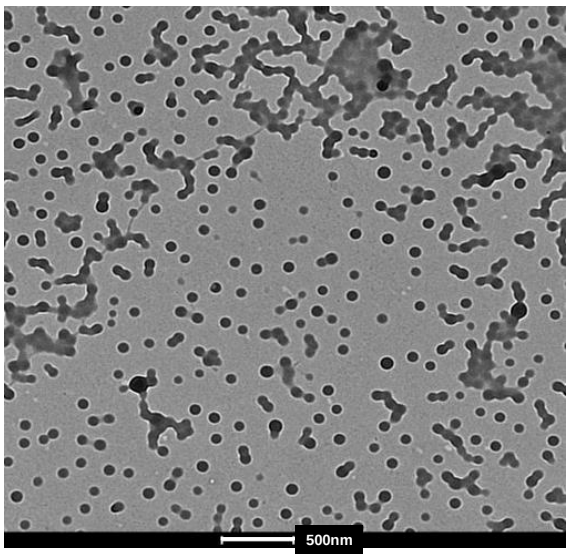

Figure 4.12: TEM image of PACA NP

Figure 4.13 below demonstrates a typical TEM micrograph of a citrate-IONP/PACA composite. Large aggregates seemed to dominate the surface of the grid, with particles of two different levels of contrast present. For comparison, a micrograph of Cit-IONP is presented (Figure 4.13 (a)), which presents the IONP in a more dispersed manner, as opposed to the more 'clustered' fashion observed in Figure 4.13(b).

Electron microscopy was used in an attempt to determine whether a composite material (i.e. one that is intimately mixed on the nanoscale), or a co-suspension, was formed from the combination of the particles. Unfortunately, little structural information could be obtained from any of the images obtained. Drying the sample onto the grid may be a contributing factor, as clearly the high monodispersity apparent from PCS was not preserved.

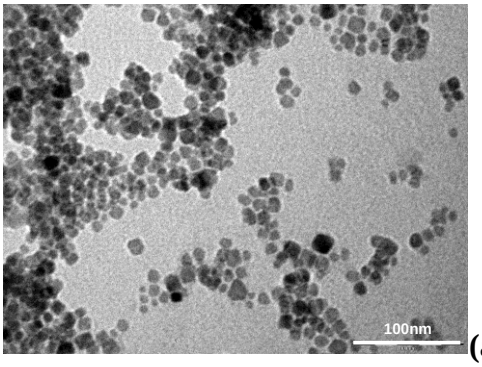

(a)

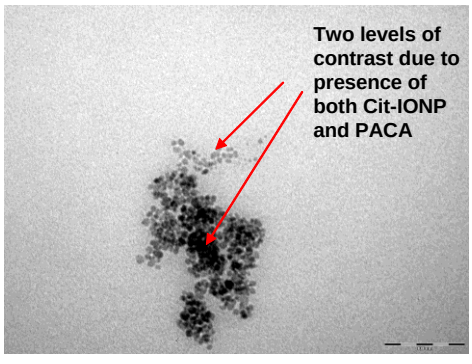

(b)

Figure 4.13: TEM image of Cit-IONP and Cit-IONP/PACA

The TEM micrograph presented in Figure 4.14 below represents a typical DTAB-IONP/PACA composite dispersion. At a first glance it appears that there are larger nanoparticle spheres present (PACA) that are decorated on the surface with particles of a much darker contrast (DTAB-IONP). On looking at the size bar beneath the image however, we see that these apparent polymer nanospheres (brighter spheres) are far in excess of 500nm. This is not in agreement with PCS measurements where d_{PCS}=151 nm. This discrepancy may be due to disruption of the composite during the drying process onto the grid. Thus we cannot decipher from imaging techniques whether composite materials were successfully prepared. However it does appear that there is a significant fraction of free DTAB-IONP on the grid, although again these may have been released during drying.

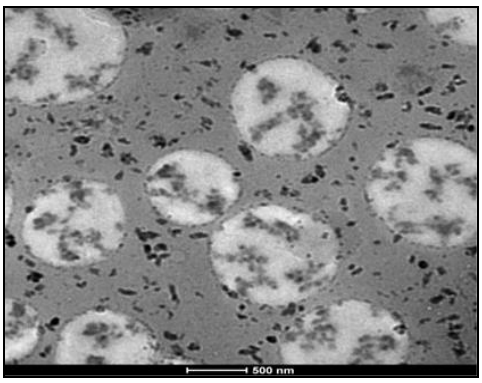

Figure 4.14: TEM of DTAB-IONP/PACA composite

4.3.5 NMRD studies

As with the NMRD profile (Figure 3.11) for the citrate-stabilised IONP prior to combination with the n-butyl cyanoacrylate monomer, a typical superparamagnetic shape is evident from the profile for Cit-IONP/PACA (Figure 4.15). In comparison to the profile for the dispersed particles, however, the observed relaxivity of the composite has essentially doubled. Note that the position of the r_1 maximum has also shifted to slightly lower frequency, which is usually taken to be indicative of increased nanoparticle size for dispersed particles. Note that this observation is similar to that observed on changing the pH of Cit-IONP in suspension (Figure 3.18).

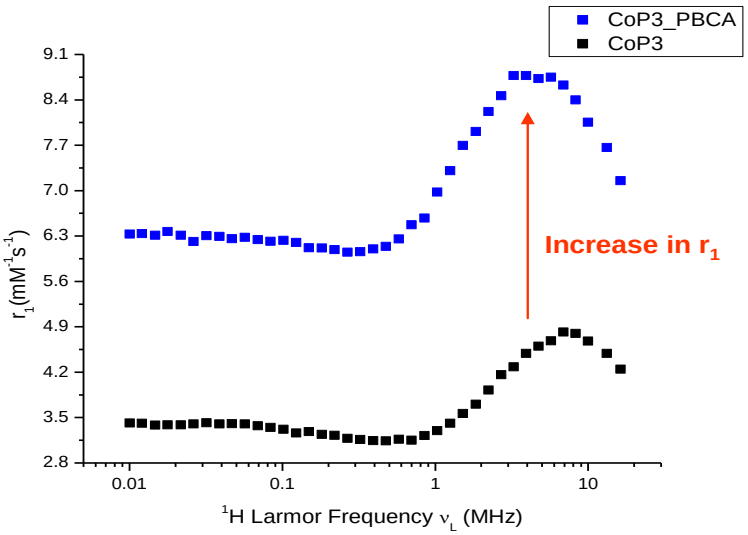

Figure 4.15: NMRD profiles of citrate-stabilised IONP (CoP 3) (d_{hyd} 15.8 nm, PDI 0.15) and Cit-IONP/PACA composite (CoP 3_PBCA) (d_{hyd} 300 nm, PDI 0.09).

4.3.6 Effect of dilution on R_1 of citrate composite

Figure 4.16 below represents relaxation (R_1) measurements made at three different fields (16, 6 and 0.1MHz) for a series of dilutions performed on a single citrate-IONP/PACA composite material. From the graph, we can see that the relationship between R_1 and concentration was proportional at all frequencies. This experiment provides the relaxivity and also shows that the suspension is stable over this dilution range.

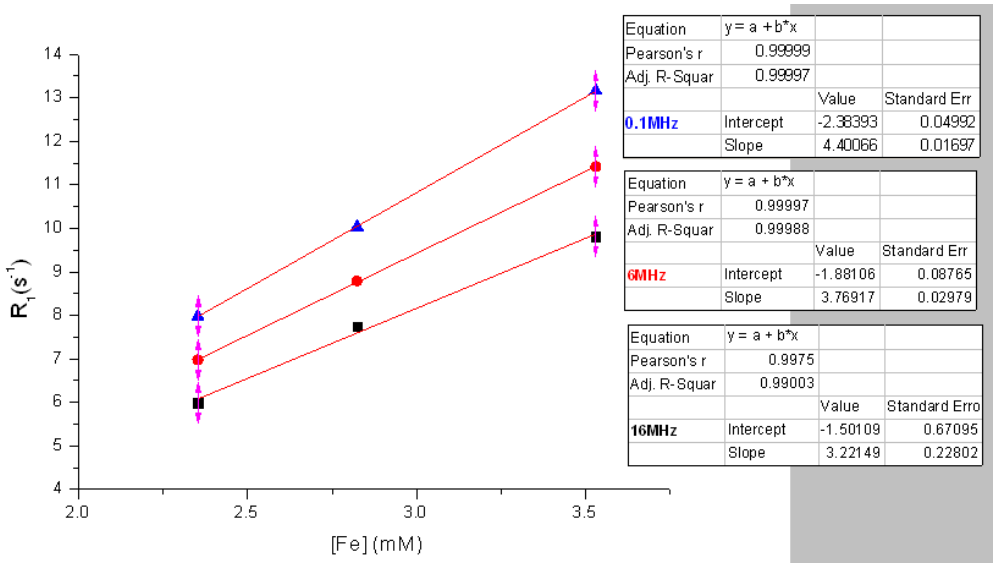

Figure 4.16: R_1 as a function of Fe concentration on dilution of citrate composite at the lower frequencies

4.3.7 Effect of nanoparticle concentration on citrate composite formation

The increase in the measured r_1 is observed on composite formation using citrate-stabilised IONP, irrespective of the r_1 on forming the composite was confirmed by a series of replicate experiments as illustrated in Figure 4.17 and Figure 4.18.

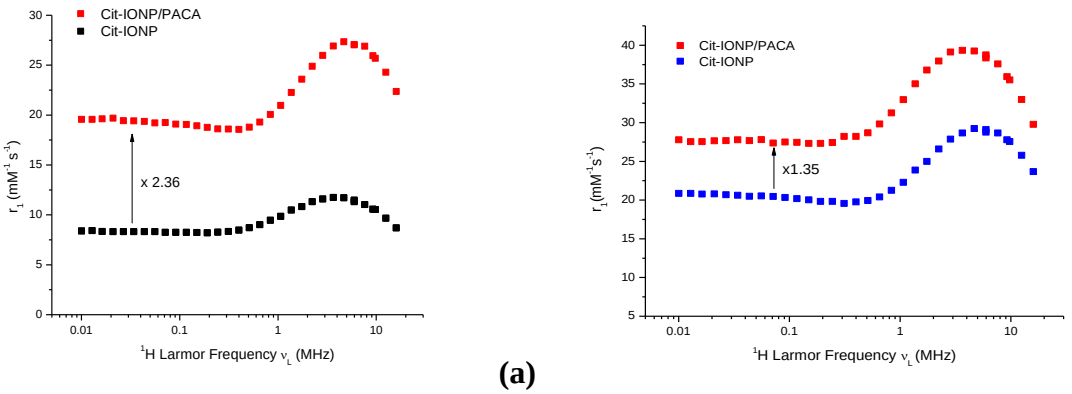

Figure 4.17: NMRD profiles for a series of replicate experiments of citrate-IONP/PACA composite formation with [cit-IONP] of (a) 12.5 mM and (b) 20 mM respectively. Monomer concentration was kept constant at 20 mg/mL

It can be noted, however, that the observed change in r_1 was not by the same factor in all cases of composite formation. A common citrate-stabilised IONP source was therefore used for a further experiment in which composite materials were prepared by varying the cit-IONP concentration, to investigate the cause of the r_1 enhancement. From the data shown in Figure 4.18 below, we can conclude that the r_1 enhancement increases as the quantity of citrate-nanoparticles introduced into the polymerisation medium increases (see Figure 4.18 below).

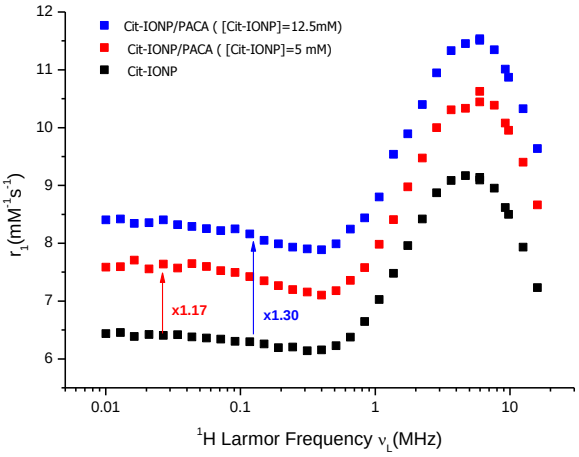

Figure 4.18: NMRD profiles for composites of varying cit-IONP concentrations using the same cit-IONP source. For the purpose of these experiments, the PACA concentration was kept constant at 20 mg/mL

4.3.8 SPM Modelling of citrate-IONP composites

The increase in r_1 on forming the Cit-IONP/PACA composite is interesting as any enhancement of relaxivity could be of use in magnetic resonance imaging. The physiochemical basis for the effect could also be of fundamental interest. It is clear that the primary nanoparticles have not changed size and the absence of a larger r_1 enhancement at low frequency suggests the absence of nanoparticle aggregation within the composite which would increase the magnetocrystalline anisotropy [121].

In the first instance, the effect of viscosity on relaxivity was investigated through SPM simulations using a similar approach to that described in Chapter 3. It should be noted that the observed increase in r_1 in that case was significantly greater. It was possible to generate good agreement with the data by taking the successful simulation for Cit-IONP and reducing the diffusion coefficient (D_{SPM}), while keeping all other parameters fixed. In the case shown in Figure 4.19, a reduction in D_{SPM} of 36% was sufficient. Physically, this situation could be interpreted as the polymer matrix reducing the local diffusion coefficient of the water in the immediate vicinity of the magnetic nanoparticles, i.e. within the polymer shell. This, however, does not confirm the formation of a core-shell composite, with the citrate-IONPs encapsulated within larger polymer spheres.

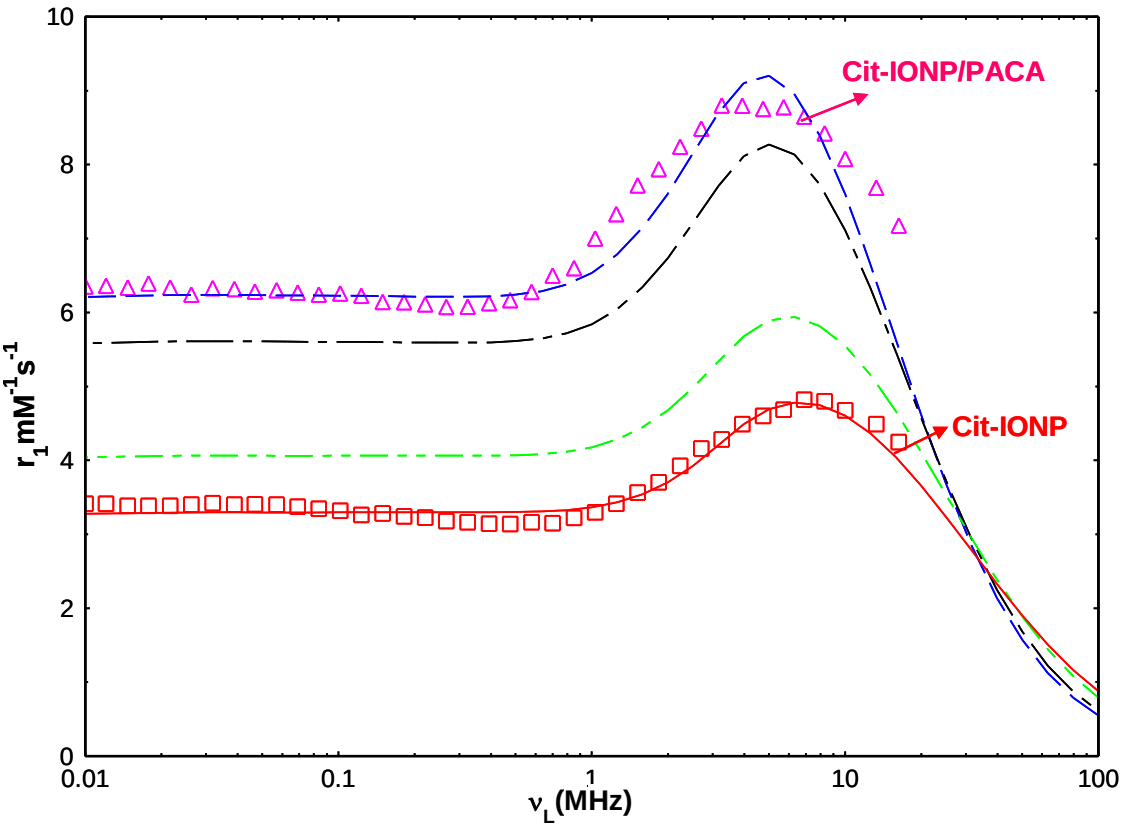

Figure 4.19: Manipulation of diffusion coefficient of Cit-IONP SPM fit in an attempt to match composite NMRD profile data (Δ) where D_{SPM}= 3.5E-5 cm^2/s (-), 2.5E-5 cm^2/s (-), 1.5E-5 cm^2/s (-), and 1.25E-5 (-), which was the best fit for the Cit-IONP/PACA NMRD data (a 36% decrease in D_{SPM}) . The other parameters for Cit-IONP were as follows: τ_N 28 ns, Ms 17emu.g^{-1}, d_{SPM} 13.6 nm.

To further investigate the effect of viscosity, we attempted to simulate the profiles of other Cit-IONP/PACA suspensions. A typical example is shown overleaf. In this case application of a 7% and 18% decrease in D_{SPM}, was unsuccessful in matching the NMRD data. On experimenting further with changing the value for D_{SPM}, we estimated that a 30% decrease would be necessary to make the simulations agree with experiment in this particular case (Figure 4.20).

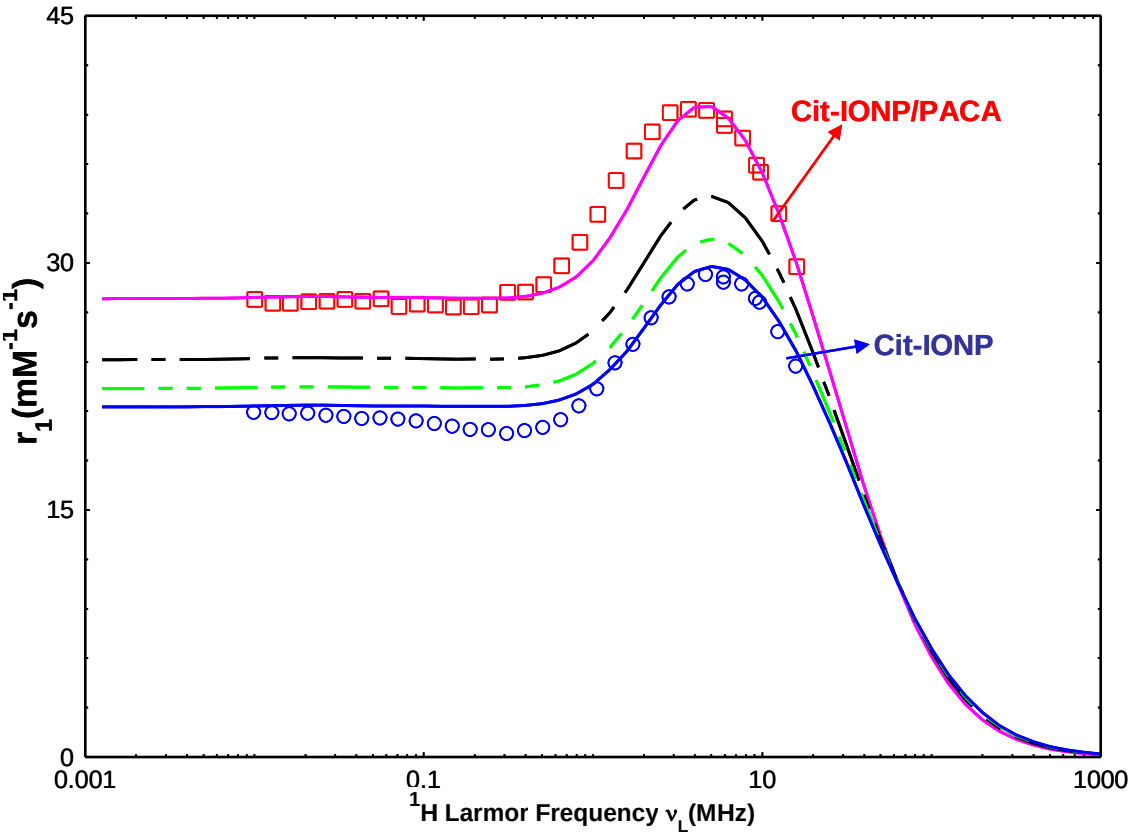

Figure 4.20: Manipulation of diffusion coefficient of a cit-IONP SPM fit (○, -) where r_1 of the IONP was higher than those represented by Figure 4.19. The diffusion coefficient of the Cit-IONP (D_{SPM}=3.5E-5 cm^2/s) was decreased in this case by 7 %, (-) and 18 %,(-) in an attempt to explain the r_1 increase on forming Cit-IONP/PACA due to viscosity effects (as was observed in Chapter 3, Figure 3.17). In this instance a 30% decrease in D_{SPM} was required to fit the composite NMRD data (□, -)

From the data presented in Figure 4.19 and Figure 4.20 above, we conclude that a 30-36% decrease in D from the value used for Cit-IONP was required in order to generate a good fit with the NMRD data for Cit-IONP/PACA. On measurement of the actual viscosity for Cit-IONP and Cit-IONP/PACA suspensions (Table 4.1), it was observed that the bulk viscosity does not change by more than 5% upon formation of the composite. Given that the measured viscosities of the Cit-IONP/PACA suspensions were close to 1 mPa/s (Table 4.1), we can conclude that the change in r_1 is not solely due to a change in viscosity of the medium.

Sample	Viscosity (mPa/s)(@25˚C)
Cit-IONP	0.99-1.00
Cit-IONP/PACA	1.03-1.04
PACA	1.31-1.32

Table 4.1 Measured viscosity ranges for Cit-IONP and Cit-IONP/PACA suspensions

We have previously shown in Chapter 3 that even a 18% increase in the viscosity is insufficient to account for changes in r_1 for dispersed particles. The simulations represented by the solid green and black lines for increases of 7% and 18% respectively in Figure 4.19 and Figure 4.20 confirm that this is also the case for Cit-IONP/PACA. We can therefore conclude that the change relaxivity arises at least in part from altered local viscosity about the Cit-IONP, perhaps within the soft PACA shell.

4.3.9 NMRD of DTAB-IONP/PACA

In comparison to the NMRD profile obtained for the DTAB- IONP, a 4-fold reduction is observed in the relaxivity of the composite material. Similar to citrate-IONP/PACA, the r_1 maximum shifted from higher frequency (~8 MHz) to lower frequency for the composite (~4 MHz). This suggests potential formation of a 'current-bun' type composite material (Figure 4.1), where the PACA nanoparticles are decorated by the iron oxide on the surface, given that the hydrodynamic size of the resulting material (151 nm) has increased by a value comparable to that obtained for DTAB-IONP prior to composite formation (19.2 nm) when compared to the size of the PACA (119 nm).

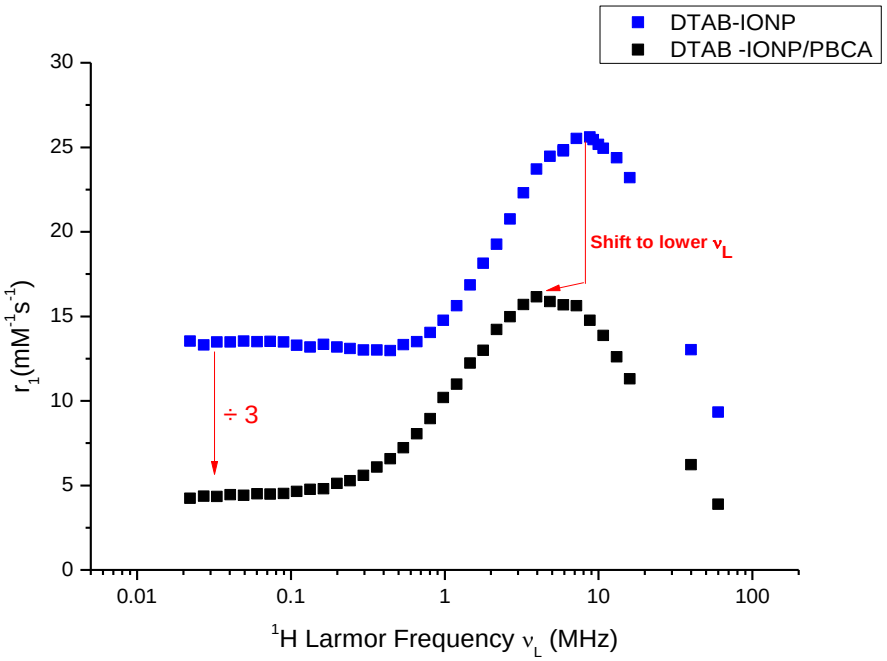

Figure 4.21: NMRD of DTAB-IONP (d_{PCS} 19.2 nm, PDI 0.20) and composite (d_{PCS} 151 nm, PDI 0.18)

4.3.10 Effect of polymer concentration on DTAB composite formation and SPM modelling

Figure 4.22 below illustrates NMRD data obtained for a number of DTAB-IONP/PACA composite materials of varying polymer concentration. It can be observed that on increasing the polymer concentration while keeping IONP concentration constant, the relaxivity of the resulting composites decreases accordingly. This result was repeated a number of times and in all cases, irrespective of the initial r_1 of the DTAB-IONP, on formation of the composite r_1 was reduced.

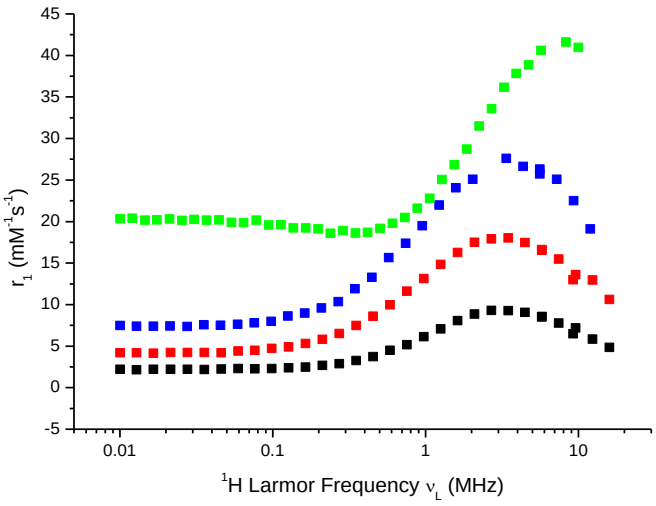

Figure 4.22: NMRD profiles for DTAB-IONP (■) and DTAB-IONP/PACA composites of varying [PACA] where [PACA] = 1 mg/mL(■), 2 mg/mL(■) and 20 mg/mL (■) respectively

Simulations using SPM theory of all DTAB-IONP-PACA composites presented above were conducted and are represented in Figure 4.23 below. These simulations provide a good reproduction of experimental data, with all calculated parameters as shown in Table 4.2.

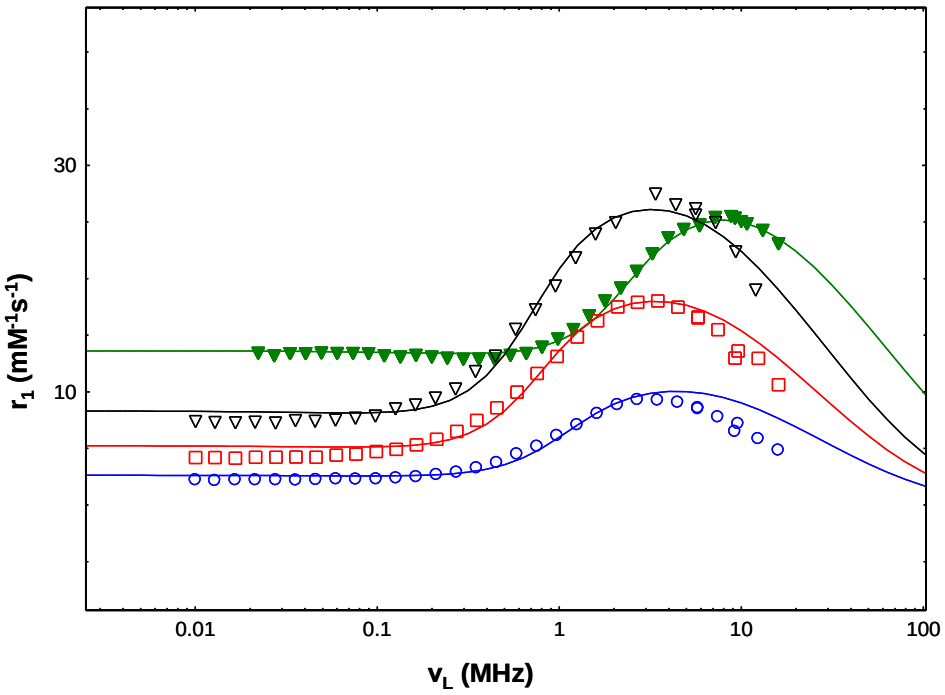

Figure 4.23: NMRD profiles and SPM simulations of DTAB-IONP (▼, -) and DTAB-IONP/PACA of [PACA] = 20 mg/mL) (○, -) , 2 mg/mL (□, -), 1 mg/mL (▽, -)

Sample	τ_n (ns)	M_s (emu.g^{-1})	d_{SPM} (nm)	d_{PCS} (nm)	ΔE (GHz)
DTAB-IONP	10	56.0	10.4	22.4	2
DTAB-IONP/PACA ([PACA] =1 mg/mL)	3	38.0	15.6	138.8	2.75
DTAB-IONP/PACA ([PACA] =2 mg/mL)	3	30.5	16.4	148	2.5
DTAB-IONP/PACA ([PACA] =20 mg/mL)	3	23.5	16.4	138.3	2

Table 4.2: Calculated SPM parameters for DTAB-IONP and all DTAB-IONP/PACA

The NMR size, d_{SPM} is found to increase from 10.4 nm for the DTAB-stabilised IONP to 15.6-16.4 nm for the composite materials. A substantial decrease in saturation magnetisation, M_s, from 56 to 23.5-38 emu.g^{-1} is also observed.

Concerning the size, d_{SPM}, it should be noted that the size obtained from NMR is really an indirect measure; the high frequency part of the profile is particularly sensitive to the diffusional correlation time, τ_D for the solvent molecules in the vicinity of the particle. This dependence on τ_D is the basis for the d_{SPM} values obtained. Note that $\tau_D = d^2/4D$, where d is the particle size and D the diffusion coefficient [102]. An increase in particle size or an increase in the local water viscosity could have the same effect on the profile; increasing τ_D and driving the maximum in r_1 back to lower frequency. Hence, the presence of the polymer may alter the local water mobility in the vicinity of the nanoparticle, so altering the NMRD profile.

We suggest, that the decrease in M_s, as sensed by the water, may be due to partial physical shielding of one whole side of the IONP surface from the diffusing ^1H nuclei in the H_2O due to its adsorption onto the solid polymer, as shown in Figure 4.24.

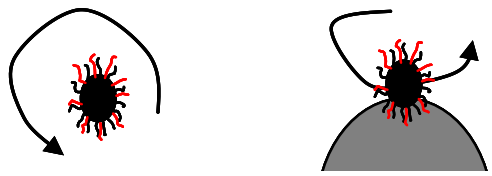

H_20 free to interact with all surfaces of IONP

Limited interaction of H_2O with surfaces of IONP

Figure 4.24: Schematic representation of the diffusion of water about IONP (left) and IONP electrostatically bound to a surface (right).

The systematic decrease in r_1 on increasing the amount of PACA NP introduced during composite formation may potentially be due to a decrease in the surface coverage of the PACA by the DTAB-IONP as shown in Figure 4.25 below. As the DTAB-IONP concentration was kept constant throughout all composite syntheses (15 mg/mL) and the amount of PACA NP present increased, the probability of all PACA NP becoming either partially or completely decorated by the DTAB-IONP will decrease. It follows that, as the water diffuses past the composite, the ^{1}H nuclei would come into contact with fewer IONP and thus a much lower relaxation enhancement will be observed.

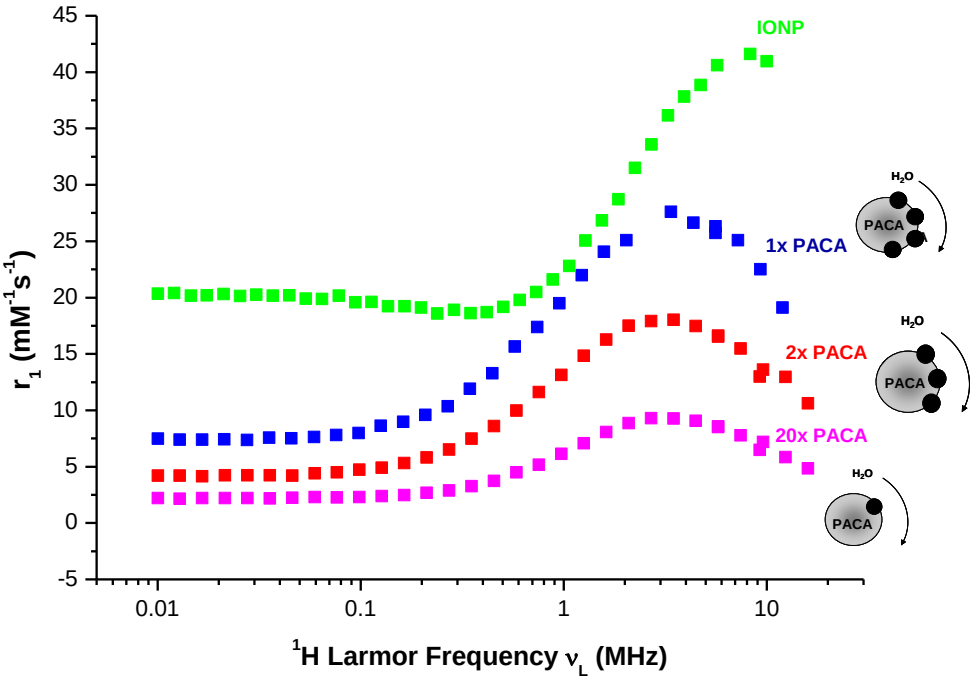

Figure 4.25: Possible explanation for r_1 decrease on increasing PACA concentration while keeping the DTAB-IONP concentration constant (15 mg/mL)

4.4 Conclusions and Future Work

In this chapter, data for composite materials derived from both citrate and DTAB-stabilised IONP (Cit-IONP/PACA and DTAB-IONP/PACA respectively) has been presented. With respect to the formation of the DTAB-IONP/PACA, the results obtained from PCS, zeta potential and NMRD analyses strongly support the formation of the proposed surface-decorated structure, where the iron oxide nanoparticles are electrostatically bound to the surface of the PACA nanospheres.

For example, the observed increase in hydrodynamic size of the composite material was almost comparable to the approximate d_{hyd} of a typical DTAB-stabilised IONP, and zeta potential measurements suggesting the formation of a near neutral material following coupling. The decrease in the observed r_1 for DTAB-IONP/PACA in the NMRD profile also strongly suggests successful attachment of the IONP onto the PACA surface. TEM imaging was not as successful in supporting the proposed structure. This, however, seemed to have been due to degradation of the materials during drying onto the grids for analysis.

The electrostatic interaction between the DTAB-IONP and the PACA, however, was not as strong as hoped. The PCS size distribution plot shown in Figure 4.26 below suggests that the magnetic nanoparticles could be easily separated from the polymer using magnetic capturing methods with high fields, where a reduction in hydrodynamic size of ~15-20 nm was observed. This may be explained by the IONP being retained in the magnetic field, while the non-magnetic material (PACA) passed through and was collected in the eluent. This suggests the need for stronger binding chemistries at the IONP-PACA interface.

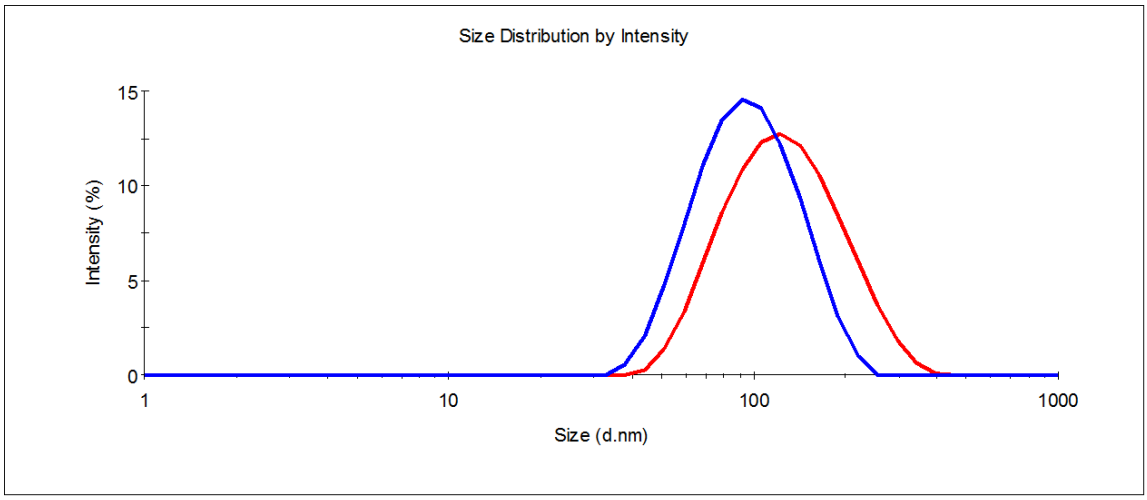

Figure 4.26: Magnetic filtration of DTAB-IONP/PACA composite where a reduction in the hydrodynamic size from 130 nm (-) to 111 nm (-) was observed. Note that the dhyd of DTAB-IONP and PACA are approx. 20 nm and 110 nm respectively.

In the case of Cit-IONP composites, an increase in r_1 was observed as compared to the data obtained for Cit-IONP. This increase was far greater than can be attributed to bulk viscosity changes within the composite medium. This observation is consistent with the formation of a composite that is water

permeable, wherein the water retention times are considerably altered as compared to Cit-IONP. It is unlikely, therefore, that a co-suspension has been formed in which both citrated-IONP and PACA co-exist in the same aqueous medium without any direct interaction

One major issue encountered on attempts to image the composite materials by TEM was the drying of the sample onto the TEM grid. In an effort to overcome this obstacle, cryo-electron microscopy could be used in future analyses in place of conventional TEM analyses, as this would remove any problems experienced during the drying process, thus resulting in more clear and conclusive images for determination of the actual structure of the nanomaterials. Cryo-SEM studies are planned with Dr. Twamley (Chemical Sciences, DCU) for the coming months.

CHAPTER 5

Non-aqueous Iron Oxide Nanoparticle Cluster Assembly

5.1 Introduction

In Chapters 3 and 4, the many benefits of using electrically charged IONP and their composite materials for biomedical application were outlined. For example, nanoparticle dispersions composed of small, individual IONP have presented themselves as good heat mediators for potential use in hyperthermic application [21, 27, 38, 42], whereas their larger composite counterparts are engineered more toward specific targeting and drug delivery [24, 122]. The one disadvantage of these larger composite materials that we have observed, however, is that the nanocomposite size cannot be easily controlled over a wide range of sizes. For this reason, iron oxide nanoparticle clusters, or IONPCs, have been extensively developed in the areas of specific site targeting and drug delivery. This is essentially due to their size-dependent magnetic properties and the ability to control the particle and cluster size. Overall size is a major determinant of bio-distribution of the IONPC-based agents *in vivo* [123].

It has been reported in the literature that the nature of the clusters formed strongly influences the magnetic anisotropy arising from interparticle interactions [49]. In addition to this, studies have shown a marked increase in the low field relaxivity on increasing the particle size [124]. The dependence of the magnetic properties on primary particle size also provides the potential to generate the maximum magnetic effect of the IONPCs while minimising the particle concentration to be introduced. The characteristic high r_2 values (and higher r_2/r_1 ratios) of these materials provides the possibility for their use as T_2 agents in a wide range of molecular imaging applications [102].

One major discovery leading to more successful targeted antitumor therapy was the discovery of the EPR effect by Matsumura and Maeda in 1986 which demonstrated that most solid tumors have a defective or 'leaky' vasculature that is highly porous and permeable, which facilitates a sufficient supply of nutrients and oxygen to tumor tissues for their rapid growth [125]. The advantage of the EPR effect is that it can be exploited for tumor-targeting chemotherapy in the delivery of macromolecular agents such as genes, antibodies, micelles, liposomes, and protein–polymer conjugates to the tumour site in addition to contrast agents for MRI imaging purposes [126].

The EPR effect is a molecular weight-dependent phenomenon where molecules or particles larger than 40 kDa, i.e. the threshold of renal clearance, demonstrate a prolonged circulation time and a much increased half life, resulting in a more gradual clearance from the body [127]. These molecules/particles gradually permeate tumors in a size-selective fashion. This provides the possibility of using IONPCs and Au-IONPCs as mentioned in this thesis for application for in vivo imaging and drug delivery applications.

A method to size-selectively produce IONPCs has been recently reported by our group through a process known as competitive stabiliser desorption (CSD) [128]. This process involves the exposure of IONP dispersed in heptane to a substrate of cyanopropyl-modified silica particles (CN-modified silica) which, over time, results in the gradual and continuous assembly of the IONP due to depletion of the surfactant ligands. As desorption of the surfactants from the surfaces is ongoing, aggregation or clustering proceeds gradually with time and the clusters increase in size, but critically size monodispersity of the clusters is maintained. This process is shown in Figure 5.1.

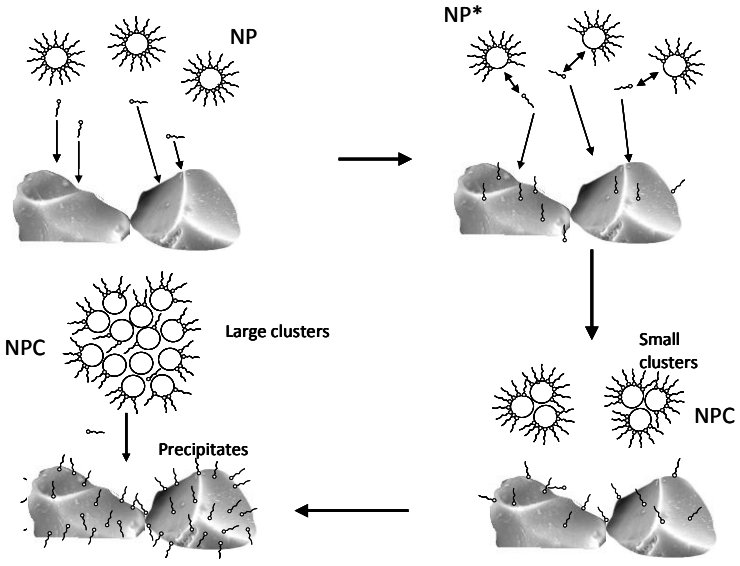

Figure 5.1: Schematic representation of the mechanism for NPC assembly by competitive stabiliser desorption as proposed by Stolarczyk et. al. [128]

The cause of IONPC assembly is the presence of the competing silica substrate (as shown in Figure 5.2), which, over time, partially depletes the NP of their

stabilising surfactant at their defect sites, generating 'activated NP', or NP^*, that possess open sites allowing for NP^*-NP^* interaction. It should be noted that the substrate acts indirectly on the NPs by depleting the heptane of any free oleic acid, thus altering the equilibrium between NP-bound surfactant and that present in the assembly medium. A sample setup of a cuvette containing IONP for assembly in the presence of a silica substrate is as shown below.

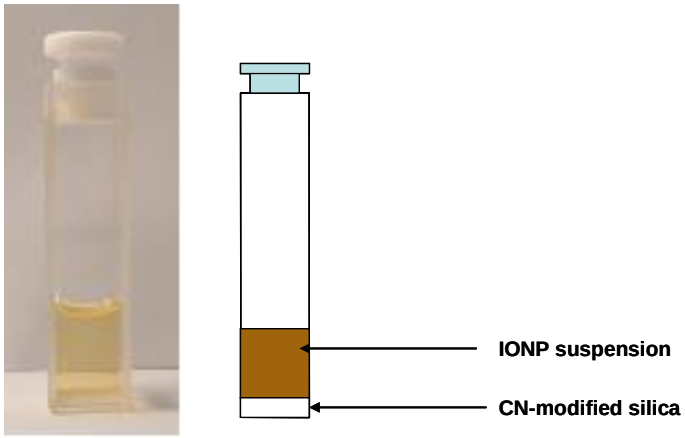

Figure 5.2: Typical setup of a cuvette for an IONPC assembly

The main advantages of this method are that the monodispersity of the cluster size is well preserved during the assembly process. Furthermore, upon removal of the suspension from exposure to the silica substrate, the assembly process can be stopped at a specific size. The resulting clusters have been observed to remain stable for extended periods of time. This allows engineering of clusters of an exact size that can be tuneable to the envisaged application of the material, although phase transfer is required.

The addition of gold nanoparticles in the CSD experiments to follow were made for the purpose of attenuating iron oxide nanocluster assembly, by blocking NP* sites formed as a result of exposure to the CN-silica substrate. The introduction of Au NPs is also advantageous as many biomedical advantages of AuNP and AuNP-coated IONPs have been reported in the literature [41, 94, 129, 130]. The well established surface chemistry of AuNP provides potential surface tunability for improved aqueous stability and biocompatibility of magnetic IONP [131]. The optical properties of AuNP, in combination with the magnetic properties of the IONP could allow for simultaneous optical and magnetic resonance imaging in

vivo. Furthermore, Au-coated IONP have been exploited for other biomedical applications such as thermoabalation and thermosensitive drug delivery [131, 132]. This is due to the fact that, when exposed to optical radiation, the electrons within the AuNP resonate with the electromagnetic field, causing them to absorb and scatter light. This phenomenon is commonly known as surface plasmon resonance (SPR), it is also associated with the conversion of light energy to heat, making Au-functionalised IONP attractive candidates for heat-mediated drug release [133]. The optimal resonance wavelength is determined by the physical parameters of the nanoparticles (e.g. size, shape, surface coverage and surface area) making the engineering of their many physiochemical properties critical [131].

Previous studies involving the use of AuNP both during and post cluster assembly have previously been reported by the group [94]. These studies involved the use of AuNP to stop IONPC assembly, producing magnetic plasmonic mixed nanoparticle clusters of controlled size. In addition to this, attempts were made for the dispersion of IONPs in aqueous medium by polymer-mediated phase transfer with some success.

The aim of the work presented in this chapter was to assess the colloidal stability of Au-stabilised IONPCs in an attempt to understand the impact of AuNPs on the cluster assembly and redispersion, with a view to optimising the composites for eventual phase transfer into aqueous medium. In the first part of this chapter, we present the synthesis of iron oxide nanoparticles by thermal decomposition, in addition to the synthesis of gold nanoparticles for NPC assembly attenuation. IONP stabilised by oleic acid/oleylamine and oleylamine only were synthesised, and the kinetics of their assembly were compared. The second part of this chapter then focuses on the assembly of IONPCs and the effects of further surfactant and/or AuNP additions on the colloidal stability of the suspensions.

5.2 Experimental

5.2.1 Synthesis of Iron Oxide nanoparticles by thermal decomposition of Iron precursors

Materials

Iron(III) acetylacetonate (≥99.9% trace metals basis), 1,2-hexadecanediol (Technical grade, 90%), oleic acid (≥99.0%), oleylamine (≥70% GC, Fluka), diphenyl ether (99%) and ammonium hydroxide (28% NH_3 in water, ≥99.99%) were purchased from Sigma Aldrich. All other bench solvents were used as required.

Synthesis

In a typical synthesis, the required amount of oleic acid and oleylamine (depending on the desired surfactant to iron precursor ratio) was weighed into a three-necked round bottomed flask. Iron (III) acetylacetonate (2 mmol) and 1,2-hexadecanediol (10 mmol) were then weighed out and transferred into the reaction vessel, along with 20 mL of diphenyl ether. All reagents, once combined, were purged with nitrogen for a period of 15 minutes before the pipette was raised from the solution and heating under reflux was commenced. A heating mantle was used to provide the heat required for the reaction, and the dial was turned to maximum to achieve an approximate reflux temperature of ~262˚C. Once this temperature had been reached, reflux for an additional 15 minutes was observed. The solution (now a dark brown colour) was allowed to cool to room temperature before adding 60 mL of ethanol, shaking the flask, and allowing the particles to precipitate over a bar magnet. Precipitation times were often slow and required to be left over night in some cases. Once precipitation was complete, the upper solvent layer (a transparent orange colour) was removed, leaving behind a dark brown (almost black) precipitate. One fifth of the initial amounts of oleic acid and oleylamine were then weighed out and mixed with a 20 mL volume of heptane. This solution was added to the reaction flask and was shaken and left to settle. After a period of 15-20 minutes, a further 60 mL of ethanol was added to the flask, and the washing process was repeated as carried out previously. The final precipitate was

redispersed in 10-15 mL heptane (SZ-IONP) and centrifuged at 13,200 RPM (16,100 RCF) to remove large aggregates.

The above synthesis was also carried out in the absence of oleic acid, with twice the typical amount of oleylamine to facilitate surface coverage of the IONP produced (SZ-OAm IONP).

5.2.2 Synthesis of Dodecanethiol (DDT)-stabilised Gold Nanoparticles

Materials

Hydrogen tetrachloroaurate (≥ 99.9%), dodecanethiol (DDT; ≥ 98%), and sodium borohydride ($NaBH_4$;≥ 98.5%), were purchased from Sigma-Aldrich. Tetraoctylammonium bromide (TOAB ≥ 98%) was obtained from Fluka.

Synthesis

Dodecanethiol-derivatised gold NPs were synthesised in a two-phase liquid-liquid synthesis as reported by Brust and co-workers [134]. Prior to nanoparticle synthesis, it was vital that all glassware was primed with aqua regia, a concentrated mix of nitric and hydrochloric acids in a volume ratio of 1:3 respectively to ensure no residual materials existed on the walls of the glassware from prior syntheses. A typical nanoparticle synthesis was then conducted as follows; a solution of TOAB in toluene (32 mL, 50 mM) was first prepared and subsequently added to a 100 mL round-bottomed flask and stirred with a magnetic stir bar under gentle heating to completely dissolve the solid material into solution. Following this, an aqueous solution of hydrogen tetrachloroaurate (10 mL, 30 mM), appearing bright yellow in colour, was added in a dropwise manner to the organic phase in the flask under vigorous stirring. The stirring was continued until the tetrachloroaurate was completely transferred into the organic layer (~30 min). The mixture turned from a yellow to red-brown colour during mixing, and separated into two phases on discontinuation of stirring, when it was observed that the mixture separated into a toluene phase (red-brown in colour) and a colourless aqueous phase. The mixture was placed into a 250 mL separating funnel, and the lower aqueous layer was removed. The toluene layer was then released into a 100 mL conical flask, and, on

continuation of magnetic stirring, a 100 μL aliquot of dodecanethiol was introduced to the mixture. A freshly prepared aqueous solution of sodium borohydride (10 mL, 0.4 mM) was then added dropwise to the flask with vigorous stirring. The colour changed from red-brown to dark purple upon reduction. The two phase mixture was covered and stirred at room temperature for 2-3 hours. The stirring was then discontinued, upon which the two phases separated, and the dark purple organic phase was removed and transferred to a separate glass flask. A 25 mL aqueous solution of H_2SO_4 (1 drop conc. H_2SO_4 in 25 mL H_2O) was added to bring the pH to 4, after which the lower aqueous layer was removed using a separating funnel. 25 mL of H_2O was then added, and the separation process was repeated. This step was carried out 4 further times before drying the organic layer over anhydrous $MgSO_4$. The resulting solution was filtered using a Buchner filtration apparatus and the suspension of TOAB-Au nanoparticles was collected in the conical flask. Ethanol (~ 50 mL) was added to the flask to precipitate the gold nanoparticles. This required the mixture to be kept in the freezer at -20°C overnight. This resulted in the formation of a dark purple-brown precipitate had settled to the bottom of the flask. The precipitate was once again filtered under reduced pressure using a Buchner funnel, washed with ethanol, and suspended in 40 mL heptane to produce the final suspension, which appeared dark purple in colour. The suspension was centrifuged a number of times for periods of 30-45 minutes at 13,200 RPM **(**16,100 RCF) using a tabletop centrifuge (Eppendorf 5415 D) to remove any larger or aggregated particles. The dark purple supernatant was collected, characterised by PCS, and utilised for nanocluster assembly experiments.

5.2.3 Nanoparticle Cluster (NPC) assembly experiments

Iron-oxide NP cluster assembly

Prior to all assembly experiments, cyanopropyl (CN)-modified silica (30-70 μm, Alltech Associates; 50.2 mg) was placed in a quartz cuvette and spread evenly to form a thin layer at the bottom. A small aliquot (3-4 drops) of heptane was then carefully dripped down the side wall of to ‘fix' the silica to the base of the cuvette in order to prevent aggregation when the nanoparticle suspensions were later added on top of the silica. A 1.2 mL aliquot of appropriately diluted iron-oxide

nanoparticle dispersion was carefully placed in the cuvette over the thin silica layer, taking care not to agitate the silica at the bottom. This was usually performed by adding two successive 600 μL aliquots. /the hydrodynamic characteristics of the suspension was then observed using PCS analyses (High Performance Particle Sizer (HPPS), or a Zetasizer NanoZS, Malvern Instruments; Worcestershire UK) where the average hydrodynamic diameter was continuously monitored). On removal of the cuvette from the instrument following assembly experiments, it was observed that the nanoparticles had deposited themselves on the surface of the silica due to them being stripped of their stabilising surfactants. All measurements recorded in the software were then exported and studies of change in the d_{hyd}, PDI and derived count rate over time were conducted and plotted as shown in the results section below.

Attenuation of IONPC assembly by addition of further surfactants

Iron-oxide nanoparticle dispersions stabilised by oleic acid/oleylamine (OAc/OAm-stabilised IONPCs) or oleylamine only (OAm-IONPCs) were subjected to the assembly process as described above. Cluster assembly was allowed to proceed for varied periods of time, after which, the measurement was temporarily terminated and the cuvette was carefully removed from the instrument. A small volume (typically 50 μL) of oleic acid, oleylamine or gold nanoparticle suspension was then slowly and carefully added to the suspension of iron-oxide clusters. The cuvette was replaced in the instrument, and the light scattering measurements were resumed for an additional 2 – 20 hours with selection of the same attenuator position and measurement positioning to ensure that comparable count rates were obtained once the measurement was continued.

5.3 Characterisation

For correction of all results obtained for iron content, ICP-AES was used as also described. Thermogravimetric curves were also obtained on a Q Series Q-50 Thermogravimetric Analyser (TA Instruments, Delaware, USA) for IONP stabilised by either a mixture of oleic acid/oleylamine or oleylamine only, in a further attempt to understand the binding chemistry of the ligands on the surface.

5.4 Results and Discussion

5.4.1 Kinetics of assembly for OAc/OAm IONPCs (mixed surfactant IONPCs)

Figure 5.3 below outlines the first of a number of experiments for determining the optimum conditions for assembly of OAC/OAm-IONPCs (*i.e.* clusters formed from IONPs prepared using a mixture of OA and OAm). The IONP concentration was approximately 2 mM in this case, or a 1:20 dilution of the neat suspension (where Fe = 41 mM). In this figure, the d_{hyd} values, derived count rate and PDI are presented. The d_{hyd}, is found to increase over time. The derived count rate is a measure of the backscattered light intensity and the observed gradual increase in the count rate is a result of an increase in the number of larger particles, i.e. IONPCs, in the suspension. PDI values remained within an acceptable range of 0.18-0.22 indicating that controlled assembly processes had been achieved.

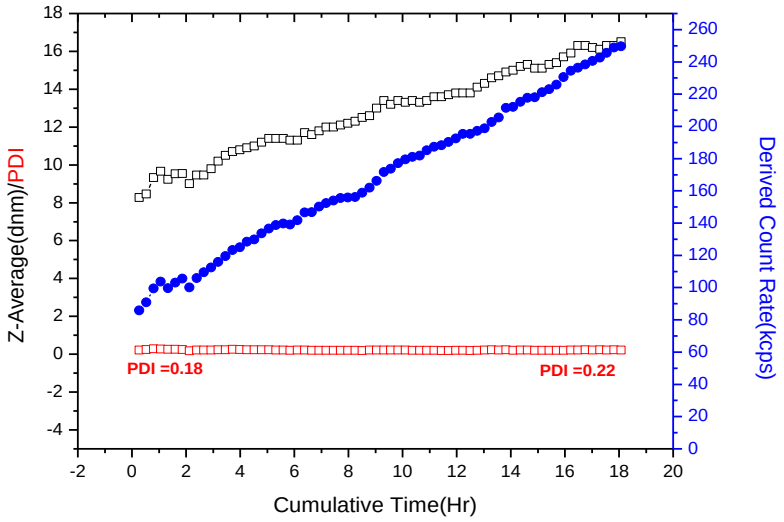

Figure 5.3: Typical assembly data obtained by PCS for the formation of OAc/OAm-IONPCs in heptane in the presence of silica. Fe concentration was approximately 2 mM. Included in the plot are values for the d_{hyd} (□), derived count rates (●) and the PDI values (□)

The growth rate in this instance, however, was very slow, with cluster sizes reaching approximately 17 nm (from a primary NP size of 8 nm) after a period of 18 hours. A more dilute nanoparticle suspension (0.8 mM Fe) was then used for the assembly process. The resulting assembly plot is as shown in Figure 5.4.

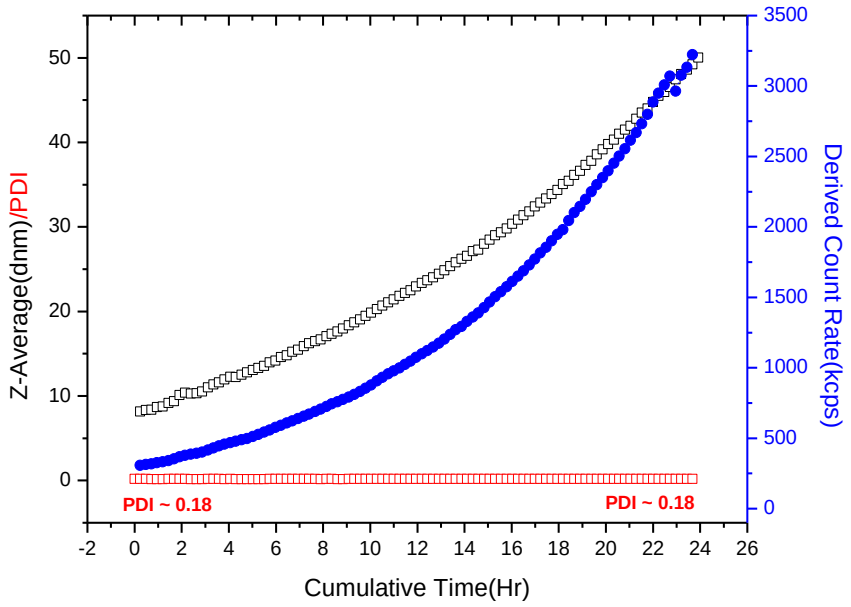

Figure 5.4: Typical assembly data obtained by PCS for the formation of OAc/OAm-IONPCs in heptane in the presence of silica. Fe concentration was approximately 0.8 mM. Included in the plot are values for the d_{hyd} (□), derived count rates (■) and the PDI values (□)

It can be noted that, at a lower IONP concentration, a more controlled and successful assembly was achieved, with clusters growing to approximately 50 nm over a 24 hour period. This increase in the observed growth rate can be attributed to the increase in the occurrence of NP^*- NP^* collisions as a result of a lower population of IONPC in the medium as compared to that used in Figure 5.3. This strongly suggests the presence of a NP^* de-activation process driven by the interaction of NP^* with NP. PDI values for the IONPCs improved from an average value of 0.20 in the initial experiment, to 0.18 in the case of the dilution used in Figure 5.4. This preservation of monodispersity, in addition to a steady increase in the d_{hyd} and derived count rate, throughout the course of the experiment is indicative of controlled NPC assembly. Nanoparticle concentrations within this range were therefore used for all subsequent assembly experiments.

5.4.2 Redispersion of OAc/OAm IONPCs using additional surfactant.

Figure 5.5 illustrates the assembly of OAc/OAm-stabilised IONPCs in heptane, with further addition of oleic acid to the growing clusters at d_{hyd} of approximately 45 nm. The observed effect was a partial yet rapid dispersion of the IONPCs to a hydrodynamic size of 34 nm, with no further decrease occurring (i.e. a plateau) in

the dispersion of the nanoparticles. In addition to this, a drop in the derived count rate is evident, which can be explained by a reduction in particle size. PDI values remained consistent throughout the course of the experiment, indicating that the observed particle size was a true representation of the entire nanoparticle suspension.

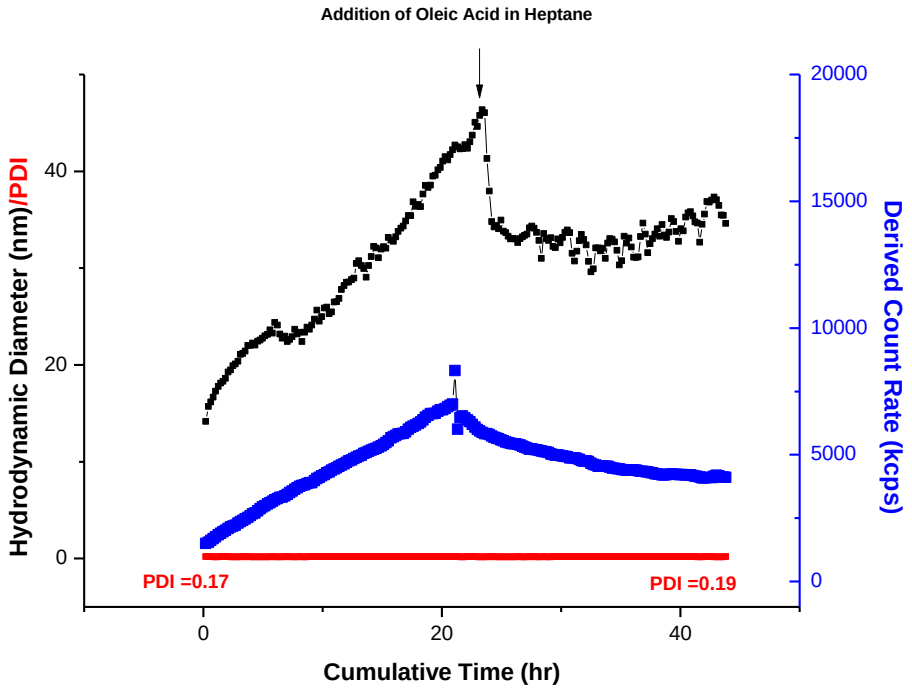

Figure 5.5 : Assembly of OAc/OAm-IONPCs in heptane with addition of oleic acid following cluster assembly. Included in the plot are values for the d_{hyd} (□), derived count rates (■) and the PDI values (■)

The introduction of oleic acid into the assembly medium stops the cluster assembly process, and a decrease in the hydrodynamic size and derived count rate is observed. We interpret this as being due to the oleic acid diffusing into the clusters and binding to the vacant sites. This increases the colloidal interparticle repulsions and the clusters partially disperse due to random thermal fluctuations.

In an attempt to observe a trend in the extent of dispersion as a function of concentration of oleic acid, the experiment represented in Figure 5.5 was repeated for three different concentrations of surfactant (Figure 5.6). Surfactant addition times varied as a result of different rates of cluster growth in all three cases. As the cluster sizes were all different, we calculated the percentage dispersion for each of the three assembly experiments. In this instance, it was observed that, as the concentration of oleic acid added to the growing clusters was decreased, the

percentage of dispersion increased from 64% for the highest concentration of oleic acid (6 mM), to 86% and 91% for the 4 mM and 2 mM solution additions respectively.

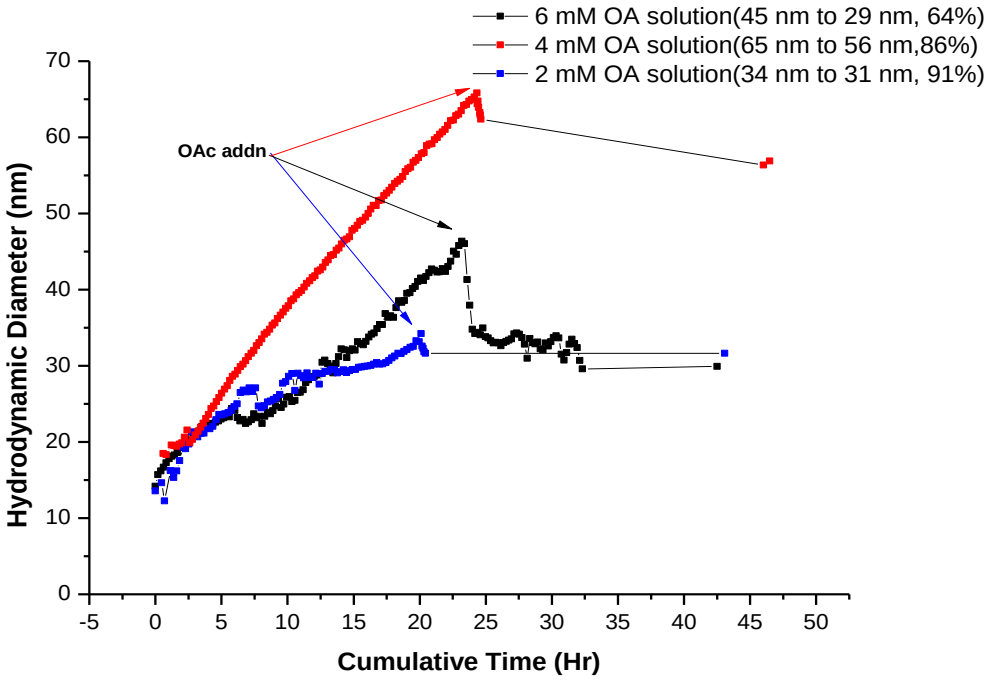

Figure 5.6: Addition of oleic acid in a range of concentrations to growing OAc/OAm-IONPCs

Due to the difference in cluster size at the time of surfactant addition, the three plots were scaled to a common value (so that the point of addition was at ~65 nm) in an effort to visually observe the effect of surfactant addition on each IONPC suspension (Figure 5.7).

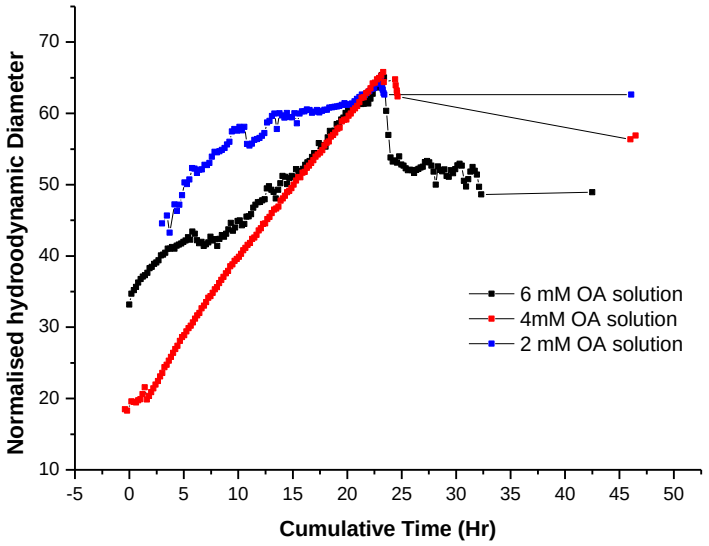

Figure 5.7: Scaled plot of oleic acid addition experiments (Figure 5.6) All sets of data were scaled to a common hydrodynamic diameter at the point of surfactant addition for the purpose of comparison.

This shows that the plateau in the size was reached more quickly at lower concentrations of oleic acid addition. As the cluster sizes upon surfactant addition in this experiment were all different, however, we cannot use this as a true representation of the relationship between surfactant addition and rate of dispersion.

A second series of experiments with varied concentrations of oleic acid were performed for three separate IONPC assemblies of similar size. The percentage dispersion (i.e. the percentage by which the clusters reduced in size following addition of oleic acid) was calculated for each experiment and the results are presented in Figure 5.8 below. It was observed that, for the highest concentration of oleic acid added (6 mM), the calculated percentage of dispersion was significantly higher (76%) than those calculated for the more dilute oleic acid additions; 44% and 55% for 3 and 2 mM OA, respectively. This suggests that the rate of dispersion is somewhat dependent on the concentration of oleic acid. We did not, however, observe proportionality between the concentration of oleic acid added and the percentage of dispersion in these experiments.

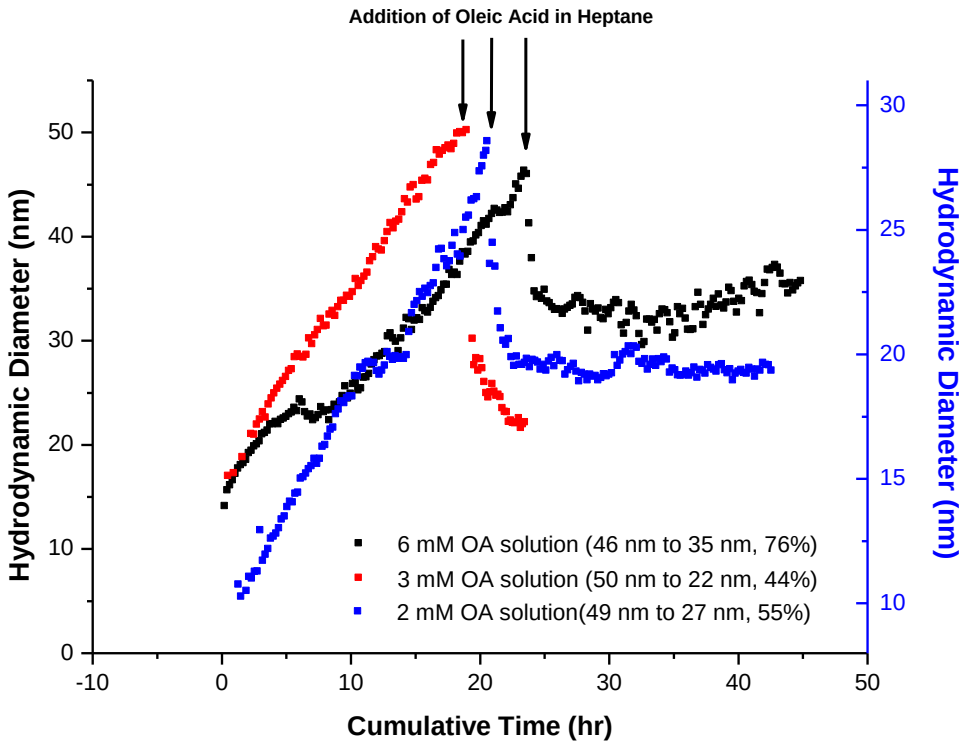

Figure 5.8: Second experiment for the addition of oleic acid in a range of concentrations to growing OAc/OAm-IONPCs

Finally, the effect of oleylamine addition to oleic acid/oleylamine stabilised NPCs was also investigated (Figure 5.9). Once again, rapid dispersion of the clusters was evident, with d_{hyd} values decreasing from 50 nm to 30 nm within 2-3 hours of surfactant addition. It should be noted again that d_{hyd} values comparable to the initial primary particle sizes were not achieved upon redispersion for both of the above addition experiments. This may have been due to an insufficient amount of surfactant being added to the suspension to encourage total cluster dispersion.

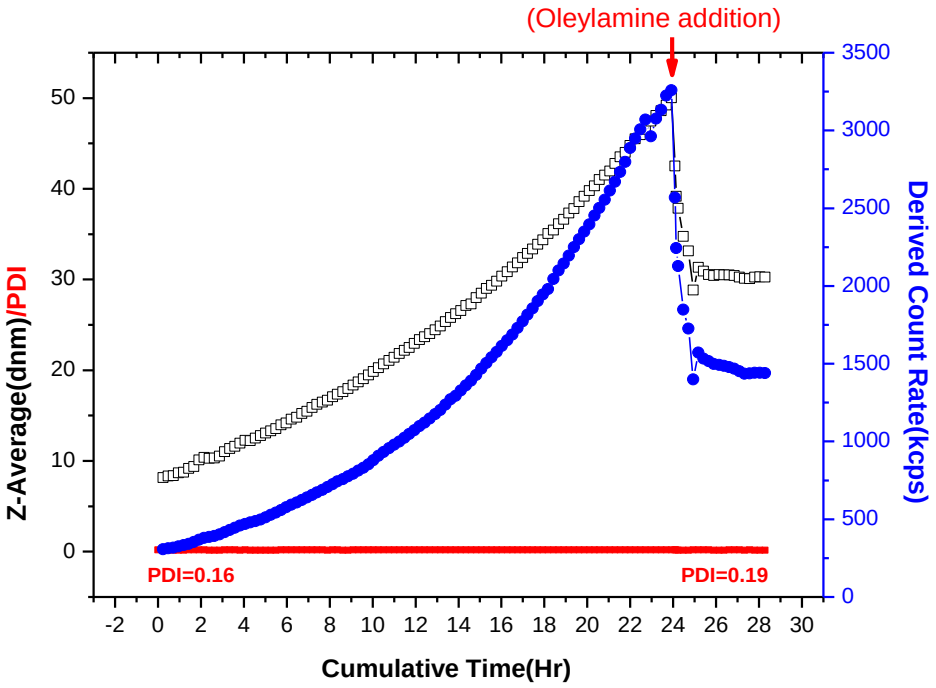

Figure 5.9: Assembly of OAc/OAm-IONPCs in heptane with addition of oleylamine following cluster assembly. Included in the plot are values for the d_{hyd} (□), derived count rates (■) and the PDI values(■)

It should be noted that concentration dependence experiments were only carried out for oleic acid additions to IONPCs, Future work could extend to similar studies of oleylamine addition in a number of different concentrations to IONP assemblies.

5.4.3 Attenuation of OAc/OAm-IONPC assembly by addition of gold NPs with addition of further surfactant following assembly.

OAc/OAm-IONPCs were then assembled to a given size and DDT-stabilised AuNPs were added prior to subsequent addition of oleic acid. In the experiment shown in Figure 5.10, 50 µL of AuNP suspension was added to 55 nm IONPCs. On addition of the AuNP to the IONPCs in heptane, a cessation (or plateau) in the assembly was evident for a period of approximately 4 hours. This shows that the presence of the AuNP stabilises the IONPCs, presumably by occupying the vacant sites on the cluster surface preventing further assembly.

It is apparent that the presence of the AuNPs had a significant effect on the rate of decrease in both the hydrodynamic size and the derived count rate following further oleic acid addition. In the absence of AuNP, both d_{hyd} and count rate decreased rapidly (12 nm/hr) (Figure 5.5), whereas a more gradual decrease was evident in this case (7 nm/hr). This may once again be attributed to increased stability of the clusters due to the presence of AuNP and the partial shielding of the surface with a non-desorbing ligand, DDT in this case.

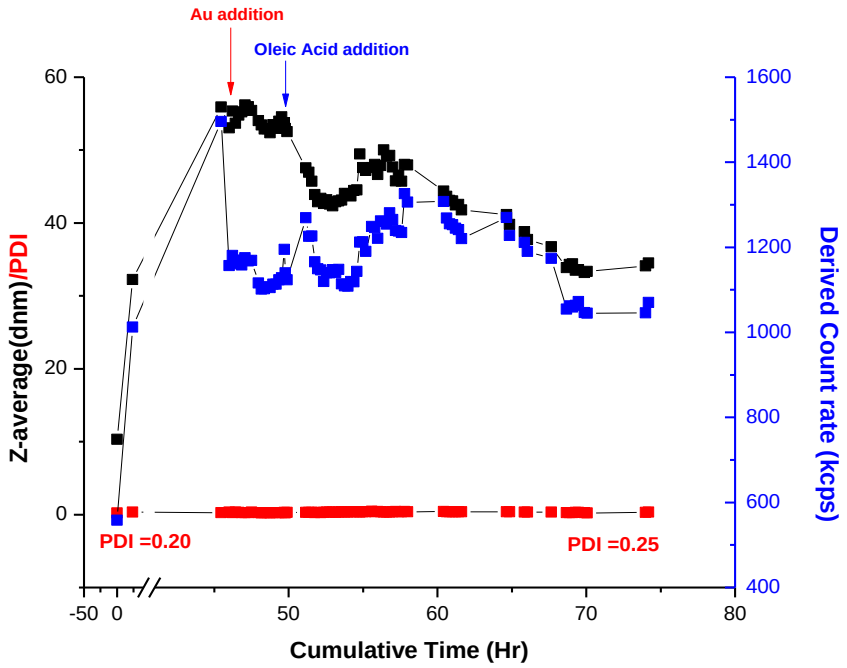

Figure 5.10: Attenuation of assembly by addition of AuNP followed by oleic acid to facilitate nanoparticle dispersion. Included in the plot are values for the d_{hyd} (□), derived count rates (■) and the PDI values (■)

The experiment shown in Figure 5.10 was then repeated for a number of concentrations of oleic acid addition, and the results are as presented in Figure 5.11. As before, the addition of AuNP (50 µL) stopped any further assembly and addition of oleic acid resulted in partial dispersion of the IONPCs. The result was a fairly similar percentage reduction in the size as the oleic acid concentration was reduced with decreases of 69%, 62% and 79% for oleic acid concentrations of 6, 4 and 2 mM, respectively. Once again, on reducing the amount of oleic acid, we observe that the plateau is reached earlier, as was the case in the absence of AuNP (Figure 5.6).

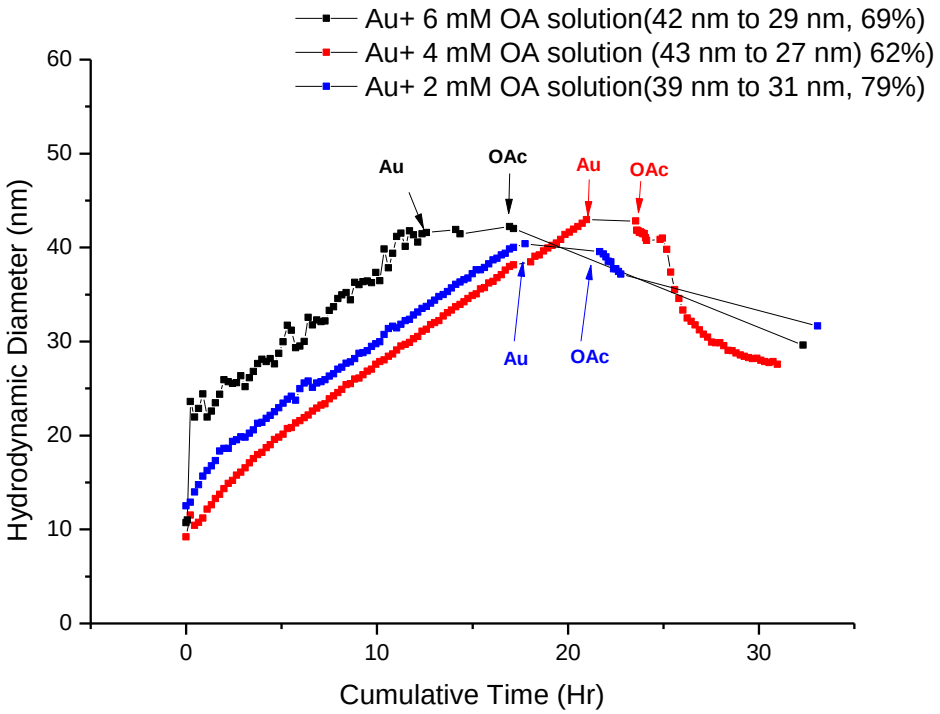

Figure 5.11: Second experiment on the addition of AuNP prior to oleic acid to growing OAc/OAm-IONPCs. Note once again that the volume of AuNP added was kept constant while the concentration of oleic acid added was varied and surfactant addition times were different as a result of varied growth rates

Similarly, the effect of AuNP on further oleylamine addition to OAc/OAm-IONPCs was also investigated (Figure 5.12). On addition of AuNP, a plateau in the size was observed (inset). However, on addition of the oleylamine, the size increased dramatically and was then observed to decrease once again. In addition to this, the PDI doubled, and the count rate was seen to decrease, suggesting that aggregates had rapidly formed and subsequently precipitated from the suspension. This suggests that some of the oleylamine becomes bound to the IONPC surface, rather than diffusing into it as in the case for oleic acid, so disrupting the colloidal stability.

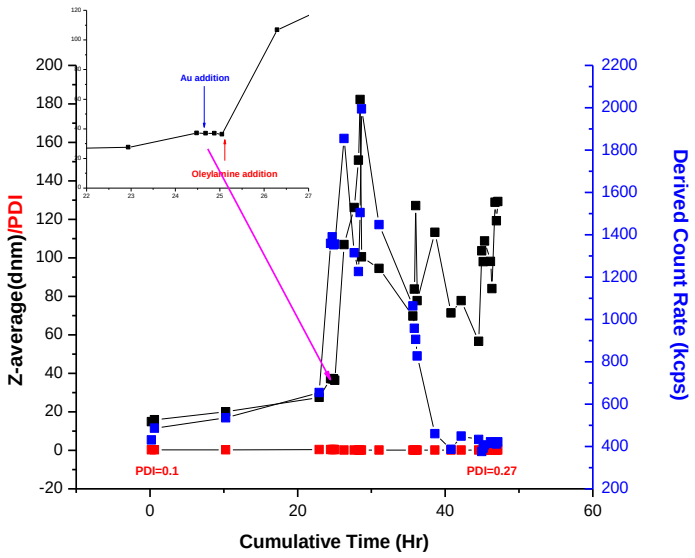

Figure 5.12: Addition of AuNP prior to oleylamine addition to growing OAc/OAm-IONPCs. . Included in the plot are values for the d_{hyd} (□), derived count rates (■) and the PDI values (■)

5.4.4 Kinetics of assembly for OAm-IONPCs (single surfactant IONPCs)

For the purpose of comparison, nanoparticles stabilised by oleylamine only were also prepared using the approach of Sun et. al. but with twice the amount of oleylamine (i.e. no oleic acid was used). The kinetics of their assembly was also studied, as shown in Figure 5.13 and Figure 5.14.

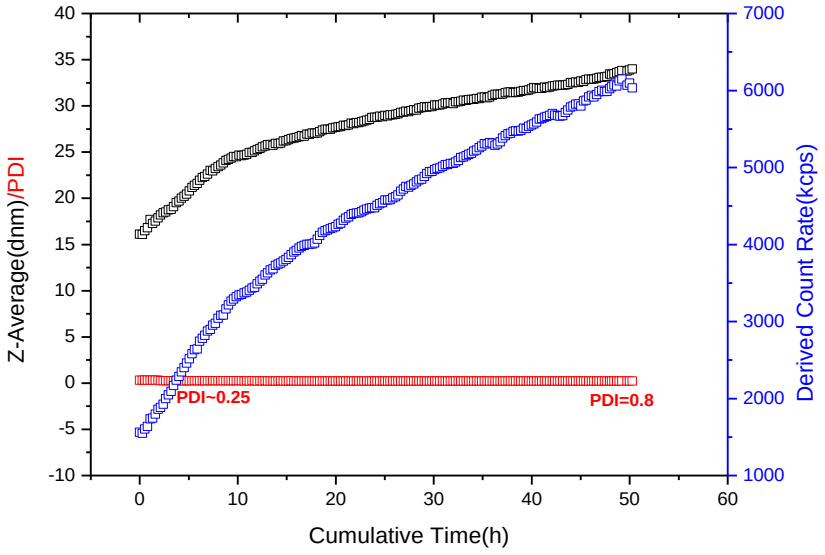

Figure 5.13: Typical assembly data obtained by PCS for the formation of OAm-IONPCs in heptane. Fe concentration was approximately 2 mM. Included in the plot are values for the d_{hyd} (□), derived count rates (●) and the PDI values (□)

Figure 5.13 shows typical assembly data for a suspension of OAm-IONP (Fe = 2 mM) in heptane. On assembly of the IONPCs at this nanoparticle concentration, we observe an increase in both the d_{hyd} and the derived count rate over time. This suggests that a gradual assembly had been achieved with IONPCs of approximately 35 nm being formed. The PDI values were seen to increase, however, indicating that the increase in the d_{hyd} is associated with uncontrolled aggregation. Despite the drawbacks, this experiment does suggest that oleylamine is subject to desorption.

A second dilution was performed at a lower nanoparticle concentration (where [Fe]=1 mM) for the OAm- IONP and the kinetics of the assembly are as shown in Figure 5.14 (below). Once again, a more dilute IONP suspension resulted in more controlled assembly, with clusters reaching approximately 60 nm while observing a steady increase in counts and PDI values of approximately 0.22 throughout the course of the experiment. It should be noted, however, that this was achieved over a period of 2 hours, indicating that the assembly was very rapid. It was concluded that, under the conditions shown here at least, the assembly of oleylamine-stabilised IONP could not be controlled as easily as their oleic acid/oleylamine stabilised counterparts. However, this is the first observation of CSD for a different ligand and it suggests the possible generality of the method.

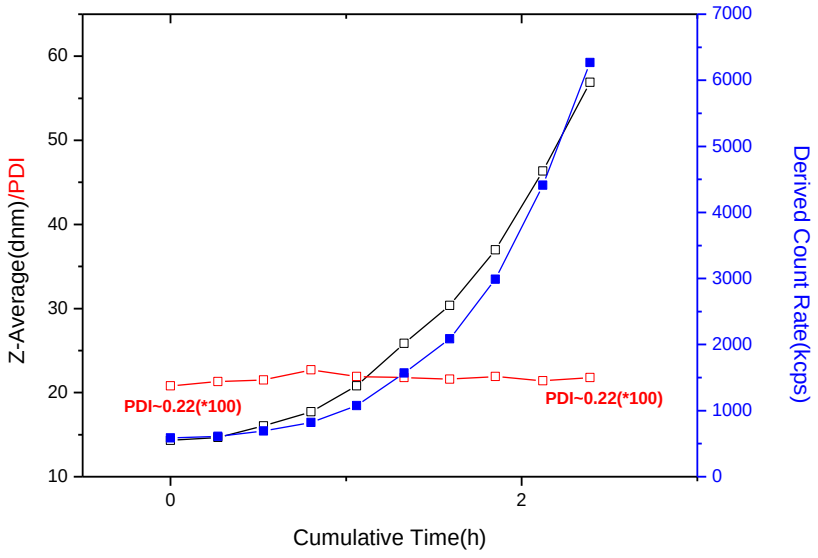

Figure 5.14: Typical assembly data obtained by PCS for the formation of OAm-IONPCs in heptane. Fe concentration was approximately 1 mM. Included in the plot are values for the d_{hyd} (□), derived count rates (■) and the PDI values (scaled by a factor of 100) (□)

5.4.5 Redispersion of OAm IONPCs using additional surfactant.

Further experiments similar to those carried out for OAc/OAm-IONPCs discussed in Section 5.4.2 above were carried out on a series of OAm-IONPC suspensions for comparison of the effect of further surfactant on the assembly process for clustered materials stabilised by a single surfactant. These studies would provide insight as to whether the method of IONP (and thus IONPC) stabilisation would impact the redispersion behaviour of the clustered materials upon further surfactant addition. It should be noted that similar Fe and surfactant concentrations were used for both mixed surfactant and single surfactant IONP experiments.

Figure 5.15 illustrates the addition of oleic acid to IONPCs stabilised using oleylamine only (OAm-IONPCs). The result was a gradual and partial dispersion of the clusters from 38 nm to 23 nm. It can be noted that the redispersion was not as rapid as previously observed for IONPCs stabilised by both oleic acid and oleylamine (Figure 5.5). This may be due to a lower affinity of the added oleic acid for the silica substrate, as compared to OA/OAm-IONPCs, as in the latter case the substrate has been exposed to OAc during the assembly stage. This could result in a slower desorption of oleylamine from the IONPC surface. Another possible explanation is that the difference is due to the process of oleic acid diffusion through the NPCs being slower for OAm-IONPCs than for the mixed surfactant IONPCs. It is difficult to explain this on the basis of the difference in headgroup as in both cases that group is bound to the NP surface. This suggests different NP surface morphology, *e.g.* phase defects or a different surface coverage for OAm stabilised NP, i.e. the nature of the NP* may be different.

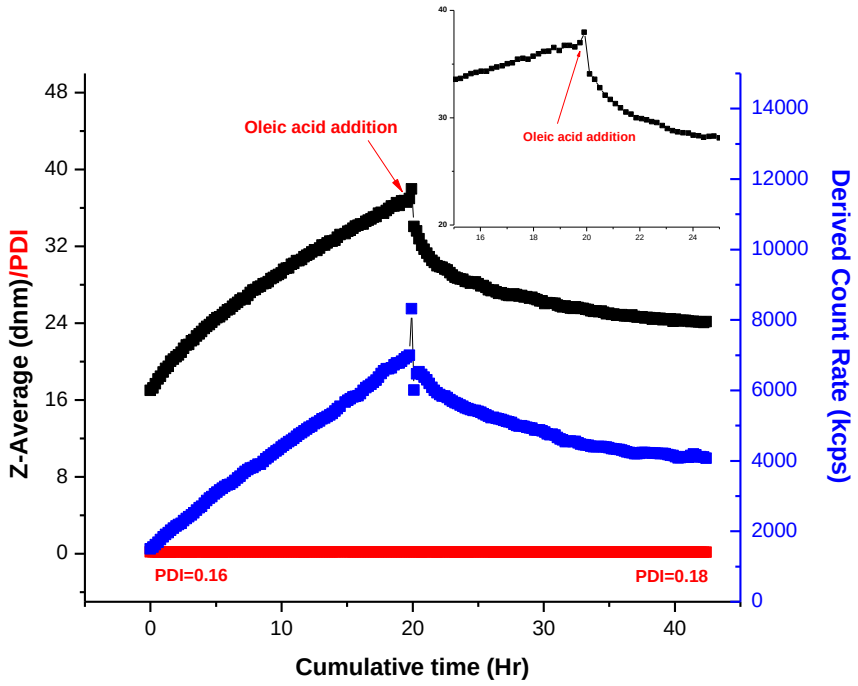

Figure 5.15: Addition of oleic acid to assembling OAm-IONPCs. Included in the plot are values for the d_{hyd} (□), derived count rates (■) and the PDI values (■)

The above experiment was then repeated for the addition of oleylamine to the nanoparticle clusters following assembly (Figure 5.16). The result was a very rapid dispersion from 42 nm to 20 nm, after which a plateau in the hydrodynamic size was observed. It should be noted that again the original dispersed IONP size was not recovered. A similar trend was observed for the mean count rate and the PDI was also observed to remain consistent throughout the experiment. In this instance, as there is no oleic acid to reduce the affinity of the oleylamine for the silica substrate, we observe a much more dramatic decrease in the measured d_{hyd} to a diameter much closer to the initial primary particle size.

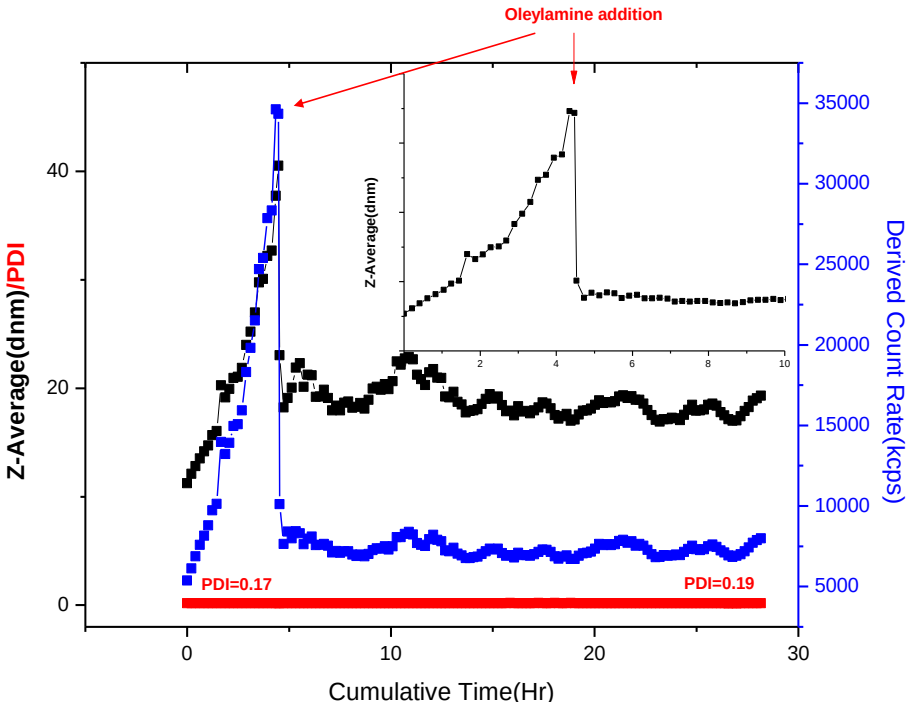

Figure 5.16: Addition of oleylamine to growing OAm-IONPCs. Included in the plot are values for the d_{hyd} (□), derived count rates (■) and the PDI values (■)

5.4.6 Attenuation of OAm-IONPC assembly by addition of AuNPs

Similar experiments to those presented in Section 5.4.3 were then repeated for OAm-IONPCs to which AuNP had been added (Figure 5.17). It should be noted that, for OAm-IONPCs, AuNP addition failed to fully attenuate assembly and, in some cases, cluster assembly appeared to continue at the same rate as was the case in Figure 5.17. In this particular experiment, 50 µL of AuNP suspension was added to the IONPC suspension in heptane at approx. 40 nm and the assembly continued at a similar rate to before AuNP addition. This could be due to an insufficient concentration of AuNPs added to attenuate the assembly, but as the same concentration was used as for the OAc/OAm-IONPC experiments, it is more likely that this observation arises due to the nature of the OAm-IONPC surface. The question remains as to whether the AuNPs have physisorbed onto the surface.

Upon oleic acid addition to Oam-IONPCs at a cluster size of ~50 nm, we do observe dispersion of the assembling IONPCs, albeit a gradual one (~2 nm/hr) similar to that observed for OAm-IONPCs in the absence of AuNP (~3 nm/hr)

(Figure 5.15). Once again, this gradual dispersion may be due to the oleic acid diffusing through the IONPCs (or Au-IONPCs).

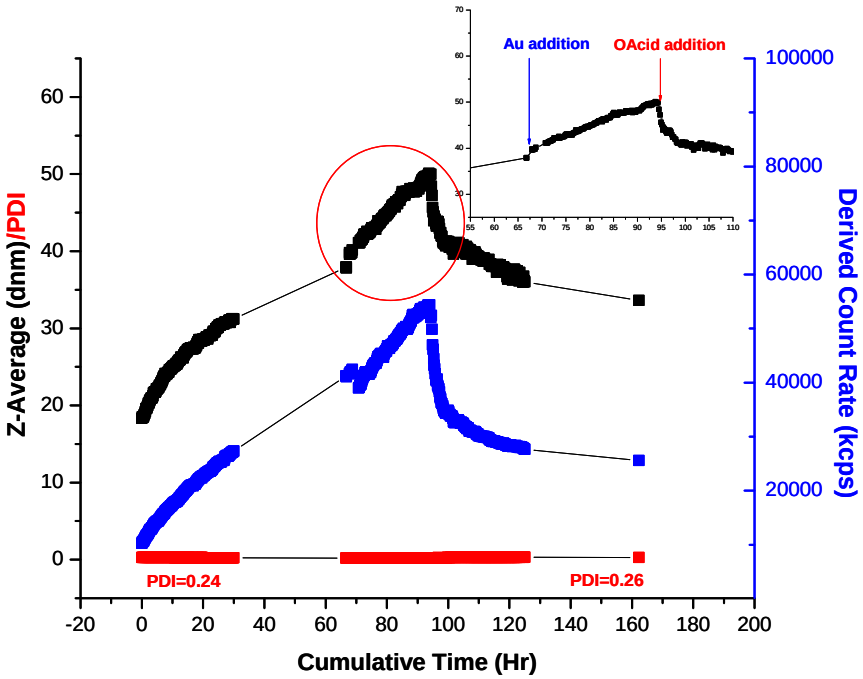

Figure 5.17: Addition of AuNP prior to oleic acid addition for growing OAm-IONPCs. Included in the plot are values for the d_{hyd} (□), derived count rates (■) and the PDI values (■)

The addition of oleylamine to Au/OAm-IONPCs, as shown in Figure 5.18 below, however, resulted in a different behaviour to that observed for OAm-IONPCs (Figure 5.16). On addition of AuNP, the assembly process was not fully attenuated, but a noticeable decrease in the growth rate was apparent, in addition to a more gradual dispersion following oleylamine addition. This may be attributed to partial stabilisation of the clusters by AuNP prior to surfactant addition, resulting in slower desorption of the surface-bound surfactant from the surface of the IONPCs, strongly suggesting the formation of Au/OAm-IONPCs as opposed to a mixture of AuNPs and OAm-IONPCs.

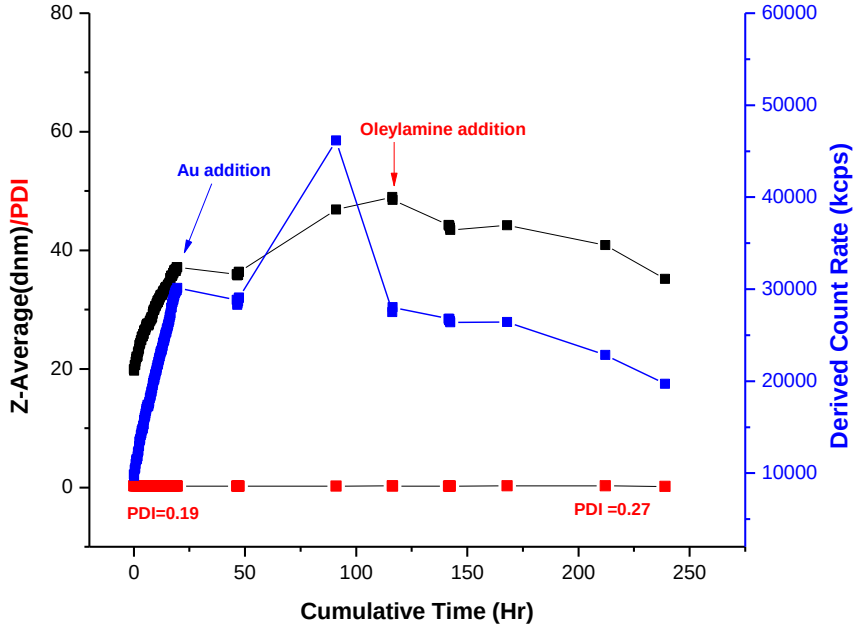

Figure 5.18: Addition of AuNP prior to oleylamine addition for growing OAm-IONPCs. Included in the plot are values for the d_{hyd} (□), derived count rates (■) and the PDI values (■)

5.5 Summary and Conclusions

The work presented in this chapter outlines the colloidal behaviour of mixed and single surfactant IONP and their assembly in organic medium in the presence of a competing substrate; CN-modified silica. In addition to this, studies on additional surfactant and/or AuNP additions were also investigated, in an attempt to understand the surface chemistry of the IONPCs, and the way in which the adsorbed surfactants were removed from their surfaces.

For mixed IONPCs, the addition of oleic acid to the clusters resulted in their dispersion, with a reduced percentage dispersion in addition to an earlier plateau observed for decreased concentrations of surfactant. Similarly, cluster dispersion was also observed upon oleylamine addition to the IONPCs, suggesting that oleylamine can diffuse into the clusters and bind to vacant sites in the absence of AuNP. On replicating these surfactant addition experiments in the presence of AuNP, the rate of dispersion was somewhat reduced upon oleic acid addition, suggesting that the AuNP act as a shield to the added surfactant attempting to bind to the IONPC surface. Further addition of oleylamine, however, resulted in further

aggregation of the clusters, possibly due to the retention of some additional oleylamine on the IONPC surface, due to the presence of surface AuNP.

For single surfactant IONPCs stabilised by oleylamine only, the addition of oleic acid resulted in a slower dispersion than observed for the mixed surfactant IONPCs with the same concentration of surfactant added in both cases. Upon oleylamine addition to OAm-IONPCs, a rapid dispersion was evident, possibly due to a difference in the nature of the activated nanoparticles (surface defects) in this case. Interestingly the TGA curves for both OAc/OAm-IONPs and OAm-IONP are identical (Figure 5.19), which supports this interpretation as opposed to the alternative; that there is a difference in the surface NP ligand density prior to initiating assembly.

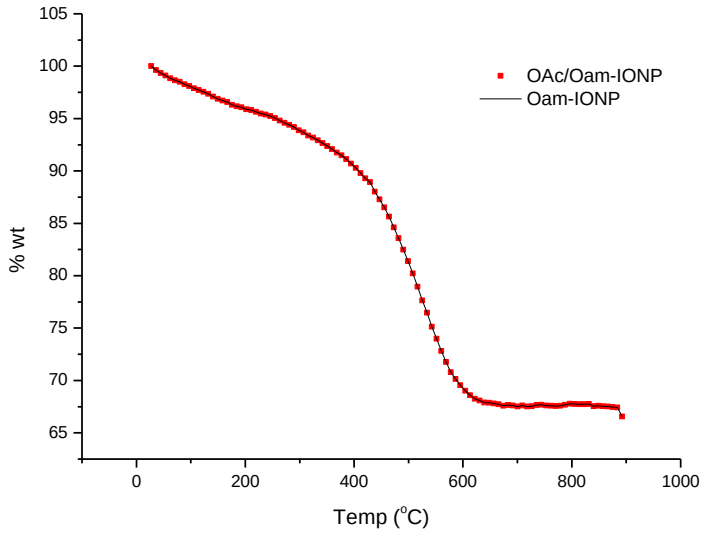

Figure 5.19: TGA curves outlining the % weight losses for both mixed surfactant (OAc/OAm) IONP and single surfactant (OAm) IONP

In the presence of AuNP, additional surfactant addition to OAm-IONPCs resulted in a reduced rate of re-dispersion in all cases which, once again, may be attributed to shielding and partial stabilisation of the IONPC surface. This, presumably, occurs by occupation of the vacant sites present on the cluster surface, thus preventing further assembly and resulting in a slower surfactant desorption from the surface of the IONPCs. This resulted in the production of Au-IONPC composite materials of controlled size by the addition of gold nanoparticles to growing IONPCs.

Several attempts were also made to complete NMRD analyses on the IONPCs shown in this chapter. Unfortunately, in each case, the colloidal stability of these materials on exposure to the magnetic field was insufficient for us to reach any firm conclusions on the magnetic order and relaxivities of the assemblies formed.

CHAPTER 6

NMRD Analysis in the Development of Composite Magnetic Nanomaterials

6.1 Introduction

In Chapter 4, we presented the formation of nanocomposite materials consisting of individually stabilised IONP and polymer nanoparticles, forming 'core-shell' structures, or 'surface decorated' materials, where NMRD studies demonstrated a noticeable increase (core-shell) or decrease (surface decorated) in the measured r_1 at all frequencies in comparison to that measured for the dispersed IONP. This chapter presents an NMRD and DLS study into the properties of two further types of IONP-based nanocomposite materials; lipid-stabilised IONPCs, or 'magnetoliposomes', and fatty acid bilayer stabilised IONPCs, or BPCs, in an attempt to understand their magnetic resonance properties and to investigate their potential as magnetic nanomaterials/drug carriers for *in vivo* imaging and cancer therapy.

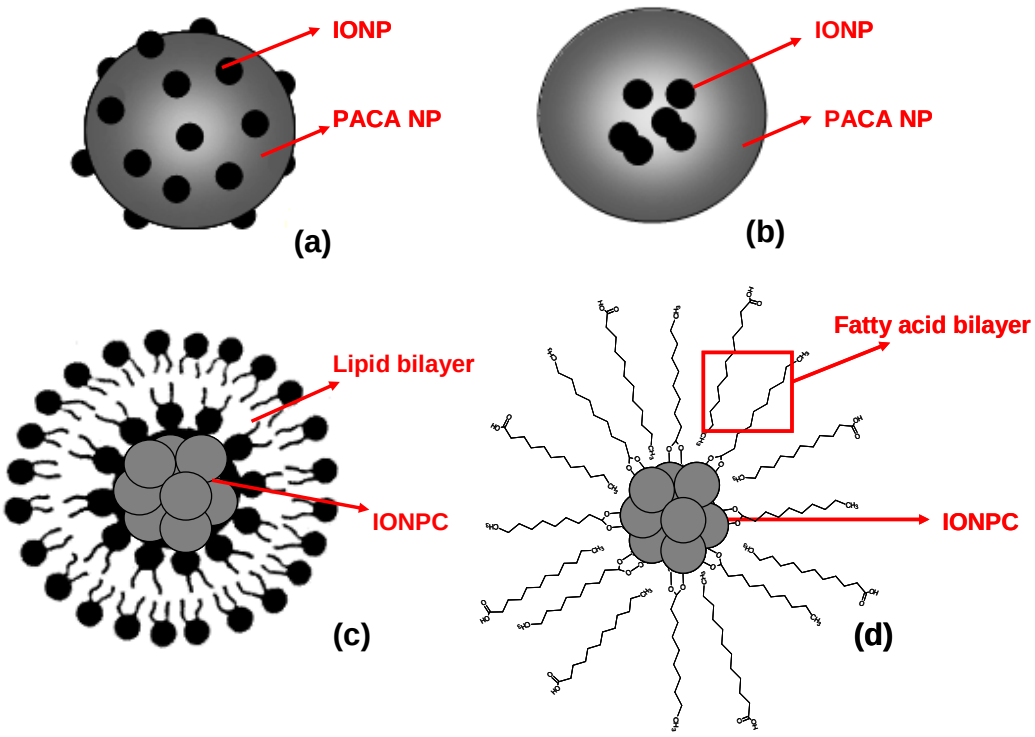

Figure 6.1: General structures for (a) surface decorated IONP/PACA (b) core-shell IONP/PACA (c) magnetoliposome and (d) fatty-acid bilayers

Liposomes, aqueous compartments formed by a lipid bilayer, were first applied in biomedicine by Bangham *et. al.* in 1965 [135]. Since then, their use in the fields of diagnostic imaging, drug delivery and hyperthermia have been extensively reported in the literature owing to numerous beneficial attributes such as their colloidal stability, biocompatibility, encapsulation potential and surface characteristics [99,

102, 136, 137]. A significant advantage of these materials is that they offer the capability to encapsulate both contrast agents and therapeutics in the same delivery vehicle, thus allowing for simultaneous diagnostic imaging and treatment. In addition, their membrane dynamics can be exploited for triggered drug release, allowing more efficient delivery of therapeutics to target tissues [138]. More interesting, for the present work, are the recently described 'magnetoliposomes' which, as the name suggests, possess a magnetic material (*i.e.* IONPs) in the interior of the liposome structure, with or without an aqueous lumen. The characteristic high magnetic moments of these materials suggests possible applications for T_2-weighted cellular imaging [52]. Bruns et. al., for example, have previously demonstrated the use of IONP-containing nanosomes of different functionalities (quantum dots, radiolabels and lipoproteins) for real-time MRI imaging and quantification of lipoprotein kinetics *in vivo* [139].

The term 'magnetoliposome' was first introduced by De Cuyper and coworkers [140], to describe structures where the interior of the phospholipid vesicle was entirely packed with magnetic nanoparticles. The phospholipids are thought to displace the surfactant molecules and arrange in a bilayer configuration around the iron-oxide core (Figure 6.1 (c)), with the inner phospholipid layer adsorbed directly onto the nanoparticle surface and form solid magnetoliposome, or SML, structures [141].

Alternatively, the solid nanoparticles may be contained within the aqueous compartment of a conventional liposome, forming what we will refer to as aqueous magnetoliposomes, or AMLs [52]. The advantage of the AML structure is that it allows for encapsulation of multiple materials (magnetic NP, therapeutics, contrast agents etc.) into the aqueous core, as shown in Figure 6.2 overleaf.

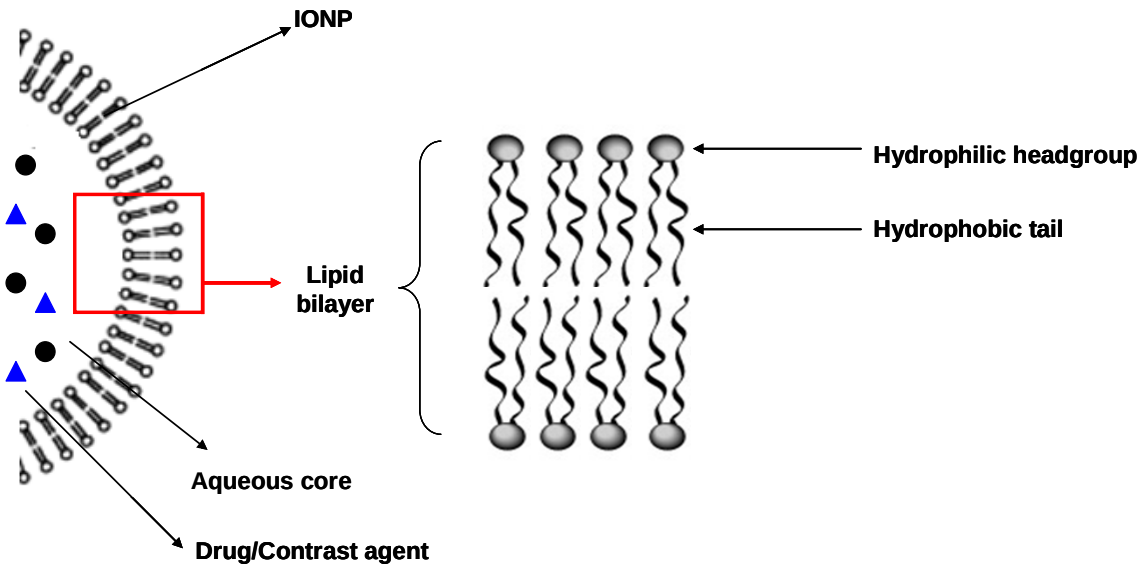

Figure 6.2: General structure for the arrangement of a lipid bilayer in an aqueous magnetoliposome structure

For the purpose of the work presented in this thesis, IONPCs were encapsulated by a bilayer of 1,2-Dioleoyl-*sn*-glycero-3-[phospho-rac-(1-glycerol)] (sodium salt) (DOPG) (18:1) as illustrated by Figure 6.3 below, to form SMLs [52].

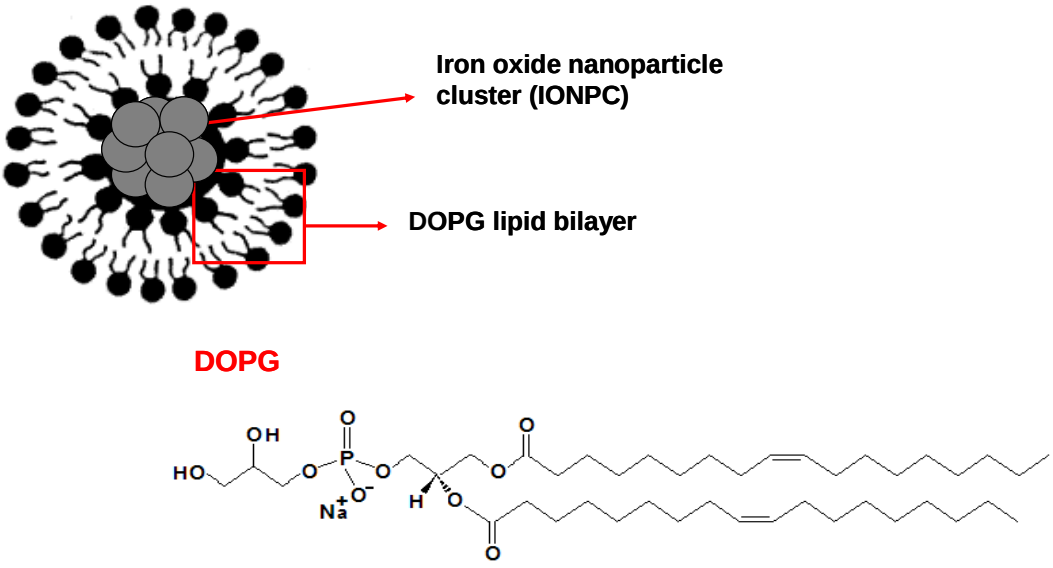

Figure 6.3: General structure for IONPCs stabilised by a DOPG bilayer

The second type of nanocomposite presented in this chapter are magnetic IONPCs stabilised by fatty acid bilayers, or BPCs. These materials are stabilised with a primary fatty acid layer that is chemisorbed onto the surface of the nanoparticle or

nanocluster, through the carboxylate groups, and a secondary physisorbed layer whose alkyl chains interpenetrate the primary layer with the hydrophilic head groups pointing outward. This provides for successful aqueous dispersion of BPCs. Materials of this type have been extensively reported in the literature as effective diagnostic T_2 contrast agents in MRI imaging as a result of their increased r_2 values (and the associated r_2/r_1 ratios) due to IONP clustering [123, 141]. The extent of this clustering has a noted effect on the magnetic properties of the material, in particular on their magnetic anisotropy [49], and is therefore critical to their efficacy for biomedical application. BPCs synthesised in the work presented here were stabilised by a primary layer of decanoic acid (C10:0) and a secondary layer of lauric acid (C12:0) [49], as illustrated by Figure 6.4 below.

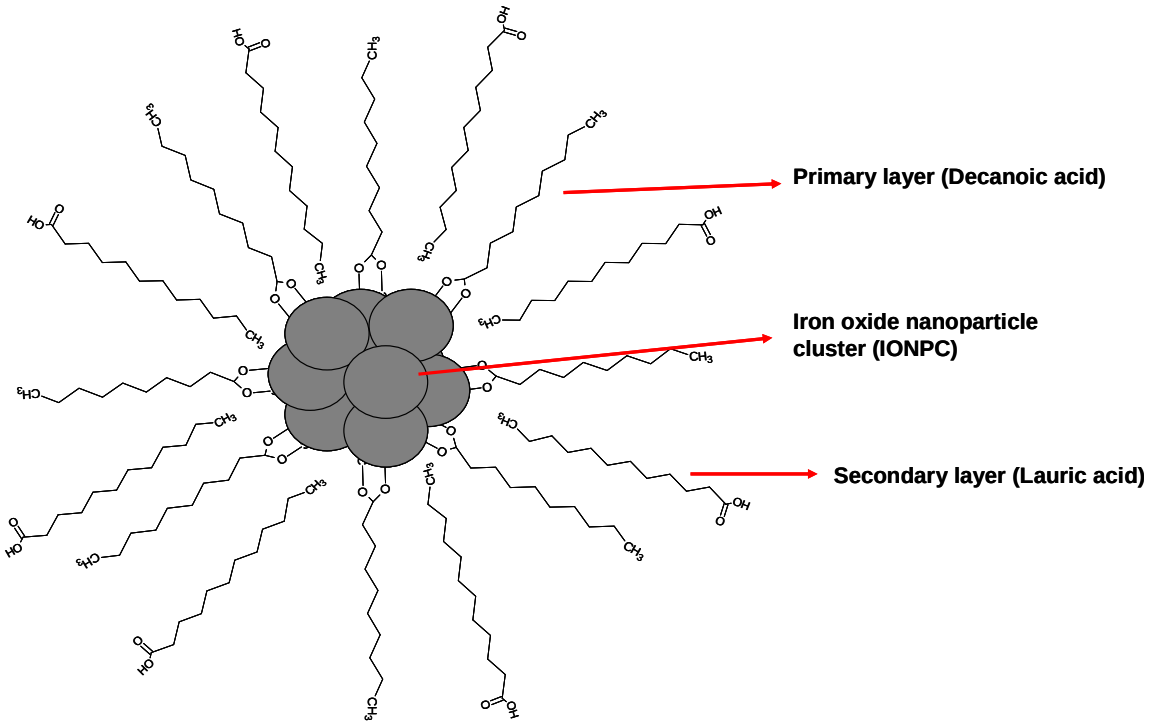

Figure 6.4: General structure for the arrangement of a BPC nanocomposite with IONPCs stabilised by decanoic acid(primary layer) and lauric acid (secondary layer)

The aim of this chapter is to present these two additional methods for controlled assembly formation, and to contrast the effect of nanocomposite structure on the materials relaxivity in the clinical ranges and on the NMRD profiles for the full range of nano-composite materials discussed in the thesis. Note that, unlike the PACA based nanocomposites, SMLs and BPCs are dense clusters of IONPs.

6.2 Experimental

6.2.1 Preparation of solid magnetoliposomes (SMLs) by alkaline coprecipitation of iron salts

Materials

1,2-Dioleoyl-*sn*-glycero-3-[phospho-rac-(1-glycerol)] (sodium salt) (DOPG) (18:1) was purchased as a lyophilised powder (> 99%) from Avanti Polar Lipids (Alabaster, AL, USA) and stored at -20°C. Iron (II) chloride tetrahydrate (> 99%) was purchased from Sigma-Aldrich (Ireland) and Iron (III) chloride-6-hydrate (> 99%) was purchased from Riedel-de-Haën (Seelze, Germany). All reagents were used without further purification.

Synthesis

The method used is a modification of that described by Meledandri *et. al.*, [52]. Iron salts ($FeCl_3$•$6H_2O$ and $FeCl_2$•$4H_2O$) in a 2:1 molar ratio were added with stirring to 20 mL deoxygenated H_2O in a 3-neck round-bottomed flask and the solution was slowly heated to 80°C under strong magnetic agitation. After 30 minutes at this temperature, one fifth of the total phospholipid to be added (0.85 mM dissolved in 0.5 mL methanol) was added to the reaction mixture, immediately followed by the addition of 1.5 mL of 33% ammonia to precipitate the metal ions. A black precipitate was immediately observed, indicating the formation of magnetite nanoparticles. The remaining DOPG (3.41 mM dissolved in 1 mL methanol) was then slowly added to the mixture over 5 minutes, after which crystal growth was allowed to proceed for a further 15 minutes with vigorous stirring. The suspension was then cooled to room temperature prior to subjecting the suspension to a washing cycle five times using a 50/50 v/v solution of acetone/methanol, and the flask containing the DOPG-coated IONP was placed over a bar magnet to isolate the nanoparticles. During the final wash cycle, the sample was resuspended in 10 mL DI H_2O in preparation for magnetoliposome formation through the addition of a secondary, physisorbed DOPG layer. In order to achieve this, the IONP temporarily dispersed in H_2O were heated to 65°C under a steady stream of N_2 with vigorous stirring in a 3-neck round-bottomed flask fitted with a water-cooled reflux condenser. After 30 minutes at 65°C, 10 mM

ammoniated DOPG was slowly added to form a secondary phospholipid layer around the nanoparticles, and the suspension was stirred for an additional 30 minutes. Upon cooling to room temperature, the suspension was sonicated for 30 minutes in a sonication bath, and was then placed over a bar magnet for 20-30 minutes. The supernatant was then decanted and retained for further characterisation.

6.2.2 Preparation of bilayer fatty acid-stabilised IONP clusters (BPCs)

Materials

Iron (II) chloride tetrahydrate (> 99%) was purchased from Sigma-Aldrich (Ireland) and Iron (III) chloride hexahydrate (> 99%) was purchased from Riedel-de-Haën (Seelze, Germany) and were used without further purification. Fatty acids (decanoic acid and lauric acid) were also obtained from Sigma-Aldrich (purity >99.9%), and again were used without further purification.

Synthesis

The method used is a modification of that described by Gosh, Clarke *et. al.*, [49]. A mixture of iron (III) chloride hexahydrate and iron (II) chloride tetrahydrate, in a molar ratio of 2:1 (typically 0.5 and 0.25 mmol), was dissolved in 20 mL deoxygenated water, heated slowly to 80°C with strong magnetic stirring and maintained for 30 min at that temperature. Following this, one fifth (0.08 mmol) of the total amount of primary surfactant (decanoic acid C10:0) was added to the reaction solution followed by immediate addition of the required volume 0.5 mL of 33% ammonia to facilitate IONP precipitate the IONP. The remaining surfactant (0.32 mmol) was then added to the mixture in five parts over a 5 minute period, after which vigorous stirring was continued for a further 15 min at 80°C. The suspension was then cooled to room temperature and precipitated in one step using a 50:50 v/v mixture of acetone and methanol and a strong bar magnet. This process was repeated five times to remove any excess surfactant that was not bound to the IONP surface. The washed particles disperse readily in non-polar organic solvents to produce concentrated non-aqueous dispersions.

In order to successfully disperse the IONP in aqueous media a secondary surfactant layer of the same or different surfactant is required. The decanoic acid-coated IONP

were re-dispersed in water and the suspension was heated to 60°C with strong stirring. The second surfactant, lauric acid (C12:0) (0.25 mmol), as its ammonium salt (pH ~10), was then added drop-wise to the suspension. The suspensions were then sonicated at 50°C for 15-20 minute cycles until a suspension of magnetite nanoparticles stabilised against agglomeration was achieved. The nanoparticle suspensions were then characterised by PCS and NMRD.

6.3 Results and Discussion

6.3.1 Solid magnetoliposome (SML) suspensions

PCS analyses of a typical SML suspensions demonstrated that suspensions of monodisperse nanoclusters were formed, with sizes ranging from 95-110 nm, PDI values of 0.22-0.24. It should be noted that these values are slightly higher than those observed for fully-dispersed individual IONP dispersions. This increase may be explained by the presence of some larger aggregates within the SML suspension, which could possibly be removed by centrifugation, sonication or magnetic filtration. Note that the fraction of these larger aggregates was very small in most cases and the NMR results are as expected, so further size selection was deemed not necessary in these instances. Size distributions for the most part were unimodal, an example is shown in Figure 6.5 below.

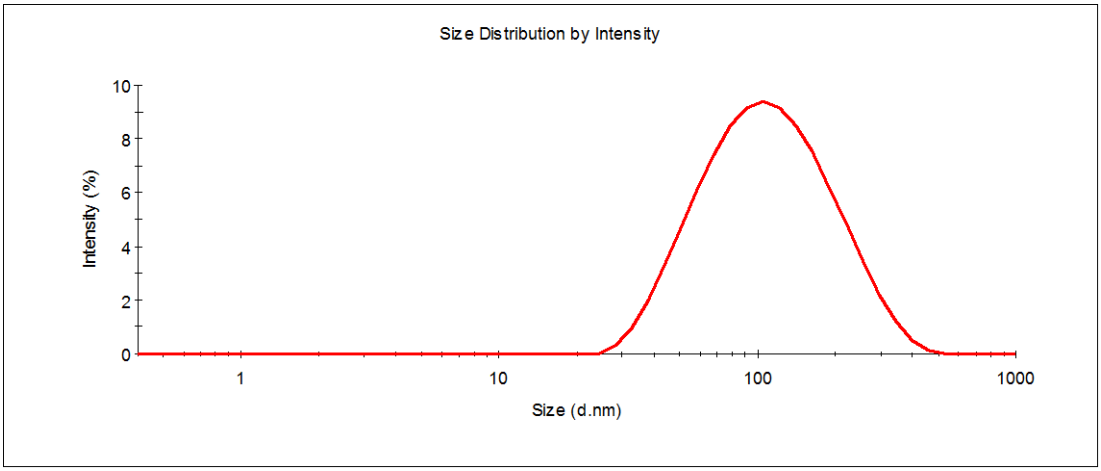

Figure 6.5: Typical PCS size distribution for a SML suspension of 104 nm, PDI 0.24

Figure 6.6 presents the NMRD profile obtained for a typical SML suspension of d_{hyd} ~104 nm (PDI 0.24). The overall shape of the profile suggests a superparamagnetic

material had been formed, with the frequency of the r_1 maximum at ~1 MHz suggesting a primary particle size of less than 20 nm [70]. In comparison to the NMRD profiles obtained for the Cit-IONP/PACA and DTAB-IONP/PACA presented in Chapter 4 (re-presented in Figure 6.9 below, the profile obtained for the SML suspension presents a much broader peak in the high frequency region, this probably arises from the broader size distribution. Significantly higher r_1 values were found across the entire frequency range and a higher r_1 plateau in the low frequency region was also observed. The former is consistent with higher M_s, associated with improved crystallinity, and the latter with greater magnetic anisotropy (see Chapter 1, Figure 1.33) for SMLs due to increased inter-particle interactions (resulting in longer Néel correlation time, see Chapter 1, Figure 1.31. for re-orientation of the magnetic moments of the dispersed IONPCs as compared to individual IONP. [121]. The expected NMRD response of a dispersed IONP suspension of core size and M_s typical for aqueous co-precipitation particle synthesis is included solid line in Figure 6.6 below, for the sake of comparison. The major difference is an increase in r_1 at low frequency of forming the clusters.

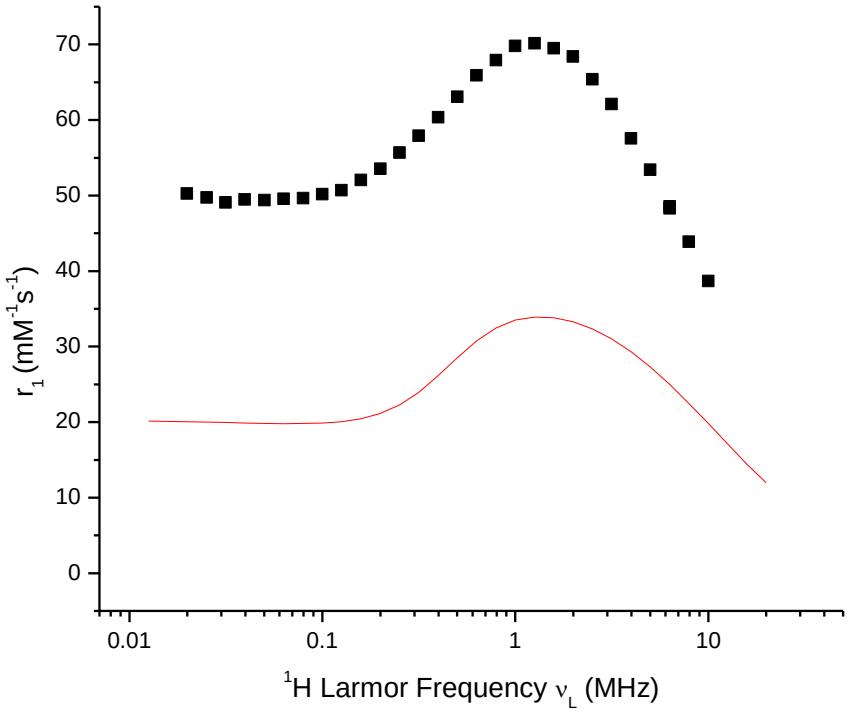

Figure 6.6: NMRD data for a typical SML suspension (■), stabilised by a DOPG lipid bilayer. A simulated profile for dispersed IONP (solid red line) is included [52]. The parameters used in the SPM simulation were M_S = 27 emu/g, d_{SPM}=20 nm, τ_N = 24 ns, ΔE_{anis} = 2.2 GHz

Although T_2 data was not collected for magnetoliposome suspensions in the work presented in this chapter, previous studies in the group, and also in the literature in general, reported high r_2 values (and thus high r_2/r_1 ratios) for materials of this type [52, 141, 142]. This allows for their consideration as potential T_2 negative contrast agents for MRI imaging.

6.3.2 Fatty-acid bilayer stabilised IONPCs (BPCs)

Turning to fatty-acid bilayer stabilised IONPCs (BPCs), in the case of decanoic/lauric acid PCS analyses indicated the formation of unimodal size distribution, with measured hydrodynamic sizes of 85-100 nm following adequate sonication of the suspensions post synthesis. PDI values varied from 0.19-0.24, indicating that fairly monodisperse suspensions were achieved.

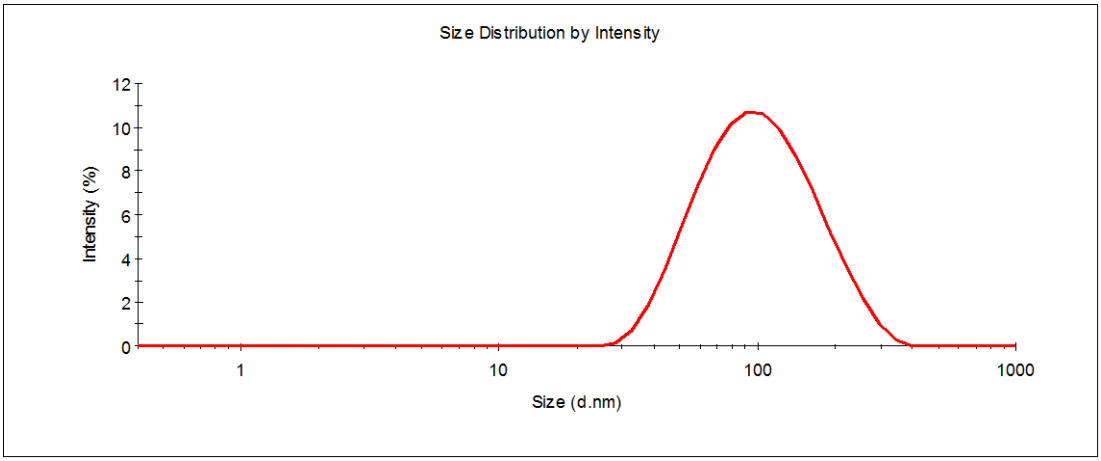

Figure 6.7: PCS data for a typical BPC suspension of 93 nm (PDI 0.24)

The NMRD profile of the BPC suspension is shown in Figure 6.8. Once again, measured r_1 values were high for all frequencies across the range, with the occurrence of a low field r_1 plateau, a prominent maximum in the low frequency range (~1 MHz) and a rapid decrease in r_1 at higher frequencies also evident, suggesting that the material was also composed of superparamagnetic particles in the sub 20 nm range. The simulated curve for dispersed IONP (identical to that used in Figure 6.6) is again included for comparison. The BPC profile is similar to that presented for SML suspensions. Both show much higher r_1 values across the entire frequency range than those obtained for Cit-IONP/PACA and DTAB-IONP/PACA,

in addition to a higher r_1 plateau in the low frequency region and this effect is stronger for BPCs. This, again, suggests higher M_s, and magnetic anisotropy for BPCs as compared to Cit-IONP/PACA and DTAB-IONP/PACA nanocomposites.

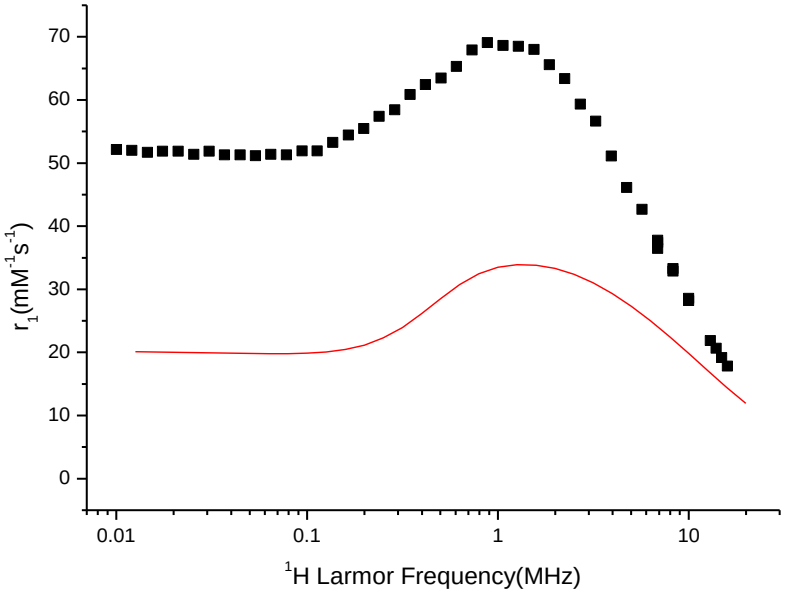

Figure 6.8: NMRD data for a typical BPC suspension (■), stabilised by a decanoic acid/lauric acid bilayer. A simulated profile for dispersed IONP (solid red line) is included [49]. The parameters used in the SPM simulation were M_S = 27 emu/g, d_{SPM} = 20 nm, τ_N = 24 ns, ΔE_{anis} = 2.2 GHz

6.4 Conclusion

From the work presented in this chapter, it has become apparent that by forming dense IONP clusters with fatty acids or lipid bilayers, an increase in the low frequency relaxivity, as compared to SPM simulations of the expected profile for dispersed IONP was observed. This is in contrast with that observed for the change in r_1 for more 'open' Cit-IONP and DTAB-IONP nanocomposites, where an overall increase or decrease in the r_1 across the entire profile was observed, when compared to that for dispersed IONP (illustrated in Figure 6.9 below). We interpret the former observation as being due to stronger inter-particle interactions for the IONP dense nanocomposites (SMLs and BPCs), giving rise to greater magnetic anisotropy and longer Néel correlation times. The contrast in the observed changes in r_1 upon composite formation between both dense and open IONPC materials provides the potential for engineering the NMRD response through modification of the composite architecture. This, in turn, presents the potential of such materials as next-generation

diagnostics, or as image-guided hyperthermically-actuated delivery vehicles for biomedical application.

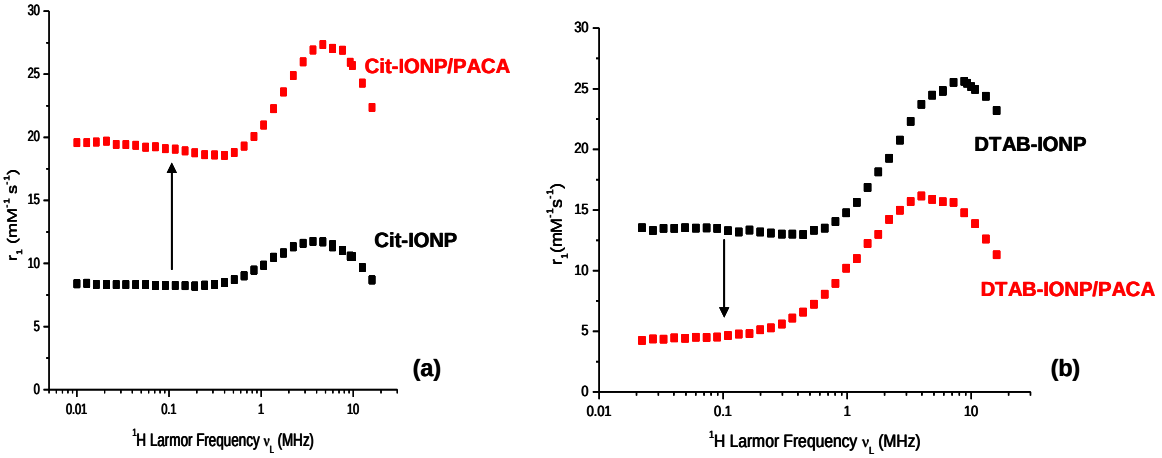

Figure 6.9: NMRD profiles for (a) Cit-IONP and Cit-IONP/PACA and (b) DTAB-IONP and DTAB-IONP/PACA as described in Chapter 4

In previous studies carried out within the group [52], IONP-dense clustered materials (SMLs and BPCs) such as those presented here have also exhibited elevated r_2 values and hence are applicable for potential T_2-weighted imaging applications.

CHAPTER 7

Thesis Summary and Conclusions

Despite the challenges presented in producing stable nanocomposites throughout the work presented in this thesis, NMRD analysis has allowed us to probe the magnetic order within soft magnetic materials in situ, thus providing direction to the development of related (second generation) materials. NMRD analysis of the composite materials presented identifies the possibility of systematically altering r_1 at some or all frequencies across the measured range. By formation of composites including PACA, namely Cit-IONP/PACA and DTAB-IONP/PACA, wherein inter-particle interactions within the clusters are minimised, r_1 was altered at all frequencies. Alternatively, by forming dense IONP clusters with fatty acids or lipids, it proved possible to drive up the low frequency relaxivity only, by controlling the effective magnetic anisotropy through the extent of interparticle interactions.

NMRD comparisons between both citrate and DTAB-stabilised IONP and their corresponding composite materials demonstrate that a change in the IONP environment could also have an impact on the NMRD response. In the case of the Cit-IONP versus Cit-IONP/PACA, for example, an increase in r_1 across the frequency range was observed. SPM modelling of the of the effect of viscosity of the dispersion medium, suggested that the effect is probably attributable to a change in the local environment about the IONP, as opposed to a change in the bulk viscosity of the medium, which supports formation of the nanocomposite. In the case of the DTAB-IONP and their corresponding composite materials, the observed decrease in the relaxivity was explained by a reduced interaction of the diffusing H_2O protons with the IONP surface following their attachment to the surface of the PACA nanospheres.

The NMRD response of these composite materials was also shown to be effectively engineered through careful selection of the IONP type used in their construction. It was found that IONP prepared by different methods have very contrasting magnetic properties, with those prepared by non-hydrolytic methods demonstrating significantly higher relaxivity than those prepared by conventional coprecipitation methods. This is because thermal decomposition produces IONP of excellent crystallinity, resulting in increased saturation magnetisation.

For biomedical application the stability of the composite materials is vital. It was found that this was essentially a consequence of the relative stability of the

individually dispersed IONP. In the case of citrate-stabilised IONP, it was observed that both particles and composites remained colloidally highly stable (hydrodynamic size, PDI and zeta potential) for extended periods of time over a relatively broad pH range, or when exposed to elevated field strengths during magnetic filtration. This stability was closely related to the surface coverage of the IONP by the citrate ligands, with a minimal surface ligand coverage required. It followed that, the majority of the composite materials prepared using these nanoparticle dispersions demonstrated similar stability, with those exhibiting more negative Zeta Potential values maintaining their hydrodynamic size and PDI values for longer periods of time, as expected.

In contrast to this, IONP stabilised by DTAB did not exhibit the same degree of stability both temporally and on exposure to a strong magnetic field. The dispersion obtained and its colloidal stability were found to be strongly dependent on the quantity of DTAB ligand used in the phase transfer process. The lack of long-term stability is most likely due to the fact that the DTAB moieties are physisorbed onto the particles and so are relatively easily displaced, as compared to the chemisorbed citrate ligands of the Cit-IONP materials. Future work could involve attachment of ligands with stronger binding chemistries, improving long-term stability for positively charged IONP used in nanocomposite formation.

Several attempts were also made to complete NMRD analyses on the IONPCs presented in Chapter 5 of this thesis. Unfortunately, in each case, the colloidal stability of these materials on exposure to the magnetic field was insufficient for us to record reliable data. Hence the magnetic order and relaxivities of the assemblies of this type remain an open question. Despite this obstacle, some insight was gained into the nature of the activated IONP, formed by partial removal of surfactant from the IONP surface (which were previously stabilised by two different ligand types) and their corresponding clustered materials. Future work could involve the preparation of more colloidally stable materials in order to determine their NMRD response, so that they may be compared to the other composites described in this thesis. Furthermore, their eventual phase transfer into water for their consideration in biomedical application would also be a key step.

We have noted that large assemblies (d_{hyd} >100 nm) of either open (porous) or dense (non-porous) IONPC architecture are both potentially effective T_2-agents for MRI applications. An alternative approach suggested by the work presented in this thesis on Cit-IONP/PACA and DTAB-IONP/PACA composite materials is the use of composites with drastically reduced inter-particle interactions (incorporating PACA, or perhaps a more stable equivalent) for developing improved agents with T_1-weighting properties for MRI.

The contrast in the NMRD behaviour between the composite materials presented in this thesis, and the manner in which their architecture can be used to engineer this response, presents potential for the development of a variety of next-generation diagnostics, in particular, for image-guided hyperthermically-actuated delivery vehicles. The principle challenge in the development of these advanced vehicles is in preparing colloidally stable composites, that are stable under a wide range of physiological conditions, while optimising their magnetic properties and thus their MRI/hyperthermic potential. Although much effort and some progress towards this goal has been shown in the work presented in this thesis, the challenge of preparing nanocomposites with both excellent physical properties and long-term colloidal stability remains.

Bibliography

1. Hergt, R., R. Hiergeist, I. Hilger, W.A. Kaiser, Y. Lapatnikov, S. Margel, and U. Richter, *Maghemite nanoparticles with very high AC-losses for application in RF-magnetic hyperthermia.* Journal of Magnetism and Magnetic Materials, 2004. **270**(3): p. 345-357.
2. Halbreich, A.e.a., *Biomedical Applications of Maghemite Ferrofluid.* Biochemie, 1998. **80**: p. 379-390.
3. Lübbe, A.S., C. Bergemann, H. Riess, F. Schriever, P. Reichardt, K. Possinger, M. Matthias, B. Dörken, F. Herrmann, R. Gürtler, P. Hohenberger, N. Haas, R. Sohr, B. Sander, A.-J. Lemke, D. Ohlendorf, W. Huhnt, and D. Huhn, *Clinical Experiences with Magnetic Drug Targeting: A Phase I Study with 4'-Epidoxorubicin in 14 Patients with Advanced Solid Tumors.* Cancer Research, 1996. **56**(20): p. 4686-4693.
4. Bonnemain, B., *Superparamagnetic Agents in Magnetic Resonance Imaging: Physicochemical Characteristics and Clinical Applications A Review.* Journal of Drug Targeting, 1998. **6**(3): p. 167-174.
5. Shubayev, V.I., T.R. Pisanic, and S.H. Jin, *Magnetic nanoparticles for theragnostics.* Advanced Drug Delivery Reviews, 2009. **61**(6): p. 467-477.
6. Jordan, A., R. Scholz, P. Wust, H. Fahling, and R. Felix, *Magnetic fluid hyperthermia (MFH): Cancer treatment with AC magnetic field induced excitation of biocompatible superparamagnetic nanoparticles.* Journal of Magnetism and Magnetic Materials, 1999. **201**: p. 413-419.
7. Lubbe, A.S., C. Alexiou, and C. Bergemann, *Clinical applications of magnetic drug targeting.* J Surg Res, 2001. **95**(2): p. 200-206.
8. Berry, C., Curtis, A., *Functionalisation of magnetic nanoparticles for applications in biomedicine.* J. Phys. D: Appl. Phys., 2003. **36**: p. R198–R206.
9. Reimer, P. and T. Balzer, *Ferucarbotran (Resovist): a new clinically approved RES-specific contrast agent for contrast-enhanced MRI of the liver: properties, clinical development, and applications.* European Radiology, 2003. **13**(6): p. 1266-1276.
10. De, M., P.S. Ghosh, and V.M. Rotello, *Applications of Nanoparticles in Biology.* Advanced Materials, 2008. **20**(22): p. 4225-4241.

11. Xu, H., T. Song, X. Bao, and L. Hu, *Site-directed research of magnetic nanoparticles in magnetic drug targeting.* Journal of Magnetism and Magnetic Materials, 2005. **293**(1): p. 514-519.
12. Neuberger, T., B. Schöpf, H. Hofmann, M. Hofmann, and B. von Rechenberg, *Superparamagnetic nanoparticles for biomedical applications: Possibilities and limitations of a new drug delivery system.* Journal of Magnetism and Magnetic Materials, 2005. **293**(1): p. 483-496.
13. Yu, M.K., Y.Y. Jeong, J. Park, S. Park, J.W. Kim, J.J. Min, K. Kim, and S. Jon, *Drug-Loaded Superparamagnetic Iron Oxide Nanoparticles for Combined Cancer Imaging and Therapy In Vivo.* Angewandte Chemie International Edition, 2008. **47**(29): p. 5362-5365.
14. Nicolas, J. and P. Couvreur, *Synthesis of poly(alkyl cyanoacrylate)-based colloidal nanomedicines.* Wiley Interdisciplinary Reviews-Nanomedicine and Nanobiotechnology, 2009. **1**(1): p. 111-127.
15. Zhang, Y., N. Kohler, and M. Zhang, *Surface modification of superparamagnetic magnetite nanoparticles and their intracellular uptake.* Biomaterials, 2002. **23**(7): p. 1553-1561.
16. Alexiou, C., W. Arnold, R.J. Klein, F.G. Parak, P. Hulin, C. Bergemann, W. Erhardt, S. Wagenpfeil, and A.S. Lübbe, *Locoregional Cancer Treatment with Magnetic Drug Targeting.* Cancer Research, 2000. **60**(23): p. 6641-6648.
17. Gref, R., Y. Minamitake, M.T. Peracchia, V. Trubetskoy, V. Torchilin, and R. Langer, *Biodegradable long-circulating polymeric nanospheres.* Science (New York, N.Y.), 1994. **263**(5153): p. 1600-1603.
18. Kohler, N., C. Sun, J. Wang, and M. Zhang, *Methotrexate-Modified Superparamagnetic Nanoparticles and Their Intracellular Uptake into Human Cancer Cells.* Langmuir, 2005. **21**(19): p. 8858-8864.
19. Mathiowitz, E. and M.D. Cohen, *Polyamide microcapsules for controlled release. V. Photochemical release.* Journal of Membrane Science, 1989. **40**(1): p. 67-86.
20. Chilkoti, A., M.R. Dreher, D.E. Meyer, and D. Raucher, *Targeted drug delivery by thermally responsive polymers.* Advanced Drug Delivery Reviews, 2002. **54**(5): p. 613-630.
21. Ito, A., M. Shinkai, H. Honda, and T. Kobayashi, *Medical application of functionalized magnetic nanoparticles.* Journal of Bioscience and Bioengineering, 2005. **100**(1): p. 1-11.

22. Simeonova, M., *Poly(butylcyanoacrylate) nanoparticles for topical delivery of 5-fluorouracil.* Int J Pharm, 2003. **263**(1-2): p. 133-140.
23. Vauthier, C., C. Dubernet, E. Fattal, H. Pinto-Alphandary, and P. Couvreur, *Poly(alkylcyanoacrylates) as biodegradable materials for biomedical applications.* Advanced Drug Delivery Reviews, 2003. **55**(4): p. 519-548.
24. Verma, A.K., Chanchal, A., Maitra, A., *Co-polymeric hydrophilic nanospheres for drug delivery: release kinetics, and cellular uptake.* Indian Journal of Experimental Biology, 2010. **48**(10): p. 1043-1052.
25. Shen, Y., E. Jin, B. Zhang, C.J. Murphy, M. Sui, J. Zhao, J. Wang, J. Tang, M. Fan, E. Van Kirk, and W.J. Murdoch, *Prodrugs forming high drug loading multifunctional nanocapsules for intracellular cancer drug delivery.* J Am Chem Soc, 2010. **132**(12): p. 4259-65.
26. Graf, A., *Colloids in Drug Delivery*, ed. M. Fanun. 2010: CRC Press
27. Aguilar, M.R., Elvira, C., Gallardo, A., Vázquez, B., San Román, J., *Topics in Tissue Engineering, Chapter 6*. Vol. 3. 2007.
28. Yallapu, M.M., S.P. Foy, T.K. Jain, and V. Labhasetwar, *PEG-functionalized magnetic nanoparticles for drug delivery and magnetic resonance imaging applications.* Pharm Res, 2010. **27**(11): p. 2283-95.
29. Wei, H., S.-X. Cheng, X.-Z. Zhang, and R.-X. Zhuo, *Thermo-sensitive polymeric micelles based on poly(N-isopropylacrylamide) as drug carriers.* Progress in Polymer Science, 2009. **34**(9): p. 893-910.
30. Simeonova, M., G. Ivanova, V. Enchev, N. Markova, M. Kamburov, C. Petkov, A. Devery, R. O'Connor, and D. Brougham, *Physicochemical characterization and in vitro behavior of daunorubicin-loaded poly(butylcyanoacrylate) nanoparticles.* Acta Biomater, 2009. **5**(6): p. 2109-21.
31. Kreuter, J., *Possibilities of using nanoparticles as carriers for drugs and vaccines.* J Microencapsul, 1988. **5**(2): p. 115-27.
32. Vijayaraghavalu S, R.D., Labhasetwar V., *Nanoparticles for delivery of chemotherapeutic agents to tumors.* Curr Opin Investig Drugs. . **8**(6): p. 477-484.
33. Nedelcu, G., *Magnetic Nanoparticles Impact on Tumoral Cells in the Treatment by Magnetic Fluid Hyperthermia.* Digest Journal of Nanomaterials and Biostructures, 2008. **3**(3): p. 103-107.
34. Kalambur, V.S., B. Han, B.E. Hammer, T.W. Shield, and J.C. Bischof, *In vitro characterization of movement, heating and visualization of magnetic*

nanoparticles for biomedical applications. Nanotechnology, 2005. **16**(8): p. 1221-1233.

35. Zhang, L.-Y., H.-C. Gu, and X.-M. Wang, *Magnetite ferrofluid with high specific absorption rate for application in hyperthermia.* Journal of Magnetism and Magnetic Materials, 2007. **311**(1): p. 228-233.
36. Hergt, R., S. Dutz, R. Muller, and M. Zeisberger, *Magnetic particle hyperthermia: nanoparticle magnetism and materials development for cancer therapy.* Journal of Physics-Condensed Matter, 2006. **18**(38): p. S2919-S2934.
37. Wang, X., H. Gu, and Z. Yang, *The heating effect of magnetic fluids in an alternating magnetic field.* Journal of Magnetism and Magnetic Materials, 2005. **293**(1): p. 334-340.
38. Mornet, S., S. Vasseur, F. Grasset, and E. Duguet, *Magnetic nanoparticle design for medical diagnosis and therapy.* Journal of Materials Chemistry, 2004. **14**(14): p. 2161-2175.
39. Ma, M., Y. Wu, J. Zhou, Y. Sun, Y. Zhang, and N. Gu, *Size dependence of specific power absorption of Fe3O4 particles in AC magnetic field.* Journal of Magnetism and Magnetic Materials, 2004. **268**(1-2): p. 33-39.
40. Häfeli, U., *Scientific and Clinical Applications of Magnetic Carriers*. 1997: Springer-Verlag New York Inc.
41. Mohammad, F., G. Balaji, A. Weber, R.M. Uppu, and C.S.S.R. Kumar, *Influence of Gold Nanoshell on Hyperthermia of Superparamagnetic Iron Oxide Nanoparticles.* The Journal of Physical Chemistry C, 2010. **114**(45): p. 19194-19201.
42. Kumar, C.S. and F. Mohammad, *Magnetic nanomaterials for hyperthermia-based therapy and controlled drug delivery.* Adv Drug Deliv Rev, 2011. **63**(9): p. 789-808.
43. Shen, L., P.E. Laibinis, and T.A. Hatton, *Bilayer Surfactant Stabilized Magnetic Fluids: Synthesis and Interactions at Interfaces.* Langmuir, 1999. **15**(2): p. 447-453.
44. Gupta, A.K. and M. Gupta, *Synthesis and surface engineering of iron oxide nanoparticles for biomedical applications.* Biomaterials, 2005. **26**(18): p. 3995-4021.
45. Carmen Bautista, M., O. Bomati-Miguel, M. del Puerto Morales, C.J. Serna, and S. Veintemillas-Verdaguer, *Surface characterisation of dextran-coated iron*

oxide nanoparticles prepared by laser pyrolysis and coprecipitation. Journal of Magnetism and Magnetic Materials, 2005. **293**(1): p. 20-27.

46. Zeng, S.S.H., *Size-Controlled Synthesis of Magnetite Nanoparticles.* J. AM. CHEM. SOC, 2002. **124**: p. 8204-8205
47. Jiang, W., K.-L. Lai, H. Hu, X.-B. Zeng, F. Lan, K.-X. Liu, Y. Wu, and Z.-W. Gu, *The effect of [Fe3+]/[Fe2+] molar ratio and iron salts concentration on the properties of superparamagnetic iron oxide nanoparticles in the water/ethanol/toluene system.* Journal of Nanoparticle Research, 2011. **13**(10): p. 5135-5145.
48. Lemos, V.P., Lima de Costa, M., Lima Lemos, R., Gomes de Faria, M. S., *Vivianite and siderite in lateritic iron crust: an example of bioreduction.* Química Nova, 2007. **30**(1): p. 36-40.
49. Ghosh, S., D. Carty, S.P. Clarke, S.A. Corr, R. Tekoriute, Y.K. Gun'ko, and D.F. Brougham, *NMR studies into colloidal stability and magnetic order in fatty acid stabilised aqueous magnetic fluids.* Physical Chemistry Chemical Physics, 2010. **12**(42): p. 14009-14016.
50. Sahoo, Y., A. Goodarzi, M.T. Swihart, T.Y. Ohulchanskyy, N. Kaur, E.P. Furlani, and P.N. Prasad, *Aqueous ferrofluid of magnetite nanoparticles: Fluorescence labeling and magnetophoretic control.* J Phys Chem B, 2005. **109**(9): p. 3879-85.
51. Sahoo, Y.P.H., Fried, T., Golodnitzky, D., Burstein, L., *Alkyl Phosphonate/Phosphate Coating on Magnetite Nanoparticles: A Comparison with Fatty Acids.* Langmuir, 2001(17): p. 7907-7911.
52. Meledandri C.J., N.T., Brougham D.F *Size-controlled magnetoliposomes with tunable magnetic resonance relaxation enhancements.* J. Mat. Chem, 2011. **21**(1): p. 214-222.
53. Park, J., J. Joo, S.G. Kwon, Y. Jang, and T. Hyeon, *Synthesis of monodisperse spherical nanocrystals.* Angew Chem Int Ed Engl, 2007. **46**(25): p. 4630-60.
54. Kwon, S.G., Piao, Y., Park, J., Angappane, S., Jo, Y., Hyeon, T., *Kinetics of Monodisperse Iron Oxide Nanocrystal Formation by "Heating-Up" Process.* Journal of the American Chemical Society, 2007. **129**: p. 12571-12584.
55. Pinna, N., Grancharov., S., Beato, P., Bonville, P., Antonietti, M., Niederberger, N., <*Pinna Chem Mater 2005.pdf*>. Chem Mater., 2005. **17**: p. 3044-3049.

56. Maity, D. and D.C. Agrawal, *Synthesis of iron oxide nanoparticles under oxidizing environment and their stabilization in aqueous and non-aqueous media.* Journal of Magnetism and Magnetic Materials, 2007. **308**(1): p. 46-55.
57. Yu, W., Chang, E., Sayes, C., Drezek, R., Colvin, V., *Aqueous dispersion of monodisperse magnetic iron oxide nanocrystals through phase transfer.* Nanotechnology, 2006. **17**: p. 4483-4487.
58. Kazuba, M. *Zeta Potential Theory*. Malvern Lecture Series, 2010.
59. Hahn, E.L., *Spin Echoes.* Phys. Rev., 1950. **80**: p. 580LP-594.
60. Carr, H.Y., Purcell, E. M., *Effects of Diffusion on Free Precession in Nuclear Magnetic Resonance Experiments.* Physical Review 1954. **94**(3): p. 630-638.
61. Canet, D., *Nuclear Magnetic Resonance: Concepts and Methods*. 1996: Wiley.
62. Jones, G., *Spin-Lattice Relaxation in the Rotating Frame: Weak-Collision Case.* Physical Review, 1966. **148**(1): p. 332-335.
63. Markisz, J.A., *Technical Magnetic Resonance Imaging*. 1996: Stamford, Appleton&Lange.
64. Watson, J.K., *Applications of Magnetism*. 1980: Wiley.
65. Cornell, R.L., *The Iron Oxides: Structures, Properties, Reactions, Occurences and Uses.* 1996: Wiley-VCH.
66. Leslie-Pelecky, D.L., Rieke, R. D., *Magnetic Properties of Nanostructured Materials.* Chem. Mater., 1996. **8**: p. 1770-1783.
67. Bean, C.P., Livingston, J. D., *Superparamagnetism.* Journal of Applied Physics, 1959. **30**: p. 120S-129S.
68. Taboada E., R., E., Roig, A., Oro, J., Roch, A., Muller R., *Relaxometric and Magnetic Characterization of Ultrasmall Iron Oxide Nanoparticles with High Magnetization. Evaluation as Potential T1 Magnetic Resonance Imaging Contrast Agents for Molecular Imaging.* Langmuir, 2007. **23**: p. 4583-4588.
69. Roch, A., P. Gillis, A. Ouakssim, and R.N. Muller, *Proton magnetic relaxation in superparamagnetic aqueous colloids: a new tool for the investigation of ferrite crystal anisotropy.* Journal of Magnetism and Magnetic Materials, 1999. **201**(1–3): p. 77-79.
70. Muller, R.N., *Theory of proton relaxation induced by superparamagnetic particles.* J. Chem. Phys, 1999. **110**(11): p. 5403-5411.
71. Laurent, S., D. Forge, M. Port, A. Roch, C. Robic, L.V. Elst, and R.N. Muller, *Magnetic Iron Oxide Nanoparticles: Synthesis, Stabilization, Vectorization,*

Physicochemical Characterizations, and Biological Applications (vol 108, pg 2064, 2008). Chemical Reviews, 2010. **110**(4): p. 2574-2574.

72. Meledandri, C.J. and D.F. Brougham, *Low field magnetic resonance techniques in the development of nanomaterials for biomedical applications.* Analytical Methods, 2012. **4**(2): p. 331-341.
73. Instruments, M. *Dynamic Light Scattering: An Introduction in 30 Minutes-Technical Note*.
74. Kazuba, M. *Dynamic Light Scattering Theory*. Malvern Lecture Series, 2010.
75. ISO22412, I.S., *Particle size analysis -- Dynamic light scattering* 2008.
76. ISO13321, I.S., *Methods for Determination of Particle Size Distribution Part 8: Photon Correlation Spectroscopy, International Organisation for Standardisation (ISO) 1996.* , 1996.
77. Lawson, C.L., Hanson, R. J., *Solving Least Squares Problems*. 1995: SIAM: Society for Industrial & Applies Mathematics.
78. Instruments, M. *Measuring zeta potential using phase analysis light scattering (PALS)-Technical Note*. 2010.
79. Anoardo, E., Galli, G., Ferrante, G., *Fast-Field Cycling NMR: Applications and Instrumentation.* Applied Magnetic Resonance, 2001. **20**: p. 365-404.
80. Kimmich, R. and E. Anoardo, *Field-cycling NMR relaxometry*. Progress in Nuclear Magnetic Resonance Spectroscopy, 2004. **44**(3-4): p. 257-320.
81. Ebdon, L., *An introduction to Atomic Absorption Spectroscopy. A Self Teaching Approach*. 1982: Heydon&Son Ltd., London.
82. Williams, D.B., Carter, C. B., *Transmission Electron Microscopy: A Textbook for Materials Science*. 1996: New York; Plenum Press.
83. Bottom, R., *Thermogravimetric Analysis*, in *Principles and Applications of Thermal Analysis*. 2008, Blackwell Publishing Ltd. p. 87-118.
84. Gabbott, P., *Principles and Applications of Thermal Analysis*, ed. P. Gabbott. 2007: Wiley-Blackwell.
85. Sichina, W.J. *Characterizing Polymer Lifetimes Using TGA Decomposition Kinetics-Perkin Elmer Technical Note*. 1996.
86. Brown, M.E., *Introduction to Thermal Analysis: Techniques and Applications*. 2001: Klewer Academic Publishers.
87. Amstad, E., S. Zurcher, A. Mashaghi, J.Y. Wong, M. Textor, and E. Reimhult, *Surface functionalization of single superparamagnetic iron oxide nanoparticles for targeted magnetic resonance imaging.* Small, 2009. **5**(11): p. 1334-42.

88. Giri, J., S. Guha Thakurta, J. Bellare, A. Kumar Nigam, and D. Bahadur, *Preparation and characterization of phospholipid stabilized uniform sized magnetite nanoparticles.* Journal of Magnetism and Magnetic Materials, 2005. **293**(1): p. 62-68.
89. Gonzales, M. and K.M. Krishnan, *Phase transfer of highly monodisperse iron oxide nanocrystals with Pluronic F127 for biomedical applications.* Journal of Magnetism and Magnetic Materials, 2007. **311**(1): p. 59-62.
90. Hao, R., R. Xing, Z. Xu, Y. Hou, S. Gao, and S. Sun, *Synthesis, functionalization, and biomedical applications of multifunctional magnetic nanoparticles.* Advanced Materials, 2010. **22**(25): p. 2729-42.
91. Jarrett, B.R., M. Frendo, J. Vogan, and A.Y. Louie, *Size-controlled synthesis of dextran sulfate coated iron oxide nanoparticles for magnetic resonance imaging.* Nanotechnology, 2007. **18**(3)
92. Liu, Z.L., H.B. Wang, Q.H. Lu, G.H. Du, L. Peng, Y.Q. Du, S.M. Zhang, and K.L. Yao, *Synthesis and characterization of ultrafine well-dispersed magnetic nanoparticles.* Journal of Magnetism and Magnetic Materials, 2004. **283**(2-3): p. 258-262.
93. Kim, D.K., Y. Zhang, W. Voit, K.V. Rao, and M. Muhammed, *Synthesis and characterization of surfactant-coated superparamagnetic monodispersed iron oxide nanoparticles.* Journal of Magnetism and Magnetic Materials, 2001. **225**(1–2): p. 30-36.
94. Meledandri C.J., S., J., Brougham D.F, *Hierarchical Gold-Decorated Magnetic Nanoparticle Clusters with Controlled Size.* ACS Nano, 2011. **5**(3): p. 1747-1755.
95. d'Orlye, F., A. Varenne, T. Georgelin, J.M. Siaugue, B. Teste, S. Descroix, and P. Gareil, *Charge-based characterization of nanometric cationic bifunctional maghemite/silica core/shell particles by capillary zone electrophoresis.* Electrophoresis, 2009. **30**(14): p. 2572-82.
96. Harris, L.A., Gof, J. D., Carmichael, A. Y., Rifle, J.S., Harburn, J. J., St. Pierre, T. G., Saunders, M., *Magnetite Nanoparticle Dispersions Stabilized with Triblock Copolymers.* Chem. Mater. , 2003. **15**: p. 1367-1377.
97. Xu, H., Z.P. Aguilar, L. Yang, M. Kuang, H. Duan, Y. Xiong, H. Wei, and A. Wang, *Antibody conjugated magnetic iron oxide nanoparticles for cancer cell separation in fresh whole blood.* Biomaterials, 2011. **32**(36): p. 9758-9765.

98. Fu, A., W. Hu, L. Xu, R.J. Wilson, H. Yu, S.J. Osterfeld, S.S. Gambhir, and S.X. Wang, *Protein-Functionalized Synthetic Antiferromagnetic Nanoparticles for Biomolecule Detection and Magnetic Manipulation.* Angewandte Chemie International Edition, 2009. **48**(9): p. 1620-1624.

99. Moghimi, S.M., Szebeni, J., *Stealth liposomes and long circulating nanoparticles: critical issues in pharmacokinetics, opsonization and protein-binding properties.* Progress in Lipid Research, 2003. **42**: p. 463-478.

100. Owens, D.E., Peppas, N. A., *Opsonization, biodistribution, and pharmacokineticsof polymeric nanoparticles.* International Journal of Pharmaceutics, 2006. **307**: p. 93-102.

101. Roser, M., D. Fischer, and T. Kissel, *Surface-modified biodegradable albumin nano- and microspheres. II: effect of surface charges on in vitro phagocytosis and biodistribution in rats.* European Journal of Pharmaceutics and Biopharmaceutics, 1998. **46**(3): p. 255-263.

102. Muller, R.N., S. Laurent, D. Forge, M. Port, A. Roch, C. Robic, and L.V. Elst, *Magnetic iron oxide nanoparticles: Synthesis, stabilization, vectorization, physicochemical characterizations, and biological applications.* Chemical Reviews, 2008. **108**(6): p. 2064-2110.

103. Meledandri, C.J., J.K. Stolarczyk, S. Ghosh, and D.F. Brougham, *Nonaqueous Magnetic Nanoparticle Suspensions with Controlled Particle Size and Nuclear Magnetic Resonance Properties.* Langmuir, 2008. **24**(24): p. 14159-14165.

104. Yu, W.W., E. Chang, C.M. Sayes, R. Drezek, and V.L. Colvin, *Aqueous dispersion of monodisperse magnetic iron oxide nanocrystals through phase transfer.* Nanotechnology, 2006. **17**(17): p. 4483-4487.

105. Zhuang, J., H. Wu, Y. Yang, and Y.C. Cao, *Supercrystalline colloidal particles from artificial atoms.* J Am Chem Soc, 2007. **129**(46): p. 14166-7.

106. Ninjbadgar, T. and D.F. Brougham, *Epoxy Ring Opening Phase Transfer as a General Route to Water Dispersible Superparamagnetic Fe3O4 Nanoparticles and Their Application as Positive MRI Contrast Agents.* Advanced Functional Materials, 2011. **21**(24): p. 4769-4775.

107. Baalousha, M., *Aggregation and disaggregation of iron oxide nanoparticles: Influence of particle concentration, pH and natural organic matter.* Sci Total Environ, 2009. **407**(6): p. 2093-101.

108. Bee, A., R. Massart, and S. Neveu, *Synthesis of Very Fine Maghemite Particles.* Journal of Magnetism and Magnetic Materials, 1995. **149**(1-2): p. 6-9.

109. Qiu, X., *Synthesis and characterization of magnetic nanoparticles.* Chinese Journal of Chemistry, 2000. **18**(6): p. 834-837.

110. Tartaj, P., Del Puerto Morales, M., Veintemillas-Verdaguer, S., Gonzalez-Carreno, T., Serna, C. J., *The preparation of magnetic nanoparticles for applications in biomedicine*

J. Phys. D: Appl. Phys., 2003. **36**: p. R182-R197.

111. Cao. C., J. Zhuang, H. Wu, and Y. Y., *Supercrystalline Colloidal Particles from Artificial Atoms.* J Am Chem Soc, 2007. **129**: p. 14166-14167.

112. Wooding, A., M. Kilner, and D.B. Lambrick, *Studies of the double surfactant layer stabilization of water-based magnetic fluids.* J Colloid Interface Sci, 1991. **144**(1): p. 236-242.

113. Crea, F., C. Stefano, F. Millero, and V. Sharma, *Dissociation Constants for Citric Acid in NaCl and KCl Solutions and their Mixtures at 25 °C.* Journal of Solution Chemistry, 2004. **33**(11): p. 1349-1366.

114. Dozier, D., Palchoudhury, S., Bao, Y. *Synthesis of Iron Oxide Nanoparticles with Biological Coatings*. JOSHUA, 2010. **7**, 16-18.

115. Padua, G.W. and S.J. Schmidt, *Proton nuclear magnetic resonance measurements on various sugar solutions.* Journal of Agricultural and Food Chemistry, 1992. **40**(9): p. 1524-1527.

116. Taupitz, M., Schnorr, J., Wagner, S., Dewey, M., Pilgrimm, H., Hamm, B., *Citrate-coated Superparamagnetic Iron Oxide Particles as a New MR Contrast Medium: Results of a Clinical Phase I Trial* Proc. Intl. Soc. Mag. Reson. Med., 2003. **11**: p. 818.

117. Khalil, K.M.S., M.M. Khalaf, H.S. Mohran, and A.A. Elsamahy, *Direct formation of iron oxide/MCM-41 nanocomposites via single or mixed n-alkyltrimethylammonium bromide surfactants.* J Colloid Interface Sci, 2012. **368**(1): p. 56-63.

118. Banerjee, S.S. and D.H. Chen, *Multifunctional pH-sensitive magnetic nanoparticles for simultaneous imaging, sensing and targeted intracellular anticancer drug delivery.* Nanotechnology, 2008. **19**(50): p. -.

119. Kim, J., H.S. Kim, N. Lee, T. Kim, H. Kim, T. Yu, I.C. Song, W.K. Moon, and T. Hyeon, *Multifunctional Uniform Nanoparticles Composed of a Magnetite Nanocrystal Core and a Mesoporous Silica Shell for Magnetic Resonance and Fluorescence Imaging and for Drug Delivery.* Angewandte Chemie International Edition, 2008. **47**(44): p. 8438-8441.

120. Kohler, N., C. Sun, A. Fichtenholtz, J. Gunn, C. Fang, and M. Zhang, *Methotrexate-Immobilized Poly(ethylene glycol) Magnetic Nanoparticles for MR Imaging and Drug Delivery.* Small, 2006. **2**(6): p. 785-792.

121. Corr, S.A., Y.K. Gun'ko, R. Tekoriute, C.J. Meledandri, and D.F. Brougham, *Poly(sodium-4-styrene)sulfonate−Iron Oxide Nanocomposite Dispersions with Controlled Magnetic Resonance Properties.* The Journal of Physical Chemistry C, 2008. **112**(35): p. 13324-13327.

122. Yang, J., H. Lee, W. Hyung, S.B. Park, and S. Haam, *Magnetic PECA nanoparticles as drug carriers for targeted delivery: synthesis and release characteristics.* J Microencapsul, 2006. **23**(2): p. 203-12.

123. Berret, J.-F., N. Schonbeck, F. Gazeau, D. El Kharrat, O. Sandre, A. Vacher, and M. Airiau, *Controlled Clustering of Superparamagnetic Nanoparticles Using Block Copolymers: Design of New Contrast Agents for Magnetic Resonance Imaging.* Journal of the American Chemical Society, 2006. **128**(5): p. 1755-1761.

124. Kumar, C.S., *Magnetic Nanomaterials: Nanomaterials for the Life Sciences*. 2009: Wiley-VCH.

125. Maeda, H., J. Wu, T. Sawa, Y. Matsumura, and K. Hori, *Tumor vascular permeability and the EPR effect in macromolecular therapeutics: a review.* Journal of Controlled Release, 2000. **65**(1–2): p. 271-284.

126. Torchilin, V.P., *Targeted Pharmaceutical Nanocarriers for Cancer Therapy and Imaging.* AAPS Journal 2007. **9**(2): p. E128-E147.

127. Maeda, H., J. Fang, K. Greish, M. Kawasuji, and A.K. Iyer, *Enhanced Permeability and Retention (EPR) Effect and Tumor-Selective Delivery of Anticancer Drugs*, in *Delivery Of Protein And Peptide Drugs In Cancer*. p. 37-52.

128. Stolarczyk, J.K., S. Ghosh, and D.F. Brougham, *Controlled growth of nanoparticle clusters through competitive stabilizer desorption.* Angew Chem Int Ed Engl, 2009. **48**(1): p. 175-8.

129. Kumagai, M., T.K. Sarma, H. Cabral, S. Kaida, M. Sekino, N. Herlambang, K. Osada, M.R. Kano, N. Nishiyama, and K. Kataoka, *Enhanced in vivo Magnetic Resonance Imaging of Tumors by PEGylated Iron-Oxide-Gold Core-Shell Nanoparticles with Prolonged Blood Circulation Properties.* Macromol Rapid Commun, 2010. **31**(17): p. 1521-8.

130. Smolensky, E.D., M.C. Neary, Y. Zhou, T.S. Berquo, and V.C. Pierre, *Fe3O4@organic@Au: core-shell nanocomposites with high saturation magnetisation as magnetoplasmonic MRI contrast agents.* Chem Commun (Camb), 2011. **47**(7): p. 2149-51.

131. Hoskins, C., Y. Min, M. Gueorguieva, C. McDougall, A. Volovick, P. Prentice, Z. Wang, A. Melzer, A. Cuschieri, and L. Wang, *Hybrid gold-iron oxide nanoparticles as a multifunctional platform for biomedical application.* J Nanobiotechnology, 2012. **10**: p. 27.

132. Huang, C., J. Jiang, C. Muangphat, X. Sun, and Y. Hao, *Trapping Iron Oxide into Hollow Gold Nanoparticles.* Nanoscale Res Lett, 2011. **6**(1): p. 43.

133. Yu M.K., P., J., Jon S., *Targeting Strategies for Multifunctional Nanoparticles in Cancer Imaging and Therapy.* Theranostics, 2012. **2**(1): p. 3-44.

134. Brust, M., M. Walker, D. Bethell, D.J. Schiffrin, and R. Whyman, *Synthesis of thiol-derivatised gold nanoparticles in a two-phase Liquid-Liquid system.* Journal of the Chemical Society, Chemical Communications, 1994. **0**(7): p. 801-802.

135. Bangham, A.D., M.M. Standish, and J.C. Watkins, *Diffusion of univalent ions across the lamellae of swollen phospholipids.* Journal of Molecular Biology, 1965. **13**(1): p. 238-IN27.

136. Gonzales, M. and K.M. Krishnan, *Synthesis of magnetoliposomes with monodisperse iron oxide nanocrystal cores for hyperthermia.* Journal of Magnetism and Magnetic Materials, 2005. **293**(1): p. 265-270.

137. Pradhan, P., J. Giri, F. Rieken, C. Koch, O. Mykhaylyk, M. Doblinger, R. Banerjee, D. Bahadur, and C. Plank, *Targeted temperature sensitive magnetic liposomes for thermo-chemotherapy.* J Control Release, 2010. **142**(1): p. 108-21.

138. Milton, B.Y., J.N. Weinstein, W.H. Dennis, and R. Blumenthal, *Design of Liposomes for Enhanced Local Release of Drugs by Hyperthermia.* Science, 1978. **202**(4374): p. 1290-1293.

139. Bruns, O.T., H. Ittrich, K. Peldschus, M.G. Kaul, U.I. Tromsdorf, J. Lauterwasser, M.S. Nikolic, B. Mollwitz, M. Merkel, N.C. Bigall, S. Sapra, R. Reimer, H. Hohenberg, H. Weller, A. Eychmüller, G. Adam, U. Beisiegel, and J. Heeren, *Real-time magnetic resonance imaging and quantification of lipoprotein metabolism in vivo using nanocrystals.* Nat Nanotechnol, 2009. **4**(3): p. 193-201.

140. Cuyper, M. and M. Joniau, *Magnetoliposomes.* European Biophysics Journal, 1988. **15**(5): p. 311-319.

141. Martina, M.-S., J.-P. Fortin, C. Ménager, O. Clément, G. Barratt, C. Grabielle-Madelmont, F. Gazeau, V. Cabuil, and S. Lesieur, *Generation of Superparamagnetic Liposomes Revealed as Highly Efficient MRI Contrast Agents for in Vivo Imaging.* Journal of the American Chemical Society, 2005. **127**(30): p. 10676-10685.
142. Terreno, E., Delli Castelli, D., Viale, A., Aime, S., *Challenges for Molecular Magnetic Resonance Imaging.* Chem. Rev., 2010. **110**: p. 3019-3042.

Appendix

Published Work

A.1 List of Papers:

- Ghosh, S., Carty, D., **Clarke, S. P.**, Corr, S.A., Tekoriute, R., Gun'ko, Y., Brougham, D.F. "NMR studies into colloidal stability and magnetic order in fatty acid stabilised aqueous magnetic fluids." Physical Chemistry Chemical Physics (2010) **12**(42): 14009-14016

- Sadeghifar, H., Filpponen,I., **Clarke, S.P.**, Brougham, D. F., Argyropoulos, D. 'Production of cellulose nanocrystals using hydrobromic acid and click reactions on their surface' J. Mater. Sci. (2011) **46**(22):7344-7355

- Lartigue, L., P. Hugounenq, Alloyeau, D., **Clarke, S.P**., Lévy, M., Bacri, J. C., Bazzi, R., Brougham, D.F., Wilhelm, C., Gazeau F. "Cooperative Organization in Iron Oxide Multi-Core Nanoparticles Potentiates Their Efficiency as Heating Mediators and MRI Contrast Agents." ACS Nano (2012) **6**(12): 10935-10949.

A.2 Conference Presentations:

- Poster Presentation: **Clarke, S.P.**, Brougham, D.F. 'Magnetic Polymer Nanocomposite Materials for Targeted Drug Release in Cancer' Magmeet, Rostock, Germany, May 2010

- Oral Presentation: **Clarke, S.P.**, Brougham, D. F., 'Synthesis and Characterisation of Charged Iron Oxide Nanoparticles and their Composite Materials for Potential Targeted Drug Delivery' 63rd Irish Univerities Research Colloquium, University of Limerick, June 2012.

Contributions to Conference Presentations:

- Poster Presentation: Connolly, D., Alwy, A., **Clarke, S.P.**, Brougham, D. F., Thokala, P., Fox, M., O Connor, B. ' Nano-agglomerated stationary phases for solid-phase extraction' Functional Materials Conference, DCU, Sept. 2012